THE UNIVERSITY OF QUEENSLAND

PhD Thesis

Presented and publicly defended to obtain the title of

DOCTOR OF THE UNIVERSITY OF LORRAINE

Discipline: GEOSCIENCES

by **Allen Yushark FOSU**

Development of a Chloride Route for Lithium Extraction from Spodumene

on 1st June, 2023

Jury Members

Director of thesis	**Mr. Alexandre CHAGNES**	**Full Professor** **Université de Lorraine, Nancy**
Co-director of thesis	**Mr. James VAUGHAN**	**Associate Professor** **The University of Queensland, Brisbane**
Reviewers	**Mrs. Véronique HUBSCHER**	**Full Professor** **Université de Strasbourg, Strasbourg**
	Mrs. Virginie LAIR	**Full Professor** **Chimie ParisTech, Paris**
Examiners	**Mrs. Marie-Odile SIMONNOT**	**Full Professor** **Université de Lorraine, Nancy (President of the Jury)**
	Mrs. Juliette SIRIEIX-PLENET	**Associate Professor** **Sorbonne Université, Paris**
Supervisor of thesis **Guest member**	**Mr. Ndue KANARI**	**Senior Researcher-HDR** **Université de Lorraine, Nancy**

ABSTRACT

Lithium is a major component of Li-ion batteries, used in the manufacture of many portable electronic devices. The energy transition is driving the shift from thermal to electric and hybrid vehicles, which relies mainly on the use of Li-ion batteries for reversible energy storage. The development of electric vehicles based on lithium-ion technology is responsible for a record demand for lithium salt (mainly lithium carbonate and hydroxide).

Spodumene is the main source of lithium from ores. Its processing requires a phase transformation from α-form to β-form, followed by roasting leading to the formation of a lithium salt after a leaching, purification, and recovery steps. In this thesis, spodumene concentrate from the Pilbara region of Western Australia was characterized for thermal and hydrometallurgical processing.

Heat treatment is responsible for the formation of cracks in the grains which become more noticeable with increasing temperature. Disintegration of the material, melting and agglomeration with minerals contained in the gangue have also been observed by increasing the temperature up to 1050 °C. Apparent activation energies of 655±20 kJ mol^{-1} was calculated for the transformation of α-spodumene which confirms a strong temperature dependence for polymorphic transformations of spodumene.

Subsequently, we investigated an alternative route to conventional methods (sulphuric acid process) to treat the spodumene concentrate with the aim of reducing the high energy consumption of the phase transformation and sulphate roasting steps. This was achieved by direct chlorination of α-spodumene with calcium chloride, followed by water leaching of the residue to recover lithium chloride.

Analysis of the residue obtained after leaching indicated that the α-form was the only polymorph present, suggesting that extraction occurs directly from the α-phase. Under optimal conditions, heat treatment at 1000 °C for 60 minutes of the spodumene concentrate in the presence of calcium chloride at a calcium chloride/spodumene molar ratio of 2.0 is required to extract nearly 90% of lithium and recover 85% in the leach liquor. An apparent activation energy of about 122±6 kJ mol^{-1} was calculated for temperatures ranging from 800 to 950 °C.

The liquor obtained after leaching was purified by ion exchange and solvent extraction to recover lithium chloride of sufficient purity for consideration as a precursor in the production of lithium-ion battery materials.

ACKNOWLEDGEMENT

I give God praise for His presence that has been with me throughout this journey and endowing me with wisdom and guidance during challenging moments of this work.

Special thanks go to my supervisors Professor Alexandre Chagnes, Professor James Vaughan, and Dr. Ndue Kanari for believing in me and accepting me into the PhD program. I am a beneficiary of your long years of experience in your respective areas of expertise. Your directions have given me more insight into chemical thermodynamics and metallurgical process development. My gratitude also goes to Professor Danièle Bartier for her assistance and instructions in X-ray diffraction analysis. My gratitude to all jury members, especially the reviewers for their suggestions and comments that helped to improve the quality of the manuscript.

LabEx RESSOURCES21 and Lorraine Universite d'excellence have been my financial backbone throughout the study with support from the hydrometallurgy department of The University of Queensland (UQ). I appreciate all the resources poured out into this research.

I express my gratitude also to personnel at GeoRessources Laboratory, both academic and administrative for their unwavering support. I cannot forget the wonderful people I met at UQ hydrometallurgy department. The people are amazing, and the atmosphere was serene for working.

My parents have passed on, but I cannot overlook their effort in raising me up and the quality education they gave me. I thank them for their sacrifices. This work has been dedicated to them.

Lastly, I thank all my friends and family for their support and encouragement. I met a great family, Kenmore Church of Christ in Australia who made my stay exciting. Many thanks to all of you.

JOURNAL/CONFERENCE PUBLICATION AND PRESENTATION

Fosu, A.Y., Kanari, N., Vaughan, J. and Chagnes, A., 2020. Literature Review and Thermodynamic Modelling of Roasting Processes for Lithium Extraction from Spodumene. Metals, 10(10), p.1312. https://doi.org/10.3390/met10101312

Fosu, A.Y., Kanari, N., Bartier, D., Hodge, H., Vaughan, J., & Chagnes, A. (2021). Physico-Chemical Characteristics of Spodumene Concentrate and its Thermal Transformations. Materials, 14(23), 7423. https://doi.org/10.3390/ma14237423

Fosu, A.Y., Kanari, N., Bartier, D., Vaughan, J. and Chagnes, A., 2022. Novel Extraction Route of Lithium from α-Spodumene by Dry Chlorination. RSC Advances, 12(33), 21468-21481. doi:10.1039/d2ra03233c

Fosu, A.Y., Kanari, N., Vaughan, J. and Chagnes, A., 2022. Thermochemical Modelling for Extraction of Lithium from Spodumene and Prediction of Promising Reagents for the Roasting Process. International Conference on Extractive Metallurgy and Mining.
May 23-24, Vancouver, Canada. (Oral Presentation)

Fosu, A.Y., Kanari, N., Vaughan, J. and Chagnes, A., 2021. Advanced Chloride Route for Lithium Extraction from Spodumene. Annual Research Committee Meeting of Labex RESSOURCES21. October 7, Vandoeuvre-les-Nancy, France (Oral Presentation).

Fosu, A.Y., Kanari, N., Deng, Y., Motuzas, J., Howes, T., Vaughan, J., Chagnes, A. Novel Extraction Route for Lithium From Alpha Spodumene By Chlorination Roasting And Inorganic Membrane Percrystalization, 26th World Mining Congress, Brisbane-Australia, June 26-29, **2023** (Paper submitted)

AWARDS AND RECOGNITION

Best Presentation Award at the International Conference on Extractive Metallurgy and Mining. May 23-24, Vancouver, Canada.

TABLE OF CONTENTS

LIST OF FIGURES

LIST OF TABLES

LIST OF ABBREVIATIONS

AAN	Average Atomic Number
BSEs	Backscattered Electrons
BEV	Battery Electric Vehicle
CAS	Calcium Aluminosilicate
CASl	Calcium Aluminosilicate Chloride
DMS	Dense Media Separation
EVs	Electric Vehicles
EDS	Energy Dispersive Spectroscopy
FCVs	Fuel Cell Vehicles
HEVs	Hybrid Electric Vehicles
ICP-OES	Inductively Coupled Plasma-Optical Emission Spectrometry
IEA	International Energy Agency
ICDD	International Centre for Diffraction Data
IX	Ion Exchange
JKMRC	Julius Kruttschnitt Mineral Research Centre
LCT	Lithium, Cesium and Tantalum
LC	Lithium Carbonate
MJ	Mega Joules
Mt	Million Tonnes
MLA	Mineral Liberation Analysis
MIF	Mineral Intensity Factor
MP-AES	Microwave Plasma Atomic Emission Spectrophotometer
MR	Molar Ratio
NYF	Niobium, Yttrium and Fluorine
ppm	Parts Per Million
PHEV	Plug-in Hybrid Electric Vehicle
PDF	Powder Diffraction File
REEs	Rare Earth Elements
RIR	Reference Intensity Ratio
SEM	Scanning Electron Microscopy
SEs	Secondary Electrons
SHE	Standard Hydrogen Electrode

SX	Solvent Extraction
STEPS	Stated Policies Scenario
SDS	Sustainable Development Scenario
UQ	The University of Queensland
USGS	United States Geological Survey
WDS	Wavelength Dispersive Spectroscopy
XRD	X-ray Diffraction
XRF	X-ray Fluorescence

INTRODUCTION

Lithium is the first and lightest metal on the periodic table. It is a member of the alkali metals with atomic number, mass number and atomic radius of 3, 9.641 $gmol^{-1}$ and 0.155 nm respectively. Isotopes ranging from ^{4}Li to ^{12}Li have been indicated but ^{6}Li and ^{7}Li with abundances 7.5 and 92.5% are known to be naturally stable [1, 2]. Lithium is normally found combined with other elements as a salt or mineral instead of its native form. It is extracted industrially from brine or minerals as a salt of chlorine, carbonate, or hydroxide. It is silvery-white in colour with concentration of about 0.007% in the earth crust [3]. It has a density of 0.534 gcm^{-3} and melts and boils respectively at 180.5 ℃ and 1342 ℃. Though it is very soft with a value of 0.6 on the Mohs scale it is harder than sodium and carbon. Its standard reduction potential is about -3.03 V when measured with reference to the standard hydrogen electrode (SHE); making it one of the most electropositive metals with incredible electrochemical properties. Its specific heat capacity of 3.56 Jg^{-1} K at 25 ℃ makes it the highest for all solid elements, which in addition to the low redox potential makes it an interesting substance. It is therefore very attractive to the battery industry [3, 4] where it serves as the anode of metal-lithium primary battery. Its ionisation energy is indicated as 519 $kJ.mol^{-1}$. Among other uses of the metal include lubricating and heat transfer purposes, as bases and nucleophilic agents in chemical industries and as a mood-stabilizer in the medical field [5].

Lithium is obtained from two main sources: Salar/brine and pegmatite ores. Around 50% of the global lithium is obtained from Salar or brine though its content in these sources is relatively lower (about 200 to 700 ppm) compared to ores [6, 7]. It is believed that brines are formed in the Andes by the washing of soluble lithium salts contained in volcanic ash into endorheic reservoirs [8]. If this phenomenon occurs in arid or a high-altitude environment where an inverse correlation exists between altitude and atmospheric pressure, a high rate of evaporation of water from the brine occurs, leaving behind dry bed commonly called Salars. The climatic conditions of Argentina, Bolivia and Chile (usually called the Lithium Triangle) promotes the formation of Salars making them host a significant portion of the global lithium reserves [4]. Some well-known Salars in this region are Salar de Uyuni, Salar de Atacama and Salar de Muerto Hombre. Brine deposits also occur significantly in the US, China, India and Canada.

Processing brine for lithium is done by pumping the brine into evaporation ponds to evaporate, taking over a year to concentrate the metal. The recovery of lithium from the

concentrated brine is achieved by crystallisation and precipitation of calcium and magnesium chloride among others using calcium carbonate. Lithium chloride can then be converted into its carbonate using sodium carbonate as precipitant after purification stages to remove boron and remaining impurities. The process is less expensive, but the management of impurities and the longer processing time required are its downside.

Geothermally hot waters have also been indicated to contain lithium with concentration ranging from 0.1 to about 500 ppm [4]. If the temperature of the water is sufficiently high, it enhances the leaching of lithium from weathered rocks and volcanic activities leading to the formation of geothermal brines. Extraction of lithium from this source is mainly by membrane filtration, ion-exchange or precipitation. Some waste products obtained from oil extraction processes may also be a rich source of lithium up to about 700 ppm. These are called oilfield brines. Lithium recovery from this source may be expensive due to the depth (more than 2 km) which the brine needs to be pumped before it gets to the earth surface. Attempts have also been made to recover the metal from the sea irrespective of its low concentration (about 0.17 ppm) [3]. This is achieved predominantly by electrodialysis or inorganic cation exchangers which has high selectivity for lithium regardless of the presence of group one and two metal ions [9–12]. The economics however, may not favour the metal's recovery from sea water looking at the volume of water which must be processed and the quantity of the metal that will be obtained from it in comparison with other sources of the metal.

Pegmatites are coarse-grained rock type that host several masses of lithium-bearing minerals as well as rare earth elements which are selectively and economically mined with simple mining techniques. This lithium deposit may be categorised into three: the NYF type which is composed of niobium, yttrium and fluorine; the LCT type which is made up of lithium, caesium and tantalum; and lastly the NYF+LCT mixed type [13]. The lithium minerals (spodumene, petalite, lepidolite, etc) and other concomitant minerals (columbite-tantalite, cassiterite, pollucite, muscovite, albite, quartz, feldspar) are commonly found associated with LCT pegmatite. The close association of lithium with pegmatites is due to its high solubility which makes it concentrated in latter stage of cooling magma and associated aqueous liquids where pegmatites are formed. Close to 145 lithium-bearing minerals including clays have been indicated of which about 25 are known to contain more than 2% Li_2O [4, 8]. Amongst the lithium bearing minerals, spodumene stands out as the most attractive for industrial extraction of lithium.

The commercialised process for beneficiating spodumene requires transforming it from α- to the β-phase at elevated temperatures. This is followed by acid roasting (or baking around 250 °C) of the activated form and a downstream processing to recover lithium. This process has inherent challenges which are discussed in the next chapter. New and improved technologies which seeks to resolve these challenges have been on the increase owing to the high demand of the metal in the last decade. This study therefore seeks to develop a complete and novel process for extracting lithium from the mineral where some of the challenges encountered in the conventional process are resolved.

Literature reviewed on the state-of-the-art revealed that one major challenge encountered in all processing routes of the mineral is the phase transformation. It is done at very high temperatures and requires appreciably longer time which makes it energy intensive with increased cost of production as well as prolonging the time. It was also realised that chlorine metallurgy is not very developed in the processing and recovery of the metal from spodumene though it has some advantages, particularly, its high efficiency at moderate operating temperatures which can be harnessed. This led to the investigation as to whether direct chlorination of α-spodumene can lead to the extraction of lithium at a reduced temperature, thereby mitigating the energy requirements in the phase transformation and the roasting step as well as the time requirement. Thus, the main focus of this thesis is to create knowledge and ascertain the technical feasibility for sustainable extraction of lithium through direct chlorination of α-spodumene.

To achieve this, spodumene concentrate obtained from the Pilbara region of Western Australia was characterised to ascertain its physical, chemical and mineralogical properties followed by investigation into its polymorphic phase transition. Several chlorine salts were explored for their ability to extract lithium from the uncalcined mineral by performing thermodynamic calculations using HSC Chemistry® 5.1. Chlorination roasting experiments with selected salt(s) were performed to optimize process parameters.

Chlorinated residues obtained were leached followed by investigation into technologies to purify the leached liquor to obtain lithium salt of high purity. Explored technologies include selective crystallisation of calcium chloride from leach liquor, ion exchange and solvent extraction

This manuscript is organised into five main chapters. In the first chapter, literature on the methods of processing lithium-bearing mineral particularly spodumene are reviewed. Thermodynamic modelling was performed on data obtained in literature for processing spodumene in order to gain more insight of the processes. In chapter 2, instrumentation and

analytical techniques used in the study is described. Spodumene sample used for the study was characterised in Chapter 3. Its transformational characteristics upon thermal treatment was examined with respect to morphology, polymorphic transformation and its thermal requirements. The fourth chapter is dedicated to studying and selection of suitable chlorinating agents based on thermochemical calculations performed with the HSC Software. Information on experimental investigations to extract lithium as a chloride with optimised conditions is also found in this chapter. The last chapter looks at purifying the leach liquor to recover the lithium.

REFERENCES

[1] T. B., Coplen, J. K., Böhlke, P., De Bievre, T., Ding, N. E., Holden, J. A., Hopple, H. R., Krouse, A., Lamberty, H. S., Peiser, K., Revesz, and S. E., Rieder, "Isotope-abundance variations of selected elements" (IUPAC Technical Report). *Pure and applied chemistry*, *74*(10), pp.1987-2017, Jan 2002.

[2] P. B. Tomascak, "Developments in the Understanding and Application of Lithium Isotopes in the Earth and Planetary Sciences," 2004.

[3] B. Swain, "Recovery and recycling of lithium: A review," *Separation and Purification Technology*, vol. 172. Elsevier B.V., pp. 388–403, Jan. 01, 2017. doi: 10.1016/j.seppur.2016.08.031.

[4] L. Kavanagh, J. Keohane, G. G. Cabellos, A. Lloyd, and J. Cleary, "Global lithium sources-industrial use and future in the electric vehicle industry: A review," *Resources*, vol. 7, no. 3. MDPI AG, 2018. doi: 10.3390/resources7030057.

[5] J.-M. Tarascon, "'Is lithium the new gold?.,'" *Nat Chem*, vol. 2, no. 6, pp. 510–510, 2010.

[6] Z. Li, J. Mercken, X. Li, S. Riaño, and K. Binnemans, "Efficient and Sustainable Removal of Magnesium from Brines for Lithium/Magnesium Separation Using Binary Extractants," *ACS Sustain Chem Eng*, vol. 7, no. 23, pp. 19225–19234, Dec. 2019, doi: 10.1021/acssuschemeng.9b05436.

[7] P. K. Choubey, M. Kim, R. R. Srivastava, J. Lee, and J.-Y. Lee, "Advance review on the exploitation of the prominent energy-storage element: Lithium. Part I: From mineral and brine resources," *Miner Eng*, vol. 89, pp. 119–137, Apr. 2016, doi: 10.1016/j.mineng.2016.01.010.

[8] D. E. Garrett, *Handbook of lithium and natural calcium chloride*. Elsevier, Apr 5, 2004.

[9] M., Abe and R., Chitrakar, "Synthetic inorganic ion-exchange materials. XLV. Recovery of lithium from seawater and hydrothermal water by titanium (IV) antimonate cation exchanger", *Hydrometallurgy*, *19*(1), pp.117-128, Oct 1987.

[10] T. Hoshino, "Preliminary studies of lithium recovery technology from seawater by electrodialysis using ionic liquid membrane," *Desalination*, vol. 317, pp. 11–16, May 2013, doi: 10.1016/j.desal.2013.02.014.

[11] S. Nishihama, K. Onishi, and K. Yoshizuka, "Selective recovery process of lithium from seawater using integrated ion exchange methods," *Solvent Extraction and Ion Exchange*, vol. 29, no. 3, pp. 421–431, May 2011, doi: 10.1080/07366299.2011.573435.

[12] K. S. Chung, J. C. Lee, W. K. Kim, S. B. Kim, and K. Y. Cho, "Inorganic adsorbent containing polymeric membrane reservoir for the recovery of lithium from seawater," *J Memb Sci*, vol. 325, no. 2, pp. 503–508, Dec. 2008, doi: 10.1016/j.memsci.2008.09.041.

[13] P. Černˊy and Č. Černˊy, "The Classification of Granitic Pegmatites Revisited," *The Canadian Mineralogist* 43, no. 6, pp 2005-2026, Dec 2005.

CHAPTER 1: Literature Review

1.1 Lithium

1.1.1 Global demand, market, reserves and resources.

Lithium is a currently a very hot commodity which has widespread application resulting from its properties enumerated in the previous section. It is undergoing rigorous investigations to meet worldwide stable supply as it is now considered a critical metal by many countries. The fuel combustion transportation system has been found as a major contributor to greenhouse emissions, particularly, CO_2. In the European Union alone, it is estimated to contribute around 27% of the global emission [1]. To curb this and achieve a net zero emission, there is an ongoing revolution to replace the traditional combustion fuel vehicles and other energy generating systems partially or wholly with clean technologies. This initiative if successful is expected to reduce the emission with a subsequent reduction in global warming.

The International Energy Agency (IEA) estimated the quantities of the metals needed by each clean energy technology sector to achieving the Paris Agreement [2]. It was revealed that, about six-fold as much as the metals used in 2020 is needed to make this goal a reality; the quantity required for electric vehicles (EVs) and batteries being significantly higher than all other technologies (Figure 1.1) [2]. They predicted the percentage demand of each metal toward the energy transition and presented their findings in Figure 1.2. Included is their Stated Policies Scenario (STEPS) which is an indicator of the direction of the energy system by sector analysis according to current policies and announcement. The figure reveals that, as high as 90% of lithium will be needed in 2040 compared to nickel and cobalt (60 to 70%), Rare Earth Elements (REEs) and copper (40%) [2, 3]. Elsewhere, about 27 fold as much as recorded in 2012 is predicted as the demand by 2050 where fairly high quantity of vehicle fleet are expected to be electrically powered to meet the decarbonisation agenda [4–6].

It is said that a classical EV needs approximately six times more lithium than that required for the same conventional type of vehicle during manufacture [2]. Several uncertainties surround the prediction of the future quantum of EVs due to the rapid rate of manufacture.

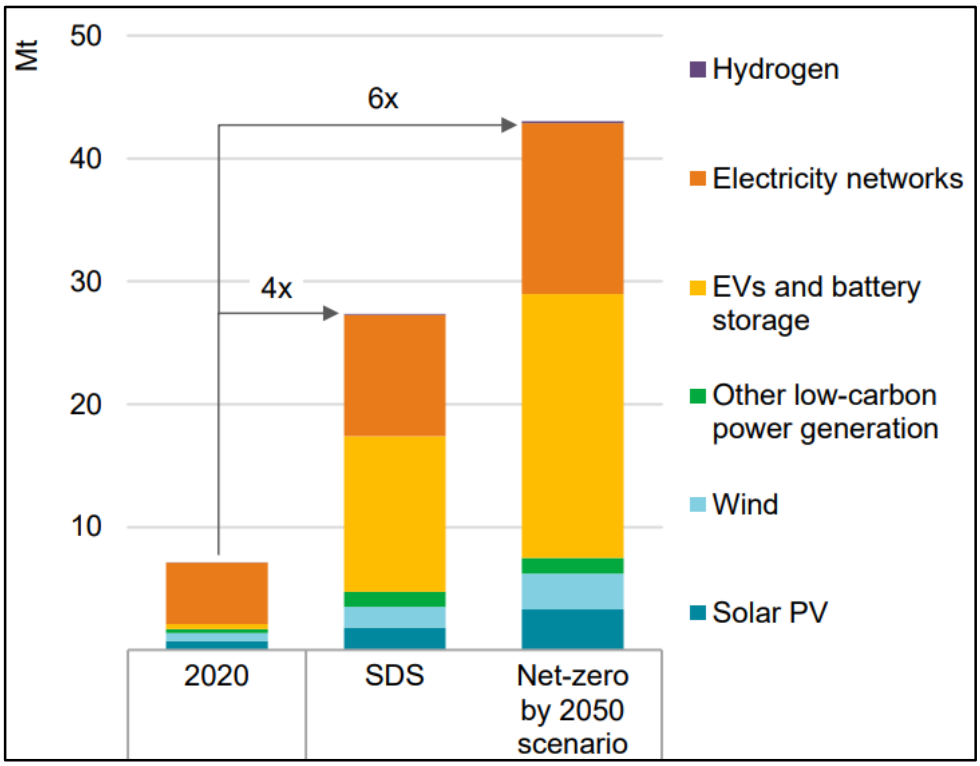

Figure 1.1: Contributions of clean energy technologies to achieve Net Zero by 2050; Sustainable Development Scenario (SDS) is an indicator of the expected demand in 2040 if this goal must be achieved by 2050 [2]**.**

For instance, Bloomberg New Energy Finance's 2030 projection of the electro-automobile demand exceeded their previous one by 40% [7–9]. Elsewhere, a yearly growth of forty-two new EVs manufactured for every thousand people in 2100 (about 630 million units) which though, corresponds to hundred percent penetration by the year 2087 [10], it may not be able to meet the global target. Taking the EU into consideration, Simon et al. [1] predicted that, depending on the brand of vehicle and battery, an optimum of 9.5 million penetration which is just a small quantity (about 30%) of what is needed for 2030.

Despite the predicted EV shortages, studies have revealed abundance of lithium reserves to match up with the rapid growing market demands except for a temporal shortage which can occur [10, 11]. Gruber et al. [10] predicted a minimum and maximum lithium demands of 12 and 20 million tonnes (Mt) respectively between 2010 and 2100.

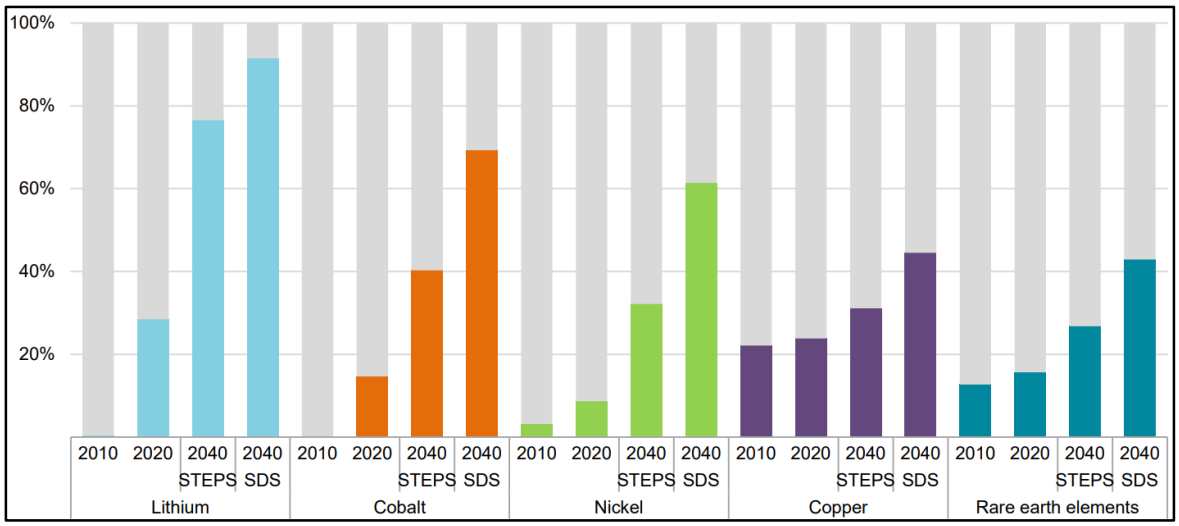

Figure 1.2: Demand of critical metals since 2010 and the projected demand to achieve SDS by 2040. [2].

They also predicted 39 Mt as the highest global resource and 19 Mt as the lowest global recoverable lithium which when compared with the demand confirms no danger of lithium scarcity for the growing market. In their analysis they argue that, though the maximum demand (20 Mt) is higher than the lower recoverable lithium, it is securely lower than the upper limit resource (39 Mt) and since there is the likelihood of obtaining higher recoveries from the lower recoverable lithium (19 Mt), there seem to be no danger of shortage [10]. The only challenge lies in the relatively longer time required for setting up of new mines and refineries to cater for the sharp market demand. It has been revealed that an average of 16 years is required from the start of mining projects until the first production [2]; thus, there can be a shortage due to this lagging time should there be a sharp rise in demand.

USGS indicated a 33% rise in lithium consumption in 2021 when it increased from 70,000 tonnes in 2020 to 93,000 tonnes whilst production rose by approximately 21% from 82,500 to 100,000 tonnes likely due to the number EVs that penetrated [12]. This is confirmed by the 2022 IEA report which revealed a doubled sales of EVs in 2021 with a total number of 6.6 million which was even predicted to go beyond 10 million in 2022 [3]. The IEA “blue map scenario” for the different EVs predicts annual sales of 14, 62, 47 and 34 million by 2050 respectively for the hybrid, plug-in hybrid, battery, and fuel cell types [13, 14]. A change over in manufacture and sales of these vehicle fleet to another is also expected such that, the battery type will dominate with 104 million sales followed by the plug-in type with 20 million; the hybrid type will be reduced to as low as 6 million whilst the fuel cell type may not be in existence.

Predicting lithium quantities required in the EVs is marked with a lot of reservations since their development is still ongoing alongside the possible different battery chemistries among other factors. This makes it difficult to predict the quantities of the metal required by a particular vehicle type since the different battery chemistries require different quantities of lithium (material intensity) for every battery energy. This has resulted in varying figures ranging from 50 to 562 g/kWh reported in literature (Table 1.1). That notwithstanding, Speirs et al. [5] after their careful analysis arrived at 190 to 380 g/kWh as the ideal. The IEA's prediction of annual sales of plug-in hybrid electric vehicle (PHEV) and battery electric vehicle (BEV) were used to determine the annual lithium demand since these vehicle types contain the highest battery size as well as the suspicion that they will be the dominant on the market compared to hybrid electric vehicles (HEVs) and fuel cell vehicles (FCVs).

Table 1.1: Reported amount of Li_2CO_3 required for each kW h of EV battery [5].

Source	Vehicle application	Mat. Int.* (kgLi/kWh)
Chemetall GmbH	BEV (25 kW h)	0.165
	PHEV (16 kW h)	0.176
	HEV (1 kW h)	0.375
Meridian International Research		0.300
Meridian International Research		0.563
Kushnir and Sanden	Average for four	0.160
Rade and Andersson	chemistries	0.140
	Li-ion (Mn)	
	Li-ion (Ni)	
	Li-ion (Co)	
Argonne National Laboratory	HEV4 (1.2 kW h)	0.308
	PHEV20 (6 kW h)	0.244
	PHEV40 (12 kW h)	0.246
	EV100 (30 kW h)	0.246
Gruber et al. [10]	Li-ion (Co, Mn, Ni)	0.114
Evans		0.113
Evans cited by Reuters	Chevrolet Volt (16 kW h)	0.158
Engel		0.050
Fraunhofer ISI	$LiCoO_2$	0.180
	$LiFePO_4$	0.120
Dundee Capital Markets		0.080
National Renewable Energy Laboratory	HEV (1.7 kW h)	0.100
	PHEV12 (5.6 kW h)	0.108
	PHEV35 (17.5 kW h)	0.110
	BEV75 (29.5 kW h)	0.112
	BEV150 (67 kW h)	0.112

Mat. Int.* represents Material Intensity

Finally, they arrived at 268 and 989 kt as the upper limit annual demand of the metal for the 2030 and 2050 “blue map market” respectively as well as 47.2 and 184 kt for the corresponding lower limits. Another source has predicted 2 Mt of lithium carbonate equivalence (LCE) demand (1.7 and 0.3 Mt respectively for battery and other demand) by 2030 which is four times of what they predicted for 2020 [7].

The supply of lithium to the market is determined by its availability (resource and reserve) and production, either from primary or secondary sources. Some researchers [10, 11, 15, 16] have estimated the global availability but leads to varying estimations which makes predicting the market supply very challenging. It is said that in 2009, the difference in the estimations between the lowest and the highest value was huge (around 700%) [5]. A source predicted an approximate supply of 1.7 Mt by 2027 (Figure 1.3) which will require an extra 500 to 1000 kt production if the sales of EV evolve as predicted in the current decade [7].

Geologist classifies the amount of the substance of interest (mineral, element, or fuel) into resource and reserve. Resource is the estimated quantity of potentially recoverable material occurring naturally in the earth crust based on theoretical knowledge whilst reserve is the amount of the resource that can be currently exploited with reference to available technology and socioeconomic conditions. Yaksic and Tilton [11] classified resources of lithium as minerals, brines, clays and seawater but reserve was only limited to minerals and brines.

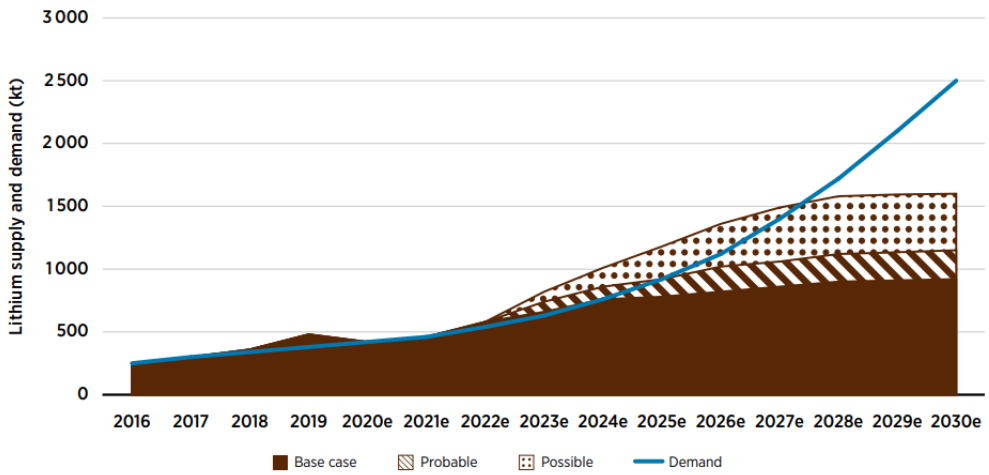

Figure 1.3: Stability demand and supply balance of lithium. “e” means expected [7].

They simplified their classifications and possible products obtainable from them alongside their uses in Figure 1.4 [11]. They also revealed that at increased price of the metal, some resources may qualify as reserves such that the recovery of the metal from seawater will be possible if the price falls within seven to ten dollar a pound. Should this be possible, about 44.8 billion tonnes of lithium from seawater can be recovered. This accounts for 20% of the total metal in seawater at its extremely low concentration (about 0.17 mg/L) [5, 11, 17].

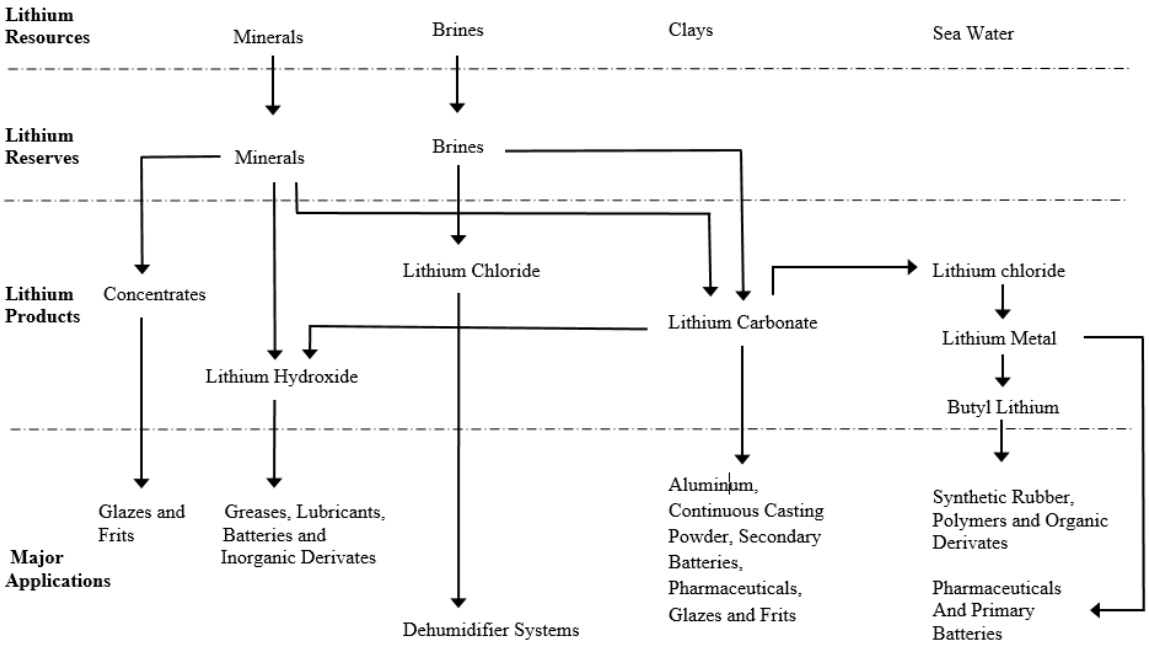

Figure 1.4: Classification of lithium resource and reserve in deposits, their recoverable products and uses [11]**.**

The exploration of the metal is still at the infantile stage and new deposits either as resource or reserve are constantly being discovered which results in changing estimation of the available lithium over time. USGS therefore, constantly updates their records to account for the changes, revealing as high as 48 and 8 Mt as the resource and reserve difference between 2015 and 2021 respectively [12, 18]. Figure 1.5 indicates the estimates as at 2022 according to USGS survey where Bolivia followed by Argentina host the world's largest resource at 21 and 19 Mt respectively. Though Chile places third globally in metal's resource, it has the largest known reserve followed by Australia at 9.2 and 5.7 Mt respectively, leaving Bolivia with no significantly known reserve even at her highest resource estimated.

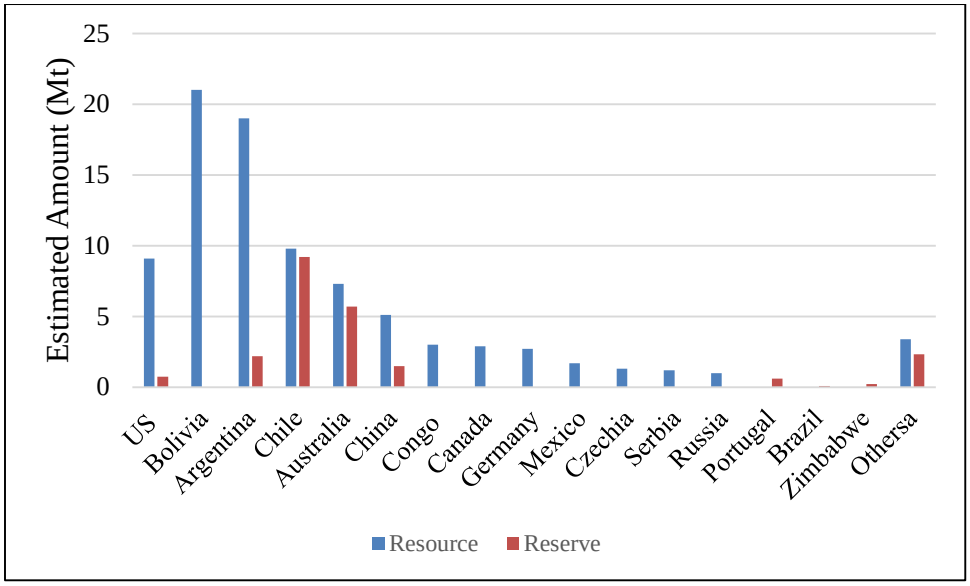

Figure 1.5: Current estimation (as at 2022) of global lithium resource and reserve. Data from USGS. "e" means expected [12].

Estimation of the annual production is faced with some difficulties as some companies consider the information proprietary. A typical example is the withholding of these data by industries in the United States (US). In Figure 1.6, the yearly production by country (except US), consumption and price from 2015 to 2021 is presented. Australia has been the largest producer throughout the years studied. Since the country's source of production is spodumene, it can be inferred that, production from minerals exceeds that of brine for the years considered even though brine hosts the major resource and reserves.

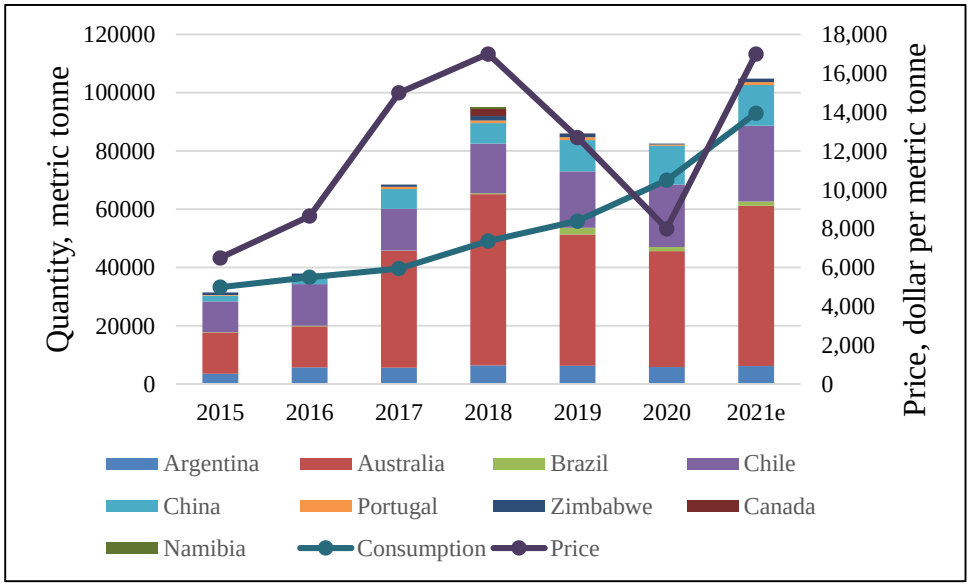

Figure 1.6: Lithium production, consumption, and price from 2015 to 2021. Data from [19]**.**

This may be attributed in part to the longer processing time required for extraction from brine and in part to less effort to maximise extraction from this source. Chile (production from brine) follows as the second whilst China places third with a mixed production from both minerals and brine. Yaksic and Tilton [11] sourced information from industries and other places and presented the cost of production from some brine and pegmatite deposits around the globe in a summary found in Table 1.2 and 1.3 respectively. Other salient information such as the grade or concentration and the magnesium to lithium ratio were also indicated. It is observed that though the magnesium to lithium ratio to some extent determines the ease of processing brine, there is no correlation between it and the production cost. The Atacama deposit in Chile produced the metal at the lowest cost between 0.70 to 1.00 dollars per pound; Australia and Zimbabwe deposit contain the highest concentration of lithium with their cost of production within the ranges 1.20 to 1.50 and 1.30 to 1.80 dollar per pound respectively.

Despite Bolivia hosting the world's largest resource of 21 Mt, USGS does not indicate any production for the years under consideration but a source [20] has however, indicated 1400 tonnes of production since 2018. The low production in the country is attributed to the restrictions of the mineral law of the country that makes the country to enjoy monopoly of the metal's production in the country. This prevents the participation of foreign companies in the production for enhanced exploitation and maximization of the abundant resource found in the country [20].

Production is seen to increase annually from 2015 until 2018 after which a decline was observed in 2019 and 2020 due to excess production over consumption and consequently, decreasing the price as observed (Figure 1.6). Afterwards, the metal saw increased production after the pandemic (2020) to meet the surging demand and price which has led to increased establishment and expansion of lithium mines and refineries worldwide.

Figure 1.7 presents the historic price of the metal since 1970, the predicted price from 2021 to 2040 roadmap to enable the attainment of net zero emission and the uncertainty band. It is observed that, the post-pandemic price increase is likely to persist and even be exorbitantly high for a longer period to the extent of affecting the time limits set for the transition to green technology [21].

Table 1.2: Characteristics of some brine deposits and their production costs [11].

Deposit	Country	Grade (%Li)	Mg/Li Ratios	Production cost*
Atacama	Chile	0.15	6.4	0.70-1.00
DXC	China (Tibet)	0.04-0.05	0.22	1.00-1.20
Zhabuye	China (Tibet)	0.05-0.1	0.001	1.00-1.20
Taijinaier	China	0.03	34	1.10-1.30
Hombre Muerto	Argentina	0.06	1.37	1.10-1.30
Olaroz	Argentina	0.09	2	1.10-1.30
Silver Peak	USA	0.023	1.5	1.10-1.30
Rincon	Argentina	0.04	8.5	1.20-1.50
Maricunga	Chile	0.092	8	1.20-1.50
Uyuni	Bolivia	0.04	19	1.30-1.80
Searles Lake	USA	0.0065	125	2.00-2.50
Salton Sea	USA	0.022	1.3	2.20-2.80
Great Salt Lake	USA	0.004	250	2.20-2.80
Dead sea	Israel-Jordan	0.002	2,000	2.40-3.00
Smackover	USA	0.0386/0.0365	20	5.00-6.40
Oceans	n/a	0.000017	n/a	7.00-10.00

Production cost***** in dollars per pound; n/a is “not applicable”.

Table 1.3: Some pegmatite deposits and their cost of production [11].

Deposit	Country	Grade (%Li)	Production cost*
Greenbushes	Australia	1.36	1.20-1.50
Masvingo (Bikita)	Zimbabwe	1.4	1.30-1.80
Bernic Lake	Canada	1.28	1.30-1.80
Cherryville	USA	0.68	1.30-1.80
Barroso-Alvao	Portugal	0.37-0.77	1.40-2.00
Covas de Barroso	Portugal	0.72	1.40-2.00
Gajika	China	n/d	1.40-2.00
Maerkang	China	n/d	1.40-2.00
Brazil	Brazil	n/d	1.50-2.00
Separation Rapids	Canada	0.62	1.80-2.20
Quebec	Canada	0.53	1.90-2.30
Jaijika	China	0.59	1.90-2.30
Qaidam Basin	China	n/d	1.50-2.50
Kings Mountain	USA	0.69	2.00-2.50
Etikinskoe	Russia	0.23-0.79	2.10-2.70
Namibia	Namibia	n/d	2.20-2.80
Manono-Kitololo	Zaire	0.58	2.40-3.00
Bougouni Area	Mali	1.4	2.40-3.00
Yellowknife	Canada	0.66	2.50-3.00
McDermitt	USA	0.24-0.53	3.50-4.70
North Carolina	USA	n/d	3.50-4.70
Russian pegmatites	Russia	n/d	3.50-4.70

Production cost***** in dollars per pound; n/d is “no data are available”.

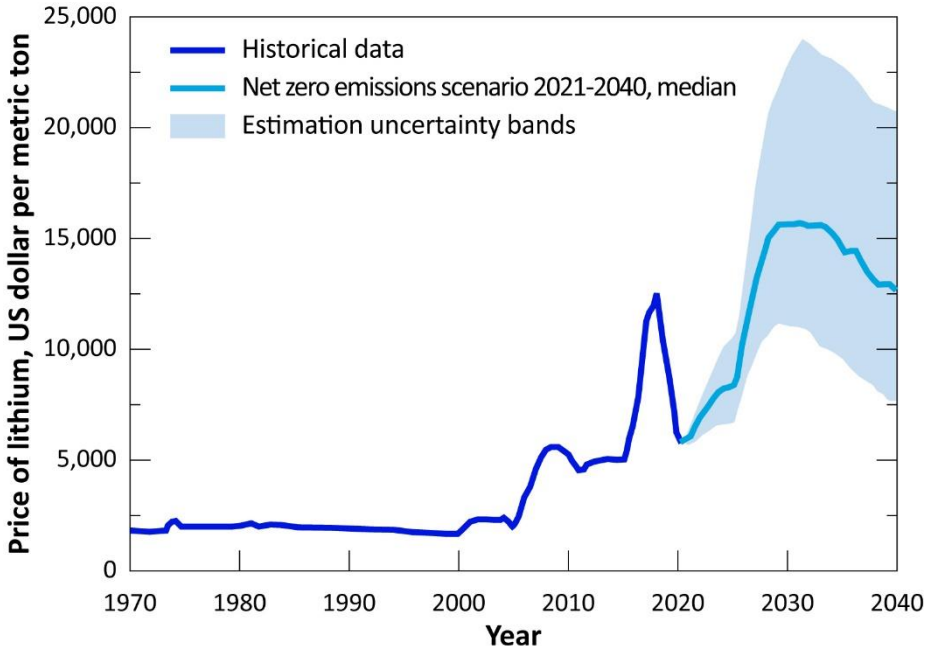

Figure 1.7: Historic and future price of lithium [21].

1.2 Lithium Minerals

As indicated earlier, lithium is found in about 145 minerals of pegmatite or sedimentary origin but only a handful have economic importance. Pegmatite containing the metal are spodumene ($LiAlSi_2O_6$), petalite ($LiAlSi_4O_{10}$) lepidolite [$KLi_2Al(Al,Si)_3O_{10}(F,OH)_2$], amblygonite [$(Li,Na)AlPO_4(F,OH)$], eucryptite ($LiAlSiO_4$) and zinnwaldite [$KLiFeAl(AlSi_3O_{10})(OH,F)_2$]. Presently, the extraction of lithium from minerals is almost solely obtained from spodumene. Clay and lacustrine evaporites are the sedimentary sources of lithium. Clayey source of lithium is hectorite [$Na_{0.3}(Mg,Li)_3Si_4O_{10}(OH)_2$] and jadarite [$LiNaSiB_3O_7(OH)$]. Hectorite (deposits found in Hector, California) is a magnesium silicate of the smectite family with trioctahedral crystal structure where there is a partial substitution of magnesium for lithium [22, 23]. Concentration of lithium ranging from 0.2 to 2wt% have been reported [24]. Jadarite is a carbonate and micaceous aggregated matter found in Jadar Basin of Serbia as a result of the sedimentation remains of evaporation (evaporite) of intermontane lakes. It also contains significant amount of boron (about 47.2% of B_2O_3) which can be economically extracted alongside lithium [25]. The grade of lithium in these minerals with some characteristics are given in Table 1.4. Major lithium minerals encountered and their global distribution is shown in Figure 1.8.

Table 1.4: Characteristics of some Li-bearing pegmatite and clay minerals [26, 27]**.**

Deposit	Mineral	Formula	% Li_2O	Hardness*	Density/gcm^{-3}
Pegmatites	Lepidolite	$K(Li,Al)_3(Si,Al)_4O_{10}(F,OH)_2$	7.7	2.5-3.0	2.8-2.9
	Zinnwaldite	$KLiFe^{2+}Al(AlSi_3)O_{10}(F,OH)_2$	3.42	3.5-4.0	2.9-3.0
	Spodumene	$LiAlSi_2O_6$	8.03	6.5-70	3.1-3.2
	Eurcyptite	$LiAlSiO_4$	11.86	6.50	2.6-2.7
	Petalite	$LiAlSi_4O_{10}$	4.5	6.0-6.5	2.4-2.5
	Amblygonite	$(Li,Na)Al(PO_4)(F,OH)$	7.4	5.5-6.0	3.0-3.1
Sedimentary rocks	Jadarite	$LiNaB_3SiO_7(OH)$	7.28	4.0-5.0	2.50
	Hectorite	$Na_{0.3}(Mg,Li)_3Si_4O_{10}(OH)_2$	1.17	1.0-2.0	2.50

Hardness* represented on the Mohs Scale.

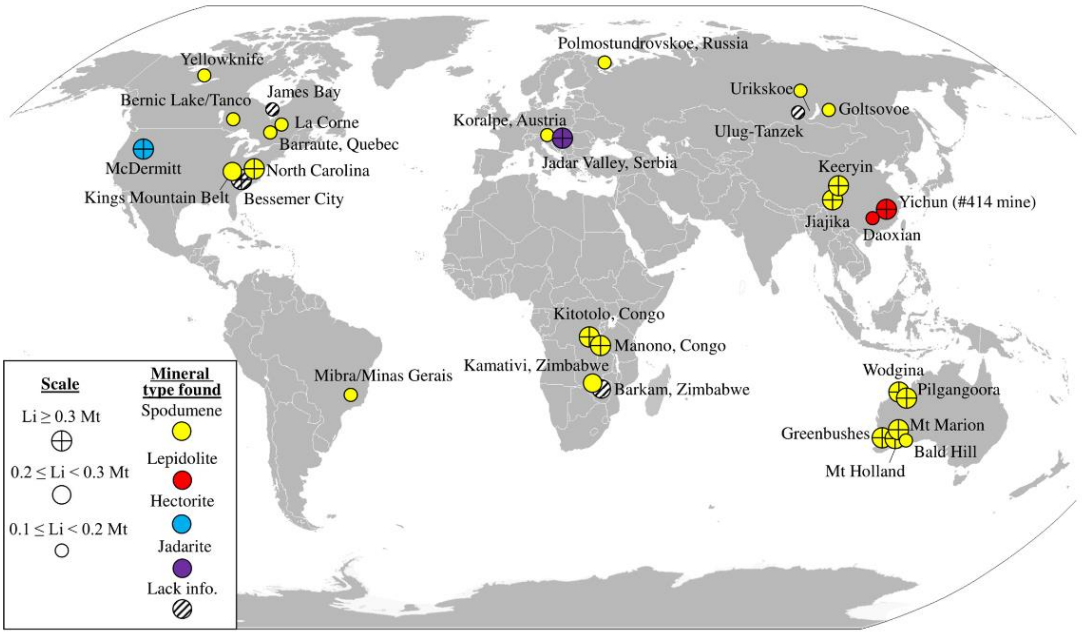

Figure 1.8: Global distribution of major lithium minerals [26]**.**

1.2.1 Spodumene

The name of the mineral originates from the Greek connotation of "burnt to ashes" (spodumenos) signifying its white-grey colour when pulverised. It is among the minerals usually hosted in pegmatites. It has a high lithium concentration (3.73% Li or 8wt% Li_2O equivalent in a pure sample) and commonly distributed in a host of deposits around the globe compared to other minerals (Figure 1.8) [16, 26]. This and other factors including the high lithium content makes it the most attractive and largely explored for lithium. It is believed to be first pegmatite to solidify from magmatic eruption due to its higher boiling point (about 1423 ℃ at atmospheric conditions) [16]. Its colour can vary from white to dark green depending on the iron concentration and ranked 6.5 to 7.0 on the Mohs scale; making

it the hardest among the minerals (Table 1.4). There are three categories: Secondary, Primary and Zonal, and Primary and Unzonal (otherwise called phenocrystic) [16]. The first two have low iron content which makes them white coloured (Figure 1.9a) with high lithium concentration whilst the latter is low grade, has high iron concentration and is greenish. The Secondary is said to be synthesised from the decomposition of petalite as $LiAlSi_4O_{10} \rightarrow LiAlSi_2O_6 + 2SiO_2$ [16]. The mineral sometimes appears in a crystal form (Figure 1.9b) which is prized by gemologist.

It is a clinopyroxene and occurs naturally as α-monoclinic polymorph. It is characterised by $[SiO_4]$ tetrahedral structure of quartz where portions of the Si^{4+} is replaced with Al^{3+} to form octahedral $[AlO_6]$ coordination. Electrical neutrality is then achieved by the addition of cations with suitable charge density like lithium (or sodium) through coulombic force of attraction. Lithium and aluminium therefore sit at the *M2* and *M1* octahedral sites respectively, whilst silicon is hosted at the middle of the tetrahedron. The octahedral parts through the sharing of common oxygen atoms, bridge to form chains. The octahedral chains are arranged parallel to Si in the tetrahedron through a strong O–Si–O ionic bond with the Li and Al atoms.

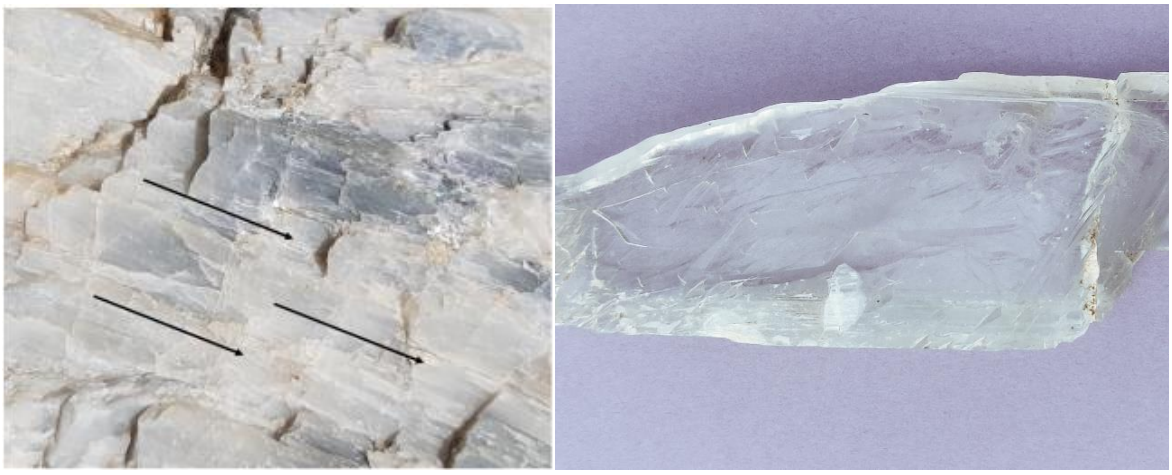

(**a**) (**b**)

Figure 1.9: Photograph of (a) high grade spodumene ore showing the direction of cleavage [28]; (b) spodumene crystal.

Lithium therefore bonds with six atoms of oxygen: with a pair of oxygen atoms having a definite Li–O bond length of 2.120, 2.267 and 2.281 Å [29]. Its original space group is C2/c but at pressures of around 3.2 GPa, it may change to P21/c upon reversible transition [30–32] and assumes cell parameters of a = 9.471 Å, b = 8.400 Å, c = 5.223 Å, α = γ = 90.0 degrees and β = 110.2 degrees.

β-spodumene, another polymorph of the mineral consists of two separate tetrahedron structures which are joined in a three-dimensional form with their central parts hosting aluminium or silicon [33]. Lithium in this phase is located between the cavity of five-member rings, formed by the individual tetrahedron. Zeolite-like channels created from the five member rings run parallel to the (100) or (010) planes [34]. The zeolite-like channels which are parallel to the *a* and *b* axis are larger and account for the tremendous ion-exchange capacity of β-spodumene during roasting [34]. It has the space group $P4_32_12$ with cell parameters $a = b = 7.534$ Å and $c = 9.158$ Å [33].

An intermediary metastable γ-phase which transforms to the β-phase upon continuous heating has also been identified. It has a hexagonal symmetry where Si and Al sit at the middle of the tetrahedrons. This polymorph of the mineral starts appearing between 700 and 900 °C during the thermal process. Thus the mineral has three polymeric phases depending on the temperature. Figure 1.10 shows the crystal structure of the various phases with the various colours red, yellow, blue and green representing oxygen, silicon, aluminium and lithium respectively.

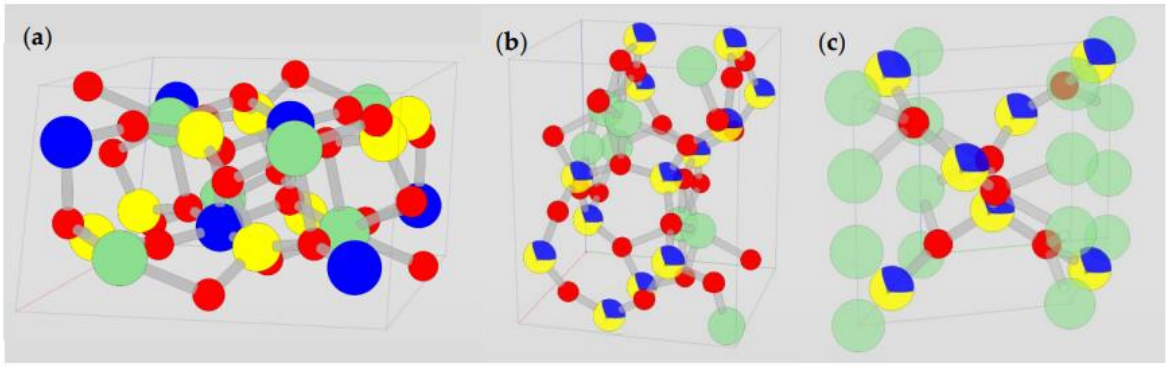

Figure 1.10: Crystal structure of (a) α- (b) β- and (c) γ-spodumene [35]**.**

Spodumene deposits are found at Greenbushes, Bikita, Minas Gerais, the Chita Region, Ontario and Manitoba, and North Carolina located in Australia, Zimbabwe, Brazil, Russia, Canada and the United States respectively. The gangue minerals (muscovite, albite, quartz and feldspar) are often by-products of spodumene concentrate which are normally used to offset some of the cost during beneficiation. Though the mineral is the most explored and economically important of the lithium bearing aluminosilicates, the cost of processing is relatively high compared to brine but the surging demand and price of lithium makes it a viable source of the metal. About half of the lithium produced is now obtained from ores with a significant portion coming from spodumene.

1.2.2 Petalite

Petalite ($LiAlSi_4O_{10}$) like spodumene is a monoclinic aluminosilicate. Its name originates from the Greek word "petalion" which means leaf or blade in reference to its basal cleavage. Its space group is P2/a with lattice parameters *a* = 11.737 Å *b* = 5.171 Å *c* = 7.630 Å β= 112.54º at room temperature and Z = 2. It has two cleavage planes; a perfect and a poor one in the (001) and (201) planes respectively which are 114° apart [16, 36]. It is said to have a three-dimensional crystal structure framework in which lithium, silicon and aluminium are coordinated with four atoms of oxygen at the corners of the tetrahedron (Figure 1.11). It is considered as phyllosilicate mineral due to the layered [Si_4O_{10}] which are parallel to the (001) plane connecting the LiO_4^- and AlO_4^- network [37, 38]. Contrary to the common feature of other aluminosilicates with $(AlO_4)^{5+}$ coordination, its iron content is negligible [16, 39]. Table 1.5 is a typical elemental composition (in their oxide) of petalite with lithium and iron oxide concentration of 4.45 and 0.008 wt%.

Table 1.5: The mineralogical composition of petalite [36]

Element	SiO_2	Al_2O_3	Fe_2O_3	MgO	CaO	Li_2O	Na_2O	K_2O	H_2O^-	LOI
%	77.80	16.41	0.008	0.038	0.018	4.45	0.048	0.076	0.08	1.72

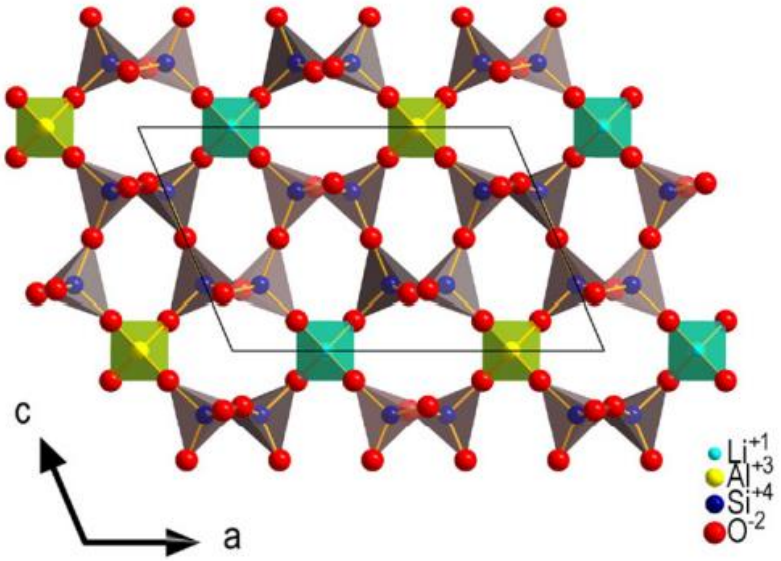

Figure 1.11: crystal structure of petalite [37]**.**

The colour may vary from yellow to grey or white depending on the gangue associations. A sample photograph of the mineral is shown in Figure 1.12. Aside being a lithium source, the mineral has its use in the manufacture of glasses such as the screens of cell phones or can

be used as a component of flux due to its resistance to heat [40]. Deposits are located in Canada, Zimbabwe, Brazil, Russia, Namibia, Finland, USA, Sweeden, etc.

Figure 1.12: Photograph of petalite.

1.2.3 Lepidolite

Lepidolite represented by the general formular $K(Li,Al)_3(Si,Al)_4O_{10}(F,OH)_2$ is a rare type of micaceous aluminosilicate which forms a solid solution ranging from the polylithionite $KLi_2Al(Si_4O_{10})(F,OH)_2$ to trilithionite $K(Li_{1.5}Al_{1.5})(AlSi_3O_{10})(F,OH)_2$ end members. It is also monoclinic whose space group is C2/m (1M) with lattice parameters *a* = 5.209(2) Å *b* = 9.011(5) Å *c* = 10.149(5) Å β= 100.77(4)^o at room temperature and Z = 2. It has a single perfect cleavage in the (001) direction [41]. It is said to be a derivative of either muscovite ($KAl_2(AlSi_3O_{10})(F,OH)_2$) or siderophyllite ($KFe^{2+}{}_2Al(Al_2Si_2)O_{10}(F,OH)_2$) which has high lithium content. Thus, muscovite or siderophyllite may be "lithanated" by the progressive replacement of aluminium or iron with lithium in their octahedral framework (Figure 1.13). This rearrangement results in an increased occupancy of the tetrahedron. In muscovite, the replacement of aluminium with lithium may be 3:1 (three Li^+ replacing one octahedral Al^{3+}) whilst in siderophyllite, it is usually 2:1.5 (two Li^+ replacing about one and half Fe^{2+}) [42]. It is worth noting that, the amount of lithium that replaces the octahedral site atoms in siderophyllite categorises its derivatives into lithian siderophylite, protolithionite, zinnwaldite and lepidolite. Lithian siderophylite has less than 0.25 of its octahedral sites occupied by Li^+; protolithionite has between 0.25and 0.75 occupied; zinnwaldite between

0.75 to 1.25; and lepidolite more than 1.25 sites occupied by Li^+ [42]. Thus the high replacement of lithium in the last two explains why they are both explored for lithium to some extent. Lepidolite has colour ranging from pink to purple depending on the concentration of manganese associated with it. Caesium, rubidium and potassium are usually associated with it which are extracted as by-products [16, 43]. Deposits are found in Zimbabwe, Canada, Brazil, and Portugal. Figure 1.14 shows a photo of a sample of lepidolite.

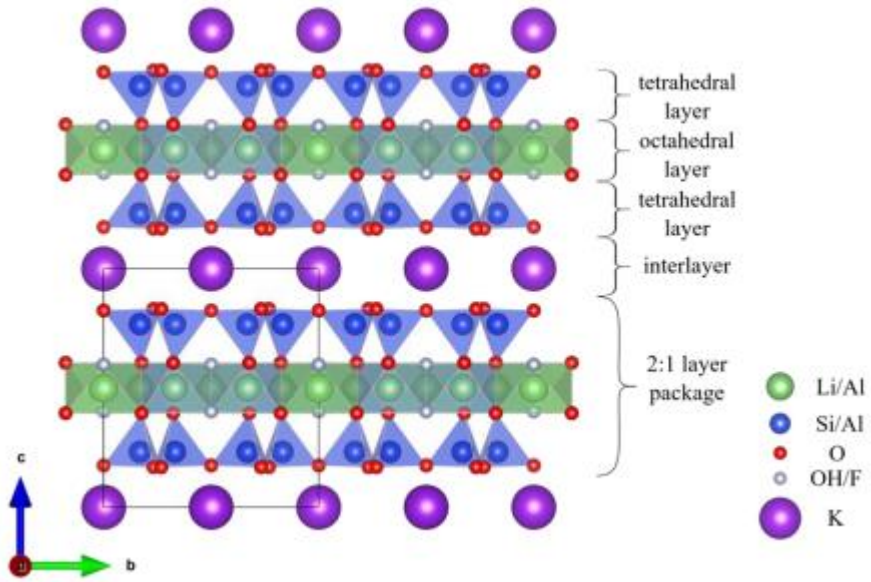

Figure 1.13: Atomic arrangement and crystal structure of lepidolite [44]**.**

Figure 1.14: Photograph of a sample of lepidolite.

1.2.4 Amblygonite

It is the end member of a solid solution series of lithium aluminophosphate which is rich in fluorine [$LiAl(PO_4)F$]. Its corresponding end member called montebrasite is obtained when all the fluorine atoms of amblygonite is replaced by hydroxyl ion which gives it the formular [$LiAl(PO_4)(OH)$]. It has the triclinic crystal structure where it crystallizes into the space group $c\bar{1}$ with cell parameters a = 6.644(2) Å b = 7.744(2) Å c = 6.910(1) Å α = 90.35(2)^o [45, 46]. It is said to be the primary phosphate that crystalizes out of LCT pegmatite [47, 48]. It is composed of a framework of octahedral aluminate chain which extends in the direction of the c-axis and coordinates at its corners with tetrahedral (PO_4). Figure 1.15 shows the crystal structure of the mineral as viewed from two different planes. The cavities or interstices arising from this coordination accommodates the lithium atoms [45, 49, 50]. It has been revealed that most of the properties of the members of the series is a function of the F/OH ratio [48]. It cleaves in all four planes with the perfect one occurring in the (100) direction. Its typical elemental composition (wt%) as oxides is P_2O_5, 48.44; Al_2O_3, 33.90; Li_2O, 10.12; F, 13.06; -O=F_2, 5.50 [46]. Theoretical lithium concentration is about 10.12% but commercially, it may be about 3.5–4.4% Li (7.5–9.5% Li_2O) [16]. Contrary to the current lithium industry, amblygonite and eucryptite were previously the favourite and mostly explored for lithium due to easy processing through direct lixiviation without roasting. Its rare occurrence resulted to the changeover to spodumene for lithium extraction. It may vary from being colourless to other pale colours though it is generally white or creamy (Figure 1.16). Deposits are found in Germany, Sweden, USA, Canada, Australia, and Mozambique [16], [46].

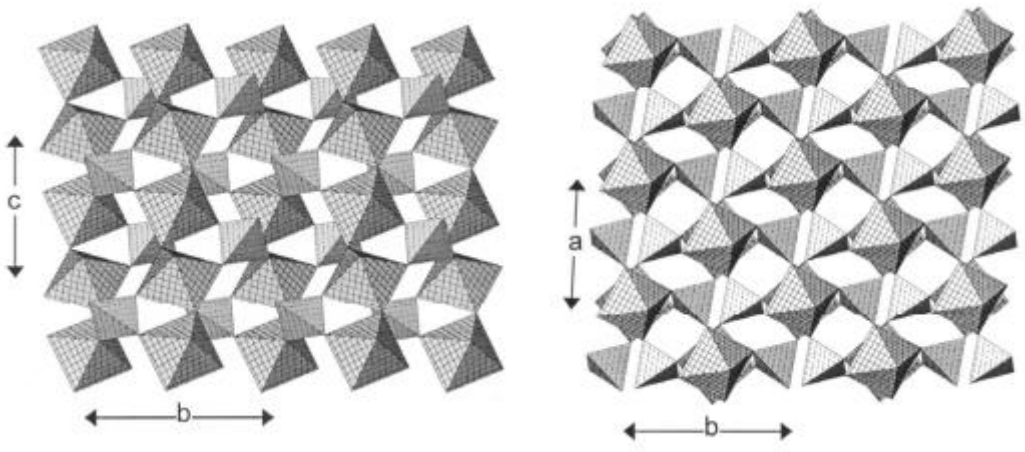

(**a**) (**b**)

Figure 1.15: Crystal structures of amblygonite projected in (a) (100) and (b) (001) planes [48]**.**

Figure 1.16: Sample photograph of amblygonite.

1.2.5 Eucryptite

It is a type of lithium aluminosilicate in LCT pegmatite with few deposits around the globe. Considerably large deposit is found in Bikita, Zimbabwe. It is believed to be formed through a hydrothermal and secondary magmatic crystallization after spodumene and petalite. The elemental composition (in their oxide form) is SiO_2, 47.68; Al_2O, 40.46 and Li_2O, 11.86 wt% which makes it the lithium mineral with the highest theoretical lithium content, but Li_2O content ranging from 4.5–6.5wt% may be found in commercial concentrates [16, 51]. Quartz is the mostly associated impurity which makes it difficult differentiating it from the mineral because of their close resemblance to each other in hardness, colour, specific gravity and magnetic properties. This makes physical separation of the two minerals almost impossible [52]. The mineral is trigonally coordinated and said to be a stuffed derivative of quartz where lithium is substituted for silicon but due to valence compensation, it adds on aluminium to give it the $LiAlSiO_4$ formula and structure [52–54]. The framework of the mineral is composed of tetrahedral SiO_4 and AlO_4 which are linked to each other at their corners with lithium ions sitting at the tetrahedral interstices (Figure 1.17) [55, 56]. It has a grey to white colour but may be brown when altered (Figure 1.18).

Apart from its large deposit at Bikita, Zimbabwe, it can also be found at North Carolina at the Kings Mountain (USA).

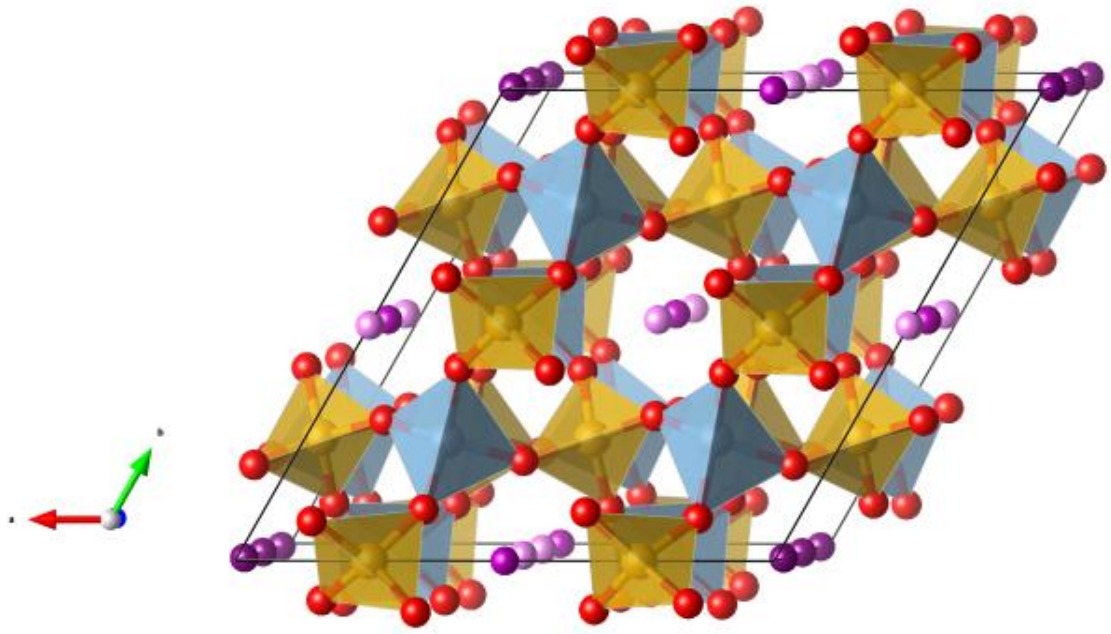

Figure 1.17: Crystal structure of eucryptite. The orange and light blue colours represent SiO_4 and AlO_4 tetrahedral; purple and red colours represent Li and O atoms respectively [56]**.**

Figure 1.18: Photograph of eucryptite sample [57].

1.2.6 Stability relationship of lithium aluminosilicates with temperature and pressure

Petalite has been observed to be metamorphosed to either spodumene or eucryptite in some deposits though the practical occurrence during magmatic crystallization is challenged by another school of thought [16, 39]. London [58] in his laboratory experiments however confirmed this transformation. As indicated earlier [16, 39], spodumene due to its high melting point crystallizes out first among the aluminosilicates (at pressures around 4kbar). β-spodumene crystallizes out of it at higher temperatures, usually above 680 ℃. As it cools below 680 ℃, the β-phase of the mineral transforms to petalite. The cooling continues such that at 320 ℃ or below and at moderate to high pressures (between 4 to 1.6 kbar), the natural α-form of spodumene forms from the cooling petalite (Figure 1.19). The transformation is represented by Equation 1.1. However, at relatively low pressures, eucryptite rather than α-spodumene is formed from the petalite (Equation 1.2). It can be inferred therefore that pressure (the depth) determines the segregation of α-spodumene from eucryptite during their formation. The stability of petalite is therefore located at the boundaries of β-spodumene at high temperatures and all pressures; α-spodumene at lower temperatures and medium pressures; and lastly, to eucryptite at low temperatures and pressures [16, 39]. It is can be found also that the quartz content of the minerals is what differentiates them and these minerals are thus, likely to be found as intergrowth with quartz as is usually observed.

$$\beta\text{-}LiAlSi_2O_6 + 2SiO_4 \xrightarrow{\leq 680\ ℃} LiAlSi_4O_{10} \xrightarrow{\leq 320\ ℃;\ \leq 4 > 1.5 kbar} \alpha\text{-}LiAlSi_2O_6 + 2SiO_2 \qquad (1.1)$$

$$LiAlSi_4O_{10} \xrightarrow{\leq 320\ ℃;\ \leq 1.5\ kbar} LiAlSiO_4 + 3SiO2 \qquad (1.2)$$

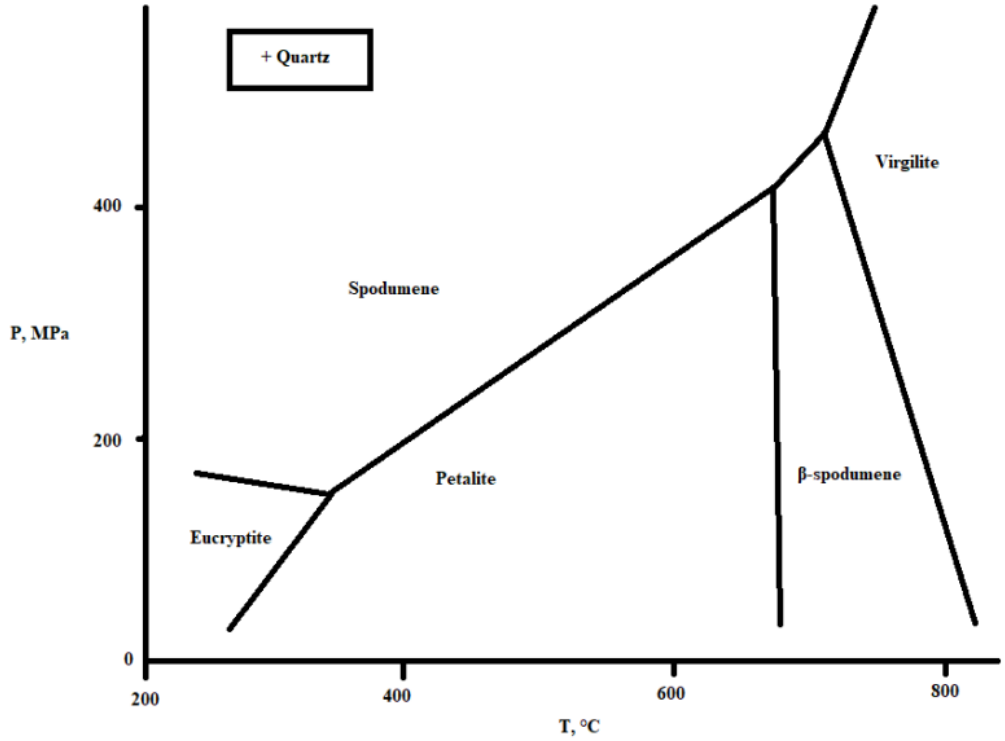

Figure 1.19: Pressure-Temperature stability diagram for spodumene, petalite and eucryptite [35]**.**

1.3 Extraction of lithium from minerals

The extraction of lithium from minerals first demands the cleavage of their M-O (where M=Al, Si, Li) bonds to make Li and/or the other metals accessible to lixiviants. Literature reveals that almost all the commercial lithium minerals may be directly treated (or baked) with reagents to directly process them except for spodumene which has complications with direct baking in its natural form. Reagents comprising acids and/or their mixtures (H_2SO_4, HF, HCl, H_2SO_4/HF) alkalis (NaOH, $Ca(OH)_2$), salts ($CaCl_2$, Na_2SO_4, K_2SO_4, CaF, NaCl, NH_4Cl) and gas like Cl_2 have been used to etch the silicate bond of the minerals to make them amenable for processing. Figure 1.20 illustrates the responsiveness of some minerals to direct H_2SO_4 roasting and/or lithium extraction where there is apparently, no lithium extraction from spodumene. The different minerals may, therefore, be processed differently; some requiring pre-treatment to facilitate the baking and/or leaching process. Others like amblygonite and eucryptite may be leached directly without roasting/baking, and some, baking preceding leaching. This leads to different processing routes for the different minerals though similar reagents are often used in almost all. Conventionally, processing spodumene requires four steps: (1) pre-treatment to convert the natural α-spodumene to β-spodumene (2) roasting β-spodumene with chemicals to form

lithium salt (3) leaching of roasted residue to release lithium in aqueous solution and (4) purification and recovery of lithium from leach liquor.

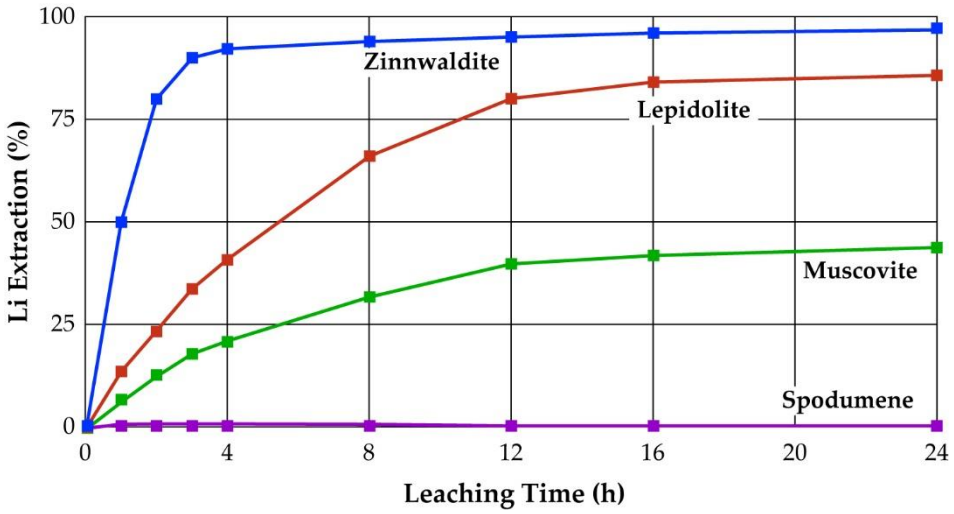

Figure 1.20: Response of α-spodumene and lithium micas to lithium extraction by sulphuric acid. Adapted from [59].

1.3.1 Pre-treatment of spodumene

Spodumene unlike other lithium minerals is not amenable to chemical treatment in its natural form because of the strong forces which binds lithium in the polyhedron structure of the mineral. Processing spodumene therefore requires an inevitable pre-treatment step which is crucial for destroying the mineral's crystalline structure to liberate lithium for chemical treatment. Though the obsolete alkaline process did not necessitate activation of the mineral before processing, it had inherent challenges including high energy requirement for the decomposition of limestone before calcination with α-spodumene. It also resulted in the formation of dicalcium silicates which releases large amount of heat and makes temperature control in the calcination stage difficult [60]. Pre-treatment to activate the mineral is, therefore, an expedient step in processing the mineral, the cost and the time requirements notwithstanding. This is achieved by two main procedures: mechanical or thermal.

Mechanical Activation

Mechanical activation is the alteration of the physicochemical features of a material to improve its responsiveness to further processes usually through grinding in a high energy grinding mill. Several procedures such as lixiviation, annealing and calcination have been known to improve after this technique [61–63]. The process imparts energy which destroys

and/or deforms the crystal structure of the material leading to increased surface area and provide highly reactive sites for chemical reactions [63, 64]. Increased recovery of metals after mechanical activation of minerals in a ball mill have been reported [61], [64–66]. The process if applied to lithium-bearing minerals can cause similar effect in the silicate framework to increase reactivity and extraction. Promising result was reported by Setoudeh et al. [65] when they applied it to petalite in the presence of Na_2SO_4. Its effect on lithium recovery using lepidolite and α-spodumene have also been reported [62, 63, 65]. Some studies on the latter have revealed the appearance of α- and β-phases in addition to the metastable γ-phase [67, 68]. Mechanical activation apart from deforming and weakening the coulombic attractive forces, induces amorphization of the material [67, 68]. It has also been suspected that, if the process is performed in aqueous media, the hydroxyl group of water may bond with silicon after the Si-O cleavage to form silica gel ($SiO_2 \cdot H_2O$) [62]. Rosales et al. [69] confirmed the release of the tightly bound lithium atoms in the crystal lattice of α-spodumene when the technique was performed in situ during lixiviation where significant quantity of lithium was reported in the leached solution.

Thermal Activation

Thermal activation otherwise called decrepitation is the change of the micro- and/or crystal-structure of substances by subjecting them to heating at elevated temperatures. It has been employed as pre-treatment technique for several minerals to open them up for further investigation or facilitate their processing. The responsiveness of spodumene to chemical processing is greatly enhanced by subjecting it to thermal treatment though, a process for direct extraction of lithium from α-spodumene have been documented [59], [70–73]. It is believed that, during this transformation process, there is a dislocation of Al^{3+} in the α-spodumene leading to a β-spodumene crystal structure with a comparably larger crystal volume. This increases the mobility of lithium atoms and their access to reagents [74–76]. Thus, decrepitation leads to volumetric expansion and makes the mineral porous with an increased surface area. The transformation has also been shown to improve comminution, as β-spodumene is relatively soft and flaky [30, 75, 77]. Recently, an intermediary hexagonal metastable γ-phase which is predicted to influence the extraction of lithium was discovered during calcination. The thermal transformation like mechanical activation is now understood to occur sequentially as α→γ→β instead of the previously known α- to β-transformation [35, 74, 75].

Extensive study by researchers on the mineral's behaviour to the thermal treatment revealed interesting findings though with contradictions [29], [74–76], [78]. Dwyer [79] advised that, it is essential for the process to be carried out below 1040 ℃ (the fusion temperature of spodumene). Though the gangue associated with the mineral can adversely affect downstream beneficiation processes, it is said to facilitate heat conduction leading to efficient transformation since spodumene itself exhibits low thermal conductivity [30, 60]. The transformation commences around 800 ℃ and is complete by 1100 ℃ if conventional heat is used but it has been reported to commence at about 634 ℃ by using microwave heating [75, 78]. Peltosaari et al. [75] considered the effect of particle size to be insignificant with respect to conversion rate of spodumene. They found that, the phase transformation and increased surface area had corresponding decrease in density in the order 3.16, 2.395 and 2.365 g/cm3 respectively for α, γ and β. It is anticipated that the α- to γ-transformation is exothermic and the heat released helps to offset the heat requirement of the process, however, the change from α directly to β is endothermic [30, 80].

Investigations by Moore et al. [29] indicated that temperature and heating method have negligible effect on the mass fraction of the phases transformed during the decrepitation process and the quantities of transformed products are almost equal at the initial stage before the final conversion to the β-phase. Conversely, Salakjani et al. [78] explained that temperature and residence time are the major factors that determine the inversion of the phases in spodumene. The temperature effect is subsequently influenced by the chemical composition and the feed particle size of the spodumene sample. The heating method employed, morphology of the sample after comminution and the quantity of gangue minerals present may also affect the extent of temperature influence during decrepitation [29], [74–76].

Heat treatment techniques during thermal activation

The conventional heating method used in processing spodumene is the muffle type of furnaces. These heating modes are clean and thus has little contamination effect on the mineral to affect downstream processing. Recently, microwave heat treatment of the mineral has been studied and compared with conventional methods [29, 74, 75, 78, 81]. Spodumene is passive to microwave irradiation so the heat treatment with this method is made possible by combined heating using silicon carbide [30, 75]. It was found that β-phase spodumene absorbs significantly higher microwave energy than the α-phase spodumene which can lead to local sintering within the temperature range of β-phase formation [30]. That

notwithstanding, it has an impressive phase transformation kinetics for the mineral than the conventional method. About 3 minutes was enough to complete α to β-phase conversion [75], but about an hour was needed by muffle furnace to achieve 100% conversion to the β-phase [30]. The temperature requirement was, nonetheless, found to be invariant with regards to the heating methods. Not much information on pyrometallurgical treatment of the mineral with microwave is known. Further research geared toward resolving challenges encountered with this treatment such as local sintering, passiveness of α-spodumene to microwave radiation and other factors affecting the efficiency is required. Stirring the sample during calcination or blending it with substances which has little or no impact on subsequent processing has been recommended as a solution to challenges of the microwave heating approach [30].

There seem to be some inconsistencies in the temperature and time requirement for the phase changes using the conventional heating method. According to Salakjani et al. [30], no transformation was observed below 950 ℃ even for an extended heating time. They observed the initial evolution of γ and β-phases at 950 ℃ for at least 30 min of calcination but Peltosaari et al. [75] observed their first γ-phase at 800 ℃. The difference in the observation may be due to factors such as different concentration of impurities, amorphous nature created during comminution and even particle size of the feed used for the study. As low as 5 min was good to almost complete the transformation by working at 1100 ˚C [74] whilst elsewhere, 15 min treatment at 1000 achieved a similar result [75]. Salakjani et al. [74] however, observed some γ-phase present even after 1 hour of residence time at 1100 ℃.

Comparing the energy requirement for the two heating techniques revealed that microwave requires a relatively low energy input for the process compared to the conventional method [78]. It requires 5 times less energy for a complete transformation to β-phase than conventional furnace. The reason for the high energy requirement in the conventional process can be due to the fact that heating begins from the outside and moves to the inside of the sample by conduction (the furnace needs to heat up evenly before the sample undergoes heating) therefore, some of the energy is wasted while in the microwave process, heating starts from the inside of the sample and extends radially outside (the sample absorbs the microwave radiation directly for heating), leading to little or no loss of energy.

In another study [81], the comparison of the microwave and conventional heat treatment for acid roasting of β-spodumene showed that microwave heating resulted in higher lithium extraction than the muffle furnace with regards to key parameters of

processing time, acid requirement and energy input. 10.4 MJ of energy was needed for the conventional process whereas only 15.4 kJ was required by the microwave for the same quantity of lithium extracted. Microwave irradiation again required shorter time (20 s) to achieve this goal while an hour was needed in the muffle furnace for the same extraction efficiency. Particle size was found to have an important effect on the extraction efficiency by microwave heat. Finer particles have been confirmed to enhance maximum (93%) lithium extraction with as low as 15% excess acid requirement as compared to 80% excess acid, which is normally used in roasting.

1.3.2 Roasting of Spodumene Ore

Roasting is a thermal process where the mineral is treated with an appropriate reagent leading to a chemoselective ion exchange reaction where lithium is exchanged for atoms of similar characteristics in the reagent to form a lithium salt. It is the normal practice for forming lithium salts in the lithium bearing micas (lepidolite and zinnwaldite) and spodumene. In spodumene, it is done after decrepitation where β-spodumene is baked with chemicals or may be performed in-situ during decrepitation. Lithium salts usually formed include Li_2SO_4, LiCl and LiF depending on the chemical used. Several reagents have been employed at this stage and rigorous investigations are ongoing for optimization and/or discovery of more efficient ones. Unlike roasting, the decrepitation process (in spodumene) appears to be nearly optimized and little can be done to further adjust parameters like the temperature and granulometry of the mineral [35]. The choice of the reagent generally depends on their selectivity for the metal, the stability of the resulting salt in the aqueous phase, environmental friendliness, cost, and ease of regeneration after leaching. These reasons have resulted in a series of investigations for suitable chemicals that satisfy most of these criteria during beneficiation of the mineral.

The reagent used for the roasting determines the name of the extraction process leading to two well-known methods: sulphation and alkaline. These methods in addition to the chlorination method is represented in the general flow diagram in Figure 1.21.

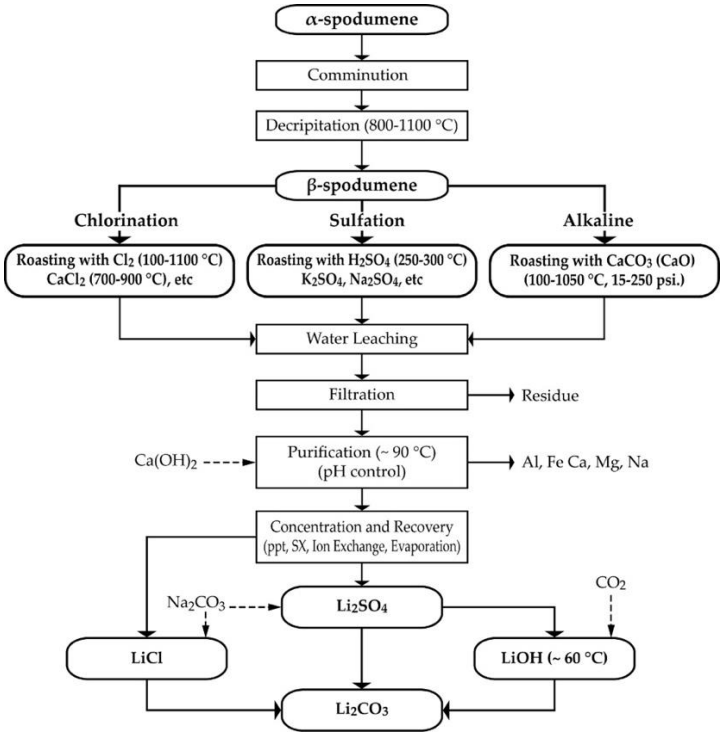

Figure 1.21: Flow diagram for acidic, alkaline and chlorination processes for extracting lithium from spodumene.

Sulphation Processing of Spodumene

In this process, sulphating agents such as sulphuric acid, alkali metal sulphates, or SO_3 are employed to produce soluble lithium sulphate which can be leached. This process benefits from the high solubility and stability of lithium sulphate in the aqueous phase during leaching. The drawbacks especially with sulphuric acid roasting are the difficulty in producing high purity lithium salt due to its unselectivity towards other metals such as Al, Na, Mg, Fe and K. Thus, there is co-leaching of significant quantity of other metals, especially, aluminium and iron which presents as impurities such that separating them from lithium by precipitation carries along some lithium, which decreases the overall lithium recovery [79]. The co-leached alkali metals also pose considerable challenge due to their similar chemistry to lithium in aqueous solution. This makes their separation difficult and can finally end up in the final product. Sulphation roasting using sulphuric acid consumes a large amount of reagent which affects the economic viability [23, 82]. The other reagents, however, have less of these challenges.

Sulphates of potassium, ammonium and sodium have been successfully used for the extraction of lithium from several lithium bearing minerals. Sulphate roasting of lepidolite followed by water leaching has been studied widely using H_2SO4, $Na_2SO_4/K_2SO_4/CaO$,

Na_2SO_4 and $FeSO_4$ at temperatures around 880, 1000 and 850 °C respectively. The reported approximate extraction extents were more than 90% respectively [83–86]. Li et al. [87] patented the production of lithium sulphate solution with subsequent recovery of lithium carbonate and lithium fluoride after sulphate roasting of lepidolite with sulphuric acid (Figure 1.22). The invention revealed the possible recovery of accessory metals which are usually hosted in the mineral including Rb, Cs, Al and K [26, 87].

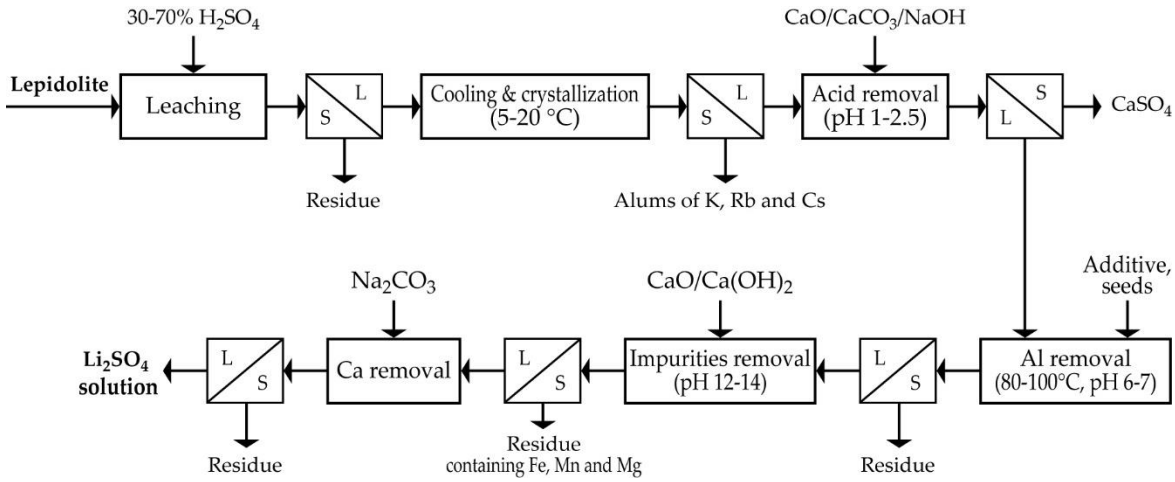

Figure 1.22: Production of Li_2SO_4 pregnant solution from H_2SO_4 roasting of lepidolite with subsequent recovery of Li_2CO_3, LiF and other metals. Adapted from [26, 87]**.**

Zhang et al. [83] suggested equation 1.3 and 1.4 as the pathways for the lepidolite-sulphuric acid roasting as:

$$KLi_{1.6}Al_{2.2}Si_{3.2}O_{10}F(OH)_{(s)} + 4H_2SO_4 + 2.6H_2O \rightarrow KAl(SO_4)_2 + 0.8Li_2SO_4 + 1.2Al(SO_4)OH{\cdot}5H_2O + 3.2SiO_2 + HF_{(g)} \quad (1.3)$$

$$KLi_{1.6}Al_{2.2}Si_{3.2}O_{10}F(OH)_{(s)} + 4H_2SO_4 + 2.1H_2O \rightarrow KAl(SO_4)_2 + 0.8Li_2SO_4 + 1.2Al(SO_4)OH{\cdot}5H_2O + 2.9SiO_2 + 0.25SiF_{(g)} \quad (1.4)$$

The L-Max® process by Johnson et al. [88] has been patented for the ability to produce Li_2CO_3 after mechanical activation of lepidolite (and zinwaldite) followed by sulphuric acid leaching [26], [88]. Sulphating behaviour of zinnwaldite, montmorillonite and petalite have also been discussed elsewhere [23], [89–91] using Na_2SO_4 and H_2SO_4, yielding appreciable extraction (90% or more).

In the case of spodumene, several authors have conducted systematic experimental studies to understand and optimize the amenability of sulphates to spodumene beneficiation [79], [81], [92–95]. The use of sulphuric acid represented by Figure 1.23 is renowned and currently, the commercialized process for lithium extraction while the others are still undergoing research. It requires baking the decrepitated mineral with sulphuric acid at about 250 °C for close to an hour (by conventional heating) or 20 s (by microwave heating) [81]. It is essential that this process is operated below 337 °C to prevent the decomposition of the acid [81]. The exchange reaction which forms leachable Li_2SO_4 is modelled by Equation (1.5). After leaching (Equation (1.6)), lime precipitation and pH adjustment is performed at 90 °C to remove impurities from the pregnant solution. Lithium is recovered in the carbonate form by the addition of sodium carbonate (Equation (1.7)).

$$2\beta\text{-}LiAlSi_2O_{6(s)} + H_2SO_{4(l)} \rightarrow Li_2SO_{4(s)} + 4SiO_{2(s)} + Al_2O_{3(s)} + H_2O_{(g)} \quad (1.5)$$

$$Li_2SO_{4(s)} \xrightarrow{H_2O} Li_2SO_{4(aq)} \quad (1.6)$$

$$Li_2SO_{4(aq)} + Na_2CO_{3(aq)} \rightarrow Li_2CO_{3(s)} + Na_2SO_{4(aq)} \quad (1.7)$$

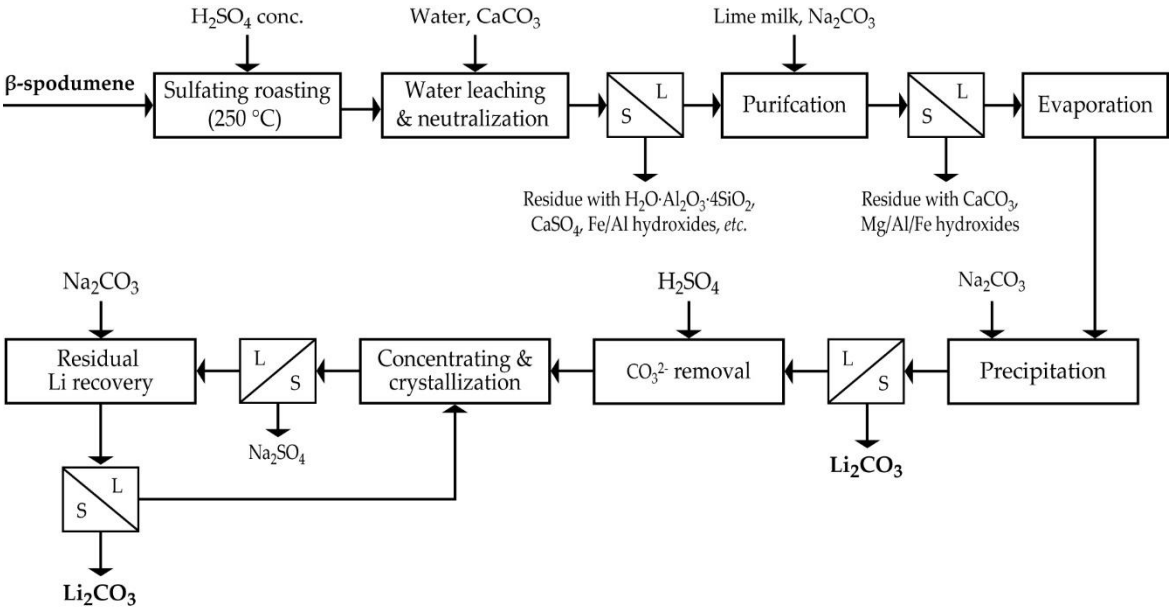

Figure 1.23: Flow diagram for the conventional processing of spodumene by sulphuric acid baking. Adapted from [26, 93, 95].

It must be noted that the diffusion of the acid through the mineral for the ion exchange is the rate determining step for the process. Unlike gaseous reagents, the viscous nature of the liquids (acid and lithium bisulphate produced around 170 °C) slows the penetration through tiny pores and cracks and consequently, slowing down the reaction [96]. In addition

to the challenges associated with the general sulphation process, the use of sulphuric acid roasting is challenged with energy recovery and temperature control. The Na_2SO_4 formed from the process also has little economic value.

Alkaline Process

This process benefits from the low cost and the nonaggressive nature of the salt used as a reagent compared to the acid process which requires the use of concentrated acid [97]. It involves roasting the mineral with lime or limestone around 100–205 ℃ or 825–1050 ℃ respectively. Roasting with limestone (Equation (1.8)) forms Li_2O which can be leached to produce aqueous LiOH solution [23, 98], and separated from solids by filtration. Instead of direct baking of spodumene with limestone, the reagent can initially be decomposed thermally to produce CaO. The quicklime produced is then mixed with water to produce lime milk and roasted with spodumene to produce LiOH as in Equation (1.9) and (1.10) respectively and patented by Nicholson [98].

$$Li_2O\cdot Al_2O_3\cdot 4SiO_{2(s)} + CaCO_{3(s)} \rightarrow Li_2O_{(s)} + CaO\cdot Al_2O_3\cdot 4SiO_{2(s)} + CO_{2(g)} \quad (1.8)$$

$$CaCO_{3(s)} \rightarrow CaO_{(s)} + CO_{2(g)} \quad (1.9)$$

$$LiAlSi_2O_{6(s)} + CaO_{(s)} + H_2O_{(l)} \rightarrow LiOH_{(aq)} + CaAl_2Si_2O_{8(s)} \quad (1.10)$$

Lithium hydroxide synthesised can be converted to LiCl or Li_2CO_3 if desired by treating with hydrochloric acid or carbon dioxide, respectively. This approach has been used by Jandova et al. [99] to recover 90% lithium from zinnwaldite waste. Some additives such as gypsum and sodium sulphate have been employed to enhance lithium recovery, yielding 96%, 96% and 90%, respectively [97, 100, 101]. The downside of this approach is the high energy requirement for the decomposition of limestone and dicalcium silicate. This may result in the evolution of unbearable heat in the system [60].

NaOH has been effectively used as a means of breaking the Si-O bonds in silica like observed in alkali-silica reactions in concrete [102]. With this background, some researchers have used the chemical as a means of destroying the silicate framework of lithium minerals to recover lithium. Xing et al. [73] recorded high extraction efficiency of about 96% from α-spodumene and NaOH in an autoclave with the recovery of hydroxysodalite as a by-product as modelled by Equation (1.11) [26, 73].

$$6\alpha\text{-}LiAlSi_2O_6 + 14NaOH \rightarrow 2Na_4Al_3Si_3O_{12}(OH) + 3Li_2SiO_3 + 3Na_2SiO_3 + 6H_2O \quad (1.11)$$

Song et al. [70] also by hydrometallurgical treatment of the mineral using NaOH and CaO under pressure reported 93% leaching efficiency. They indicated NaOH concentration, temperature, and mass ratio of CaO to ore as major contributing factors to the efficiency of lithium extraction which is governed by equation (1.12) as:

$$LiAlSi_2O_6 + 2CaO + 3NaOH + 2HO_2 \rightarrow NaCaHSiO_4 + LiOH + NaAl(OH)_4 \quad (1.12)$$

The suggested flow diagram for their process with optimal condition which led to the recovery of lithium phosphate after sodium phosphate precipitation is indicated in Figure 1.24. Though the use of NaOH yields promising results with the advantage of eliminating pre-treatment of the stage, it requires high concentration of NaOH and special equipment (autoclave) in addition to long processing time.

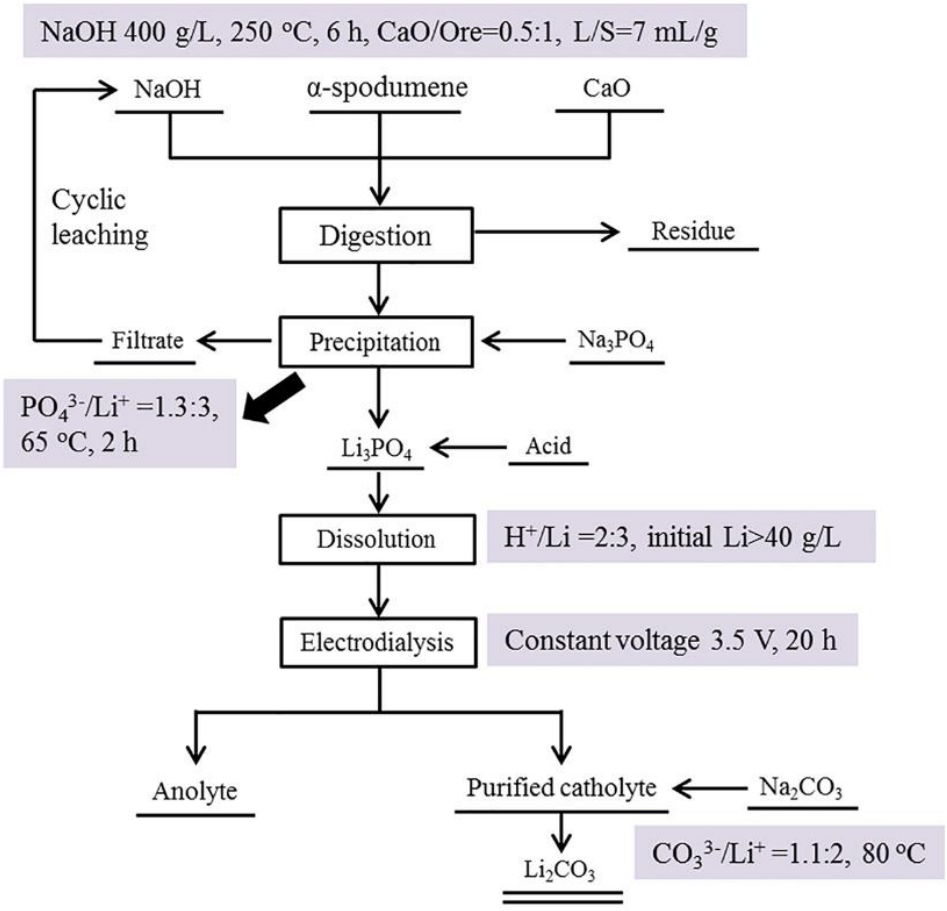

Figure 1.24: Alkaline processing route for spodumene by autoclave roasting using NaOH [70].

Lithium Australia has used the weakening ability of NaOH on silicate bond to develop the LieNA® process. Here, fine spodumene particles are digested and converted into intermediary lithium sodalite. Lithium in this phase is separated from the liquid portion and the weakly bound lithium in the solid is leached with a weak acid to recover lithium as a phosphate (Figure 1.25).

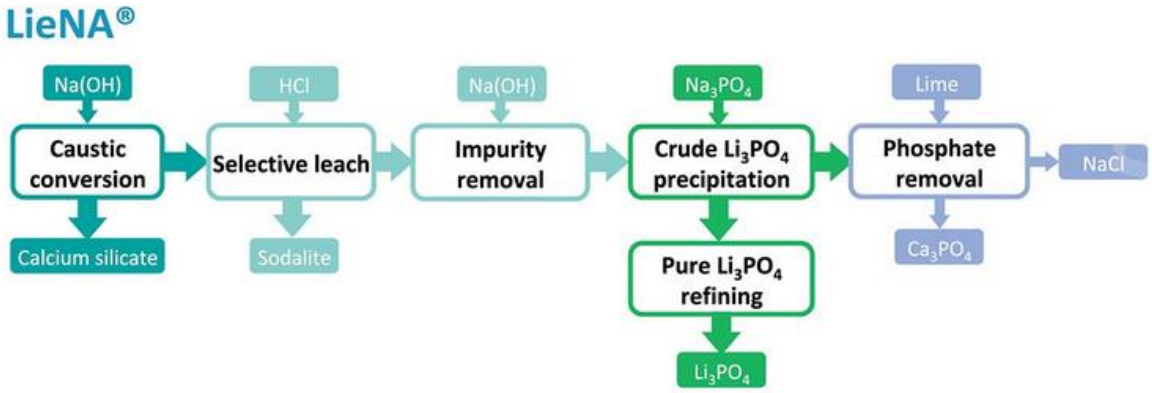

Figure 1.25: Flow diagram of LieNA® process to recover lithium phosphate [103]**.**

Chlorination Process

Chlorination is not very popular in mineral beneficiation partly due to the toxicity of chlorine gas that may be generated alongside the products and the need for high-cost corrosion resistant equipment for the process. Despite its downside, it has some advantages (discussed in Chapter 4) which can be harnessed for processing lithium minerals with some literature information already reported. Chlorination of lepidolite using sodium and calcium chloride at 880 °C yielded 93% lithium recovery [104]. In a recent study by Zhang et al. [105], calcium chloride-sodium chloride mixture to recover lithium alongside rubidium, caesium, and potassium from lepidolite reported excellent results; achieving close to 93% each for lithium and potassium; and 98% each for rubidium and caesium.

Peterson et al. [72] patented a blend of muriate of potash and sylvinite ore (sodium and potassium chloride) to recover lithium from its ores at 980–1100 ℃. The ion exchange reaction led to the formation of LiCl and a subsequent conversion to lithium carbonate by reaction with sodium carbonate. About 97.5% of lithium carbonate was recovered by this approach. Afterwards, Gabra et al. [106] in 1975 documented the possible extraction and recovery of the metal from calcined spodumene with sodium chloride in the presence of lime milk in an autoclave. The flow chart for their process shown in Figure 1.26 led to production of high purity lithium chloride. The latest study on chlorination study on spodumene was by Barbosa et al. [107], [108] where chlorine gas and calcium chloride,

respectively were used to pyrometallurgically recover the metal. 900 °C and 120 min were suggested as the optimal chlorination conditions, which resulted in 90% lithium extraction when calcium chloride was used.

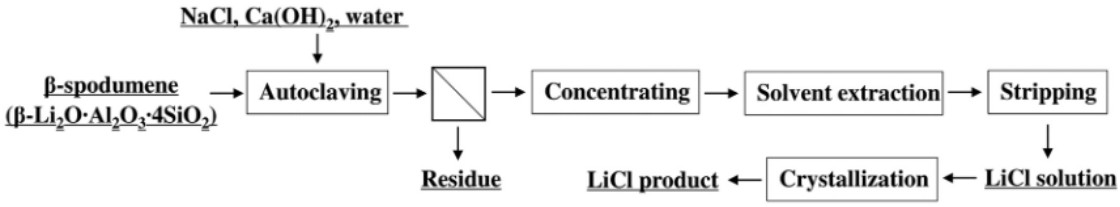

Figure 1.26: Flow diagram for chlorination roasting of spodumene using NaCl [26], [106].

Carbonizing Process

Another less known method for beneficiating lithium ores worthy of discussion is the carbonizing. Lithium carbonate can be produced by carbonizing lithium bearing ore with sodium carbonate between 525 and 675 °C in a solid–solid intimate reaction followed either directly by leaching or hydrothermal decomposition treatment (between 90 and 225 °C) prior to leaching [109]. It is advised that, the process must be carried out above the minimum temperatures suitable for the individual lithium bearing mineral (1080, 850, 980 and 870 °C respectively for petalite, lepidolite, eucryptite and spodumene). They indicated the need to carry out the process in the presence of alkali metal chlorides, alkali metal sulphate or carbon dioxide which act as a catalyst. However, a specific preference for sodium and potassium chloride or sulphate was indicated. By this process, 75–97% of lithium contained in the ore could be leached for recovery.

Some advantages which include the possibility of using Na_2CO_3 as the only reactant to produce Li_2CO_3 of high purity was highlighted [109]. They indicated that the reagent is normally employed in other process to decompose refractory ores into fragments to enhance leaching. In such route, serious purification steps are required since the decomposition may give rise to several impurities. Using it solely in the plant to produce Li_2CO_3 with good recovery and high purity without major purification is therefore a breakthrough. The approach is also said to have a short processing time with improved economics. This is because, the reagent is added to the cooling calcined spodumene midway for it to react, hence, reducing the processing time and utilizing the energy which would otherwise have gone wasted. The Outotec Lithium Hydroxide Process® used this technique as modelled in equation 1.13 to produce lithium carbonate from spodumene followed by hydrothermal

thermal leaching to produce lithium products (Equation 1.14 and 1.15). This led to the production of battery grade LiOH from the mineral after polishing the pregnant leach liquor by ion exchange. The flow diagram for this piloted process is shown in Figure 1.27.

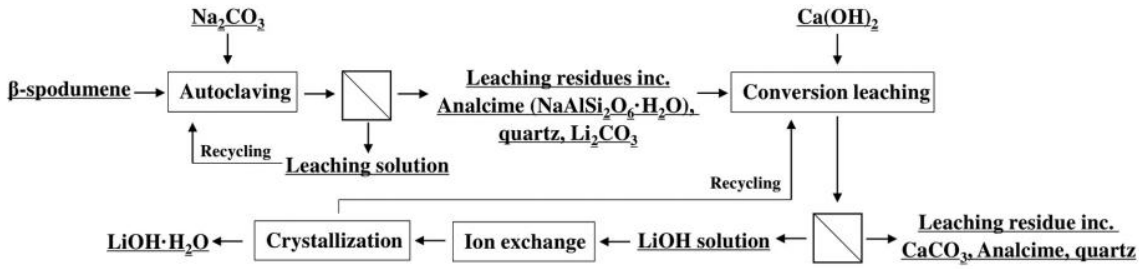

Figure 1.27: Flow diagram for Outotec Lithium Hydroxide Process® [26, 110].

$$2LiAlSi_2O_{6(s)} + Na_2CO_{3(s)} + 4H_2O_{(l)} \rightarrow Li_2CO_{3(s)} + Na_2O.Al_2O_3.4SiO_2.H_2O_{(s)} \quad (1.13)$$

$$Li_2CO_{3(s)} + Ca(OH)_{2(s)} \rightarrow 2LiOH_{(aq)} + CaCO_{(s)} \quad (1.14)$$

$$Li_2CO_{3(s)} + CO_{2(g)} + H_2O_{(l)} \rightarrow 2LiHCO_{3(s)} \quad (1.15)$$

Several investigations which revolve around this invention have been developed for optimization [111, 112]. Chen et al. [111] employed pressurized roasting of spodumene concentrate with sodium carbonate in an autoclave, yielding 94% lithium carbonate with 99.6% purity. Research by dos Santos et al. [112] using spodumene and sodium carbonate, promoted by sodium chloride, resulted in 70% lithium yield. The involvement of NaCl by [112] was to aid the extraction of the residual lithium bound at the interstitial positions of the ore. The reaction was conducted within 550–650 °C for 120 min.

Fluorination Process

The only fluorination roasting report in literature where fluorine salt was used to recover lithium from spodumene is performed by Rosales et al. [113]. In the NaF approach, β-spodumene was roasted with the salt at 600 °C, spodumene/NaF mixture from 1:1 to 1:2.5 for a maximum of 4 hours. 90% lithium recovery was achieved which occurred at spodumene/NaF of 1:2 for 2 h of roasting. Equation (1.16) illustrates the reaction process:

$$2LiAlSi_2O_{6(s)} + 2NaF_{(s)} \rightarrow 2LiF_{(s)} + NaAlSi_3O_{8(s)} + NaAlSiO_{4(s)} \quad (1.16)$$

The other investigations were done with HF or HF/H_2SO_4 mixture as fluorination agents [71, 114]. The study using HF/H_2SO_4 mixture conducted by Guo et al. [71] and described by Equation 1.17 was geared towards extracting the metal from the α-phase of the mineral.

$$2\alpha\text{-}LiAlSi_2O_{6(s)} + 24HF_{(aq)} + 4H_2SO_4 \rightarrow Li_2SO_{4(aq)} + Al_2(SO_4)_{3(aq)} + 4H_2SiF_{6(aq)} + 12H_2O \quad (1.17)$$

They revealed that, the HF was the actual lixiviant rather than the mixture of the two acids. The H_2SO_4 only helped to stabilize the leached metals in the pregnant solution due to the high stability of Li_2SO_4 in aqueous systems. At optimal conditions, they recovered 96% lithium from the mineral. Rosales et al. [114] studied a temperature dependant extraction of lithium from the calcined mineral (β-spodumene) using HF and achieved 90% extraction of the lithium content during leaching at 75 °C for 20 min and a pulp density of 1.82% as optimal conditions. Due to the low solubility of LiF, the low pulp density was important to enable good recovery.

An alternative way of the fluorination approach which prevents the evolution or the direct use of harmful HF is it's in situ production using fluorspar, CaF_2 (a mineral which contains more than 97% fluorine) in the presence of H_2SO_4 [115]. This approach was used in SiLeach® to extract lithium from micaceous minerals and spodumene by Lithium Australia NL (ASX:LIT) in collaboration with ANSTO Minerals [59]. The flow diagram for the process is shown in Figure 1.28 which comprises six steps: Leaching, pre-neutralization, impurity removal, softening, evaporation and primary lithium carbonate (primary LC) precipitation. Lean to high grade spodumene and micaceous concentrates (0.8 to 3.0 wt% Li) have been studied to recover 90 to 95% lithium during 16-24 hours leaching at as low as 100°C. The reagent consumption was found to be dependent on the mineralogy and the mineral type. Pre-neutralization of residual acid and precipitation of co-leached potassium, rubidium, and caesium as alunite [$KAl_3(SO_4)_2(OH)_6$], aluminium (as AlF_3) and calcium (as $CaSO_4 \cdot xH_2O$) was conducted with lime after the leaching. Residual calcium is removed at the softening stage using the conventional procedure rather than ion exchange from which the resulting solution is evaporated to recover lithium as the carbonate by crystallization (Figure 1.28).

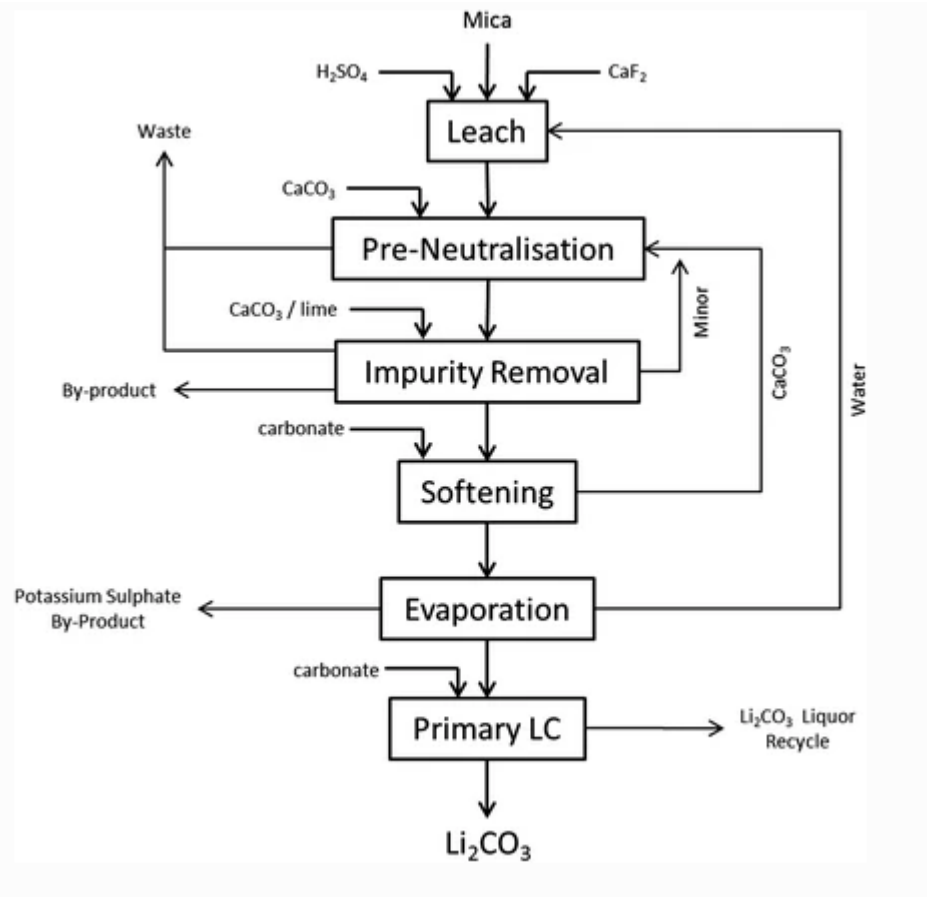

Figure 1.28: Flow diagram for SiLeach® process [59]**.**

Some processing routes for the mineral discussed with some relevant information are summarized in Table 1.6 below:

Table 1.6: Summary of literature for the recovery of lithium from spodumene using the major beneficiation processes.

Process	Experimental Conditions						Product	Recovery/%	Reference
	Roasting			Leaching					
	Reagent	Temp./℃	Time/min.	Time/hr	Temp./ ℃	Lixiviant			
Sulfating	Conc.·H_2SO_4	200–300	30–60	-	-	H_2O	Li_2SO_4	85	[116]
	Na_2SO_4 + CaO	-	-	3	230	Na_2SO_4 + CaO	Li_2SO_4	93	[95]
	Na_2SO_4 + NaOH	200–300	-	3	230	Na_2SO_4 + NaOH	Li_2SO_4	91	[95]
	$(NH_4)_2SO_4$	150–370	-	-	-	NH_3 (aq)	Li_2SO_4	-	[79]
	$CaSO_4$ + $CaCO_3$	1000–1150	120-180	-	-	H_2O	Li_2SO_4	85-90	[117]*
	Conc. H_2SO_4	250–300	-	1	-	H_2O	Li_2SO_4	86	[94]
	H_2O+O_2 + SO_3	350–425	10-40	-	-	H_2O	Li_2SO_4	97	[96]
Alkaline	CaO + H_2O	100–205	60			H_2O	LiOH	~97	[98]
	CaO + H_2O	1000–1230			100	H_2O	LiOH	80	[98]*
Chlorination	KCl, NaCl	1000–1050	15-60	-	85	H_2O/HCl	LiCl	85–98	[72]
	Cl_2	1100	150	-	-	-	LiCl	-	[107]
	$CaCl_2$	900	120	-	60	H_2O	LiCl	90	[108]
	$CaCl_2$	800–1200	-	-	-	Alcohol	LiCl	9.5–99	[118]
Carbonizing	Na_2CO_3	525–675	10–120	-	-	H_2O, NH_4^+ (aq)	Li_2CO_3	75–97	[109]
	Na_2CO_3	150–250	10–120	--	-	H_2O	Li_2CO_3	~94	[111]
	Na_2CO_3 + NaCl	~923	120	-	-	H_2O	Li_2CO_3	70	[112]
Fluorination	NaF	600	120	0.5	25	HF	LiF	90	[113]

* roasting of spodumene done in the alpha phase.

1.4 Chemical Thermodynamic Modelling of Roasting Processes for Lithium Extraction from Spodumene using HSC Chemistry Software

Thermodynamic modelling of processes for extracting lithium from spodumene is scarce in literature. This section, therefore, aims to use HSC Chemistry® 5.1 to model and explain the results and findings encountered by some processes used to extract the metal from spodumene. The gaps in the processing routes are identified for consideration and future studies. The software is a thermochemical tool which can be used to model metallurgical process feasibility and/or predict possible equilibrium composition or products prior to experimental investigation. The process feasibility is predicted by using the reaction equation module of the software and data stored in it to calculate the Gibbs free energy changes of the reaction(s) governing the process within the temperature range under investigation. The equilibrium composition is also predicted using the equilibrium module of the software. The phase composition was selected by inputting the elements of the raw materials and deleting all unstable phases that the software suggests. All suspected or stable products which may be absent from the composition was manually added to avoid errors in calculation. The initial amount of the raw materials and the temperature range under study were then inputted. At a fixed pressure and using the free energy minimisation approach, the Gibbs solver computes the equilibrium composition of the process as equilibrium amount (in kilomoles) versus temperature.

It must be mentioned that, as the software can give important and reliable information on processes, it has some shortfalls which must be considered by the operator. First, a closed system is assumed by the software; thus, it considers that no specy (reactant or product) is lost in the process and if gases are generated, they remain and interact with the system. This does not always happen in real life. In a situation of an open system, an appreciable amount of nitrogen gas (an inert gas) can be added to account for the anomaly. Also, the software depends on data stored in it. The correctness of calculations therefore depends on the accuracy of the database. Lastly, it does not take the kinetics of processes into account.

1.4.1 Process feasibility using the reaction equation module

The study was limited to selected salts and some gases encountered in literature which have been used for sulphation (K_2SO_4, Na_2SO_4, H_2SO_4, SO_3), alkaline (CaO), chlorination ($CaCl_2$, Cl_2) and fluorination (NaF) processing of spodumene. The various equations are indicated from Equations (1.18) to (1.30). Their standard Gibbs free energy changes obtained from the software were plotted as a function of temperature for each process and

the results shown in Figure 1.29. Calculation of the Gibbs free energy changes for the processes were done with reference to one mole of the reagents rather than the spodumene (Eq. (1.18)-(1.30)). It was however, observed that, performing these calculations with reference to one mole of the spodumene instead of the reagent did not affect the sign of the Gibbs free energy changes (feasibilities prediction) except the magnitude. Hence, the process feasibilities as a function of temperature which is of much interest in this study is unaffected in either case.

$$2\beta\text{-}LiAlSi_2O_{6(s)} + K_2SO_{4(s)} \rightarrow Li_2SO_{4(s)} + 2KAlSi_2O_{6(s)} \quad (1.18)$$

$$2\beta\text{-}LiAlSi_2O_{6(s)} + Na_2SO_{4(s)} \rightarrow Li_2SO_{4(s)} + 2NaAlSi_2O_{6(s)} \quad (1.19)$$

$$2\beta\text{-}LiAlSi_2O_{6(s)} + H_2SO_{4(aq)} \rightarrow Li_2SO_{4(s)} + 4SiO_{2(s)} + Al_2O_{3(s)} + H_2O_{(g)} \quad (1.20)$$

$$2\beta\text{-}LiAlSi_2O_{6(s)} + SO_{3(g)} + 3H_2O_{(g)} \rightarrow Li_2SO_{4(s)} + 4SiO_{2(s)} + 2Al(OH)_{3(s)} \quad (1.21)$$

$$6\beta\text{-}LiAlSi_2O_{6(s)} + Fe_2(SO_4)_{3(s)} \rightarrow 3Li_2SO_{4(s)} + 3Al_2O_{3(s)} + Fe_2O_{3(s)} + 12SiO_{2(s)} \quad (1.22)$$

$$6\beta\text{-}LiAlSi_2O_{6(s)} + Al_2(SO_4)_{3(s)} \rightarrow 3Li_2SO_{4(s)} + 4Al_2O_{3(s)} + 12SiO_{2(s)} \quad (1.23)$$

$$0.5\beta\text{-}LiAlSi2O_{6(s)} + CaO_{(s)} \rightarrow 0.5LiAlO_{2(s)} + CaSiO_{3(s)} \quad (1.24)$$

$$2\beta\text{-}LiAlSi_2O_{6(s)} + CaCl_{2(s)} \rightarrow 2LiCl(s) + 2SiO_{2(s)} + CaAl_2Si_2O_{8(s)} \quad (1.25)$$

$$2\beta\text{-}LiAlSi_2O_{6(s)} + Cl_{2(g)} \rightarrow 2LiCl_{(s)} + 4SiO_{2(s)} + Al_2O_{3(s)} + 0.5O_{2(g)} \quad (1.26)$$

$$2\beta\text{-}LiAlSi_2O_{6(s)} + Na_2CO_{3(s)} \rightarrow Li_2O_{(s)} + 2NaAlSi_2O_{6(s)} + CO_{2(g)} \quad (1.27)$$

$$2\beta\text{-}LiAlSi_2O_{6(s)} + Na_2CO_{3(s)} \rightarrow Li_2CO_{3(s)} + 2NaAlSi_2O_{6(s)} \quad (1.28)$$

$$\beta\text{-}LiAlSi_2O_{6(s)} + NaF_{(s)} \rightarrow LiF_{(s)} + 0.5NaAlSi_3O_{8(s)} + 0.5NaAlSiO_{4(s)} \quad (1.29)$$

$$\beta\text{-}LiAlSi_2O_{6(s)} + KCl_{(s)} \rightarrow LiCl_{(s)} + 2SiO_{2(s)} + KAlO_{2(s)} \quad (1.30)$$

Explanation of the process feasibility using Figure 1.29 and the various reagents (or processes) encountered in literature is detailed in the first journal paper from this study (Literature Review and Thermodynamic Modelling of Roasting Processes for Lithium Extraction from Spodumene) found in the Appendix of the manuscript. Comparing and contrasting previous thermodynamic study of chlorination by Barbosa et al. [107, 108] with our study revealed parallel feasibility results when $CaCl_2$ used. However, our findings were contrary to theirs when Cl_2 was used. They indicated feasibility even at higher temperatures whilst our study revealed spontaneity only at lower temperatures. The reason for this difference is not yet apparent.

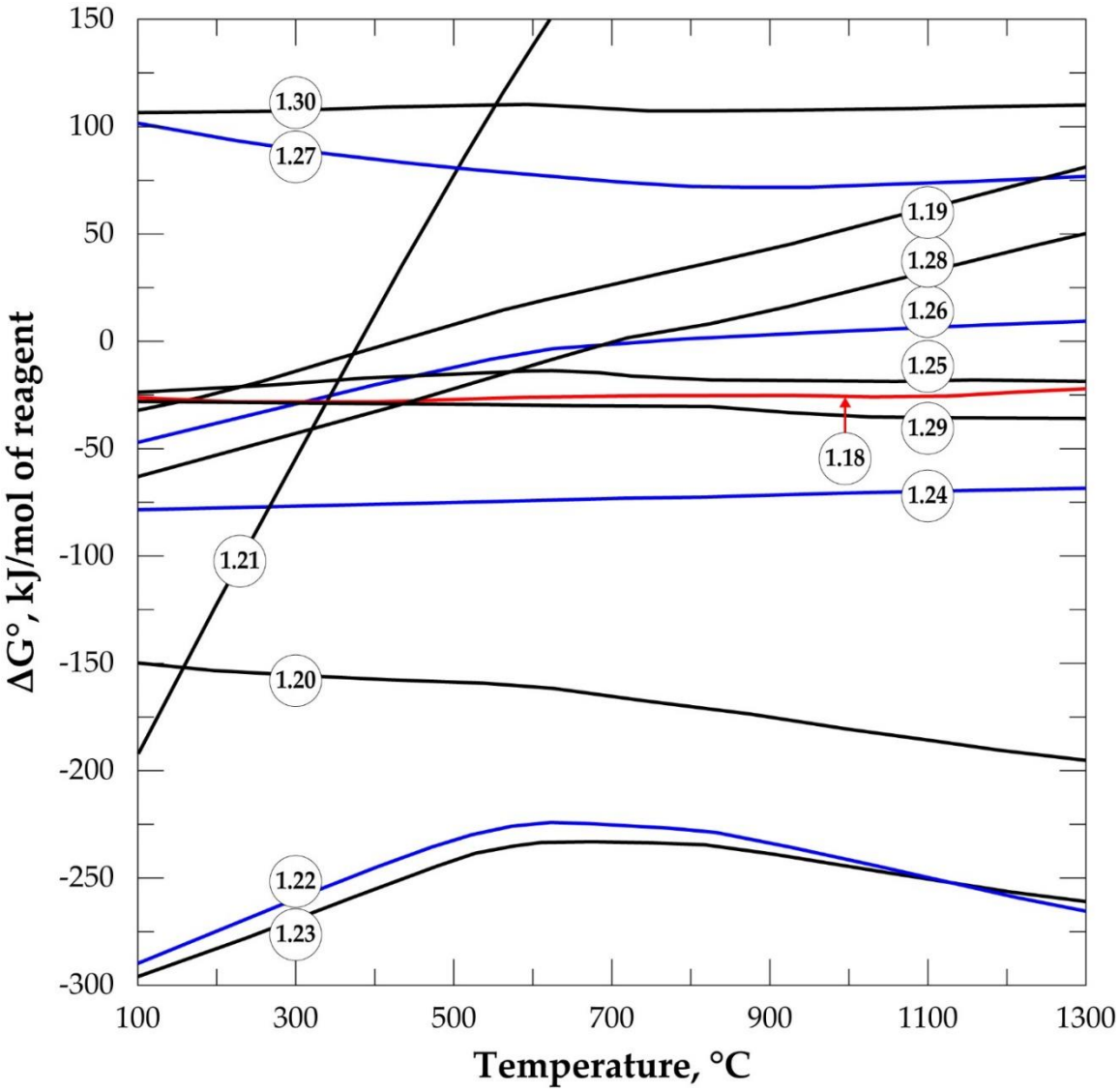

Figure 1.29: The standard Gibbs free energies versus temperature for roasting processes of spodumene encountered in literature (reactions (1.18)–(1.30)) (data from the HSC Chemistry® 5.1).

1.4.2 Equilibrium composition of phases

To gain a deeper understanding of the approaches outlined, the equilibrium module of the software was used to investigate the equilibrium composition of phases evolving in each process as a function of temperature. Figure 1.30 displays the modelling for the sulphating process using Na_2SO_4, K_2SO_4, H_2SO_4, $SO_3(g)/H_2O(g)$, $Fe_2(SO_4)_3$ and $Al_2(SO_4)_3$ as reagents. It can be seen from Figure 1.29 that, using Na_2SO_4 (Eq (1.19)) is feasible only below 400 °C. It is only below this temperature that the equilibrium moles of the products (lithium sulphate and sodium aluminosilicate, $NaAlSiO_6$) are higher than spodumene in Figure 1.30a, confirming feasibility. It can be inferred that the highest amount of lithium sulphate can be obtained below 200 °C above which it starts decreasing until 400 °C, where the reaction

ceases feasibility. Around 400 °C and above, solid lithium sulphate begins to change into a liquid state due to the increasing temperature, but the amount is relatively small in the system, resulting from the decreased feasibility of the reaction. Temperatures less than 400°C appear to be the best for Na_2SO_4/spodumene roasting, however, 1000 °C was required to achieve 90.4% lithium extraction according to Luong et al. [86] for Na_2SO_4/lepidolite roasting for 30 min. Unlike Na_2SO_4, K_2SO_4 drives the reaction to the right within the whole temperature range considered, forming lithium sulphate in the solid phase (Eq (1.18), Figure 1.29); moles of lithium sulphate are higher than spodumene within the entire temperature range considered which also suggests feasibility (Figure 1.30b). There is a steady decrease in moles of solid lithium sulphate and a simultaneous increase of the liquid phase with increasing temperature. This is a result of the continuous conversion of the solid into liquid as it is formed until around the melting point (859 °C); where all the solid phase changes to liquid and remains constant.

Thermodynamics of the sulfuric acid process predicts feasibility throughout the entire temperature range studied with ΔG^o becoming more negative with increasing temperature (Figure 1.29). The highest amount of Li_2SO_4 produced by modelling of this process occurs around 200 °C. When the temperature is close to 300 °C and beyond, there is a steady decrease in quantity. These revelations are in line with observations by Salakjani et al. [81] whose maximum recovery occurred at 250 °C, but a decrease in lithium recovery was observed at 300 °C and beyond. This occurrence is because of the decomposition of sulfuric acid between 300 and 400 °C (Figure 1.30c). However, the process remains spontaneous even after the decomposition of the acid because the products of the decomposition (SO_3 and H_2O) from Equation (1.31) can drive the reaction to the product as seen in Equation (1.21) or (1.32) but with a limited amount of lithium sulphate production. SO_3 breaks down further into SO_2 and O_2 (Equation (1.33)), which remain as spectator species. Precautionary measures are advised at this point due to the toxicity of SO_2. Thus above 400 °C the sulfuric acid process has thermodynamic behaviour similar to the sulphation process using $SO_3(g)/H_2O_{(g)}$ as invented by Maurice et al. [96].

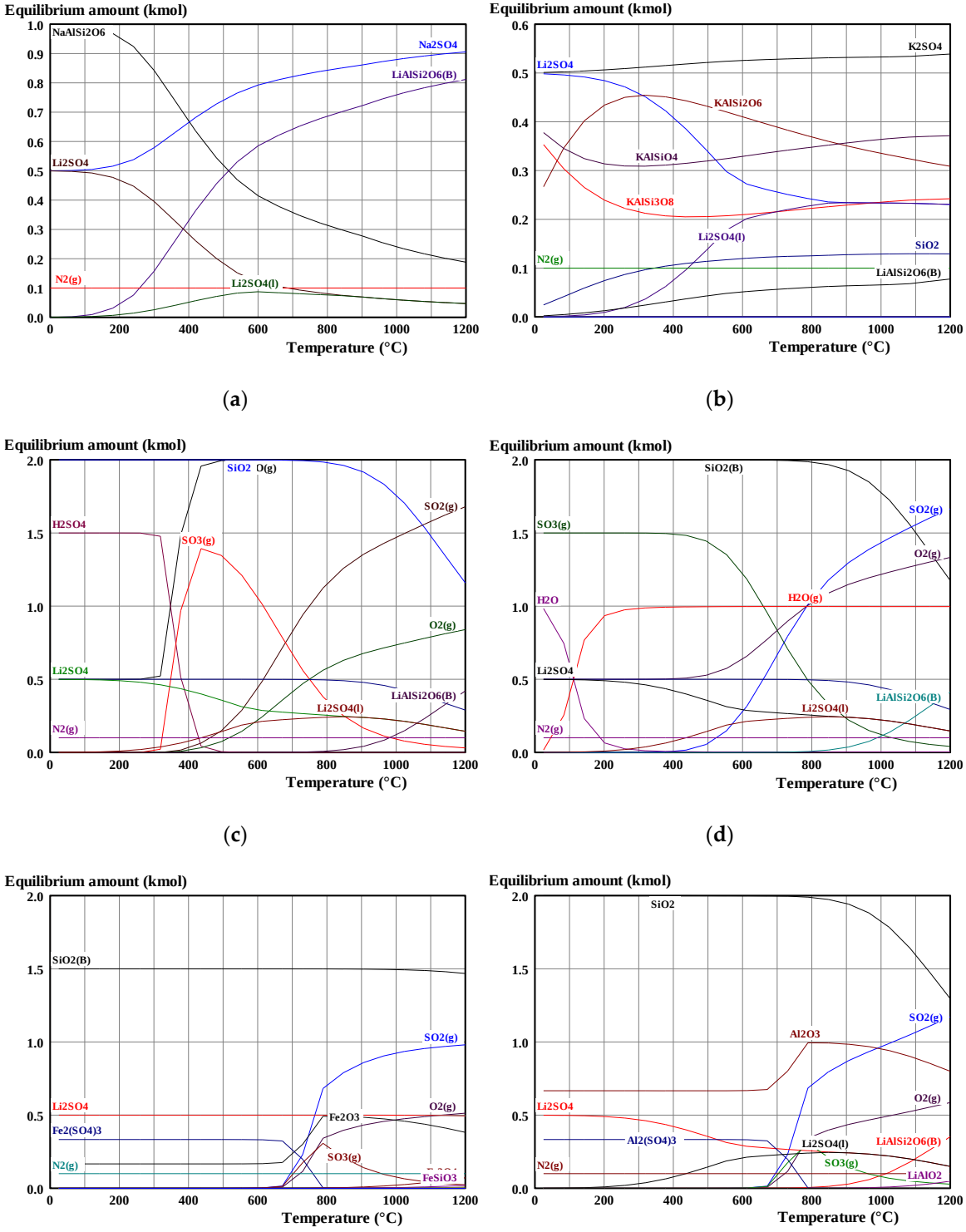

Figure 1.30: Equilibrium amounts versus temperature for sulphate roasting of spodumene using (a) Na_2SO_4, (b) K_2SO_4, (c) H_2SO_4, (d) $SO_{3(g)}$, (e) $Fe_2(SO_4)_3$ and (f) $Al_2(SO4)_3$ (data from HSC Chemistry 5.1 software).

The equilibrium amount of lithium sulphate decreases after the decomposition of the acid, but the kinetics of the process is expected to be favoured. This is because the gaseous

reactants produced can diffuse easily and faster to access reaction sites than sulfuric acid as a result of its viscosity. Around 900 °C and above the sulphation process with sulfuric acid and $SO_3(g)/H_2O(g)$ ceases spontaneity, signified by a sharp increase in the amount of spodumene in Figure 1.30c,d. This observation is attributed to the sintering effect and the formation of lithium silicate, which has close resemblance to β-spodumene [119, 120].

$$H_2SO_{4(aq)} \rightarrow SO_{3(g)} + H_2O_{(g)} \quad (1.31)$$

$$Li_2O{\cdot}Al_2O_3{\cdot}4SiO_{2(s)} + SO_{3(g)} + 4H_2O_{(g)} \rightarrow Li_2SO_{4(s)} + Al_2O_3{\cdot}4SiO_2{\cdot}H_2O_{(s)} \quad (1.32)$$

$$2SO_{3(g)} \rightarrow 2SO_{2(g)} + O_{2(g)} \quad (1.33)$$

Spodumene roasting using $Fe_2(SO_4)_3$ and $Al_2(SO_4)_3$ have similar behaviour (Figure 1.30e,f), except for a constant production of Li_2SO_4 in the case of $Fe_2(SO_4)_3$, but its amount is higher only at temperatures below 500 °C for $Al_2(SO_4)_3$. Metal sulphates also break down, producing SO_3/SO_2 at higher temperatures, which may influence the roasting process. According to Luong et al. [85], Na_2SO_4 like K_2SO_4 has high thermal stability, ergo they break down at higher temperatures, producing a small amount of SO_3/SO_2, which apparently has no effect on the process. This is confirmed by the absence of these gases in their modelled process (Figure 1.30a,b). For iron and aluminium sulphates, the amount of the gases generated during the decomposition is large enough to influence the process. From Figure 1.30e,f, the sulphate of these metals is observed to decompose around 700 °C, producing the gases but their effect is minimal in spodumene as compared to observation in lepidolite according to Luong et al. [85], which may be due to the sintering of spodumene above 800 °C [119, 120].

Calcium oxide was considered the reagent for alkaline roasting of spodumene. $LiAlO_2$ is predicted by HSC Software as a product of the reaction (Equation (1.24)). $Ca(OH)_2$ may be produced from the reaction of Equation (1.34) to reacts with $LiAlO_2$ (Equation (1.35)), producing LiOH in the solid or liquid phase depending on the temperature.

$$CaO_{(s)} + H_2O_{(g)} \rightarrow Ca(OH)_{2(s)} \quad (1.34)$$

$$2LiAlO_{2(s)} + Ca(OH)_{2(s)} \rightarrow 2LiOH_{(s)} + CaAl_2O_{4(s)} \quad (1.35)$$

It can be found from Figure 1.29 that this process is feasible throughout the temperature range considered. This is confirmed by Figure 1.31 where soluble lithium hydroxide is

formed as the useful product. Other products formed include silica, silicates and calcium aluminosilicate with traces of calcium hydroxide. The moles of lithium hydroxide in the solid phase decreases sharply with increasing temperature. This occurrence is attributed to the conversion of the solid into the liquid phase, confirmed by the sharp rise of the liquid phase with increasing temperature until around its melting point (462 °C), where there is a total transformation into the liquid phase (Figure 1.31).

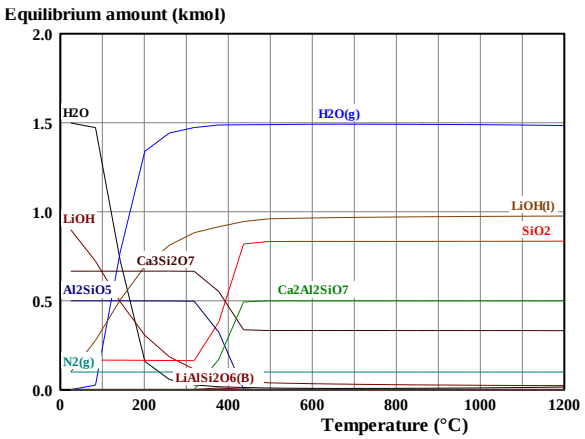

Figure 1.31: Equilibrium amounts versus temperature for alkaline roasting of spodumene using CaO (data from HSC Chemistry 5.1 software).

Figure 1.32 shows the modelling of chlorination roasting using $CaCl_2$, Cl_2 and KCl. These reagents have been used by some researchers to extract lithium from spodumene [72, 107, 108, 118]. From Figure 1.29, the reactions with $CaCl_2$ and Cl_2 are favoured either at a point or entire temperature range considered in this simulation, however, it is not feasible with KCl. This infeasibility is confirmed in Figure 1.32c where an appreciable amount of spodumene is observed in the equilibrium mixture. There is an onset production of solid LiCl which is converted into the liquid phase as soon as it is produced if $CaCl_2$ and Cl_2 are used (Figure 1.32a,b). At ~610 °C (the melting point of lithium chloride) lithium chloride in the medium is predominantly in the liquid phase. A high volatilization temperature is expected due to the high vapor pressure of LiCl. Barbosa et al. [107] observed the gaseous phase at ~1000 °C, however, it was not the case in the chlorination processes that were modelled in this study.

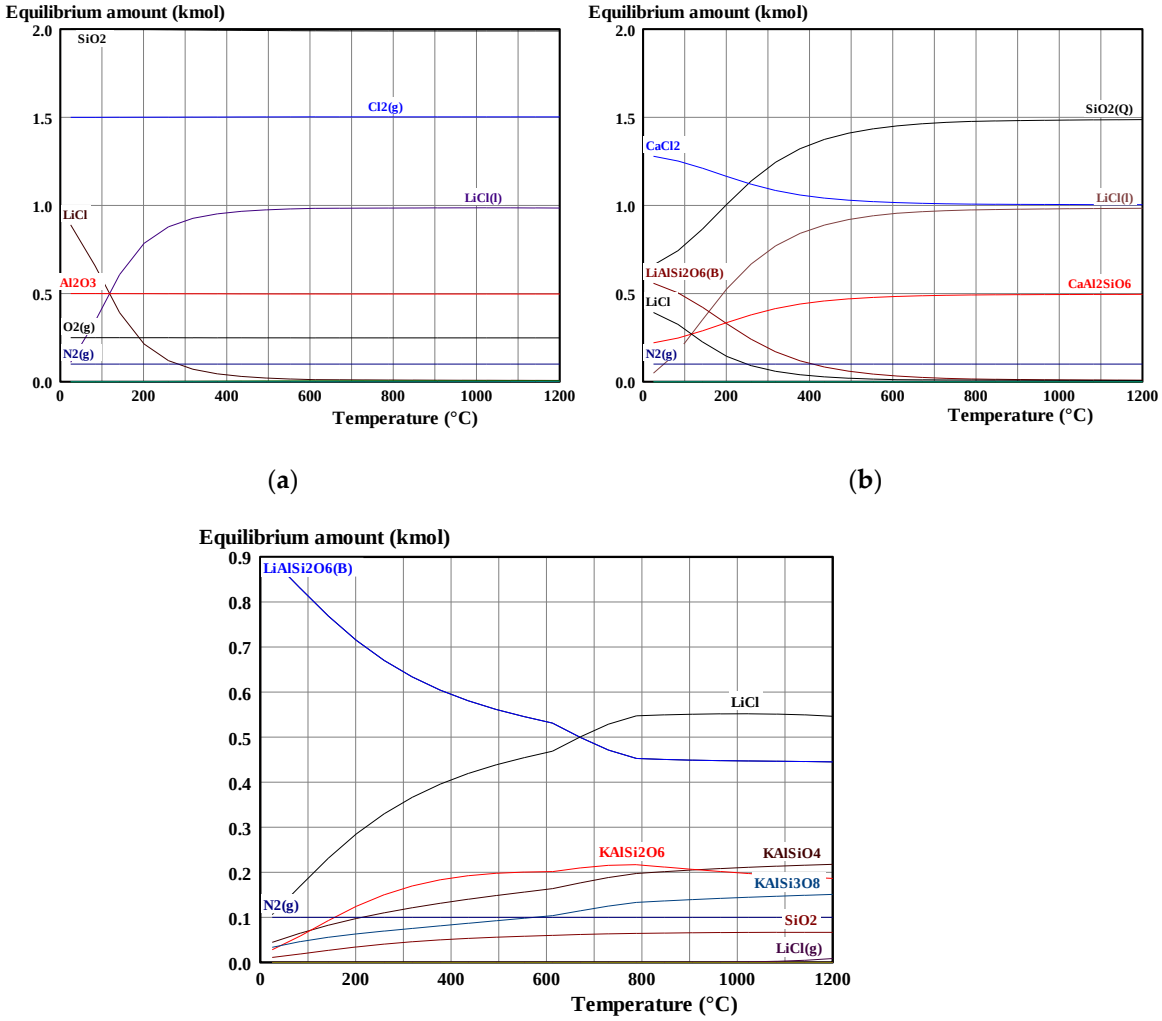

Figure 1.32: Equilibrium amounts versus temperature for chlorination of spodumene using (a) $CaCl_2$, (b) Cl_2 and (c) KCl (data from HSC Chemistry 5.1 software).

Apart from the path followed by KCl in Equation 1.30, another path which forms potassium aluminosilicate ($KAlSi_2O_6$) is also possible according to Equation (1.36):

$$\beta\text{-}LiAlSi_2O_{6(s)} + KCl_{(s)} \rightarrow LiCl_{(s)} + KAlSi_2O_{6\,(s)} \qquad (1.36)$$

However, the latter like the former is not feasible according to the software's predictions. Though some negative Gibbs free energy change is achieved when Equation (1.36) is followed, the values are relatively small and occur at higher temperatures (above 1000 °C) which makes the extraction of lithium by this route practically impossible.

Carbonizing roasting of spodumene using Na_2CO_3 as seen earlier in Equations (1.27) and (1.28) may yield either Li_2O or Li_2CO_3.The Li_2O that is produced can be made to go

into leaching to produce LiOH but the prediction from the HSC software indicates that the reaction is not spontaneous except for the production of Li_2CO_3 (Figure 1.29). The unfeasibility of Equation (1.27) is confirmed in Figure 1.33a, where there is apparently, no leachable lithium product formed. The production of Li_2CO_3 from this process is feasible below 700 ℃ (Figure 1.29) which is confirmed in Figure 1.33b where Li_2CO_3 is observed below this temperature. Around 300 °C, the Li_2CO_3 that was produced decomposes, forming carbon dioxide, silicates, aluminates and aluminosilicates. Thus, though there is feasibility until 700 °C, it is not recommended to operate up to this temperature due to the decomposition which occurs alongside the process. This confirms investigations by [109] that the ideal hydrothermal decomposition temperature for the process as 90–225 °C. It is mentioned that the mixture of products from the decomposition may be converted to sodic zeolite which when tapped increases the recovery and the purity of lithium carbonate synthesised. 94% and 70% lithium recovery were reached by working under high pressure and by adding sodium chloride, respectively, with this process [111, 112].

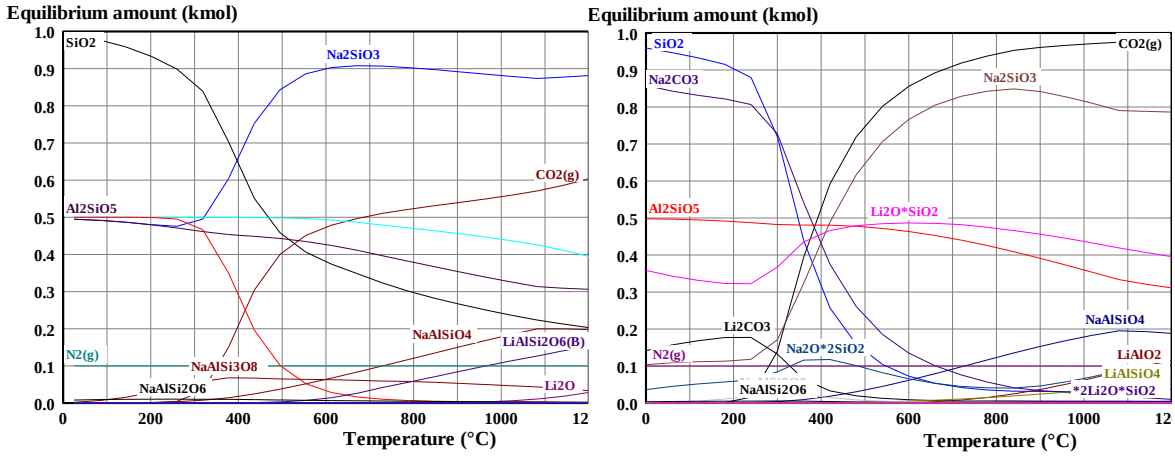

(**a**) (**b**)

Figure 1.33: Equilibrium amounts versus temperature for carbonizing roasting of spodumene according to (a) Equation (1.27) and (b) Equation (1.28) (data from HSC Chemistry 5.1 software).

Fluorination roasting of calcined spodumene using NaF is found favourable throughout the temperatures (Figure 1.29), which is confirmed by the formation of lithium fluoride in the solid or liquid phase (Figure 1.34). Earlier investigation [113] predicted a possible reversal of the process based on HSC Software calculation due to evolution of spodumene phase in their model at increased temperature. The assertion is, however, contrary to our findings. The disparity may be attributed to the absence of liquid lithium fluoride phase in their model. Solid lithium fluoride begins to form but it melts, and its

amount decreases due to the simultaneous formation of the liquid phase with increasing temperature. The liquid phase becomes the stable one at higher temperatures and its absence from their HSC equilibrium calculation leads to some errors in the result. There is a levelling of the liquid phase at around 845 °C (the melting point of LiF) due to the transformation of all the solid phase into liquid. Their maximum LiF extraction achieved by the previous researchers [113] was ~90% which occurred at 600 °C; which is just around the temperature predicted in this study. Gaseous lithium fluoride was not observed within this temperature range, but it is expected to appear around its boiling point (1676 °C) and beyond.

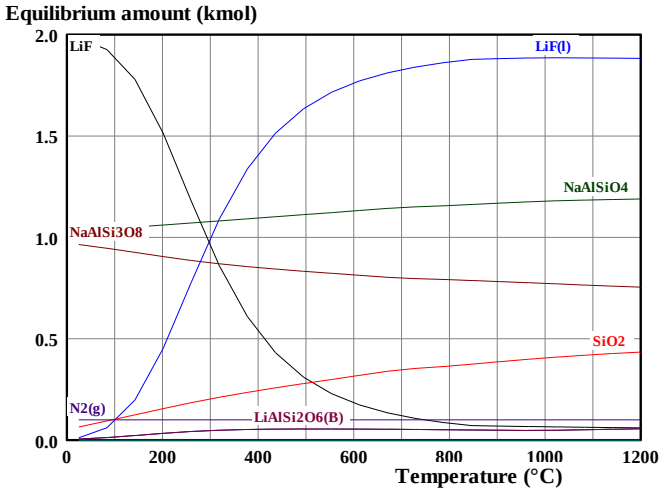

Figure 1.34: Equilibrium amounts versus temperature for fluorination roasting of spodumene using NaF (data from HSC Chemistry 5.1 software).

1.5 Conclusions

Lithium will play a significant role to achieve the net zero carbon emission envisaged by 2050. It stands tall among other critical metals needed for the green technology with its demand and price expected to increase astronomically in the coming years. This calls for concerted effort to intensify the recovery of the metal from minerals through the development of new and efficient metallurgical processes to supplement its undersupply from brine. To achieve this, several processes have been developed to recover lithium from micas (zinnwaldite, lepidolite, etc) and spodumene. Among the lithium-bearing minerals, spodumene is currently, the most attractive and largely explored for lithium though processing it goes with a high cost. A significant portion of the cost is linked to the pre-treatment required during the processing of the metal from spodumene. Modern technologies for processing the mineral are therefore geared towards reducing the energy requirements of this step or eliminating it totally from the process.

Processes for extracting lithium from minerals are normally categorised into sulphation, alkaline, fluorination, chlorination and carbonizing. The HSC Chemistry® 5.1 thermochemical software was used to evaluation and explain the chemical thermodynamics of processes encountered in literature for extracting lithium from spodumene. It was found that, sulphation, alkaline, fluorination, chlorination as well as carbonizing to produce lithium carbonate are processes which have the required thermodynamic driving force to move the reaction to the products. It is therefore not surprising sulphation (using sulfuric acid) and alkaline processes are considered as an industrial approach for lithium extraction. Looking at the mild nature of the reagents in the alkaline processes, it will be a real contender to the acidic process if the high energy requirement in the decomposition of limestone can be decreased by some means. Though roasting with lime is feasible even at lower temperatures, the decomposition of limestone is a precursor for the industrial production of lime which makes the overall process energy intensive. Future work must be focused on reducing the high heat needed for decomposing limestone to make the alkaline process economically viable. In the acid roasting process, SO_3 and H_2O from the acid decomposition may drive the reaction to produce at a faster rate due to the higher diffusion rate of gases compared to liquids. Despite the expected faster rate of reaction of these gases (SO_3 and H_2O), little is known concerning their use for beneficiating lithium bearing minerals. It will be interesting if the behaviour of these species as well as other gases are considered for processing lithium from ores. Sulphation as a method of spodumene beneficiation is mostly limited to sulphuric acid, with little focus on other sulphating reagents, but from the thermodynamics of this group of compounds it will also be interesting to pay attention to other members of this compound. There is considerable literature on the use of some alkali and alkaline earth metal sulphates as well as sulphates of ammonium for processing other lithium bearing minerals than spodumene. Even in those cases, there is minimal explanation of the chemical thermodynamics of the processes. Future work must therefore look at the use of other sulphating reagents for spodumene processing as well as their thermodynamics, both on spodumene and other lithium bearing minerals. Chlorination and fluorination have been found to be promising for lithium extraction. Few chlorination and fluorination agents are encountered in the literature for the process, despite their thermodynamic feasibility. More research should be pursued in search for new fluorination and chlorination agents and the processes should be optimized. The thermodynamics of the carbonizing process yielding lithium carbonate is very interesting, particularly, its low operating temperature and the direct production of a considerably pure product. It is

surprising that it has not attracted much attention. Further research must be pursued to optimize the process. From a thermodynamic point of view, temperatures below 300 °C are predicted for the acid process and the feasible carbonizing process due to the acid and lithium carbonate decomposition. For the other processes discussed, temperatures less than 600 °C are advised, except for fluorination, which works well a little above 600 °C.

REFERENCES

[1] B. Simon, S. Ziemann, and M. Weil, "Potential metal requirement of active materials in lithium-ion battery cells of electric vehicles and its impact on reserves: Focus on Europe," *Resour Conserv Recycl*, vol. 104, pp. 300–310, Nov. 2015, doi: 10.1016/j.resconrec.2015.07.011.

[2] International Energy Agency, "The Role of Critical Minerals in Clean Energy Transitions." Part World Energy Outlook Special Report, May 2021. https://iea.blob.core.windows.net/assets/ffd2a83b-8c30-4e9d-980a-52b6d9a86fdc/TheRoleofCriticalMineralsinCleanEnergyTransitions.pdf (Accessed 25-03-2023).

[3] International Energy Agency, "World Energy Outlook 2022," IEA, 2022 https://iea.blob.core.windows.net/assets/830fe099-5530-48f2-a7c1-11f35d510983/WorldEnergyOutlook2022.pdf (Accessed 25-03-2023)

[4] J. H. Miedema and H. C. Moll, "Lithium availability in the EU27 for battery-driven vehicles: The impact of recycling and substitution on the confrontation between supply and demand until2050," *Resources Policy*, vol. 38, no. 2, pp. 204–211, Jun. 2013, doi: 10.1016/j.resourpol.2013.01.001.

[5] J. Speirs, M. Contestabile, Y. Houari, and R. Gross, "The future of lithium availability for electric vehicle batteries," *Renewable and Sustainable Energy Reviews*, vol. 35. Elsevier Ltd, pp. 183–193, 2014. doi: 10.1016/j.rser.2014.04.018.

[6] Z. Li and K. Binnemans, "Selective removal of magnesium from lithium-rich brine for lithium purification by synergic solvent extraction using β-diketones and Cyanex 923," *AIChE Journal*, vol. 66, no. 7, Jul. 2020, doi: 10.1002/aic.16246.

[7] D. Gielen and W. Bank, Critical Materials For The Energy Transition: Lithium. 2022. https://www.irena.org/-/media/Files/IRENA/Agency/Technical-Papers/IRENA_Critical_Materials_Lithium_2022.pdf

[8] BloombergNEF, “BloombergNEF’s global EV outlook 2021: Commercial vehicles,” *https://www.bloomberg.com/professional/blog/bloombergnefs-global-ev-outlook-2021-commercial-vehicles/*, 2021 (Accessed 25-01-2023).

[9] BloombergNEF, “ Electric Vehicle Outlook 2020,” *https://about.bnef.com/electric-vehicle-outlook-2020/*, 2020 (Accessed 25-01-2023).

[10] P. W. Gruber, P. A. Medina, G. A. Keoleian, S. E. Kesler, M. P. Everson, and T. J. Wallington, “Global lithium availability: A constraint for electric vehicles?,” *J Ind Ecol*, vol. 15, no. 5, pp. 760–775, Oct. 2011, doi: 10.1111/j.1530-9290.2011.00359.x.

[11] A. Yaksic and J. E. Tilton, “Using the cumulative availability curve to assess the threat of mineral depletion: The case of lithium,” *Resources Policy*, vol. 34, no. 4, pp. 185–194, Dec. 2009, doi: 10.1016/j.resourpol.2009.05.002.

[12] U.S. Geological Survey (USGS), “Mineral Commodity Summaries 2022 - Lithium,” https://pubs.usgs.gov/periodicals/mcs2022/mcs2022-lithium.pdf 2022 (Accessed 25-01-2023).

[13] International Energy Agency, *Energy technology perspectives 2010 : scenarios and strategies to 2050*. IEA, 2010, https://iea.blob.core.windows.net/assets/04776631-ea93-4fea-b56d-2db821bdad10/etp2010.pdf , (Accessed 25-01-2023).

[14] J. Speirs, M. Contestabile, Y. Houari, and R. Gross, “The future of lithium availability for electric vehicle batteries,” *Renewable and Sustainable Energy Reviews*, vol. 35. Elsevier Ltd, pp. 183–193, 2014. doi: 10.1016/j.rser.2014.04.018.

[15] W. T. Research Director, “The Trouble with Lithium Implications of Future PHEV Production for Lithium Demand,” 2007.

[16] D. E. Garrett, *Handbook of lithium and natural calcium chloride*. Elsevier, 2004.

[17] M. Abe and R. Chitrakar, “Synthetic Inorganic Ion-Exchange Materials. XLV. Recovery of Lithium from Seawater and Hydrothermal Water by Titanium (IV) Antimonate Cation Exchanger,” 1987.

[18] U.S. Geological Survey (USGS), “Mineral Commodity Summaries 2016 - Lithium,” 2016, https://d9-wret.s3-us-west-2.amazonaws.com/assets/palladium/production/mineral-pubs/lithium/mcs-2016-lithi.pdf, (Accessed 05-02-2023).

[19] U.S. Geological Survey (USGS), “Lithium Statistics and Information,” https://www.usgs.gov/centers/national-minerals-information-center/lithium-statistics-and-information, (Accessed 25-01-2023).

[20] Ian Morse, “Bolivia looks to opaque methods, firms to build lithium powerhouse,” Dec. 12, 2022, *https://news.mongabay.com/2022/12/bolivia-looks-to-opaque-methods-firms-to-build-lithium-powerhouse/* (Accessed 05-01-2023).

[21] Boer Lukas, Pescatori Andrea, Stuermer Martin, and Valckx Nico, “Soaring Metal Prices May Delay Energy Transition,” Nov. 10, 2021 *https://www.imf.org/en/Blogs/Articles/2021/11/10/soaring-metal-prices-may-delay-energy-transition* , (Accessed 05-01-2023).

[22] R. M., Cowsert, "Hectorite as a Critical Element in the Manufacturing of Floor/Wall Tile." In *Qualicer 96. IV World Congress on Ceramic Tile Quality. General Conferences and Communications. Pt. 2. Castellon,* vol. 10, no. 13. 1996.

[23] P. Meshram, B. D. Pandey, and T. R. Mankhand, “Extraction of lithium from primary and secondary sources by pre-treatment, leaching and separation: A comprehensive review,” *Hydrometallurgy*, vol. 150, pp. 192–208, Dec. 2014, doi: 10.1016/j.hydromet.2014.10.012.

[24] H. E., Kluksdahl,. "Extraction of lithium from lithium-containing materials." U.S. Patent 4,588,566, issued May 13, 1986.

[25] C. J. Stanley *et al.*, “Jadarite, $LiNaSiB_3O_7(OH)$, a new mineral species from the Jadar Basin, Serbia,” *European Journal of Mineralogy*, vol. 19, no. 4, pp. 575–580, Sep. 2007, doi: 10.1127/0935-1221/2007/0019-1741.

[26] H. Li, J. Eksteen, and G. Kuang, “Recovery of lithium from mineral resources: State-of-the-art and perspectives – A review,” *Hydrometallurgy*, vol. 189, Nov. 2019, doi: 10.1016/j.hydromet.2019.105129.

[27] H. Vikström, S. Davidsson, and M. Höök, “Lithium availability and future production outlooks,” *Appl Energy*, vol. 110, pp. 252–266, 2013, doi: 10.1016/j.apenergy.2013.04.005.

[28] B. Tadesse, F. Makuei, B. Albijanic, and L. Dyer, “The beneficiation of lithium minerals from hard rock ores: A review,” *Minerals Engineering*, vol. 131. Elsevier Ltd, pp. 170–184, Jan. 15, 2019. doi: 10.1016/j.mineng.2018.11.023.

[29] R. L. Moore, J. P. Mann, A. Montoya, and B. S. Haynes, “In situ synchrotron XRD analysis of the kinetics of spodumene phase transitions,” *Physical Chemistry Chemical Physics*, vol. 20, no. 16, pp. 10753–10761, Apr. 2018, doi: 10.1039/C7CP07754H.

[30] N. K. Salakjani, P. Singh, and A. N. Nikoloski, “Production of Lithium – A Literature Review Part 1: Pretreatment of Spodumene,” *Mineral Processing and Extractive*

Metallurgy Review, vol. 41, no. 5, pp. 335–348, Sep. 2020, doi: 10.1080/08827508.2019.1643343.

[31] C. Yonghua, Duan and Lishi, Ma and Ping, Li and Yong, "First-principles calculations of electronic structures and optical, phononic, and thermodynamic properties of monoclinic α-spodumene," *Ceram Int*, vol. 43, no. 8, pp. 6312--6321, 2017, doi: 10.1016/j.ceramint.2017.02.038.

[32] R. Arlt, T and Angel, "Displacive phase transitions in C-centred clinopyroxenes: spodumene, $LiScSi_2O_6$ and $ZnSiO_3$," *Phys Chem Miner*, vol. 27, no. 10, pp. 719--731, 2000, doi: 10.1007/s002690000116.

[33] R. L. Moore, B. S. Haynes, and A. Montoya, "Effect of the Local Atomic Ordering on the Stability of β-Spodumene," *Inorg Chem*, vol. 55, no. 13, pp. 6426–6434, 2016, doi: 10.1021/acs.inorgchem.6b00344.

[34] D. R. Li, Chi-Tang and Peacor, "The crystal structure of $LiAlSi_2O_6$-II ("β spodumene″)," *Zeitschrift fur Kristallographie-Crystalline Materials*, vol. 126, no. 1–6, pp. 46–65, 1968, doi: 10.1524/zkri.1968.126.16.46.

[35] C. Dessemond, F. Lajoie-Leroux, G. Soucy, N. Laroche, and J. F. Magnan, "Spodumene: The lithium market, resources and processes," *Minerals*, vol. 9, no. 6, Jun. 2019, doi: 10.3390/min9060334.

[36] Hanbook of minerlalogy-Petalite, https://www.handbookofmineralogy.org/pdfs/petalite.pdf (Accessed 09-02-2023).

[37] A. A. Kaminskii *et al.*, "Lithium silicate, $LiAlSi_4O_{10}$ (petalite) - A novel monoclinic SRS-active crystal," *Laser Phys Lett*, vol. 12, no. 8, Aug. 2015, doi: 10.1088/1612-2011/12/8/085002.

[38] E. Haussühl, J. Schreuer, B. Winkler, S. Haussühl, L. Bayarjargal, and V. Milman, "Structure-property relations and thermodynamic properties of monoclinic petalite, $LiAlSi_4O_{10}$," *Journal of Physics Condensed Matter*, vol. 24, no. 34, Aug. 2012, doi: 10.1088/0953-8984/24/34/345402.

[39] D. London, P. Cerny. "Crystal Chemistry and Stability of Petalite," (1983)

[40] A. Stempkowska, "Characteristics of thermal parameters and some physical properties of mineral eutectic type: Petalite–alkali feldspars," *Materials*, vol. 14, no. 23, Dec. 2021, doi: 10.3390/ma14237321.

[41] Hanbook of minerlalogy-Lepidolite, https://www.handbookofmineralogy.org/pdfs/lepidolite.pdf (Accessed 09-02-2023).

[42] M. D. Foster and T. B. Nolan, "Interpretation of the Composition of Lithium Micas."

[43] "Lepidolite," https://www.ufrgs.br/minmicro/Lepidolite.pdf.

[44] L. Sulcek, R. Langner, U. Werner-Zwanziger, J. W. Zwanziger, C. Martineau-Corcos, and M. Fechtelkord, "Solid-state nuclear magnetic resonance investigation of synthetic phlogopite and lepidolite samples," *Magnetic Resonance in Chemistry*, vol. 58, no. 11, pp. 1099–1108, Nov. 2020, doi: 10.1002/mrc.4998.

[45] L. A. Groat, B.C., Chakoumakos, D.H., Brouwer, C.M., Hoffman, C.A., Fyfe, H. Morell, and A.J., Schultz, "The amblygonite ($LiAlPO_4F$)-montebrasite ($LiAlPO_4OH$) solid solution: A combined powder and single-crystal neutron diffraction and solid-state ^6Li MAS, CP MAS, and REDOR NMR study," *American Mineralogist*, vol. 88, no. 1, pp. 195–210, 2003, doi: 10.2138/am-2003-0123.

[46] Hanbook of minerlalogy-Amblygonite, https://www.handbookofmineralogy.org/pdfs/amblygonite.pdf (Accessed 09-02-2023).

[47] P. Černý, and T., S., Ercit. "The classification of granitic pegmatites revisited." *The Canadian Mineralogist* 43, no. 6 (2005): pp 2005-2026. https://pubs.geoscienceworld.org/canmin/article-abstract/43/6/2005/126681/THE-CLASSIFICATION-OF-GRANITIC-PEGMATITES?redirectedFrom=PDF (Accessed 20-01-2023).

[48] Y. Shirose and S. Uehara, "Microtexture investigation of amblygonite-montebrasite series with lacroixite: Characteristics and formation process in pegmatites," *American Mineralogist*, vol. 103, no. 1, pp. 75–84, Jan. 2018, doi: 10.2138/am-2018-6049.

[49] F. C. Hawthorne, "Structure and chemistry of phosphate minerals." *Mineralogical Magazine* 62, no. 2 (1998): pp 141-164.

[50] D. M. C. Huminicki and F. C. Hawthorne, "The Crystal Chemistry of the Phosphate Minerals," *Rev Mineral Geochem*, vol. 48, no. 1, pp. 123–253, Jan. 2002, doi: 10.2138/rmg.2002.48.5.

[51] Hanbook of minerlalogy- Eucryptite https://www.handbookofmineralogy.org/pdfs/eucryptite.pdf (Accessed 09-11-2022).

[52] S. I. Lahti, P. Kallio, and O. von Knorring, "The Composition, Physical Properties and Occurrence Of Eucryptite from the Haapaluoma Pegmatite, Finland." *Bull. Geol. Soc. Finland* 54 (1982): 5-13.

[53] B. E. Douglas, "Stuffed Derivatives of Close-Packed Structures," *Journal of chemical education* 84, no. 11 (2007): pp 1846.

[54] M. J. Buoncon, "The Stuffed Derivatives of the Silica Structures." *American Mineralogist: Journal of Earth and Planetary Materials* 39, no. 7-8 (1954): pp 600-614.

[55] A. Gordeeva, I. Z. Jenei, K. Spektor, O. Y. Vekilova, and U. Haüssermann, "Thermal conversion of the hydrous aluminosilicate $LiAlSiO_3(OH)2$into γ-eucryptite," *Zeitschrift fur Naturforschung - Section B Journal of Chemical Sciences*, vol. 76, no. 10–12, pp. 599–606, Nov. 2021, doi: 10.1515/znb-2021-0095.

[56] "The Fascination of Crystals and Symmetry," *https://crystalsymmetry.wordpress.com/2018/02/01/eucryptite/*, (Accessed 21-06-2022).

[57] Eucryptite – Properties and Occurrences," https://assignmentpoint.com/eucryptite-properties-and-occurrences/ (Accessed 19-10-2022).

[58] D. London, "Experimental phase equilibria in the system $LiAlSiO_4$–SiO_2–H_2O: a petrogenetic grid for lithium-rich pegmatites," *American Mineralogist*, vol. 69, no. 11–12, pp. 995–1004, 1984.

[59] C. S. Griffith, A. C. Griffin, A. Roper, and A. Skalski, "Development of SiLeach® Technology for the extraction of lithium silicate minerals," in *Proceedings of the First Global Conference on Extractive Metallurgy*, 2018, pp. 2235–2245.

[60] G. D. White and T. N. McVay, "Some Aspects of The Recovery of Lithium From Spodumene," Oak Ridge, TN (United States), Apr. 1958. doi: 10.2172/4352576.

[61] C. Sasikumar, D. S. Rao, S. Srikanth, B. Ravikumar, N. K. Mukhopadhyay, and S. P. Mehrotra, "Effect of mechanical activation on the kinetics of sulfuric acid leaching of beach sand ilmenite from Orissa, india," *Hydrometallurgy*, vol. 75, no. 1–4, pp. 189–204, Nov. 2004, doi: 10.1016/j.hydromet.2004.08.001.

[62] N. P. Kotsupalo, L. T. Menzheres, A. D. Ryabtsev, and V. v. Boldyrev, "Mechanical activation of α-spodumene for further processing into lithium compounds," *Theoretical Foundations of Chemical Engineering*, vol. 44, no. 4, pp. 503–507, Aug. 2010, doi: 10.1134/S0040579510040251.

[63] G. D. Rosales, A. C. J. Resentera, R. G. Wuilloud, M. H. Rodriguez, and M. R. Esquivel, "Optimization of combined mechanical activation-leaching parameters of low-grade α-spodumene/NaF mixture using response surface methodology," *Miner Eng*, vol. 184, Jun. 2022, doi: 10.1016/j.mineng.2022.107633.

[64] H. Ebadi and P. Pourghahramani, "Effects of mechanical activation modes on microstructural changes and reactivity of ilmenite concentrate," *Hydrometallurgy*, vol. 188, pp. 38–46, Sep. 2019, doi: 10.1016/j.hydromet.2019.06.001.

[65] N. Setoudeh, A. Nosrati, and N. J. Welham, "Lithium extraction from mechanically activated of petalite-Na_2SO_4 mixtures after isothermal heating," *Miner Eng*, vol. 151, Jun. 2020, doi: 10.1016/j.mineng.2020.106294.

[66] A. Zahiri, A. Ahmadi, A. Foroutan, and M. Ghadiri, “Improvement of zinc bioleaching from a zinc flotation concentrate using mechanical activation,” *Miner Eng*, vol. 163, Mar. 2021, doi: 10.1016/j.mineng.2021.106793.

[67] A. Berger, V. Boldyrev, and L. Menzheres, “Mechanical activation of β-spodumene,” *Materials chemistry and physics* 25, no. 4 (1990): pp 339-350.

[68] N. P. Kotsupalo, L. T. Menzheres, A. D. Ryabtsev, and V. v. Boldyrev, “Mechanical activation of α-spodumene for further processing into lithium compounds,” *Theoretical Foundations of Chemical Engineering*, vol. 44, no. 4, pp. 503–507, Aug. 2010, doi: 10.1134/S0040579510040251.

[69] G. D. Rosales, A. C. J. Resentera, R. G. Wuilloud, M. H. Rodriguez, and M. R. Esquivel, “Optimization of combined mechanical activation-leaching parameters of low-grade α-spodumene/NaF mixture using response surface methodology,” *Miner Eng*, vol. 184, Jun. 2022, doi: 10.1016/j.mineng.2022.107633.

[70] Y. Song, T. Zhao, L. He, Z. Zhao, and X. Liu, “Hydrometallurgy A promising approach for directly extracting lithium from α-spodumene by alkaline digestion and precipitation as phosphate,” *Hydrometallurgy*, vol. 189, no. July, p. 105141, 2019, doi: 10.1016/j.hydromet.2019.105141.

[71] H. Guo, G. Kuang, H. Wang, H. Yu, and X. Zhao, “Investigation of Enhanced Leaching of Lithium from α-Spodumene Using Hydrofluoric and Sulfuric Acid,” *Minerals*, vol. 7, no. 11, p. 205, Oct. 2017, doi: 10.3390/min7110205.

[72] J. A., Peterson, G. H., Glioss, “Lithium Values Recovery Process,” U.S. Patent No. 2,893,828, 7 July 1959.

[73] P. Xing, C., Wang, L., Zeng, B., Ma, L., Wang, Y., Chen, and C., Yang, “Lithium Extraction and Hydroxysodalite Zeolite Synthesis by Hydrothermal Conversion of α-Spodumene,” *ACS Sustain Chem Eng*, vol. 7, no. 10, pp. 9498–9505, May 2019, doi: 10.1021/acssuschemeng.9b00923.

[74] N. K. Salakjani, P. Singh, and A. N. Nikoloski, “Mineralogical transformations of spodumene concentrate from Greenbushes, Western Australia. Part 1: Conventional heating,” *Miner Eng*, vol. 98, pp. 71–79, Nov. 2016, doi: 10.1016/j.mineng.2016.07.018.

[75] O. Peltosaari, P. Tanskanen, E.-P. Heikkinen, and T. Fabritius, “α→γ→β-phase transformation of spodumene with hybrid microwave and conventional furnaces,” *Miner Eng*, vol. 82, pp. 54–60, Oct. 2015, doi: 10.1016/j.mineng.2015.04.012.

[76] A. A. Abdullah, H. C. Oskierski, M. Altarawneh, G. Senanayake, G. Lumpkin, and B. Z. Dlugogorski, “Phase transformation mechanism of spodumene during its calcination,” *Miner Eng*, vol. 140, p. 105883, Aug. 2019, doi: 10.1016/j.mineng.2019.105883.

[77] Foster. Fraas, O. C. Ralston, U. States., and B. of Mines., *Beneficiation of spodumene by decrepitation*, Washington, D.C., U.S. Dept. of the Interior, Bureau of Mines, 1937.

[78] N. K. Salakjani, A. N. Nikoloski, and P. Singh, “Mineralogical transformations of spodumene concentrate from Greenbushes, Western Australia. Part 2: Microwave heating,” *Miner Eng*, vol. 100, pp. 191–199, Jan. 2017, doi: 10.1016/j.mineng.2016.11.004.

[79] T. E. Dwyer, “Recovery of lithium from spodumene ores,” US Patent 2,801,153, 1957 [Online]. Available: https://patents.google.com/patent/US2801153A/en

[80] H. Gasalla and E. Pereira, “Activation-deactivation mechanisms in spodumene samples,” *Solid State Ion*, vol. 42, no. 1–2, pp. 1–6, Sep. 1990, doi: 10.1016/0167-2738(90)90251-L.

[81] N. K. Salakjani, P. Singh, and A. N. Nikoloski, “Acid roasting of spodumene: Microwave vs. conventional heating,” *Miner Eng*, vol. 138, pp. 161–167, Jul. 2019, doi: 10.1016/j.mineng.2019.05.003.

[82] P. K. Choubey, M. Kim, R. R. Srivastava, J. Lee, and J.-Y. Lee, “Advance review on the exploitation of the prominent energy-storage element: Lithium. Part I: From mineral and brine resources,” *Miner Eng*, vol. 89, pp. 119–137, Apr. 2016, doi: 10.1016/j.mineng.2016.01.010.

[83] X. Zhang, X. Tan, C. Li, Y. Yi, W. Liu, and L. Zhang, “Energy-efficient and simultaneous extraction of lithium, rubidium and caesium from lepidolite concentrate via sulfuric acid baking and water leaching,” *Hydrometallurgy*, vol. 185, pp. 244–249, May 2019, doi: 10.1016/j.hydromet.2019.02.011.

[84] Q. Yan, X., Li, Z., Wang, X., Wu, H., Guo, Q., Hu, W., Peng, and J., Wang, “Extraction of valuable metals from lepidolite,” *Hydrometallurgy*, vol. 117–118, pp. 116–118, Apr. 2012, doi: 10.1016/j.hydromet.2012.02.004.

[85] V. T. Luong, D. J. Kang, J. W. An, D. A. Dao, M. J. Kim, and T. Tran, “Iron sulphate roasting for extraction of lithium from lepidolite,” *Hydrometallurgy*, vol. 141, pp. 8–16, Jan. 2014, doi: 10.1016/j.hydromet.2013.09.016.

[86] V. T. Luong, D. J. Kang, J. W. An, M. J. Kim, and T. Tran, “Factors affecting the extraction of lithium from lepidolite,” *Hydrometallurgy*, vol. 134–135, pp. 54–61, Mar. 2013, doi: 10.1016/j.hydromet.2013.01.015.

[87] L. Li, N. Hu, X. Huang, X. Xiong, X. Zeng, and S. Luo, " Method for producing refined lithium sulfate solution used in lepidolite lithium-extracting technique by sulfuric acid process," CN Patent 100503849C, 2006

[88] Johnson Gary Donald, Urbani Mark Daniel, and Vines Nicholas John, "Recover Process," WO Patent 2016/ 054683 A1, 2016

[89] E. Siame and R. D. Pascoe, "Extraction of lithium from micaceous waste from china clay production," *Miner Eng*, vol. 24, no. 14, pp. 1595–1602, Nov. 2011, doi: 10.1016/j.mineng.2011.08.013.

[90] O. Sitando and P. L. Crouse, "Processing of a Zimbabwean petalite to obtain lithium carbonate," *Int J Miner Process*, vol. 102–103, pp. 45–50, Jan. 2012, doi: 10.1016/j.minpro.2011.09.014.

[91] A. M. Amer, "The hydrometallurgical extraction of lithium from egyptian montmorillonite-type clay," *JOM*, vol. 60, no. 10, pp. 55–57, Oct. 2008, doi: 10.1007/s11837-008-0137-5.

[92] F. Lajoie-Leroux, C. Dessemond, G. Soucy, N. Laroche, and J.-F. Magnan, "Impact of the impurities on lithium extraction from β-spodumene in the sulfuric acid process," *Miner Eng*, vol. 129, pp. 1–8, Dec. 2018, doi: 10.1016/j.mineng.2018.09.011.

[93] Q. Tian, B. Chen, Y. Chen, L. Ma, and X. Shi, "Roasting and leaching behavior of spodumene in sulphuric acid process," *Xiyou Jinshu/Chinese Journal of Rare Metals*, 2011, doi: 10.3969/j.issn.0258-7076.2011.01.022.

[94] L. K. Ellestad, R.B., Milne, "Method of extracting lithium values from spodumene ores," 2,516,109, 1950 [Online]. Available: https://patents.google.com/patent/US2516109A/en

[95] G. Kuang, Y. Liu, H. Li, S. Xing, F. Li, and H. Guo, "Extraction of lithium from β-spodumene using sodium sulfate solution," *Hydrometallurgy*, vol. 177, pp. 49–56, May 2018, doi: 10.1016/j.hydromet.2018.02.015.

[96] C. A. Maurice, A., Macewan, J.U., Olivier, "Method of producing lithium carbonate from spodumene," 3,017,243, 1962

[97] J. Jandová, P. Dvořák, and H. N. Vu, "Processing of zinnwaldite waste to obtain Li2CO3," *Hydrometallurgy*, vol. 103, no. 1–4, pp. 12–18, Jun. 2010, doi: 10.1016/j.hydromet.2010.02.010.

[98] N. C. Mcintosh, "Production of lithium compounds," U.S. Patent No. 2,413,644, December 1946.

[99] J. Jandová, H. N. Vu, J. Kondas, and P. Dvořák, "Lithium recovery from wastes after mining of Sn-W ore," in *Proceedings - European Metallurgical Conference, EMC 2007*, 2007.

[100] J. Jandova and H. N. Vu, "Processing of zinnwaldite wastes to obtain lithium and rubidium compounds," in *Proceedings of the 2008 Global Symposium on Recycling, Waste Treatment and Clean Technology, REWAS 2008*, 2008.

[101] J. Jandová, H. N. Vu, T. Beloková, P. DvořÁk, and J. Kondás, "Obtaining Li_2CO_3 from Zinnwaldite wastes," *Ceramics - Silikaty*, 2009.

[102] The Alkali-Silica Reaction in Concrete (1st ed.). CRC Press. Swamy, R.N. (Ed.). (1991) https://doi.org/10.4324/9780203036631

[103] Lithium Australia, "About LieNA®," https://www.lithium-au.com/about-liena/, (Accessed 12-08-2022).

[104] Q. YAN *et al.*, "Extraction of lithium from lepidolite using chlorination roasting–water leaching process," *Transactions of Nonferrous Metals Society of China*, vol. 22, no. 7, pp. 1753–1759, Jul. 2012, doi: 10.1016/S1003-6326(11)61383-6.

[105] X. Zhang, T. Aldahri, X. Tan, W. Liu, L. Zhang, and S. Tang, "Efficient co-extraction of lithium, rubidium, cesium and potassium from lepidolite by process intensification of chlorination roasting," *Chemical Engineering and Processing - Process Intensification*, vol. 147, Jan. 2020, doi: 10.1016/j.cep.2019.107777.

[106] G. G. Gabra, A. E. Torma, and C. A. Olivier, "Pressure leaching of beta-spodumene by sodium chloride," *Canadian Metallurgical Quarterly*, vol. 14, no. 4, pp. 355–359, Oct. 1975, doi: 10.1179/000844375795050049.

[107] L. I. Barbosa, G. Valente, R. P. Orosco, and J. A. González, "Lithium extraction from β-spodumene through chlorination with chlorine gas," *Miner Eng*, vol. 56, pp. 29–34, Feb. 2014, doi: 10.1016/j.mineng.2013.10.026.

[108] L. I. Barbosa, J. A. González, and M. del C. Ruiz, "Extraction of lithium from β-spodumene using chlorination roasting with calcium chloride," *Thermochim Acta*, vol. 605, pp. 63–67, Apr. 2015, doi: 10.1016/j.tca.2015.02.009.

[109] A. Maurice, C. A. Olivier, "Carbonatizing Roast of Lithium Bearing Ores," U.S. Patent No. 3,380,802, 30 April 1968.

[110] M. Tiihonen, L. Haavanlammi, S. Kinnunen, and E. Kolehmainen, "Outotec lithium hydroxide process - a novel direct leach process for the production of battery grade lithium hydroxide monohydrate from calcined spodumene.," in *Proceedings of ALTA 2019.* , 2019.

[111] Y. Chen, Q. Tian, B. Chen, X. Shi, and T. Liao, “Preparation of lithium carbonate from spodumene by a sodium carbonate autoclave process,” *Hydrometallurgy*, vol. 109, no. 1–2, pp. 43–46, Sep. 2011, doi: 10.1016/j.hydromet.2011.05.006.

[112] L. L. dos Santos, R. M. do Nascimento, and S. B. C. Pergher, “Beta-spodumene:Na_2CO_3:NaCl system calcination: A kinetic study of the conversion to lithium salt,” *Chemical Engineering Research and Design*, vol. 147, pp. 338–345, Jul. 2019, doi: 10.1016/j.cherd.2019.05.019.

[113] G. D. Rosales, A. C. J. Resentera, J. A. Gonzalez, R. G. Wuilloud, and M. H. Rodriguez, “Efficient extraction of lithium from β-spodumene by direct roasting with NaF and leaching,” *Chemical Engineering Research and Design*, vol. 150, pp. 320–326, Oct. 2019, doi: 10.1016/j.cherd.2019.08.009.

[114] G. D. Rosales, M. D. C. Ruiz, and M. H. Rodriguez, “Novel process for the extraction of lithium from β-spodumene by leaching with HF,” *Hydrometallurgy*, vol. 147–148, pp. 1–6, Aug. 2014, doi: 10.1016/j.hydromet.2014.04.009.

[115] D. T. Meshri, “The Modern Inorganic Fluorochemical Industry,” *Journal of fluorine chemistry*, 33, no. 1-4, pp 195-22, 1986.

[116] G. P., Robinson, “Recovery of Lithium from ore,” U.S. Patent No. 2,983,576, 9 May 1961.

[117] F. P. Hayes, E.T., Williams and W. M. Sternberg, “Production of lithium chloride from spodumene,” U.S. Patent No. 2,533,246, 12 December, 1950.

[118] H. D. W. Erasmus, “Method of treating lithiferous ores to recover lithium as lithium chloride,” U.S. Patent No. 2,561,439, 24 July, 1951.

[119] H. J. Sharratt, “The extraction of lithium from spodumene,” MSc Thesis, McGill University, 1955.

[120] N. K. Salakjani, P. Singh, and A. N. Nikoloski, “Production of Lithium –A Literature Review. Part 2. Extraction from Spodumene,” *Mineral Processing and Extractive Metallurgy Review*, pp. 1–16, Dec. 2019, doi: 10.1080/08827508.2019.1700984.

CHAPTER 2: Instrumentation and Analytical Techniques

2.1 Introduction

The study employed several analytical tools for sample characterisation to investigate experimental conditions. These tools include X-ray Fluorescence (XRF), Scanning Electron Microscopy with Energy Dispersive Spectroscopy (SEM/EDS), X-ray Diffraction (XRD), Mineral Liberation Analysis (MLA) and Inductively Coupled Plasma-Optical Emission Spectrometry (ICP-OES). This chapter focusses on describing principles underlining the operation of these tools for sample analysis.

2.2 X-ray Fluorescence (XRF)

In general, X-ray spectroscopic technique makes use of characteristic X-ray produced from a sample when its atoms are excited by a high energy beam. It is used for both qualitative and quantitative determination of chemical elements. Characteristic X-ray may be analysed by either referring to its wavelength or energy. If the analysis is based on its wavelength, it is called Wavelength Dispersive Spectroscopy (WDS), but it is Energy Dispersive Spectroscopy (EDS) if its energy is used.

XRF uses high energy X-rays produced from a high voltage source (between 30 to 50 kV) as the energy beam source to excite the atoms of the sample. Characteristic X-rays emitted are then analysed using their wavelengths [1]. Thus, the XRF uses WDS as a spectrometer for the chemical analysis of a sample. It detects characteristic X-ray signals of elements with atomic number of six (carbon) or more [1]. The energies of the X-rays are quantized and characteristic of atomic number of the emitting atom.

The XRF device basically consists of an X-ray tube (X-ray source), X-ray detection system and a data assembly and processing unit (Figure 2.1). In operation, primary X-ray is produced in the X-ray tube to excite atoms in the sample. The excitation in turn produces the characteristic X-rays which are diffracted and collimated onto the photon counter of the detection unit. The unit scans the photons in a 2θ range to determine the wavelength (λ) using Brag's law (Equation 2.1):

$$\lambda = \frac{2d\sin\theta}{n} \qquad (2.1)$$

Where d is the interplanar distance between adjacent atoms, θ, the angle of incidence (the angle between the crystallographic plane generating the diffraction and the incident beam) and "n" is the diffraction order.

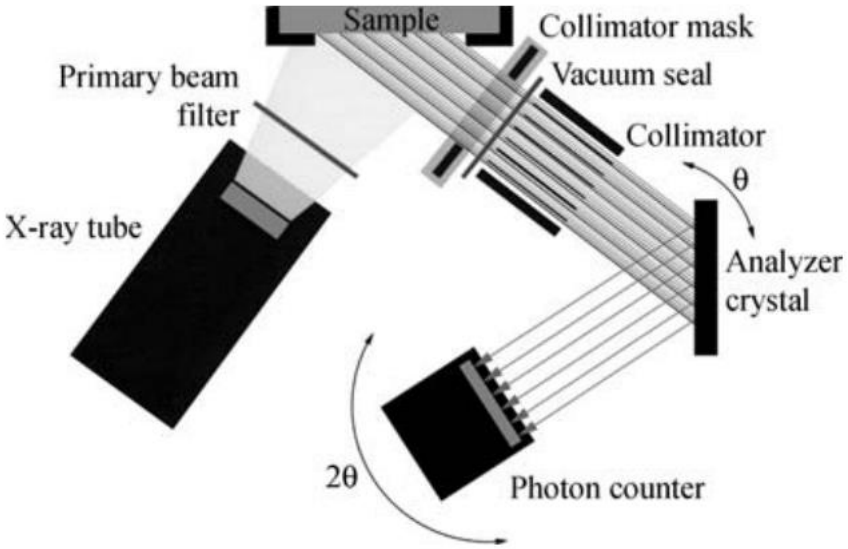

Figure 2.1 Essential parts and arrangement showing the operation of an XRF device [1].

A WDS spectrometer measures and records the wavelength as a spectrum of wavelength versus intensity (height) where each spectrum corresponds to the element generating it. The elements of the sample may then be identified by matching them to their respective spectrum. It is also possible to identify elements by atomic number determination using Moseley's law (Equation 2.2):

$$\lambda = \frac{B}{(Z-\sigma)^2} \tag{2.2}$$

Where B and σ are constants relating to the shells of the transitioning electrons, λ and Z are the wavelength of the X-ray and the atomic number respectively.

Quantitative determination is made by comparing the relative heights of the peaks in the spectrum. The weight fraction (W) of an element in the sample is related to the matrix factor (M), instrument factor (K) and relative intensity height (I_R) in Equation 2.3 as:

$$W = MKI_R \tag{2.3}$$

To obtain an accurate estimation for *W*, an internal standard is normally used with the assumption that, *M* and *K* are constant. With this assumption, the weight fraction (W_e) of the sample element can be calculated from its measured intensity (I_e), weight fraction of the standard (W_s) and corresponding intensity (I_s) by comparison using Equation (2.4):

$$\frac{W_e}{W_s} = \frac{I_e}{I_s} \tag{2.4}$$

The internal standard method is, nonetheless, suitable for quantifying single elements in a sample. New XRF instruments use the fundamental parameter method which compares theoretically calculated intensities of elements with measured intensity spectrum of the elements in the sample to estimate their composition. To achieve this, the calculated intensities (usually a relative parameter) is first normalised (by multiplying with the instrumental sensitivity). The results are then compared with the sample intensity spectrum. The difference in intensity triggers another calculation cycle until the difference is minimal (less than the threshold) where the final composition of the sample is estimated.

In this study, the major minerals in the concentrate were identified and quantified using XRF by a commercial laboratory (ALS Environmental Testing, Stafford, QLD).

2.3 Scanning Electron Microscopy with Energy Dispersive Spectroscopy (SEM/EDS)

Scanning Electron Microscopy (SEM) is a technique for investigating material's microstructure and morphology by directing electrons to the material's surface to give images. SEM may be equipped with Energy Dispersive Spectroscopy (EDS) which enables the retrieval of the chemical composition of the material, leading to the combination SEM/EDS as an analytical technique. SEM device is essentially made up of electron source (produced by a voltage source operating between 1 to 40 kV) and series of electromagnetic lenses which aid in the formation of electron probe used for scanning the surface of the sample [1].

In operation, the electron probe moves and forms a rectangular raster over the surface of the sample. The electrons interact with the atoms of the specimen and are scattered backward or eject electrons from the atoms of the sample. The resulting electron signals in conjunction with the pixels of raster formed, are detected, and amplified to form an image

of the specimen. Two types of electron signals are thus, used to form the image: (1) Backscattered Electrons (BSEs) and (2) Secondary Electrons (SEs).

If the incident electrons are scattered backward after interacting with the atoms of the specimen, the scattering is termed “elastic” and produces BSE signals. The ability for the incident electrons to undergo elastic scattering is predicted by a factor called “backscatter coefficient” which varies with the atomic number. Different BSEs collected are detected as different gray levels by the detector. An atom with a higher BSEs means higher backscatter coefficient value, high atomic number, which results in greater scattering and the specimen will appear bright. The BSEs therefore gives the compositional contrast and hence, an idea of chemical composition of a specimen.

Contrary to BSEs, SE signals are produced when incident electrons after striking the surface of a specimen, eject electrons from the atoms of the sample after receiving kinetic energy from the incident electrons. This is called inelastic scattering. A schematic diagram of SEM showing BSE and SE signals is indicated in Figure 2.2.

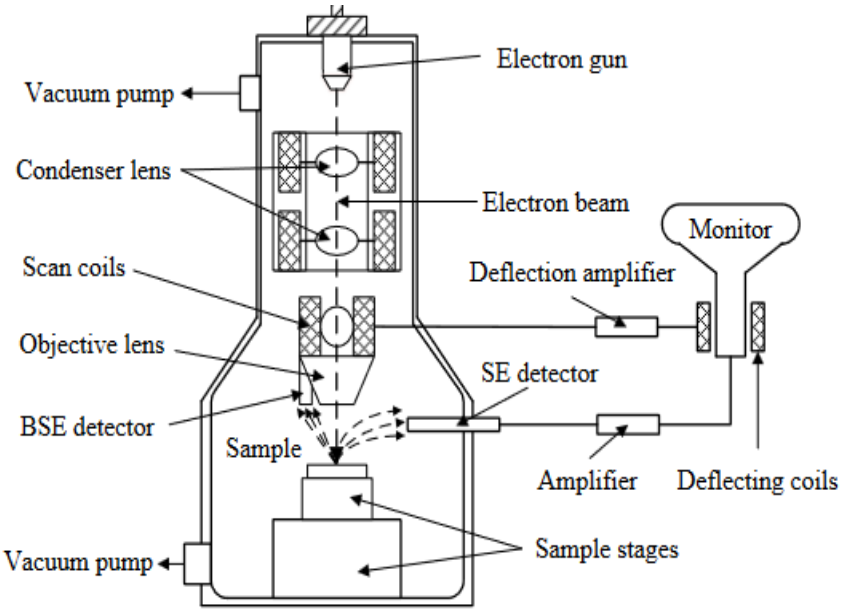

Figure 2.2 Schematic diagram of an SEM indicating BSEs and SEs [2].

SE signals produce topographic contrast which is the basic contrast of SEM images. Topographical contrast may arise due to the orientation of the detector relative to the sample and the trajectory of the emitted electrons. A higher number of electrons will reach a detector from a sample whose surface faces it. Images which arise from this kind of effect are bright and vice-versa. The place on the surface of the sample where the incident electrons strike can also create another kind of contrast. If the incidence electrons strike the specimen’s flat

surface, few electrons are emitted giving rise to dark contrast, but a high number of electrons are reflected when they strike the surface at an angle such as an outline of its hole, sphere or an elevated portion. This effect called electron number effect results in a bright contrast.

EDS microanalysers are normally coupled with electron microscope for elemental analysis. SEM/EDS functions similarly like XRF just that the former uses electron as energy beam to excite and produce characteristic X-ray which are analysed with reference to the energy. Also, XRF analyses the chemical composition of the whole sample whereas SEM/EDS is used to analyse targeted spot(s) of the sample. XRF may use internal standard whilst electron microscope uses external standard sample containing the elements to be analysed. The ZAF method which is based on Equation (2.5) is the mostly used quantitative technique.

$$\frac{W_i}{W_{(i)}} = (Z_i A_i F_i)\frac{I_i}{I_{(i)}} = (Z_i A_i F_i)K_i \qquad (2.5)$$

Where W_i and $W_{(i)}$ are the weight fractions of element *i* in the sample and standard respectively; I_i and $I_{(i)}$ are their corresponding intensities. $(Z_i A_i F_i)$ is a matrix correction factor for element *i* where Z_i, A_i, and F_i are the matrix effect due to atomic number, X-ray absorption and fluorescence respectively. Thus, to use the ZAF procedure, the matrix correction factor for each element in the sample must be calculated. This method hypothesises that, the surface of the sample is flat microscopically and it is present in bulk.

The quantification is achieved by calculating the relative intensities of elements in the sample from the sample spectrum as the ratio of the intensity height of an element to the sum of all intensity heights in the sample spectrum. The matrix correction factor for all the elements is then estimated to enable the calculation of their K_i which is compared with the measured K_is. The calculation is repeated several times until the two parameters agree to enable the estimation of the elemental composition.

In this study, SEM/EDS was used to study the spodumene concentrate, decrepitated samples and leached residues of chlorination using BSEs. Two preparation procedures were employed on samples before analysis. In the first preparation, powdered samples were glued on a graphite support for the analysis. The second was prepared by placing the sample in an epoxy resin and allowing to stand until it hardened. Surfaces of the hardened materials were polished and ultrasonically cleaned with deionized water to achieve a microscopically flat and highly polished surface. Due the electrically nonconductive nature of the samples, their

surfaces were coated with a thin film of carbon to enhance good electrical conductivity and prevent charging during analysis.

Mineral Liberation Analysis

Mineral Liberation Analysis (MLA) was carried out by *Julius Kruttschnitt Mineral Research Centre (JKMRC)* of the Sustainable Mineral Institute in Australia. The equipment used in this study makes use of BSE images and point-generated X-ray signals coupled with modern image and pattern identification for its measurements [3, 4]. The samples were prepared by allowing the untreated concentrate to stand in resin to harden, followed by surface polishing as in SEM-EDS second sample preparation. The prepared samples were then subjected to the MLA. Grain particles touching each other due to their settling mode in the resin were detected by DataView with its online program software package and then separated from each other using the shadow/boundary identification procedure. This was to ensure that, all grain particles in the sample were well separated from each other to avoid possible interference which may lead to errors in liberation results and mineral phase identification. Mineral phase identification was achieved by comparing elemental composition X-ray analysis with a standard database. Here, particles of the concentrate (which are in the resin) were divided into their individual mineral grains and their boundaries demarcated using their average BSE grey level. The device performs a systematic point X-ray elemental map which is associated with specific grains based on the differences in the grey level from the BSE map of the composite particles. The X-ray elemental map generated is matched to the corresponding average atomic number (AAN) of each mineral for their identification. In situations where mineral identification uncertainties arise due to overlap of grey level or minerals of similar AAN, the area X-ray analysis detects these anomalies and with the help of X-ray mapping, these minerals are discriminated and identified. Data obtained on the minerals are then stored for presentation in MLA DataView software.

2.4 X-ray Diffraction (XRD)

X-ray diffraction is a non-destructive technique used to identify and quantify phases in a sample based on their specific chemistries and atomic arrangement. The rays are produced when of fast-moving electrons accelerated by electric voltage are stopped by a metal target. The kinetic energy of the electrons after a rapid deceleration

are converted to this electromagnetic radiation which has a very short wavelength called X-ray. The rays after production are collimated and focused onto the sample to interact with the atoms which subsequently diffracts the rays at their crystallographic planes onto the detector. A diffractometer is thus, essentially composed of an X-ray tube, sample holder and a detector (Figure 2.3).

When the device is in operation, there is a relative motion between the components and if the components align such that a constructive interference occurs between the incidence beam, it obeys the Bragg's law (Equation 2.1) and a peak intensity is detected, measured and registered.

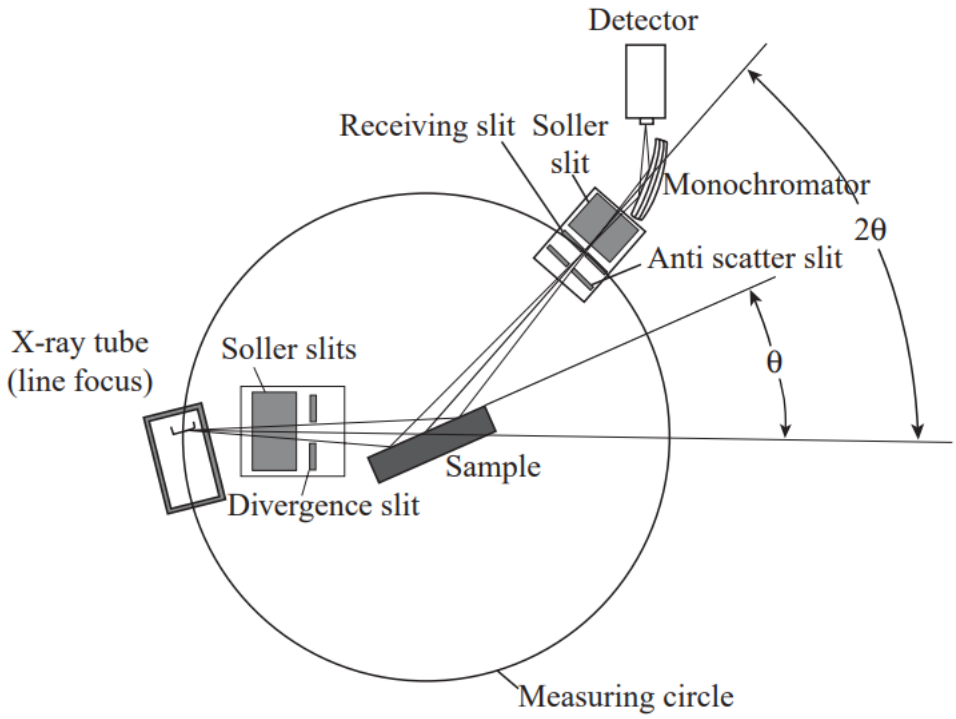

Figure 2.3 Arrangement of the components in a diffractometer [1]**.**

By continuously changing the incidence angle, a diffractogram which is a plot of intensity (count per second) versus 2θ is generated where each spectrum corresponds to a phase. Sample of a raw diffractogram generated by treatment of spodumene sample is shown in Figure 2.4.

Identification of phases in the diffractogram is made possible by matching the pattern of the sample with that of a known sample usually stored in a powder diffraction file (PDF) database published by the International Centre for Diffraction Data (ICDD). On the other hand, the d-spacing are obtained from the Bragg's law and stored in the PDF which can also be used to identify phases in the sample spectrum.

Two methods are broadly used to quantify phases in the sample: single reflection method and whole pattern method. The single reflection is based on an individual's choice to estimate the amount of a phase by comparing with the weight percent of a standard which is usually a natural sample such as corundum (α-Al_2O_3) or zincite (ZnO). Depending on how the standards are applied for the analysis, the single reflection method may be subdivided into internal standard and external standard method.

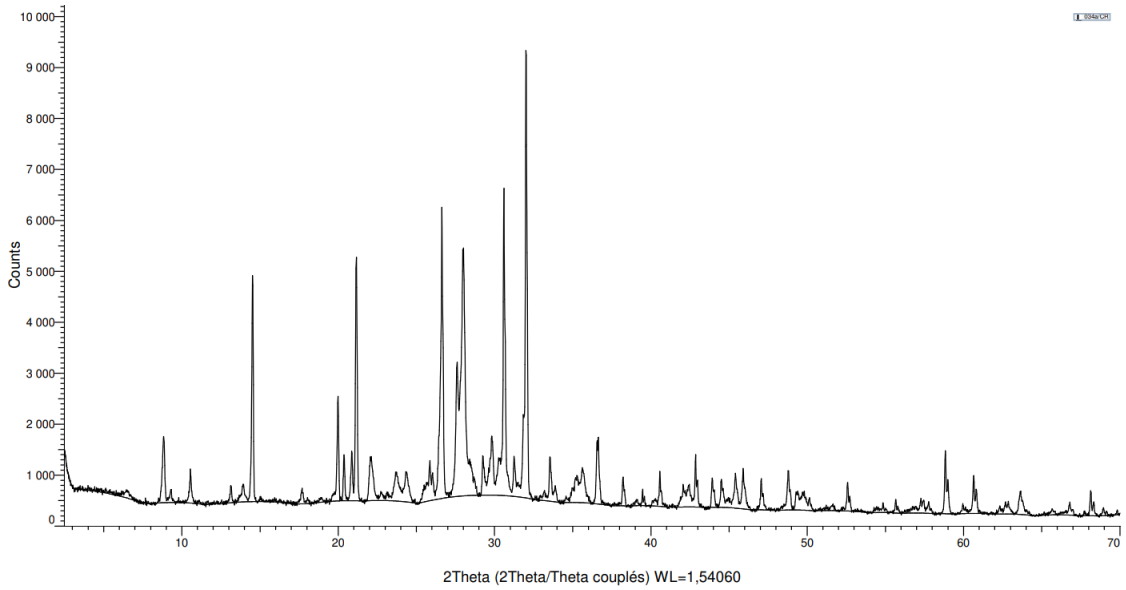

Figure 2.4 Sample diffractogram generated by the diffractometer.

In the internal standard method, the standard is added to the sample and analyzed in-situ with the sample after which the mineral phase of the sample is quantified based on a comparison with the standard. The Reference Intensity Ratio (RIR) and the Mineral Intensity Factor (MIF) are both single reflection internal standard method; if α-Al_2O_3 is used as the internal standard it is called RIR but it is called MIF if ZnO is used. The single reflection external standard method contrary to its internal standard counterpart does not introduce the standard into the sample during XRD measurements.

To use the RIR method for phase quantification, RIR_{cor} or I/I_{cor} values ("cor" referring to corundum used as standard) are estimated from the ratio of the intensity of the most intense line of the phase of interest to that of corundum obtained from a scan of their 1:1 binary mixture. RIR_{cor} values have been determined and stored in the PDF database from which semi-quantification of phases are estimated.

Semi-quantitative relative abundances of the phases in this study were estimated using the EVA© software coupled with the PDF2 database of the ICDD. It was performed based on the sample pattern's relative heights and I/Icor values by assuming that all crystalline phases were detected, and their sum was 100%. To obtain accurate estimation, a good preparation of samples through grinding to obtain fine powdered samples which have non-oriented flat plates were used. The preparation was essential to avoid preferential orientation and favoring certain diffraction peaks and cleavable minerals. The preparations were also made under the same conditions as far as possible to avoid the influence of external factors.

Diffractograms of samples were collected using a CuKα radiation D2 Phaser Bruker diffractometer which is equipped with LYNXEYE detector under 30 kV and 10 mA with measurements made at ambient temperature. The patterns were recorded between $2\theta = 2.5°$ and 70° at a scan step of $2\theta = 0.02°$ and step exposure time of 1 s.

2.5 Inductively Coupled Plasma-Optical Emission Spectrometry (ICP-OES)

This technique uses the photophysical properties of elements for their detection and quantification. It employs the wavelengths and intensities of light emitted from electrons of atoms to respectively identify and quantify them when they return to their ground states after being excited. The device is composed basically of a sample injection system (pump, nebulizer, spray chamber and sample injector), torch (which houses the plasma), radio frequency generator (or microwave radiation), the optics and detector (Figure 2.5). The device is used for measuring liquid samples hence, any solid material to be analyzed by this technique must first be solubilized by digestion.

When in operation, the sample by peristalsis mechanism of the pump is introduced into the nebulizer to vaporize and convert it into aerosols which enters the spray chamber to filter and allow finer and uniform aerosols (about 10 microns) to proceed to the torch via the sample injector [5]. The torch is supplied with argon gas which is used to generate the plasma through the application of high-power radio frequency (about 700 to 1500 W) [5] or microwave irradiation to ionize the gas.

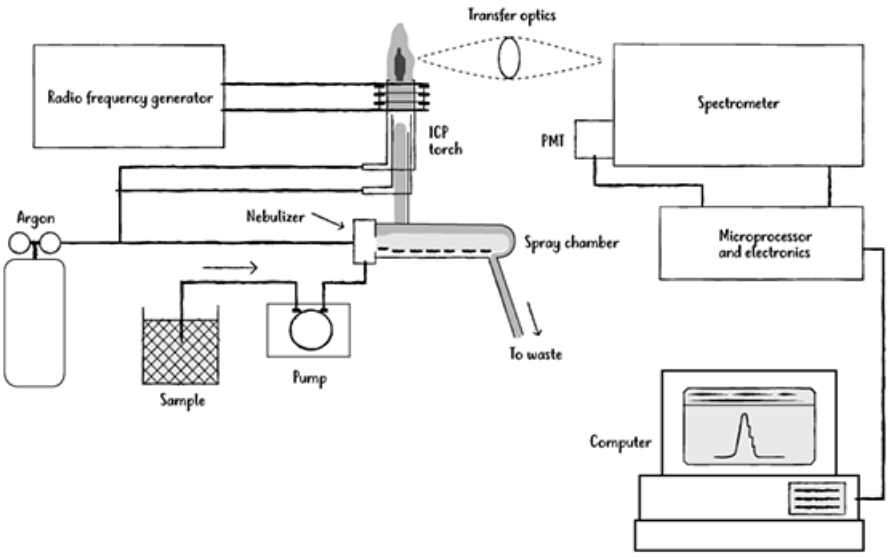

Figure 2.5 Schematic diagram of the ICP-OES [6].

This forms an argon gas-cloud (consisting of argon, ions, and electrons) called plasma operating between 8000 to 10000 K [5]. The aerosol samples as they approach this high temperature plasma are desolvated to release the component salts which melt and dissociate into their constituent atoms following excitation by the plasma.

When excited electron(s) return to the ground state, they emit light energy with wavelength(s) which is/are characteristic of the atom(s) emitting it. The emitted light is focused onto the optics of the device to disperse and separate the wavelengths onto the detector which identifies the elements based on their characteristic wavelengths. Quantification is based on the intensity of light reaching the detector. It uses the Beer-Lambert law which indicates that, the intensity is proportional to the concentration of the element emitting it (Equation 2.6).

$$I = \varepsilon c l \tag{2.6}$$

where I is the intensity and ε, c, and l are the molar absorption coefficient, molar concentration, and optical path length respectively. To determine the concentration of an unknown sample, solutions of known concentrations (standards) of the analyte(s) is/are analyzed and the result is used the construct a calibration curve from which the unknown concentration is estimated.

REFERENCES

[1] Y. Leng “Materials Characterization: Introduction to Microscopic and Spectroscopic Methods,” John Wiley & Sons, 2009.

[2] S. Yao, H. Li, S. Pang, B. Zhu, X. Zhang, and S. Fatikow, “A Review of Computer Microvision-Based Precision Motion Measurement: Principles, Characteristics, and Applications,” *IEEE Transactions on Instrumentation and Measurement*, vol. 70. Institute of Electrical and Electronics Engineers Inc., 2021. doi: 10.1109/TIM.2021.3065436.

[3] Y. Gu, “Automated Scanning Electron Microscope Based Mineral Liberation Analysis An Introduction to JKMRC/FEI Mineral Liberation Analyser,” *Journal of Minerals and Materials Characterization and Engineering*, vol. 02, no. 01, pp. 33–41, 2003, doi: 10.4236/jmmce.2003.21003.

[4] R. Fandrich, Y. Gu, D. Burrows, and K. Moeller, “Modern SEM-based mineral liberation analysis,” *Int J Miner Process*, vol. 84, no. 1–4, pp. 310–320, 2007, doi: 10.1016/j.minpro.2006.07.018.

[5] S. R. Khan, B. Sharma, P. A. Chawla, and R. Bhatia, “Inductively Coupled Plasma Optical Emission Spectrometry (ICP-OES): a Powerful Analytical Technique for Elemental Analysis,” *Food Analytical Methods*, vol. 15, no. 3. Springer, pp. 666–688, Mar. 01, 2022. doi: 10.1007/s12161-021-02148-4.

[6] B., Charles and K. J., Fredeen, “Concepts, instrumentation and techniques in inductively coupled plasma optical emission spectrometry,” *Perkin Elmer Corp* 3, no. 2, 1997.

CHAPTER 3: Physico-chemical Characteristics of Spodumene Concentrate and its Thermal Transformations

3.1 Introduction

The sample used for the study is obtained from the Pilgangoora LCT pegmatite deposit found at the Pilbara Craton located in the Pilbara region of Western Australia. Figure 3.1 shows the sample location (Pilgangoora) alongside other LCT pegmatite deposits in Western Australia.

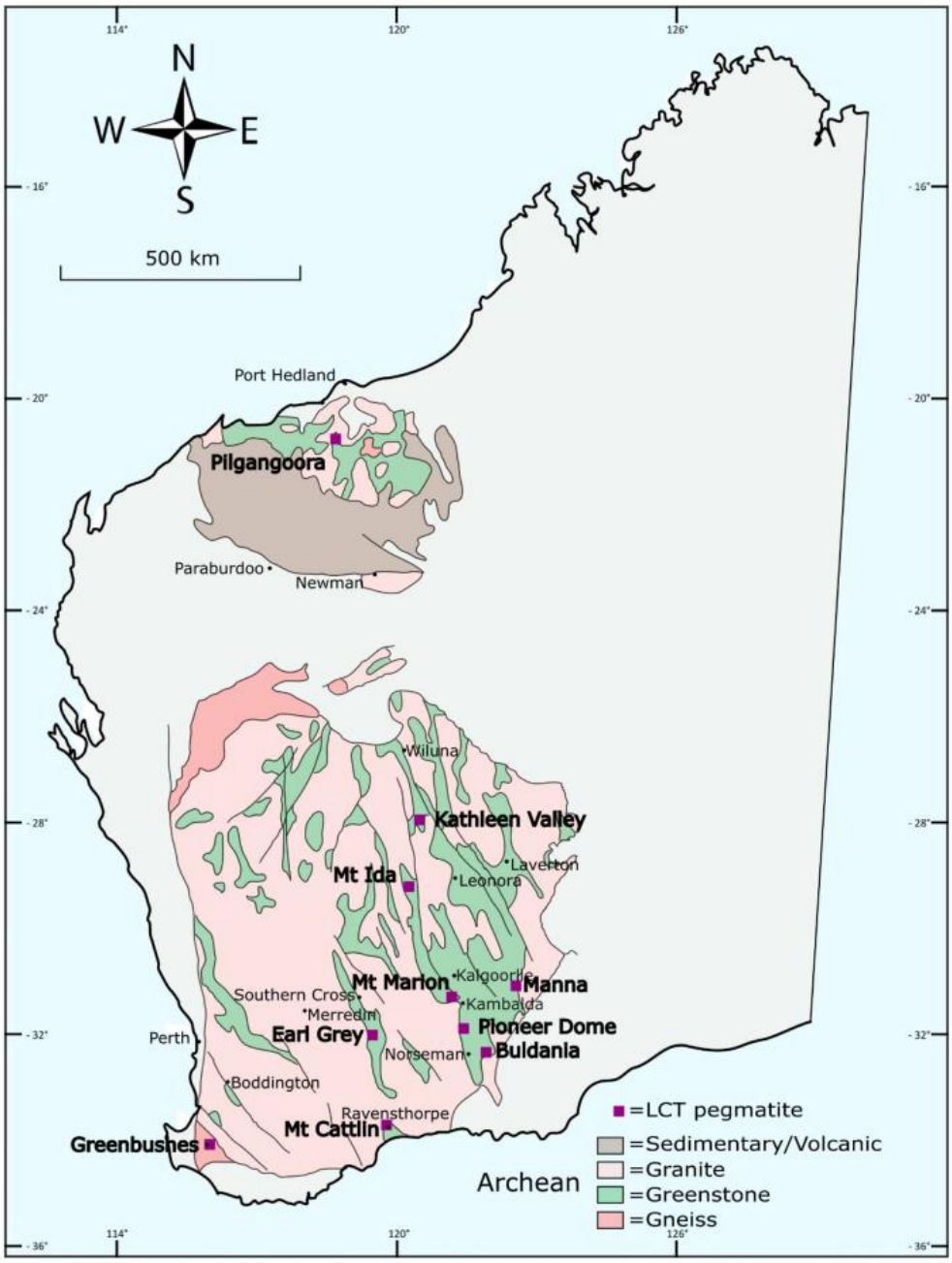

Figure 3.1: Location of Pilgangoora and other pegmatite deposits in Western Australia [1].

The pegmatite has an open surface in greenstone belt with a weathered surface and composed of several mineral assemblage including elongated and very coarse spodumene. The spodumene content of the pegmatite is estimated to vary from 75 to 80% but another source indicates more than 85%. This pegmatite source contributes significantly (about 226 Mt) to the world lithium resource with a lithium oxide content of about 1.27 wt% distributed evenly throughout the pegmatite [2, 3].

3.2 Characterisation of Spodumene Concentrate

3.2.1 Spodumene Concentrate Preparation

Method

The concentrate was achieved by several unit operations including crushing, grinding, gravity separation (Dense Media Separation (DMS)) and froth flotation. The ore was crushed with primary and secondary crushers to particle size of 32 mm onto a stockpile. It was then fed into High-Pressure Grinding Rolls to reduce the size further to 3.35 mm. This was followed by a two-stage DMS which led to the recovery of course spodumene concentrate. The lower grade unrecovered material was fed into a ball mill which reduced the size to 115 microns prior to tantalite recovery as a by-product via gravity separation. The spodumene-containing fraction was conditioned at a little above 50% pulp density in a neutral pH using sodium oleate as collector. Spodumene in the conditioned material was floated at 30% pulp density and gangue minerals rejected to tailings. This led to 85% recovery and an upgraded concentrate of about 4.6% Li_2O. The floated material then entered the cleaning stage yielding the concentrate. The concentrate produced as described above was then used for the study.

It consisted of damp, fine-grained material with a significant portion composed of large, agglomerated particles that were several centimetres in diameter. The bulk of the material was greenish brown in colour. Breaking apart the agglomerate particles revealed a light grey material. An image of the bulk and grey material is shown in Figure 3.2. The different colouration observed may be due to the presence of varying concentrations of Fe and Mn which substitute for Al at the various locations. Spodumene is usually associated with Fe which gives it a greenish colour. At lower Fe concentration, a grey/white colour is observed as in this case [4].

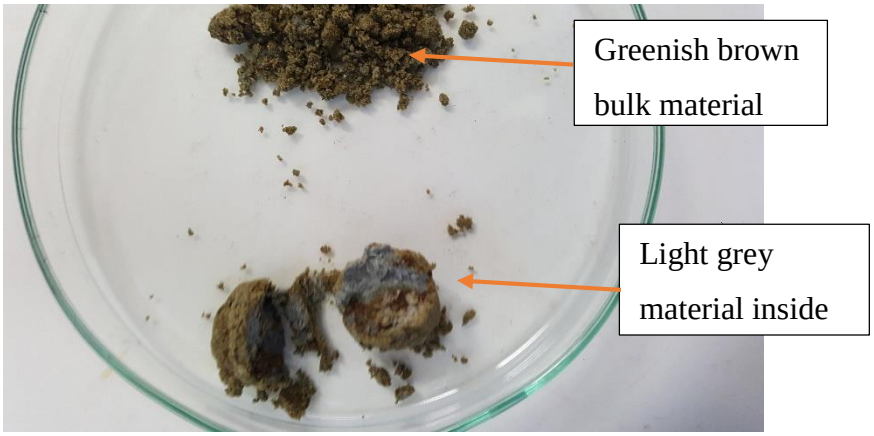

Figure 3.2: Optical image showing both the bulk and grey material contained in agglomerate particles.

The as-received sample was formed into a cone and tarp and then cut into approximately two portions. A portion was dried at 60 °C for 48 h after which it was passed through a 3.25 mm screen to break agglomerate particles. The dried material was split into eight subsamples using a rotary splitter. These subsamples were further split using a riffle splitter to generate representative samples of about 1 kg in mass. A representative subsample of the other moist portion was sectioned off by pie splitting which was used to determine the elemental and mineral composition.

Particle Size Distribution

A representative subsample of the dried material was used to determine the particle size distribution. This analysis was performed by staff at the hydrometallurgy department of The University of Queensland, Australia. Approximately, 15 g of the sample was slurred in a 1 L stirred baffled reactor containing water. A small amount of detergent was added to enhance breaking the agglomerates and reduce hydrophobicity. This slurry was then sampled using a pipette across the entire depth of the reactor. Sample was transferred to a Malvern Mastersizer for particle size analysis. A total of 5 repeats with two additional rejected runs were completed.

Spodumene concentrate characterisation technique

The spodumene sample obtained was characterised using XRF, SEM/EDS, XRD, MLA and ICP-OES. The sample preparation and mode of operation of analytical equipment for the characterisation is elaborated in Chapter 2. All treated samples were investigated by one or a combination of the technique(s).

3.3 Thermal Treatment of Spodumene Concentrate

Carbolite Gero electric furnace was used for the thermal treatment of the concentrate and chlorination roasting. The reactor is made of quartz tube which was placed inside the furnace and the whole setup operated in air with a flow rate of 25 L/h. The heat which is generated by an electric source provides a constant homogeneous heating 20 cm at its centre up to 1500 °C, therefore, samples placed in the middle have constant temperature throughout the experiment. A cylindrical quartz crucible was used to hold the sample for heating. Before experimental work, the furnace was calibrated such that, the extent of deviation from the set temperature was ±5 °C throughout the study. It was then preheated for 60 min to achieve a steady temperature so that samples can attain the reaction temperature within the shortest possible time for accurate time measurements. Residence time was measured immediately after the sample was introduced into the furnace until the specified time elapsed. Figure 3.3 shows the experimental set-up used for the study.

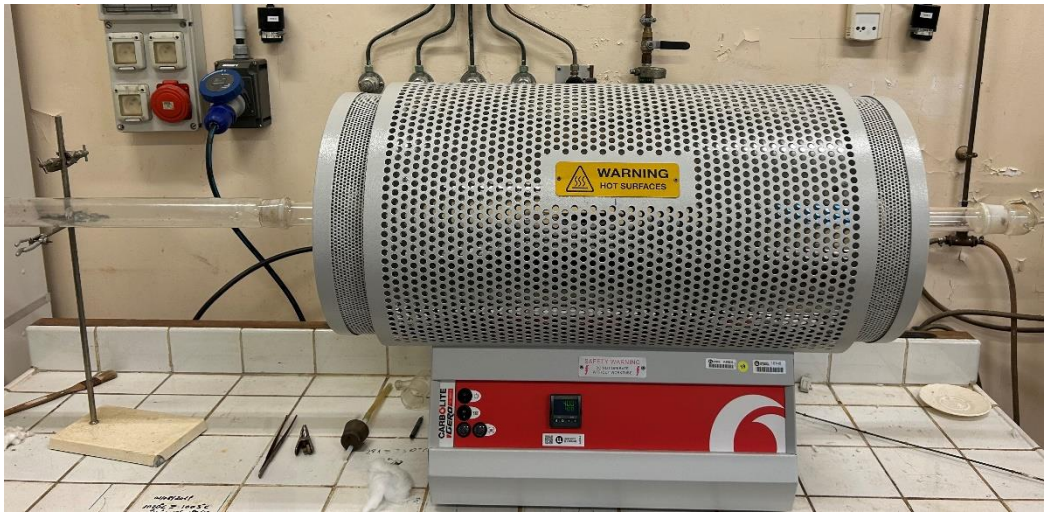

Figure 3.3: Experimental set-up for thermal treatment of samples.

Method

After achieving and stabilizing the required temperature as indicated earlier, samples were introduced at the centre of the reactor and the air supply connected. Roasting at varying temperatures from 900 to 1050 °C at 25 °C intervals and residence times of 7.5, 15, 30, 60, 240 and 480 min for the decrepitating experiments. Residence time was measured immediately after the sample was introduced into the furnace until the specified time elapsed. Samples were weighed after the thermal treatments and prepared for analysis as required.

3.4 Results and Discussion

3.4.1 Spodumene Concentrate

Bulk Chemical Analysis

The result of the elemental composition of the concentrate as oxides obtained from XRF and ICP-OES is presented in Table 3.1 The lithium content was determined as 2.14 wt.%; consequently, the calculated lithium oxide and spodumene content were 4.61 wt.% and 57.39 wt.% respectively. This is in close agreement with the 60.21 wt.% spodumenes indicated by the MLA result (Table 3.2) and 3 wt.% Li content in spodumene from the Pilgangoora deposit reported in the literature [4].

Table 3.1: Elemental composition of concentrate determined by XRF and ICP-OES.

Major	**Al_2O_3**	**CaO**	**Cr_2O_3**	**Fe_2O_3**	**K_2O**	**MgO**	**MnO**	**Na_2O**	**P_2O_5**	**SO_3**	**SiO_2**	**TiO_2**	**Li_2O**	**LOI**
(wt%)	20.79	1.72	0.03	4.29	1.26	1.30	0.32	1.14	0.33	0.15	61.31	0.10	4.61	1.95
minor	**Cs**	**Rb**	**Ta**	**Nb**	**Sn**									
(ppm)	116	1033	202	180	140									

Table 3.2: MLA modal mineralogy.

Mineral	**Formula**	**wt%**
Spodumene	$LiAlSi_2O_6$	60.21
Pyrite	FeS_2	0.13
Quartz	SiO_2	7.58
Orthoclase	$KAlSi_3O_8$	4.00
Albite	$NaAlSi_3O_8$	9.10
Anorthite	$CaAl_2Si_2O_8$	1.00
Biotite	$KMg_{2.5}Fe^{2+}0.5AlSi_3O_{10}(OH)_{1.75}F_{0.25}$	3.32
Muscovite	$KAl_3Si_3O_{10}(OH)_{1.9}F_{0.1}$	4.90
Chlorite	$(Mg,Fe)_3(Si,Al)_4O_{10}(OH)_2 \cdot (Mg,Fe)_3(OH)_6$	0.33
Amphibole	$CaFeSi_2O_6$	7.30
Spessartine	$Mn_2^{+3}Al_2(SiO_4)_3$	0.61
Tantalite-(Mn)	$MnTa_2O_6$	0.12
Calcite	$CaCO_3$	0.47
Apatite	$Ca_5(PO_4)(F,Cl,OH)$	0.93

All elements identified are also in agreement with the previous investigation by Aylmore et al. [4] except for Ba and Co which were not identified in this study.

Mineralogy

XRD spectra of the concentrate are shown in Figure 3.4. Spodumene, mica (muscovite and biotite), quartz, feldspars (orthoclase, albite, anorthite) and the amphiboles are the

predominant minerals identified which are typical minerals of spodumene ore of Pilbara. XRD has become the common analytical tool for determining the mineral composition of samples, it has, therefore, been used with the support of other analytical techniques (MLA and EDS) for the finest detection of mineral assemblage in the concentrate.

The modal mineralogy identified by MLA with their amounts are shown in Table 3.2. This result is consistent with the XRD analyses, however, spessartine, tantalite, calcite, and apatite which appeared as trace minerals were not identified by XRD. An operator decision was made to consider only minerals that present at least two diffraction peaks (the main and secondary peaks). Thus, minerals with a very low concentration and showing only their main peak, which was difficult to dissociate from the background noise, could have been neglected. This could result in some trace minerals unidentified by XRD contrary to MLA and EDS point analysis.

The results are in close agreement with the mineralogy of LCT-spodumene ore except with the presence of amphibole which is identified in this work. Elemental assay of the concentrate was also calculated by MLA and the results are presented in Table 3.3. Computing the oxides of these elements shows a close agreement with chemical analyses in Table 3.1. The results of this computation are shown in Table A.1 of the appendix.

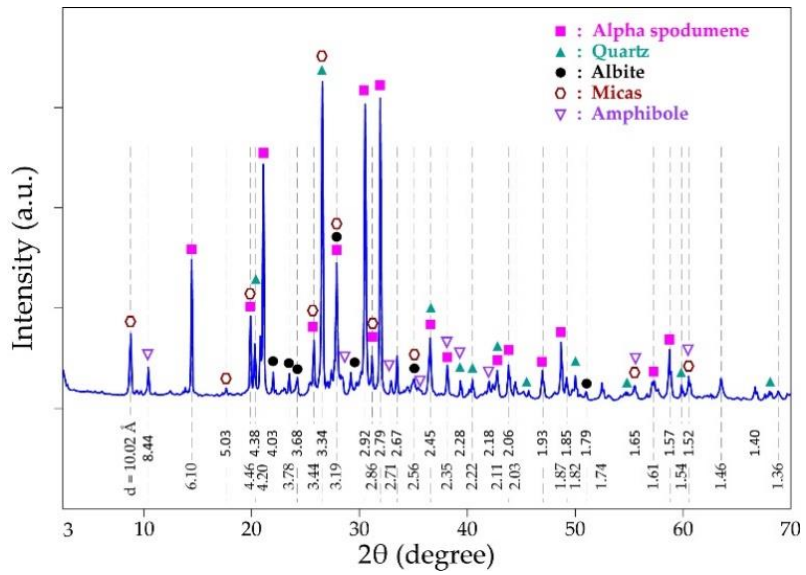

Figure 3.4: XRD patterns of spodumene concentrate.

Table 3.3: Calculated elemental assay from MLA.

Li	Al	Si	C	S	Fe	K	Na	Ta	P	Mn	Mg	Ca	Cl	F	H	O
1.96	11.58	29.47	0.06	0.07	2.00	1.34	0.76	0.09	0.17	0.22	0.50	1.97	0.02	0.09	0.04	49.39

The particle size of the major minerals was also determined by MLA and the corresponding results are displayed in Figure 3.5. There are no significant differences between the particle sizes of the minerals in the concentrate. The grain sizes are small with the majority below 100 microns (d80 around 100 microns). At this particle size, the minerals are well liberated as the degree of liberation of all of them is above 90% (Figure 3.6). Spodumene is the most liberated mineral as its degree of liberation reaches nearly 99%. It follows that the comminution conditions employed for processing this ore are satisfactory; since minerals in the concentrate were well liberated for subsequent processing to enable maximum lithium extraction, provided the spodumene itself does not passivate. A raw MLA data generated for obtaining Figure 3.6 is provided in Table A.2 (in Appendix).

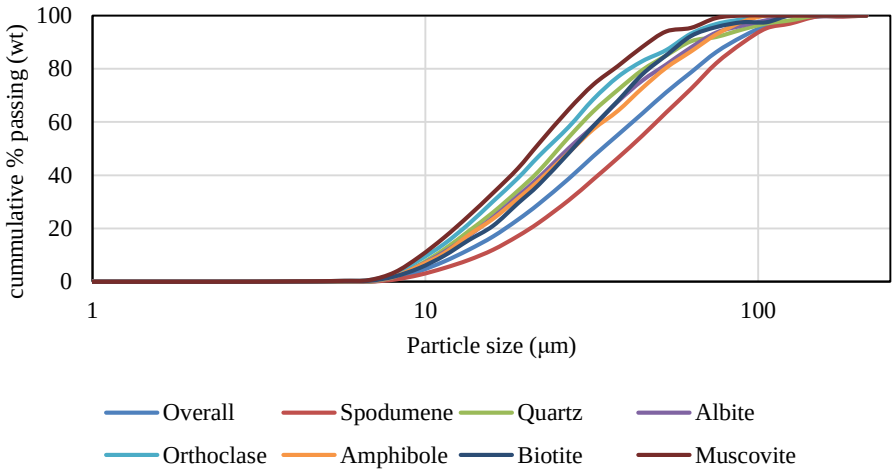

Figure 3.5: Mineral particle size determined by MLA.

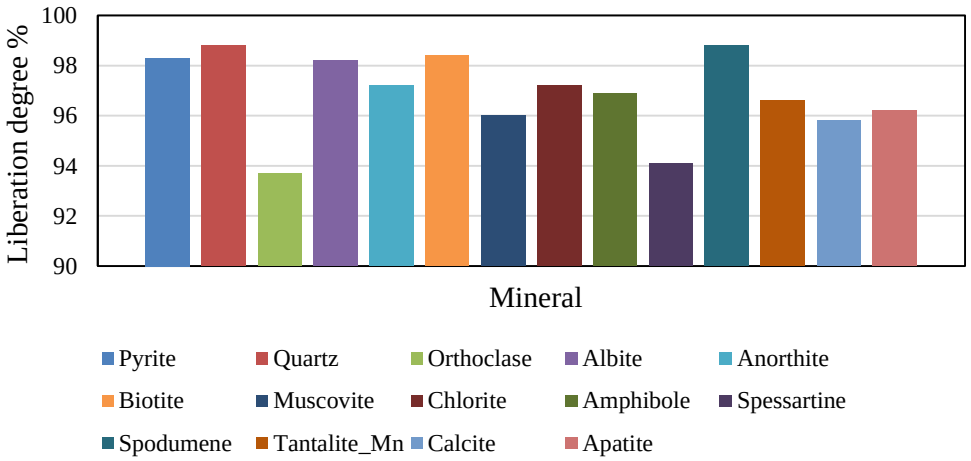

Figure 3.6: Degree of liberation of the main mineral phases.

Morphology, Texture of Particles and Mineralogy

Figure 3.7 shows the volume distribution and cumulative passing of the concentrate particles. Particle diameter ranges from 10 to 200 microns with about 68% of the total volume being 80 microns in diameter. The d_{50} and d_{80} are indicated as 57 and 113 microns respectively. The d80 found is in close agreement with the 100 microns suggested earlier. Considering the higher liberation of spodumene grains, it may be indicated that, d80 of 113 microns and particle diameter of 80 microns are good comminution parameters for processing spodumene ore, particularly the one of Pilgangoora origin.

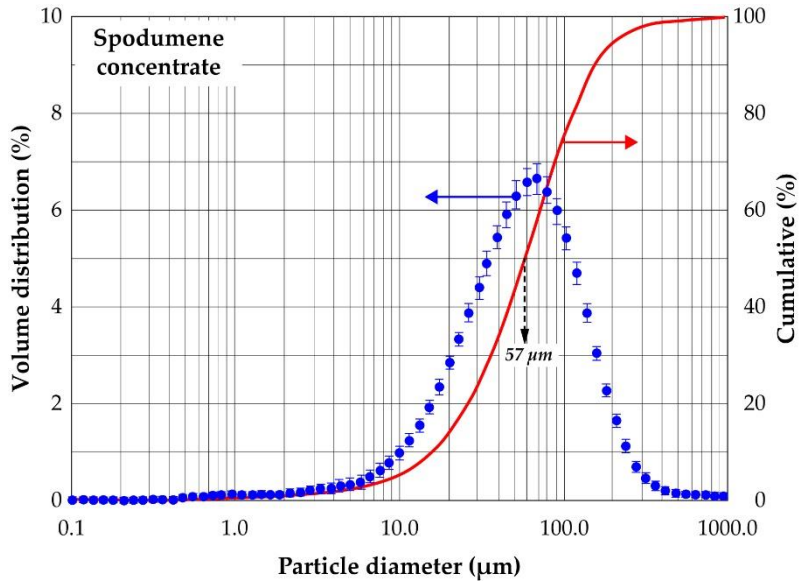

Figure 3.7: Volume distribution and cumulative passing of spodumene concentrate.

Physicochemical Characteristics

The BSE mode of the SEM was used to investigate the morphology and texture of particles in the concentrate. It was coupled with EDS to determine the elemental composition at some points and hence the mineral composition. Figure 3.8 and Table 3.4 are the SEM photomicrograph and spot elemental composition of the concentrate respectively. It is observed (from Figure 3.8a,b) that, it is a well liberated coarse and loose material with varying particle size of several microns in diameter; confirming earlier observation.

Spodumene grains were identified using the Si/Al atomic ratio since EDS cannot detect the presence of lithium. The atomic ratio of Si to Al in spodumene is 2.0, hence, grains with spot elemental composition mainly of Al, Si, O and Si/Al ratio of approximately 2.0 corresponds to spodumene. All spots indicated “1” are identified as spodumene. Figure

3.8c,d confirms that spodumene is a coarse, dense, crystalline solid with a smooth surface, however, scratches were observed on some grains, which may be due to abrasion during comminution. It suggests that spodumene is a hard mineral that resists wear and tear except when in contact with a harder material. This is confirmed by its relatively high 6.5 to 7.0 value on the Mohs scale of mineral hardness. Spodumene is the major mineral found in the concentrate.

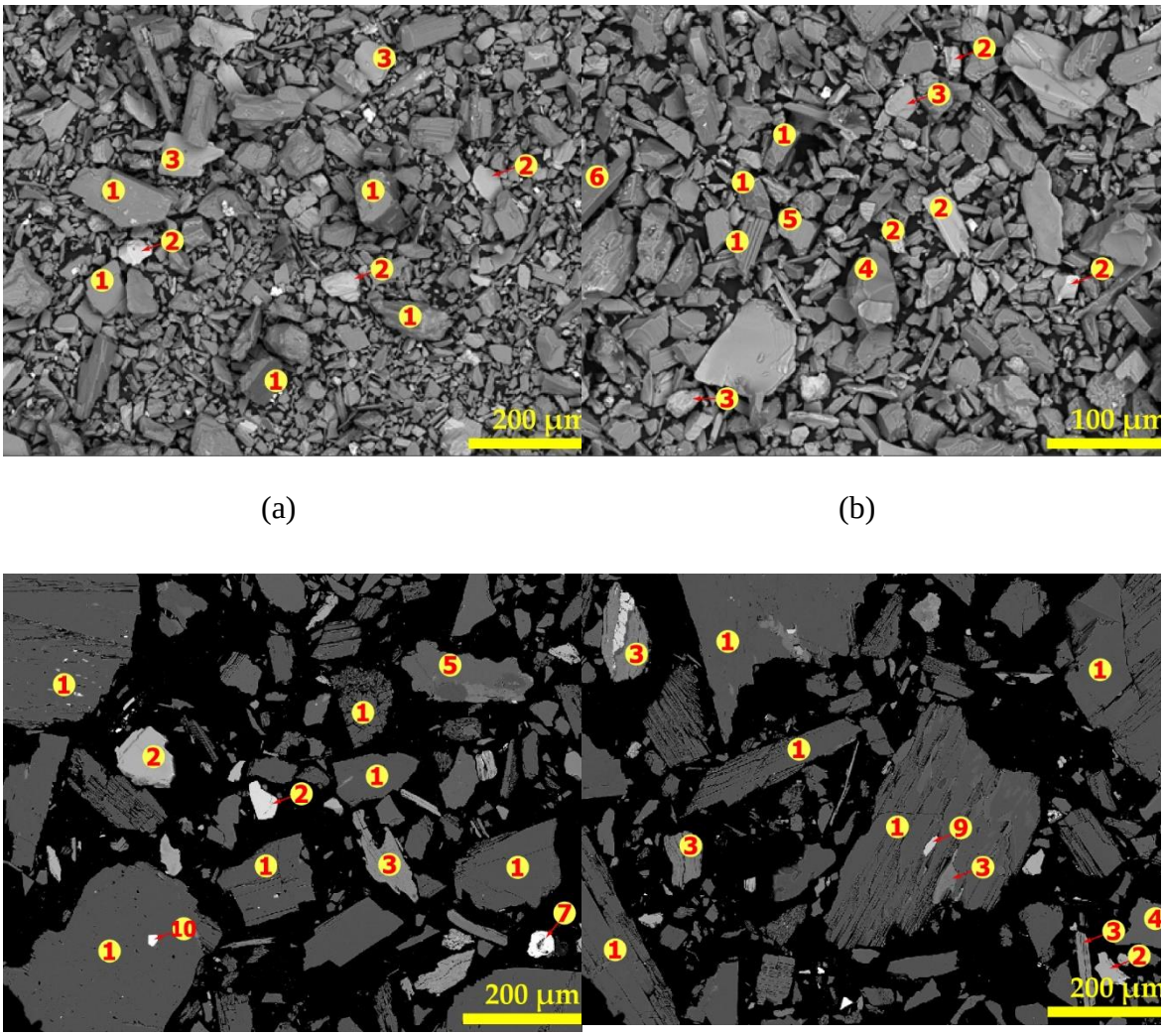

(a) (b)

(c) (d)

Figure 3.8: SEM of powdered (a,b) and polished samples (c,d) of concentrate. The numbers (1 to 7, 9, 10) indicate the locations of the elemental determination.

Spot "2" has a complex composition with Fe, Mg, Ca, Al, Si, O as the major elements but with varying concentrations at different spots. We attribute these grains to the amphibole group of minerals as indicated in XRD pattern due to the higher concentration of Fe, Mg and Ca at some spots. We could not attribute them to the mica group since the mica group identified by MLA in the concentrate are muscovite and biotite which all contain K in their

chemistry, but K is absent at these spots. Spots identified as amphibole do not have specific colour but ranges from light gray to white depending on the concentration of heavy metals that may be present. The micas (muscovite and biotite) are identified by spot 3 where there is an appreciable high concentration of K. Spots "4" are composed mainly of Si and O with O/Si atomic ratio of approximately 2.0 and therefore identified as quartz. Spots "5" and "6" have a complex composition of Ca, K and Na and are linked to the feldspars, specifically, alkali feldspars and anorthite.

Table 3.4: Atomic percentage of elemental composition identified by SEM-EDS.

Elements	Spot "1"	Spot "2"	Spot "3"	Spot "4"	Spot "5"	Spot "6"	Spot "7"	Spot "9"	Spot "10"
O	64.7	60.9	54.4	66.7	61.9	61.6	60.1	56.6	67.8
Al	11.5	5.2	4.1		7.7	7.5	0.4		
Si	23.6	16.8	16.1	33.3	23.3	23.2	0.6		
Fe	0.2	6.2	2.2				38.9		
Mg		4.3	10.6				0.1		
Ca		4.8			0.2			20.2	
Mn		0.2							
Na		1.1			6.9	2.4			
K		0.5	3.9			5.2			
F			8.6					8.6	
P								14.6	
Nb									
Ta									0.4
N									6.2
Sn									25.6

Spot "5" is specifically identified as albite due to the high concentration of Na at these areas and spots "6" as other feldspars. Hematite was not identified by XRD nor MLA but Spot "7" is identified as such based on the composition. It is composed mainly of Fe and O with an O/Fe atomic ratio of approximately 1.5, confirming its identity. Apatite which is typical of LCT-spodumene ore of the Pilbara region are also identified at spot "9". The standard deviations calculated for atomic percent obtained on some mineral grains in the concentrate are shown in the Appendix (Tables A.3–A.9). Spot "10" is composed of Sn, Ta, N and O. Though the identification of Sn by EDS is a confirmation of elemental composition in Table 3.1, we could not link the identity of this spot to any mineral since its composition did not match with any. We treat it as an impurity that is locked up in the spodumene grain.

All major minerals in the concentrate were identified using spot elemental identification by EDS, confirming XRD and MLA analytical results. Raw data (elemental spectrum with their corresponding intensities, weight percent, etc.) generated by SEM-EDS

instrument for elemental composition determination which enabled the mineral phases' identification can be found in Figures A.1–A.8 and Tables A.10–A.17. Other elements such as Cr, Ti, F, Th, Sn, Zn, Cu, Ni, V, and S were also identified which are associated with the fine inclusion of some minerals. Though Ta, Nb, Sn and other valuable metals were observed, their concentrations are too low to be extracted economically.

3.4.2 Thermal Treatment of Spodumene Concentrate

Physicochemical transformations

The morphological changes in the spodumene grain during decrepitation are of great importance since it gives an indication of the extent of structural changes and openness of the mineral for chemical treatment. Changes in the morphology of spodumene grains were studied on residues treated at 900, 950, 1000 and 1050 °C using the BSE mode of SEM coupled with EDS. Figure 3.9 and Figure A.8 (in Appendix) gives the SEM images with spots analysed by EDS for both polished and unpolished samples respectively. Cracks preceding disintegration were observed in spodumene grains which were also followed by melting and agglomeration with increasing temperature (Figure 3.9a–d). At 900 °C, micro-cracks are observed (Figure 3.9a) which becomes prominent at 950 °C (Figure 3.9b) such that at 1000 °C (Figure 3.9c), the spodumene grains had disintegrated and was well open for chemical processing. At 1050 °C, melting and agglomeration of spodumene with impurities are observed (Figure 3.9d). A closer look at a portion in Figure 3.9d (square "A") confirms the melting and agglomeration (Figure 3.9e). We observe several regions of dark and light grey as well as dotted white regions with each coloration corresponding to a mineral phase which are fused together in Figure 3.9e due to melting. Specifically, spots "1", "2", "4" and "6" were identified in Figure 3.9e which corresponds to spodumene, amphibole, quartz and feldspars which were fused together. Tantalite and other minerals were also seen fused with some spodumene grains at other portions. Most investigations of lithium extraction from spodumene are performed at decrepitation temperature of 1050 °C, however, we advise 1000 °C as the ideal decrepitation temperature for this concentrate. This is due to the degree of material disintegration at 1000 °C and the agglomeration which occurs at temperatures higher that it (1000 °C), which can affect downstream processes and the extraction efficiency of lithium.

Most minerals were identified in the residues and thermal treatment did not have any major influence on their composition except melting and agglomeration of the particles at higher temperatures.

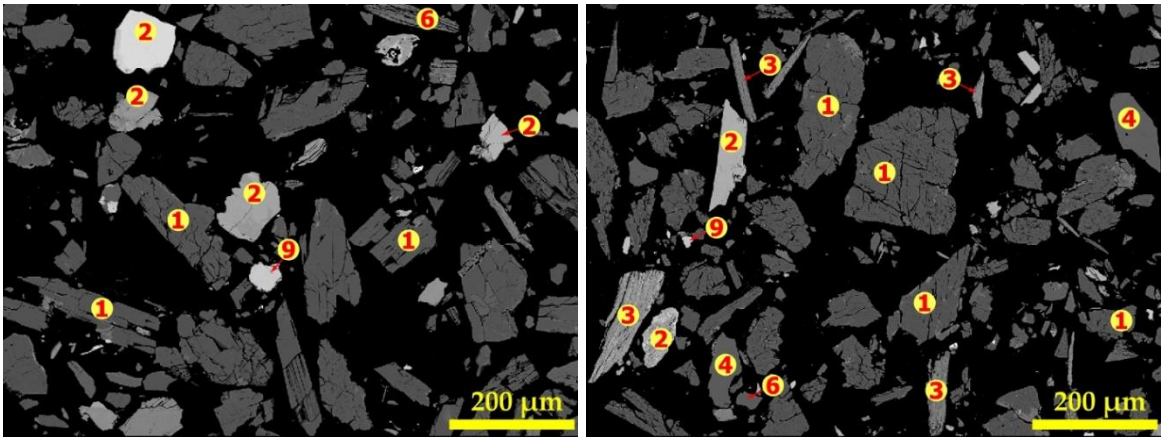

(a) (b)

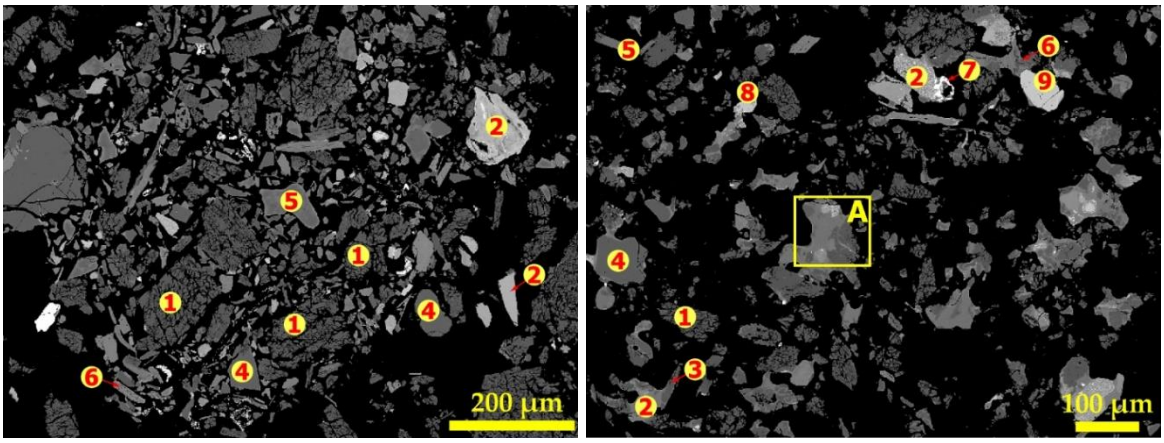

(c) (d)

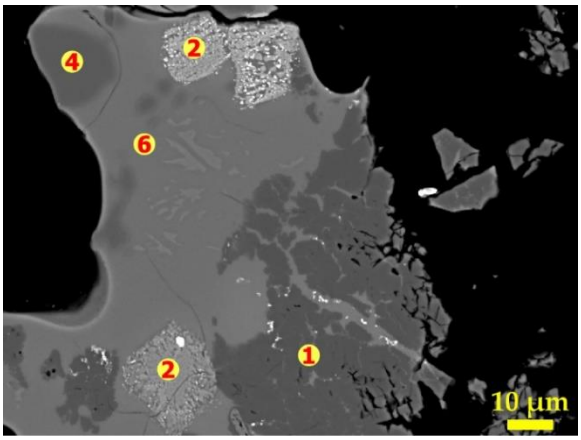

(e)

Figure 3.9: SEM and spot elemental composition determination of polished sample obtained after treatment in air at (a) 900 °C, (b) 950 °C, (c) 1000 °C, (d) 1050 °C and (e) melting and agglomeration occurring in square "A". The numbers (1 to 9) indicate the locations of the elemental determination.

A representative elemental composition as determined by EDS for samples treated at 900, 950 and 1000 °C are indicated in Tables A.18–A.20. Though there was no major effect of

thermal treatment on the mineral phases, ionic diffusion was observed in some of the residues at increased temperatures which becomes prominent at 1050 °C. Due to this diffusion, the segregation of the feldspars into their individual minerals as well as differentiating them from the micas by EDS becomes a challenge since they appear to have similar elemental compositions. Table 3.5 shows some elemental associations with spodumene (spot "1"), amphiboles (spot "2") and representative composition of micas and feldspars (spot "3", "5", "6") as a result of ionic diffusion between minerals at 1050 °C. The composition of quartz, hematite, tantalite and apatite were not greatly affected regarding the ionic diffusion and are indicated at spots 4, 7, 8 and 9, respectively.

Table 3.5: Atomic percentage of elemental composition identified by SEM-EDS at 1050 °C.

Elements	Spot n° 1	Spot n° 2	Spot n° 3,5&6	Spot n° 4	Spot n° 7	Spot n° 8	Spot n° 9
O	64.3	54.9	62.8	66.7	60.1	67.3	56.9
Al	11.4	3.4	6.6		0.4		
Si	23.1	19.5	24.3	33.3	0.6		
Fe	0.2	14.4	0.8		38.9	1.9	
Mg	0.2	3.9	0.3		0.1		
Ca	0.1	1.7	0.5				20.4
Mn	0.1	0.2				8.5	0.3
Na	0.6	0.9	2.0				
K	0.2	0.8	2.7				
Ti		0.3					
F							7.9
P							14.5
Nb						12.1	
Ta						10.3	

Conversion Extent of α-Spodumene

Percent weight (wt%, the mass of one phase of the mineral in the sample expressed as a percentage) was investigated to determine the extent of conversion of α-spodumene to both γ and β from 900 to 1000 °C as a function of residence time (7.5 to 480 min). The result is presented in Figure 3.10. It is evident that the transformation increases with temperature and residence time. At 900 °C, conversion of the α-phase was observed after 60 min treatment which is characterized by peaks of γ and β in XRD diffractogram in Figure 3.11a. Almost complete conversion was achieved at 975 and 1000 °C as XRD patterns do not show the presence of the α-phase after 240 and 60 min, respectively (Figure A.10c,d). At 900 °C, transformation increased slightly over time. Only 25% conversion was achieved even after 480 min, 17% of the transformed phase being the β-phase (Figure 3.10). After 480 min the

α-phase was still dominant indicating that the phase transformation is more sensitive to temperature than dwelling time. A sharp increase in conversion is observed by increasing the temperature a little above 900 °C (925 °C). More than 60% transformation was attained after 480 min. Small amount of the transformed phase (17%) is due to the γ-phase and the majority (about 50%) are the β-phase. Peaks of the initially dominant α-phase gradually decreased whilst the β-phase increased with residence time (Figure A.10a), confirming also increasing transformation with time.

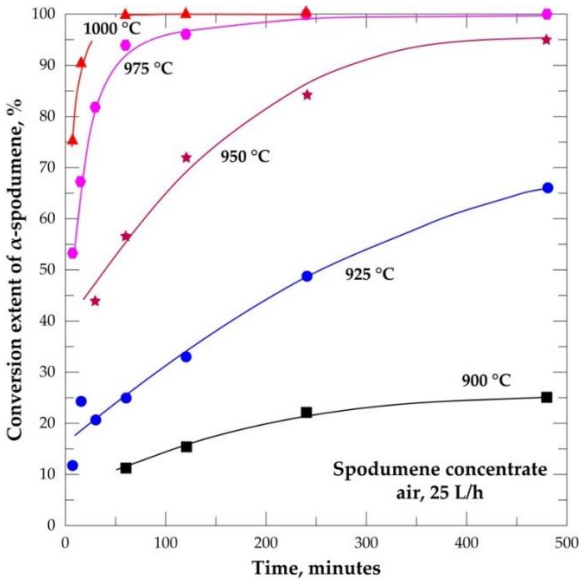

Figure 3.10: Conversion extent of α-spodumene into (β+γ) form during treatment of the concentrate between 900 and 1000 °C as a function of residence time.

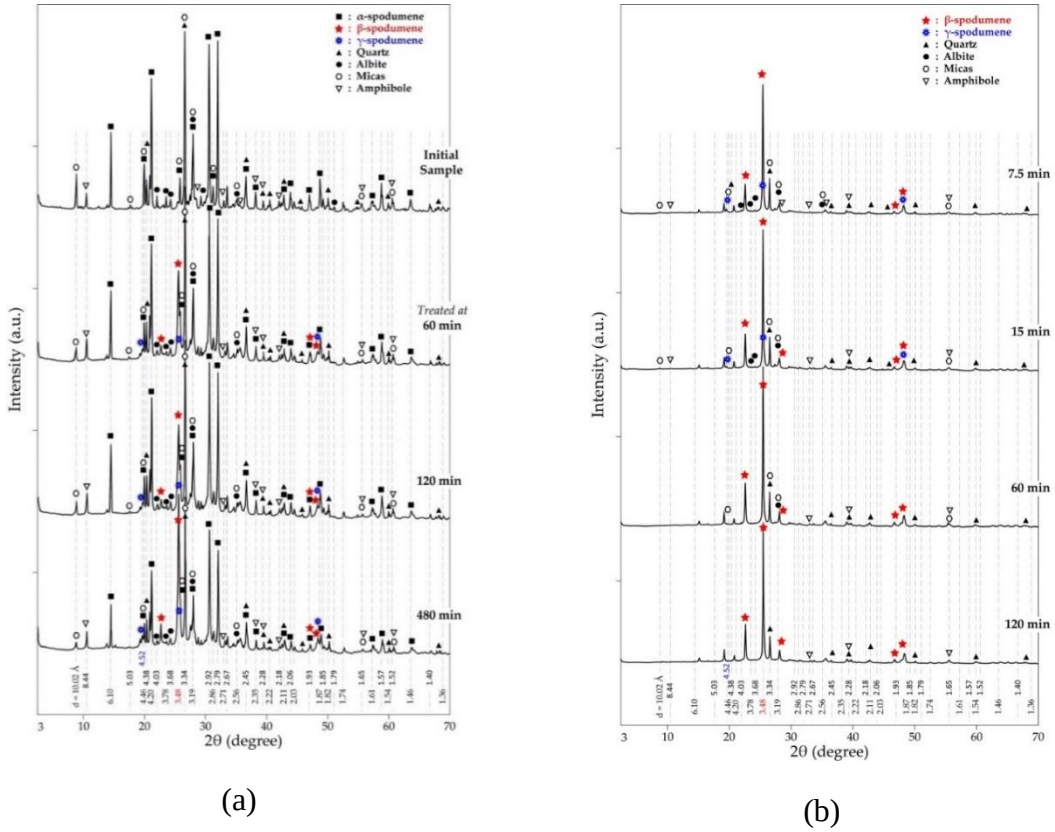

Figure 3.11: XRD patterns of residues obtained after concentrate treatment in air as a function of residence time at 900 °C (a) and 1050 °C (b).

The higher experimental temperature required a shorter residence time for the transformation and vice versa. Further investigations at 1025 and 1050 °C also did not show any significant peaks of α-phase in the XRD pattern (Figure A.10e,f).

Evolution Extent of β-Spodumene

The formation of β-spodumene is favoured by increasing the temperature and residence time (Figure 3.12). The maximum formed at 900 °C is about 17% while almost 100% formation was achieved at 1050 °C after 60 min. Temperature is observed to be the most sensitive parameter for the process and once the threshold temperature is attained, few minutes of heating result in appreciable formation. The temperature of 1050 °C is found as the threshold in this study for treating the concentrate, resulting in almost 100% α-conversion and 85% β-formation in just 7.5 min respectively. This is seen in Figure 3.11b where only γ and β-phases are present in the diffractogram after 7.5 min of treatment. The threshold temperature for the process was also documented elsewhere [5, 6]. Investigations by Peltosari et al. [7] and Salakjani et al. [8] revealed a comparatively higher temperature

(1100 °C) as the threshold for the β-phase formation. We suspect that the difference in temperatures reported in the literature and that presented in this study are due to different gangue concentrations in the samples, the heat treatment process as well the nature of calibration applied to the furnace. Peltosari et al. [7] nor Salakjani et al. [8], however, gave detailed information on these parameters in order to confirm this speculation.

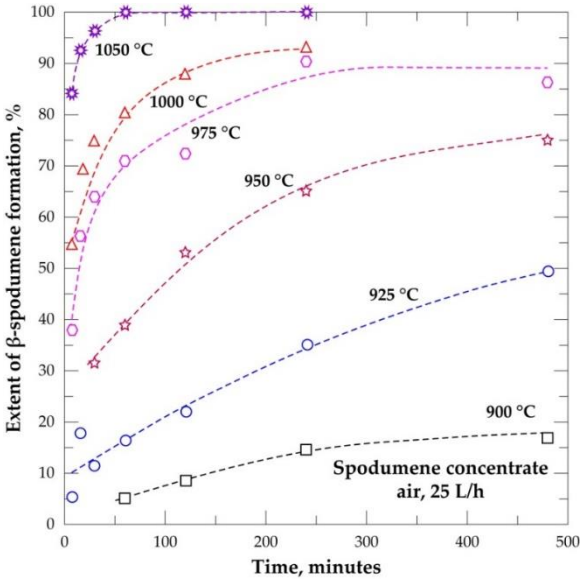

Figure 3.12: β-spodumene formation during treatment of concentrate between 900 and 1050 °C as a function of residence time.

Additionally, there is an influence due to particle size; a higher reaction rate at a lower particle size was observed by Peltosari et al. [7]. The particle size identified in this concentrate is, however, good enough to achieve considerable mineral liberation as well as a β-phase formation at a comparatively lower temperature.

Evolution of the Relative γ-Spodumene

Peaks of metastable γ-phase are seen in XRD diffractogram from the start of the experiment and persist throughout until after 60 min treatment at 1050 °C where it disappears. This phase might be formed at lower temperatures below the minimum temperature of this study as mentioned by Moore et al. [9] and Peltosaari et al. [7] who identified it at 800 and 896 °C respectively. The present observation agrees with what was reported at 915 °C by Abdullah et al. [10]. The peaks are not very intense compared to the other phases due to the continuous conversion into β-form as it is formed. The percent evolution of the γ-phase throughout the operating temperatures as a function of the residence time in this study is shown in Figure A.11. About 23% was the maximum quantity formed

in this study at 975 °C after 120 min (Figure A.11d), which is comparable to the maximum quantity identified by Abdullah et al. [10] at 1125 °C. Likewise, Moore et al. [3] and Peltosaari et al. [7] recorded 35% and 40% as the highest in their studies, respectively. According to Abdullah et al. [10] and Gasalla et al. [11], the quantity of this phase formed is influenced by the particle size of the feed as well as the heat treatment technique employed; finer particles impact amorphicity which easily recrystallises into the γ-phase on heating compared to larger-sized particles. The heating rate employed also influences the quantity formed; slow heating rates form higher amounts due to the slow rate of conversion to the β-form. There was no major change in the quantity of this phase formed as a function of the residence time in the present work. This may be because of the constant heating rate, which was maintained throughout the study, hence converting it to the β-form at the same rate. Though Moore et al. [9] indicated the importance of residence time on the transformation, they observed only a marginal 20% increase in this phase after increasing time from 45 min to 240 min at 981 °C.

It is interesting to note that, the shape of the curves in Figure A.11 may predict the rate of its formation and conversion into the β-phase. There is a gentle rise and fall of the curve at lower residence time which becomes steeper with increasing residence time. This indicates a lower rate of formation and conversion at lower residence time and vice versa.

Effect of Temperature on Phase Composition

Phase composition (wt%) of the polymorphs after 60 minutes treatment was investigated as a function of temperature. From Figure 3.13, both γ- and β-phases evolve from the onset of the experiment, but their composition varies considerably; the quantity of γ-phase being always lower than the β-phase. This observation is contrary to research by Moore et al. [9] who indicated that both phases occur in equal amounts with no preference of formation of one phase over the other. We also found that the quantity of each phase formed is temperature dependent with increasing temperature favouring the quantities evolved, which is also in opposition to their findings. After 975 °C, almost all the α-phase had decayed, and subsequent β-phase formation was solely dependent on the available γ-phase.

Dessemond et al. [12] investigated the effect of γ-phase concomitant with the β-phase and its effect on lithium extraction. They indicated that its presence adversely affects the lithium extraction if its content is above 10%, however, below it, its effect is minimal, and a typical industrial lithium recovery of 95% is attainable. This therefore calls for a closer

look at the ideal temperature and residence time required for the process, paying attention to the economics, possible melting and agglomeration and its effects on downstream processes.

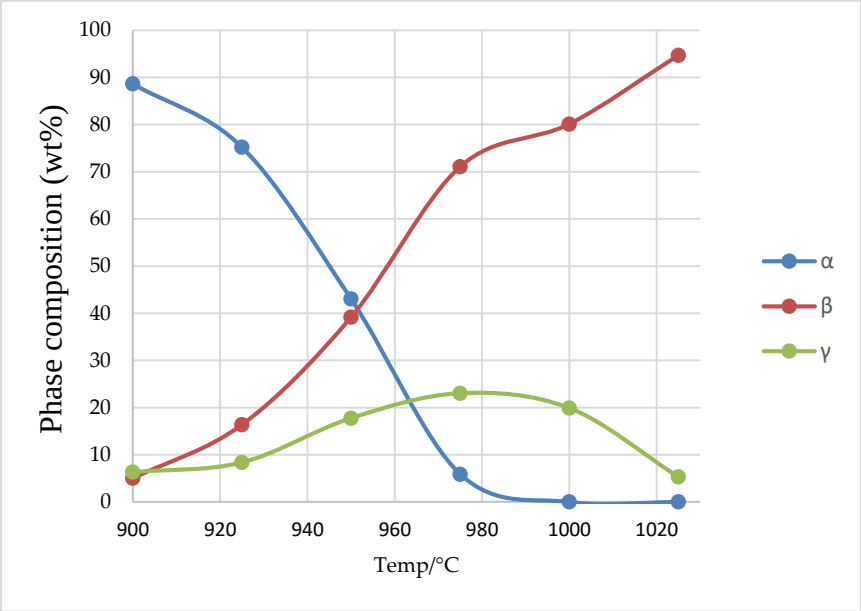

Figure 3.13: Evolution of spodumene polymorph concentration as a function of temperature for 60 minute treatment.

3.4.3 Phase Transformation and Kinetic Parameters

The composition of the polymorphs during decrepitation studies of the concentrate at 925, 950, 975 and 1000 °C as a function of time (30 to 480 minutes) is shown in Figure 3.14. It is observed that, the concentration of α-phase decreases at all temperatures with a corresponding increase of the β. The kinetics of both phase change is favoured at high temperatures than low temperatures such that, after 30 minutes the α-phase decreases in an approximate order 80, 56, 18 and 3%, corresponding to 9, 32, 64 and 75% β-phase formed. Generally, the transformation is observed to be temperature dependent than kinetic.

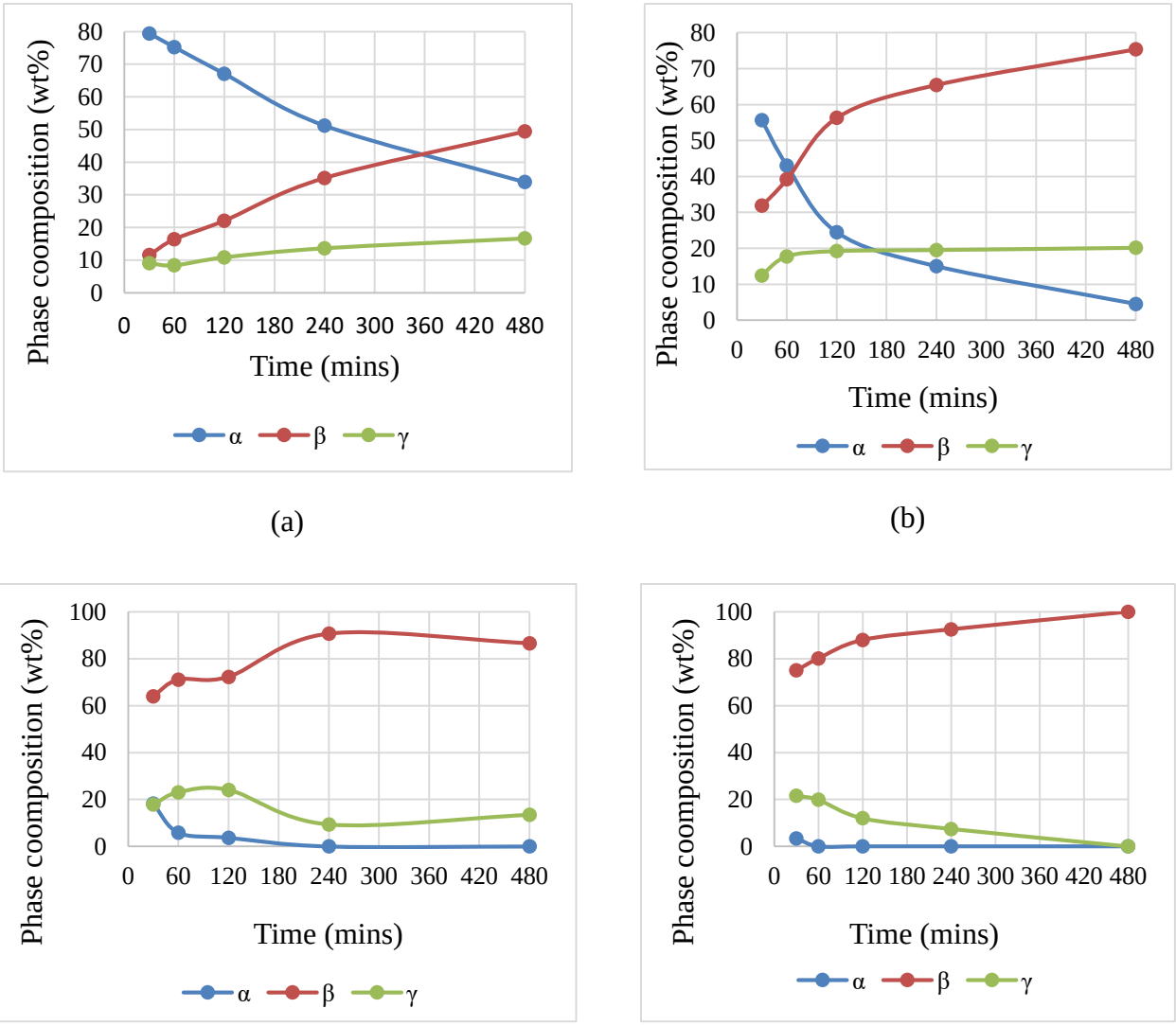

Figure 3.14: Spodumene polymorph concentration at (a) 925, (b) 950, (c) 975 and (d) 1000 °C and varying times.

The phase transformation of spodumene during thermal treatment has been studied extensively by many researchers [7, 9, 10] revealing α, γ and β as the polymorphs which are present during the process. The transition is generally known to follow the following pathways:

$$\alpha \xrightarrow{k_1} \gamma + \beta \qquad (3.1)$$

$$\gamma \xrightarrow{k_2} \beta \qquad (3.2)$$

where k_1 and k_2 are the rate constants for α and γ decay respectively.

Thus, from Equation (3.1), α-spodumene decays to form γ and β phases. The γ-phase formed is metastable and consequently, transforms to the final β-phase (Equation (3.2)). Previous studies suggested a first-order kinetic model for the two transitions. We therefore apply this kinetic theory to both transitions to estimate the fitting kinetic parameters. From an integrated rate Equation of (3.1) it follows that:

$$\ln \%\alpha_t = \ln \%\alpha_o - k_1 t \quad (3.3)$$

where $\%\alpha_t$ is the percentage of α-phase at time t and $\%\alpha_o$ is the initial percentage of α-phase.

The rate constant (k_1) is estimated by plotting data in Table A.21 using Equations (3.3). The fittings of the experimental data and the corresponding regression coefficients (R^2) which enabled the estimation of k_1 in Table 3.6 are shown in Figure A.12 and Table A.23, respectively. The k_1 values are found to increase with increasing temperature, which confirm the sensitivity of the processes to temperature. The activation energy can be obtained from a linearized Arrhenius Equation in (3.4):

$$\ln k = lnA - \frac{E_a}{RT} \quad (3.4)$$

where *k* is the rate constant, *A* is the pre-exponential factor, E_a is the activation energy, *R* represents the gas constant and *T* is the absolute temperature.

The apparent activation energy for the α-decay obtained from the Arrhenius plot in Figure 3.15 using data in Table A.25 is 655±20 kJ mol^{-1}.

Table 3.6: Reaction rate constants k_1 estimated for α-decay.

T (°C)	**k_1 (min^{-1})**
900	0.0004
925	0.0019
950	0.0054
975	0.0224
1000	0.0850

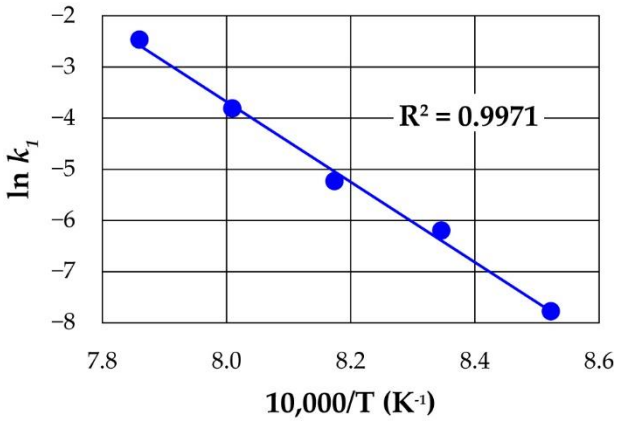

Figure 3.15: Arrhenius plot for the determination of activation energy for α-decay.

For a consecutive first order reaction, it is required that only a single intermediary product forms. This product which is metastable then transforms to the final product. For our study to fit this model (consecutive first order) well, the sequential phase transformation expected is α → γ → β. However, the α-decay was observed to yield two products (some portion being the metastable γ and the remaining portion being the β-phase) before the decay of the γ-portion to the final β-phase (thus, α → γ + β; γ → β). Despite this complication, the model is employed to investigate the γ-decay since a sequential transformation is observed. The rate constant (k_2) for the decay of the intermediary product (in this case γ) using the model can be estimated by the following relationship:

$$\%\,\gamma_t = \%\alpha_o\left(\frac{k_1}{k_2 - k_1}\right)[e^{-tk_1} - e^{-tk_2}] \qquad (3.5)$$

where $\%\gamma_t$ is the percentage of γ-phase at time, t; $\%\alpha_o$, the initial amount of α-phase (in percentage); k_1 and k_2 are the rate constants for α and γ decay, respectively.

Initial concentrations of the α-phase ($\%\alpha_o$) are estimated from Figure A.12 as the intercepts on the y-axis and results are presented in Table 3.7. The k_2 values for 900 to 1000 °C are estimated using the Excel solver by means of Equation (3.5), the k_1, $\%\alpha_o$ and $\%\gamma$ values from Table 3.6, Table 3.7 and Table A.22se, respectively. The values (k_2) obtained were used to calculate %γ-values ($\%\gamma_{calc}$) using the model in Equation (3.5) and then compared with experimental %γ-values ($\%\gamma_{exp}$). The regression coefficient (R^2) and the slope (μ) of the plot of $\%\gamma_{calc}$ vs $\%\gamma_{exp}$ and k_2 values used for the calculation are gathered in Table 3.8.

Table 3.7: Estimated initial concentrations of α-phase ($\%\alpha_o$) from 900 to 1000°C.

T (°C)	ln $\%\alpha_o$	$\%\alpha_o$
900	4.48	88.35
925	4.43	83.54
950	4.04	56.97
975	3.70	40.57
1000	3.73	41.47

Table 3.8: Calculated rate constants, slopes and regressions from 900 to 1000 °C at 60 minutes treatments.

T (°C)	k_2	μ	R^2
900	0.002	0.7317	0.8655
925	0.006	0.8277	0.8978
950	0.017	0.3296	0.6648
975	0.005	0.9421	0.9013
1000	0.015	1.0604	0.9456

A plot of both $\%\gamma_{calc}$ and $\%\gamma_{exp}$ as a function of all the residence time employed in the study were produced and results are presented in Figure 3.16. It is observed that, the model though, not perfect gives a good trend of the experimental data. It gets somehow closer at higher temperatures and residence time, especially, at thermal treatment of 1000 °C.

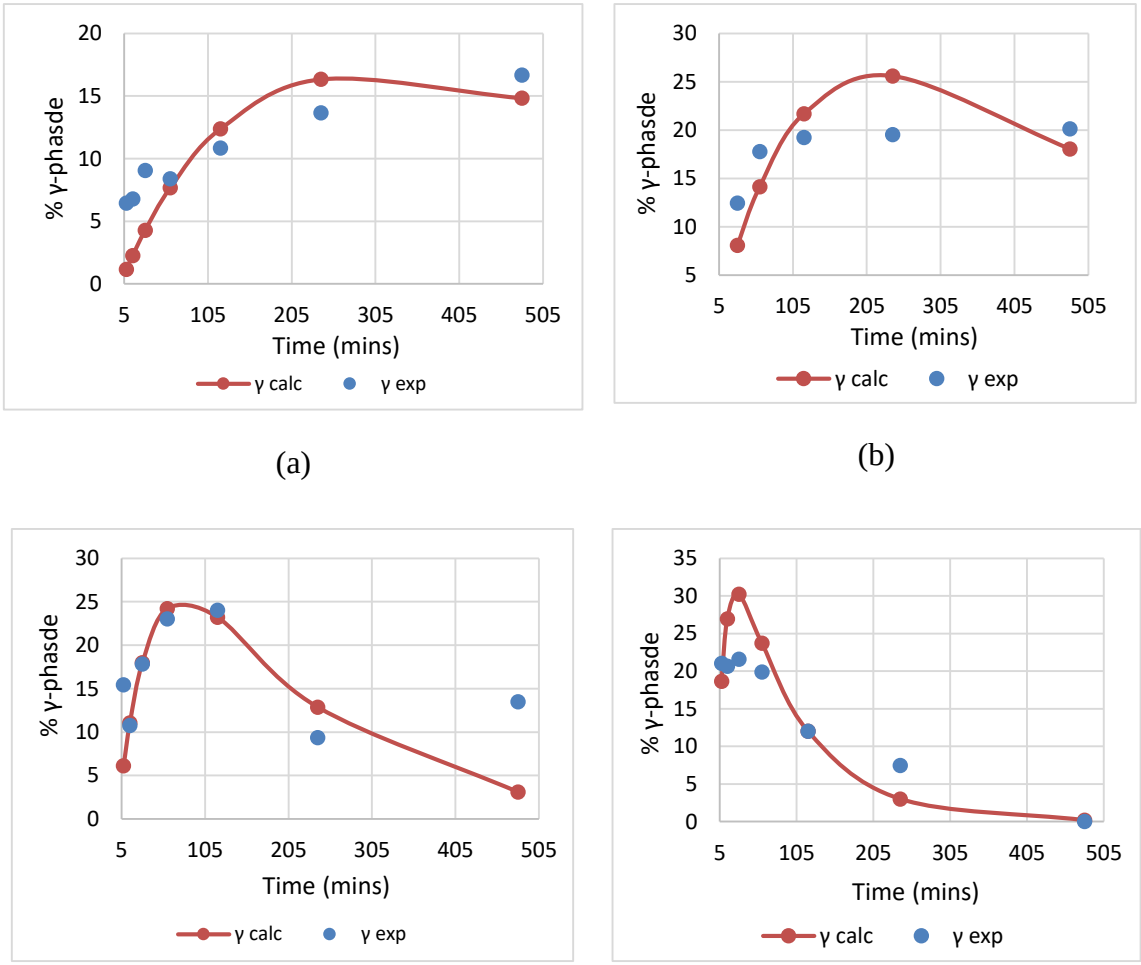

Figure 3.16: Plot of experimental and calculated gamma values at (a) 925, (b) 950, (c) 975 and (d) 1000 °C as a function of residence time.

3.5 Conclusions

The characterisation of spodumene concentrate obtained from Pilgangoora pegmatite revealed the d50 and d80 as 57 and 113 microns, respectively. Particle diameter ranges from 10 to 200 microns with about 68% of the total volume being 80 microns in diameter. At these conditions, spodumene is well liberated at approximately 99%, indicating that sufficient particle size reduction was achieved to enable further processing. Spodumene, mica (muscovite and biotite), feldspars (orthoclase, albite, anorthite), quartz and the amphiboles are the predominant minerals identified. Significant amount of the concentrate (60.21 wt%) were found to be spodumene which contains about 2.14 wt% lithium.

Phase transformation of the sample during thermal treatment from 900 to 1050 °C and 7.5 to 480 min dwelling time indicated that, α-phase transformation can be completed at 975

or 1000 °C depending on the residence time. Full transformation of γ-phase can also occur at 1025 °C and 1050 °C all at different treatment times. About 23% was the maximum quantity of γ-phase formed. We indicate 1050 °C as the threshold temperature for maximum β-phase formation. That notwithstanding, the process must be optimized since previous studies have indicated that the presence of less than 10% γ-phase in the residue does not have a major adverse effect on lithium extraction efficiency. Should this study be valid, then we recommend 1000 °C thermal treatment for 60 min as an ideal decrepitation temperature for this concentrate considering the economics and quantity of γ-phase formed. However, if only a β-phase is required for industrial application, then a choice must be made at 1025 or 1050 °C, paying attention to the time required for the transformation, as well as the melting, which occurs at 1050 °C and its effect on downstream processing. In view of these uncertainties, we recommend further investigation between these temperatures which leads to good lithium extraction efficiency on this material.

Applying a first-order kinetic models to α-decay provides a satisfactory fit to the experimental data and yields kinetic parameters and apparent activation energies of 655±20 kJ mol^{-1}. Application of a consecutive first order kinetic model to the γ-decay also conformed to trends of experimental data though not perfect. SEM investigations reveal that, with increasing intensity of thermal treatments, spodumene grains undergo cracking, disintegration, followed by melting and agglomeration.

REFERENCES

[1] Z. Phelps-Barber, A. Trench, and D. I. Groves, "Recent pegmatite-hosted spodumene discoveries in Western Australia: insights for lithium exploration in Australia and globally," *Applied Earth Science: Transactions of the Institute of Mining and Metallurgy*, vol. 131, no. 2, pp. 100–113, 2022, doi: 10.1080/25726838.2022.2065450.

[2] M.T., Sweetapple, J., Holmes, J., Young, M.W., Grigson, L., Barnes and S., Till, Australian Ore Deposits monograph.

[3] J. S. Holmes and J. L. Grigson, "Pilgangoora Lithium-Tantalum Project: deposit geology and new constraints on rare-metal pegmatite genesis," *Exploration Geophysics*, vol. 2019, no. 1, 2019, doi: 10.1080/22020586.2019.12073052.

[4] M. G. Aylmore, K. Merigot, W. D. A. Rickard, N. J. Evans, B. J. Mcdonald, and P. Spitalny, "Assessment of a spodumene ore by advanced analytical and mass spectrometry

techniques to determine its amenability to processing for the extraction of lithium," pp. 1–21.

[5] Q. Tian, B. Chen, Y. Chen, L. Ma, and X. Shi, "Roasting and leaching behavior of spodumene in sulphuric acid process," *Xiyou Jinshu/Chinese Journal of Rare Metals*, 2011, doi: 10.3969/j.issn.0258-7076.2011.01.022.

[6] G. D. White and T. N. McVay, "Some Aspects of the Recovery of Lithium from Spodumene," Oak Ridge, TN (United States), Apr. 1958. doi: 10.2172/4352576.

[7] O. Peltosaari, P. Tanskanen, E.-P. Heikkinen, and T. Fabritius, "α→γ→β-phase transformation of spodumene with hybrid microwave and conventional furnaces," *Miner Eng*, vol. 82, pp. 54–60, Oct. 2015, doi: 10.1016/j.mineng.2015.04.012.

[8] N. K. Salakjani, P. Singh, and A. N. Nikoloski, "Mineralogical transformations of spodumene concentrate from Greenbushes, Western Australia. Part 1: Conventional heating," *Miner Eng*, vol. 98, pp. 71–79, Nov. 2016, doi: 10.1016/j.mineng.2016.07.018.

[9] R. L. Moore, J. P. Mann, A. Montoya, and B. S. Haynes, "In situ synchrotron XRD analysis of the kinetics of spodumene phase transitions," *Physical Chemistry Chemical Physics*, vol. 20, no. 16, pp. 10753–10761, Apr. 2018, doi: 10.1039/C7CP07754H.

[10] A. A. Abdullah, H. C. Oskierski, M. Altarawneh, G. Senanayake, G. Lumpkin, and B. Z. Dlugogorski, "Phase transformation mechanism of spodumene during its calcination," *Miner Eng*, vol. 140, p. 105883, Aug. 2019, doi: 10.1016/j.mineng.2019.105883.

[11] E. Gasalla, HJ and Aglietti, EF and Lopez, JM Porto and Pereira, "Changes in physicochemical properties of α-spodumene by mechanochemical treatment," *Mater Chem Phys*, vol. 17, no. 4, pp. 379–389, 1987, doi: 10.1016/0254-0584(87)90088-5.

[12] P. Dessemond, Colin and Soucy, Gervais and Harvey, Jean-Philippe and Ouzilleau, "Phase Transitions in the α–γ–β Spodumene Thermodynamic System and Impact of γ-Spodumene on the Efficiency of Lithium Extraction by Acid Leaching," *Minerals*, vol. 10, no. 6, p. 519, 2020, doi: 10.3390/min10060519.

CHAPTER 4: Extraction route for lithium from α-spodumene by dry chlorination

4.1 Introduction

Chlorination is gaining popularity in mineral processing due to the advantages it presents for processing ores, concentrates and end-of-life resources. The merits of this technique for metal extraction stem from the high reactivity and selectivity of chlorine and chlorinating agents to many metals at minimal temperatures. The selectivity of this technique is seen in earlier work [1] where sodium chloride was used to produce appreciably pure lithium chloride (about 91%) before purification of the leach liquor. They revealed that, the simplicity of purification of their liquor (by ion exchange) is due to the high selectivity of chlorinating agents. Also, the resulting products (metal chlorides/oxychlorides) from chlorination processes have considerable difference in boiling point which makes management of impurities and product choices easier. Chlorination agents are readily available at reasonable prices. The waste generated can easily be treated and disposed with little or no environmental impact compared to other approaches [2–4]. For instance, chlorinated waste unlike other metallurgical wastes, may be easily neutralized with alkaline reagents. These factors make chlorination attractive for treating lean minerals and secondary materials as well as providing new pathways for some refractory ores that do not respond well to conventional approaches. Metal chlorides, Cl_2 and HCl have been used to treat ore types (silicates, oxides and sulphides) for subsequent processing according to Equations (4.1)-(4.7):

$$M_2''SiO_3 + M'Cl_2 \rightarrow 2M''Cl + M'SiO_3 \quad (4.1)$$

$$M_2''S + M'Cl_2 \rightarrow 2M''Cl + M'S \quad (4.2)$$

$$M_2''O + M'Cl_2 \rightarrow 2M''Cl + M'O \quad (4.3)$$

$$M_2''O + Cl_2 \rightarrow 2M''Cl + ½O_2 \quad (4.4)$$

$$M_2''S + Cl_2 \rightarrow 2M''Cl + S \quad (4.5)$$

$$M_2''O + 2HCl \rightarrow 2M''Cl + H_2O \quad (4.6)$$

$$M_2''S + 2HCl \rightarrow 2M''Cl + H_2S \quad (4.7)$$

Where M′ is a chlorine bearing metal used as chlorinating agent and M″ is a monovalent metal of interest present in the ore.

Chlorination sometimes requires a reducing environment to enhance the process. Due to this, carbochlorination of metal oxides and silicates have been investigated by some researchers [5, 6] where the carbon or carbonaceous material acts as reducing agent to enable or enhance reactions.

4.1.1 Selection of chlorination agent(s)

Thermodynamic calculations with HSC Chemistry® 5.1 was used as a guide to select chlorination agents. Gibbs free energy changes for some chlorination and carbochlorination reactions with α-phase spodumene (Equation (4.8)-(4.17)) is shown in Figure 4.1. After 800 °C, Cl_2 feasibly reacts with spodumene to form LiCl (Equation 4.14). This reaction is said to be enhanced in a reducing environment. Investigating this assertion in Equation (4.15) and (4.16) using C and CO respectively as reducing agents seems to be true. These reactions have stronger thermodynamic driving force (Figure 4.1) than by using Cl_2 alone. Except for NaCl, all chloride salts studied had a feasible reaction with the mineral. However, not all can practically be used for the study. The thermal stability of a salt as a function of temperature is another factor that was considered for the selection. It is ideal that the chosen salt has high stability temperature range before it volatilises and/or decomposes. Decrepitation studies in Chapter 2 revealed that, the mineral's crystal structure opens fully around 1000 °C which indicates that, any salt selected must remain in the liquid phase around or a little above this temperature. This will enable appreciable penetration of the molten salt through the bulk sample and enhance extraction. $AlCl_3$, NH_4Cl and $FeCl_3$ have feasible reactions with the mineral (Equation (4.11)-(4.13)) but NH_4Cl decomposes around 530 °C whilst $AlCl_3$ and $FeCl_3$ volatilise around 180 and 305°C respectively. Thus, these salts will escape from the system before a possible reaction with the mineral begins. They cannot, therefore, be good candidates for the study. $MgCl_2$, $CaCl_2$ and NaCl meet this requirement, however, NaCl does not exhibit a spontaneous reaction with spodumene (Equation 4.17) according to thermodynamic predictions. $MgCl_2$ and $CaCl_2$ were selected as salts for further investigation, however, as it was obvious that reaction with $CaCl_2$ is feasible, that of $MgCl_2$ depends on the products formed. It is feasible if cordielite ($Mg_2Al_4Si_5O_{18}$) is the product (Equation 4.8) but not feasible if sapphirine ($Mg_2Al_4SiO_{10}$) is formed (Equation 4.9).

$2LiAlSi_2O_6 + MgCl_2 = 2LiCl + 1.5SiO_2 + 0.5Mg_2Al_4Si_5O_{18}$ (4.8)

$2LiAlSi_2O_6 + MgCl_2 = 2LiCl + 3.5SiO_2 + 0.5Mg_2Al_4SiO_{10}$ (4.9)

$2LiAlSi_2O_6 + CaCl_2 = 2LiCl + 2SiO_2 + CaAl_2Si_2O_8$ (4.10)

$3LiAlSi_2O_6 + AlCl_3 = 3LiCl + 2Al_2O_3 + 6SiO_2$ (4.11)

$LiAlSi_2O_6 + NH_4Cl = LiCl + 0.5Al_2O_3 + 2SiO_2 + NH_3(g) + 0.5H_2O(g)$ (4.12)

$3LiAlSi_2O_6 + FeCl_3 = 3LiCl + 1.5Al_2O_3 + 6SiO_2 + 0.5Fe_2O_3$ (4.13)

$2LiAlSi_2O_6 + Cl_2(g) = 2LiCl + Al_2O_3 + 4SiO_2 + 0.5O_2(g)$ (4.14)

$2LiAlSi_2O_6 + Cl_2(g) + 0.5C = 2LiCl + Al_2O_3 + 4SiO_2 + 0.5CO_2(g)$ (4.15)

$2LiAlSi_2O_6 + Cl_2(g) + CO(g) = 2LiCl + Al_2O_3 + 4SiO_2 + CO_2(g)$ (4.16)

$LiAlSi_2O_6 + NaCl = LiCl + SiO_2 + NaAlSiO_4$ (4.17)

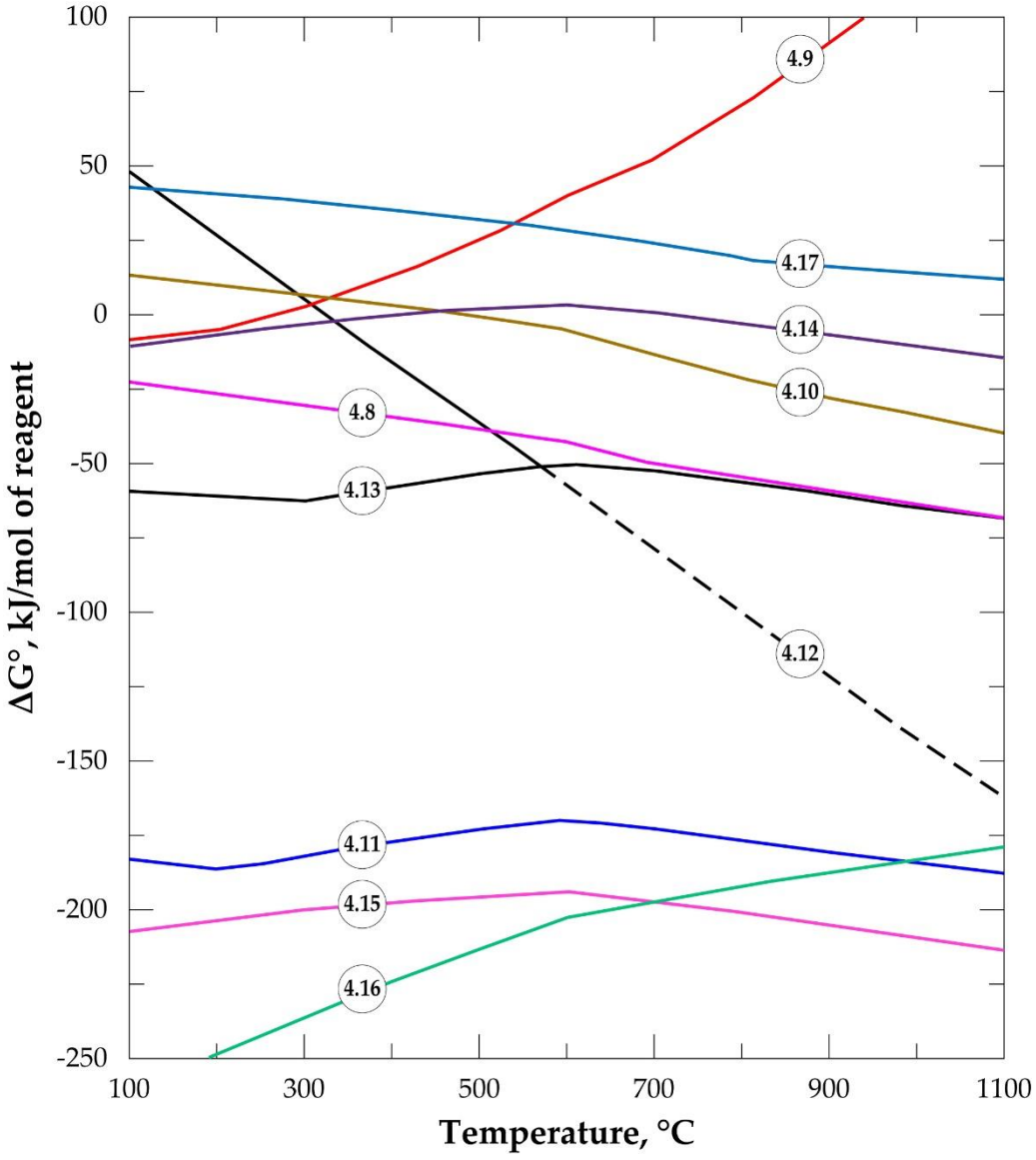

Figure 4.1: The ΔG° of α-spodumene reactions with various chlorinating reagents (Eqs (4.8)-(4.17)) as a function of the temperature (dashed line: extrapolation of data).

Preliminary investigations were conducted with both $CaCl_2$ and $MgCl_2$ and it revealed that, whilst $CaCl_2$ could extract some lithium and recovered to leach solution, $MgCl_2$ did not. This suggests that reaction path in Equation (4.9) is followed by $MgCl_2$ and sapphirine may be the product.

Further studies were conducted by directly baking α-spodumene using $CaCl_2$ to recover lithium.

4.1.2 Thermochemical behavior of α and β-spodumene chlorination

All thermodynamic studies in literature on the roasting of spodumene with reagents are performed with the β-phase. In this section, α to β-phase transformation of the mineral, followed by a comparative study of thermodynamic behaviour of both phases with $CaCl_2$ using HSC Software is considered. The suggested phase transformation and chemical equations of the mineral in both phases with $CaCl_2$ are given as:

$$\alpha\text{-}LiAlSi_2O_6 \rightarrow \beta\text{-}LiAlSi_2O_6 \quad (4.18)$$

$$2\alpha\text{-}LiAlSi_2O_6 + CaCl_2 \rightarrow 2LiCl + 2SiO_2 + CaAl_2Si_2O_8 \quad (4.19)$$

$$2\beta\text{-}LiAlSi_2O_6 + CaCl_2 \rightarrow 2LiCl + 2SiO_2 + CaAl_2Si_2O_8 \quad (4.20)$$

In Fig. 4.2, the Gibbs free energy change of the transformation and the reaction of both polymorphs of spodumene with $CaCl_2$ (Equation (4.18)–(4.20)) as a function of temperature up to 1100 °C are plotted. It can be observed that, the phase transformation is feasible after 750 °C but after 927 °C (indicated by short dashes), the software relies on extrapolated data for the α-phase. This may be attributed to two reasons: either the software does not have data for the transformation beyond 927 °C or the transformation was complete.

Roasting the mineral in the β-phase with $CaCl_2$ is spontaneous throughout the temperatures studied whilst the direct roasting of α-phase is only feasible beyond 500 °C. Thus, the prior decrepitation of the mineral makes it feasible with $CaCl_2$ during chlorination roasting in a wider range of temperatures. From the above scenarios, one can infer that, production of LiCl below 750 °C occurs strictly and directly from the α-phase (Equation (4.19)). Above this temperature, however, the phase transformation begins (according to thermodynamic predictions) and a mixture of both polymorphs may exist. LiCl can thus be

obtained from both phases (Equations (4.19) and (4.20)) which should lead to higher lithium recovery.

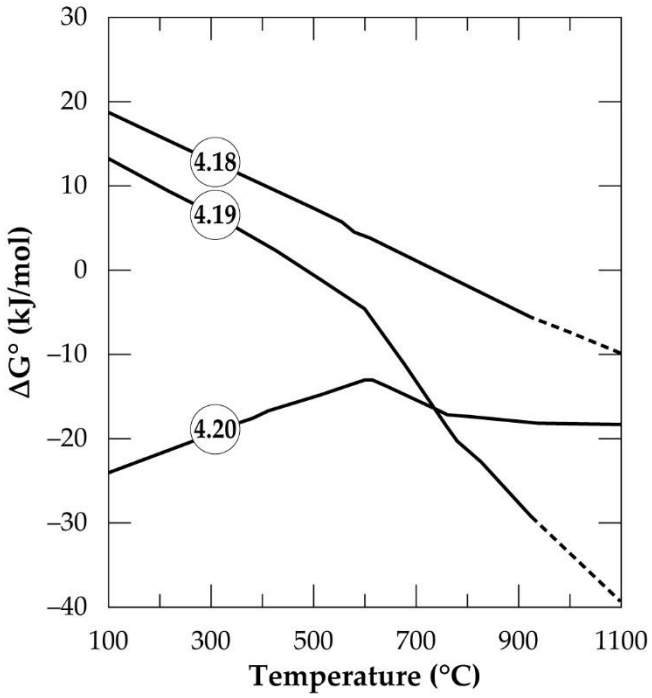

Figure 4.2: Standard Gibbs free energy changes as a function of temperature for α to β transformation (Eq (4.18)), reaction of spodumene with $CaCl_2$ in α-phase (Eq (4.19)) and β-phase (Eq (4.20)) (data from HSC Chemistry® 5.1).

A transition point is observed between 600 and 800 °C for both α- and β-phase chlorination (Figure 4.2). This range of temperature is named "reaction initiation zone" in this study where melting of $CaCl_2$ and reaction with the mineral begin.

A differential thermal analysis by both Barbosa et al. [7] and Dang et al. [8] revealed interesting results in this temperature range during their study on spodumene and simulated slag respectively with $CaCl_2$. They both observed two endothermic peaks within this range where the low and high temperature peaks were linked to the commencement of reaction and the melting of $CaCl_2$ respectively. Chemical thermodynamic predictions have a downside of inability to give insight into the kinetics of processes. One may however, suspect that since the change in the Gibbs free energy remains almost constant for the β-phase after 800 °C (Figure 4.2), it may be more kinetically dependant than thermodynamic. For the α-phase, chlorination may be both thermodynamic and kinetic controlled since the Gibb's free energy change decreases significantly with increasing temperature which confirms a strong dependence of α-phase chlorination on the thermodynamics.

The equilibrium composition module of the software was further used to simulate the process. Figure 4.3 is the simulation showing the equilibrium composition at varying temperatures. Lithium chloride (LiCl), wollastonite ($CaSiO_3$) and anorthite ($CaAl_2Si_2O_8$) are new phases synthesized at the end of the process with the latter being predominant. All the new phases can be said to be obtained from the decomposition of spodumene since their synthesis have a corresponding decrease in the quantity of spodumene.

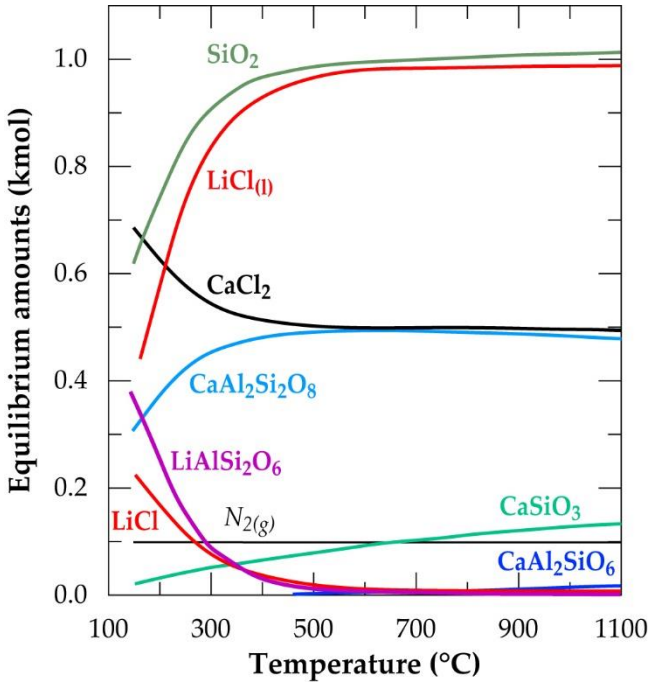

Figure 4.3: Equilibrium amounts as a function of temperature for chlorination of α-spodumene using $CaCl_2$ (data from HSC Chemistry®5.1).

4.2 Materials and methods

4.2.1 Spodumene concentrate sample

Spodumene concentrate sample produced and characterised in Chapter 3 was used for the study. Analytical grade $CaCl_2$ supplied by Sigma-Aldrich, France was used as chlorination agent.

4.2.2 Chlorination and leaching experiments

Direct chlorination of α-spodumene was performed using a mixture of 5 g of the dry uncalcined spodumene concentrate and anhydrous $CaCl_2$. Alumina crucible was used as the reaction vessel while heating in a Carbolite Gero electric furnace which was conditioned as

discussed in Chapter 3. Chlorinated samples were cooled to room temperature in a desiccator and weighed before leaching tests.

Leaching was carried out with deionized water at ambient temperature, solid/liquid ratio of 50 g/L and agitated using a Gerhardt laboratory thermoshake. The solid and liquid phases were separated with a 3–16 L Sigma Laboratory Centrifuge operating at 3000 rpm for 2 minutes. Leached residues were washed thoroughly with distilled water and dried at room temperature for further analysis. The leached liquor obtained was analysed for lithium and other metals using the Microwave Plasma Atomic Emission Spectrophotometer (4210 MP-AES) manufactured by Agilent Technologies. Percent lithium recovery (%Li) was calculated using Equation 4.21:

$$\%Li = \frac{\boldsymbol{Amount\ of\ lithium\ recovered\ in\ solution}}{\boldsymbol{Amount\ of\ lithium\ in\ concentrate}} * \mathbf{100} \quad (4.21)$$

Extraction efficiencies achieved was obtained by residual lithium determination, followed by mass balance calculation. Probing into the reaction mechanism, the leached residues were analysed for their physicochemical alterations using SEM-EDS. Methods of sample preparation for XRD and SEM-EDS were as in Chapter 2.

4.3 Results and discussion

4.3.1 Chlorination of α-spodumene

Effect of $CaCl_2$/spodumene molar ratio

The effect of $CaCl_2$/spodumene molar ratio (MR) on lithium recovery was studied in the range of 1.0 to 2.25, at 900 °C for 60 minutes residence time; the results are presented in Figure 4.4. Lithium recovery increases with increasing molar ratio until it remains nearly constant after MR=2.0. Previous studies [8–10] have reported a decreased recovery for gaseous chlorination agents after the optimum flow rate is achieved with several explanations proposed by Bidaye et al. [10] for the observation. MR of 2.0 was selected as the optimum for further investigation since there was no significant increase in the amount of lithium recovered after that.

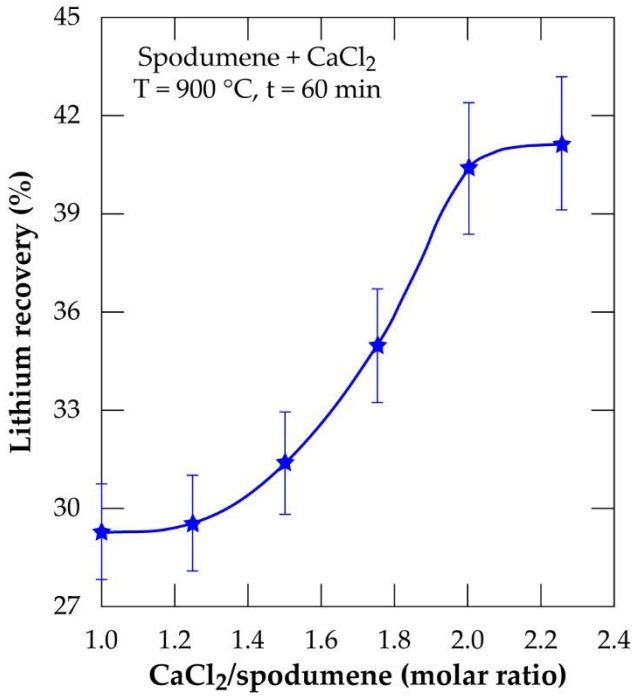

Figure 4.4: Percent lithium recovery obtained as a function of $CaCl_2$/spodumene molar ratio for samples treated at 900 °C for 60 minutes.

Effect of temperature

Chlorination was performed at 60 minutes residence time and MR of 2.0 in order to optimize the temperature. During the simulation using the equilibrium composition module of HSC Software (Figure 4.3), it was found that lithium chloride in the liquid phase attains a maximum concentration after 600 °C. Based on this, temperatures ranging from 700 to 1050 C at 50 °C intervals were selected for the chlorination and results are presented in Figure 4.5a. Recovery increases with increasing temperature until it peaks at 1000 °C. From 700 to 800 °C which falls within the initiation zone of the process, the lowest quantity of LiCl (about 17%) is produced. This is expected since $CaCl_2$ (with melting point around 770 °C) starts melting to initiate reaction with spodumene to yield products. The range of this temperature, however, may not be sufficient to provide appropriate conditions for appreciable extraction and recovery. After 800 °C, a sharp increase in recovery is observed until 1000 °C. It has established previously that, spodumene when heated gains minor cracks which become prominent with increasing temperature until it disintegrates. 1000 °C was indicated as the temperature where sufficient disintegration is attainable but above it, melting and agglomeration occur. Thus, increasing temperature has a remarkable effect on the opening of the mineral for more lithium atoms to interact with molten $CaCl_2$.

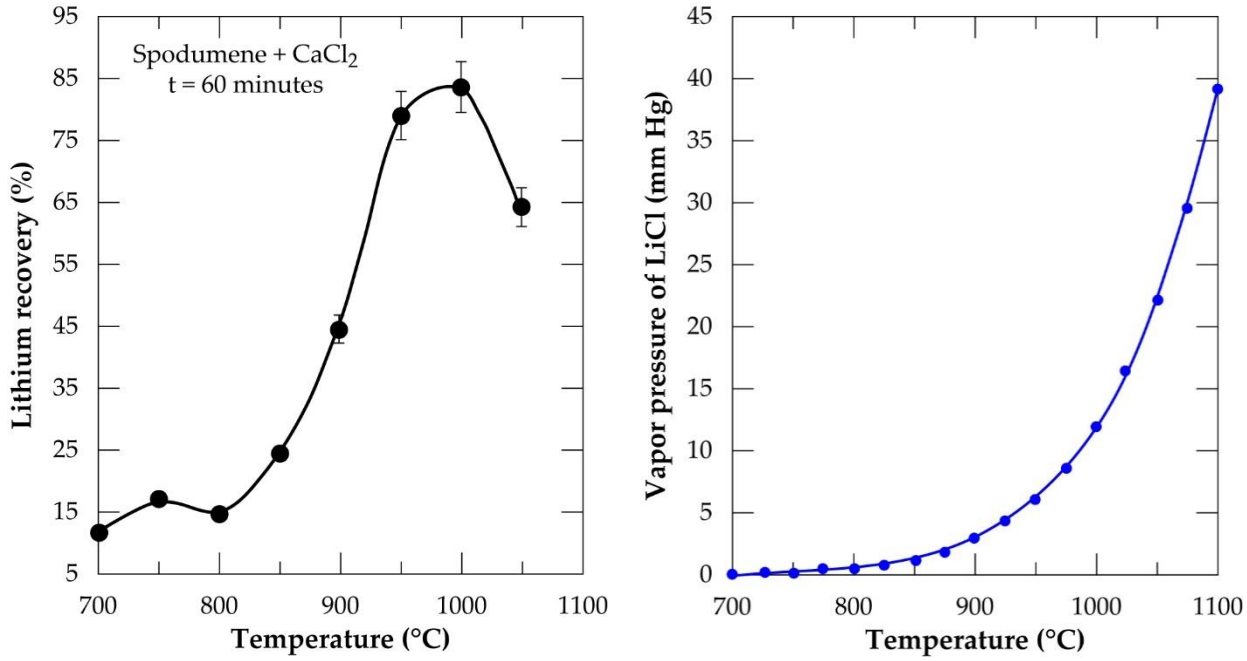

(**a**) (**b**)

Figure 4.5: (a) Percent lithium recovery versus temperature at $CaCl_2$/spodumene molar ratio of 2.0- and 60-min residence time; (b) vapor pressure of lithium chloride versus temperature (data from HSC Chemistry 5.1®).

This leads to the production of more LiCl until it peaks at 1000 °C. After 1000 °C (1050 °C), a decline in recovery is observed. This may be attributed to two factors, either melting and agglomeration of spodumene with impurities or the evaporation of LiCl from the reaction medium as it is formed. It is possible also that, both mechanisms all contribute to the decline. A mass balance was performed on the leached residues to compare lithium recovery achieved and extraction efficiency and also, to investigate the factor(s) responsible for the decline in recovery. These results are presented in Table 4.1. Residual lithium in residues is observed to decrease with increasing temperature with a corresponding increase in both recovery and extraction efficiency up to 1000 °C. Beyond 1000 °C, there is an increase in residual lithium. This may be attributed to melting and agglomeration which locks up some lithium atoms within the agglomerated matter, hence, preventing their access by $CaCl_2$ for subsequent extraction. Recovery and extraction efficiency are comparable up to 1000 °C after which about 20% higher extraction was observed than recovery (Table 4.1). The difference may be linked to the evaporation of LiCl as well as melting and agglomeration of materials suspected earlier.

Table 4.1: Mass balance comparison of percent lithium recovery and extraction at different temperatures.

Temperature (°C)	Residual lithium (wt%)	Recovery (%)	Extraction (%)
900	1.15	45.3	46.3
950	0.50	79.1	76.6
1000	0.23	83.5	89.3
1050	0.32	64.3	85.1

A previous study [11] confirmed formation and/or evaporation of lithium chloride at 1000 °C and above. They suggested the effect of vapour pressure evolution with temperature as a possible cause of the observation. A plot of changing vapour pressure of LiCl with temperature is shown in Figure 4.5b. It increases sharply above 950 °C, where lithium chloride can volatilise and be entrained in the off-gas. We suspect also, the possible formation of $CaCl_2$/LiCl, KCl/LiCl or $CaCl_2$/LiCl/KCl eutectic mixtures, which can result in the evaporation of LiCl at relatively low temperature. It can therefore be inferred that, both phenomena (melting and agglomeration and LiCl evaporation) play a role in the decline of lithium recovery.

The Arrhenius diagram for the chlorination process from 800 to 950 °C resulted in an apparent activation energy of 122±6 kJ mol^{-1} (Figure 4.6).

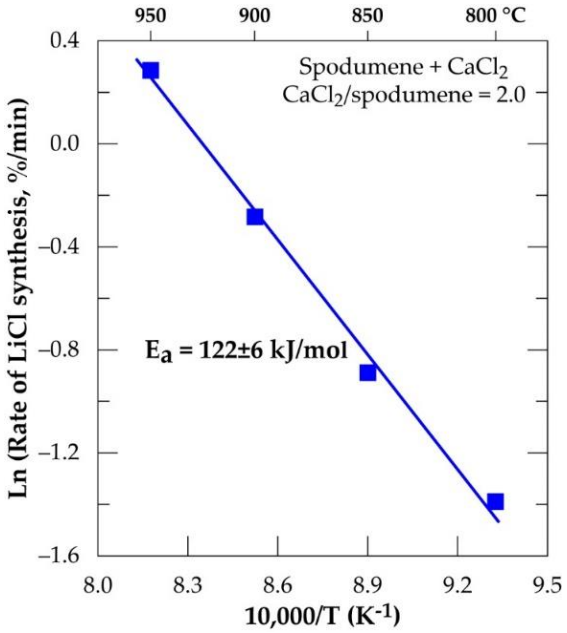

Figure 4.6: Arrhenius diagram for lithium recovery during chlorination of spodumene concentrate between 800 and 950°C, residence time = 60 minutes, $CaCl_2$/spodumene = 2.0.

SEM-EDS investigation

To confirm the supposed phenomena, SEM-EDS analysis was performed on leached residues and results are presented in Figure 4.7. Though the evaporation effect could not be established by this approach, a clear melting and agglomeration which could hinder lithium extraction is observed in Figure 4.7F (treatment at 1050 °C) but it did not occur at lower temperatures. It is also clear that, $CaCl_2$ selectively attacks spodumene grains at the peripheries at lower temperatures, decolorizing its dark colour to several shades of grey. Thus, after decolorizing the exterior portions of spodumene grains, it gradually attacks the internal parts by forming channels through them at increasing temperature. Details of spodumene grain remains in leached residue in Figure 4.7A–F (treatment at 750, 800, 850, 950, 1000, and 1050 °C respectively) are shown in Figure 4.8A1–F1, respectively.

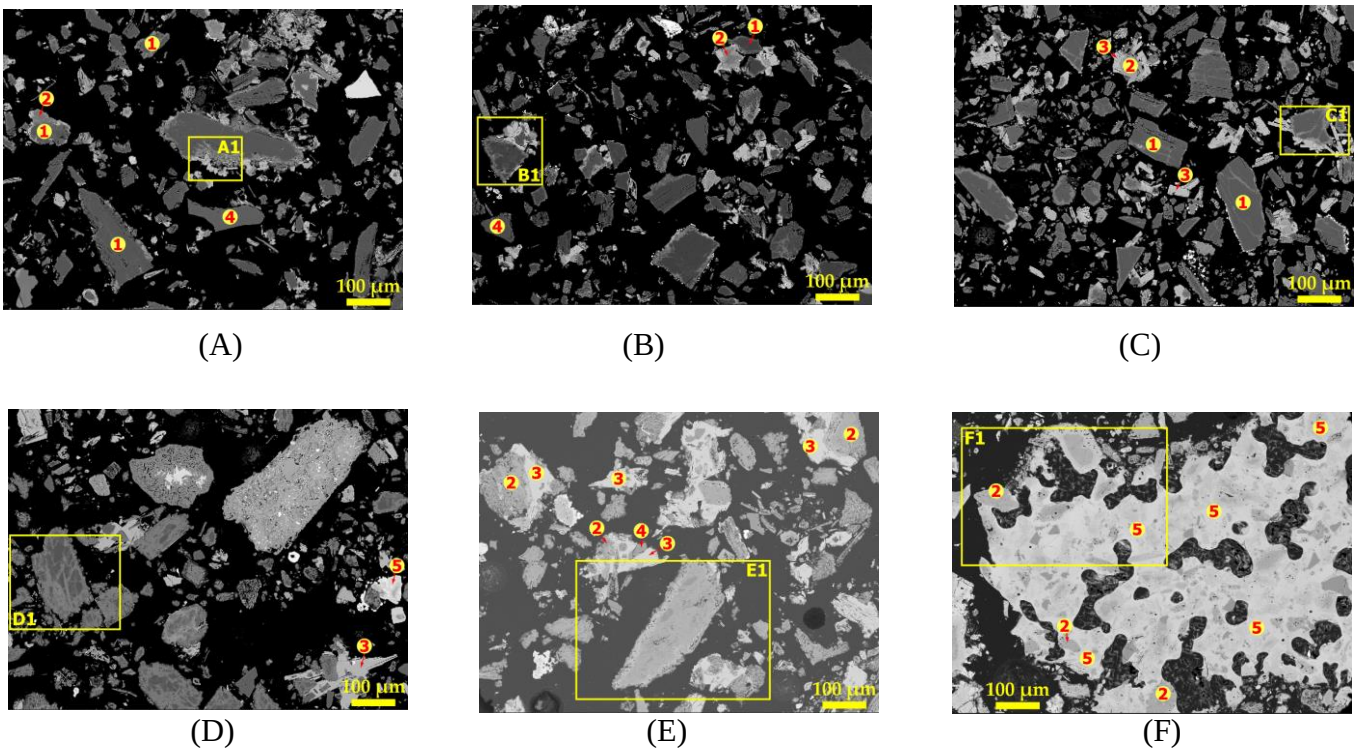

(A) (B) (C)

(D) (E) (F)

Figure 4.7: SEM photomicrographs showing morphological changes of spodumene during 60 min and MR = 1.75 treatment at (A) 750 °C**, (B) 800** °C**, (C) 850** °C**, (D) 950** °C**, (E) 1000** °C**, (F) 1050** °C.

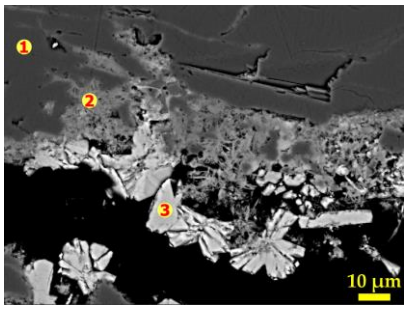

(A1)

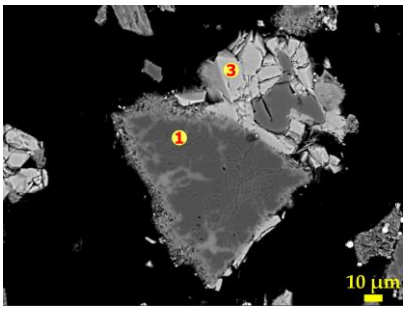

(B1)

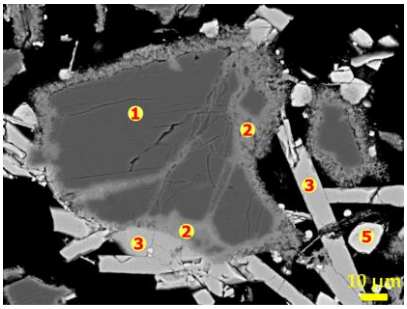

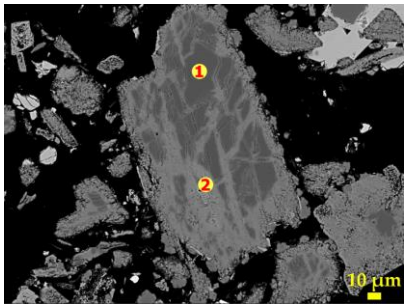

(D1)

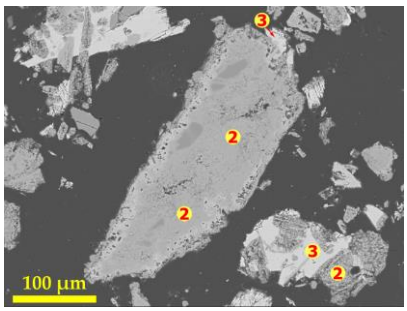

(E1)

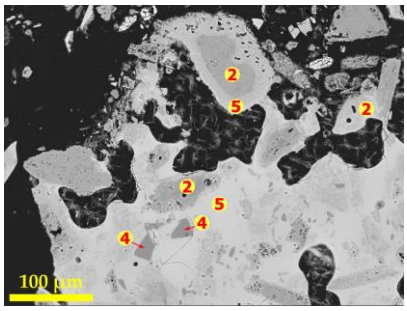

(F1)

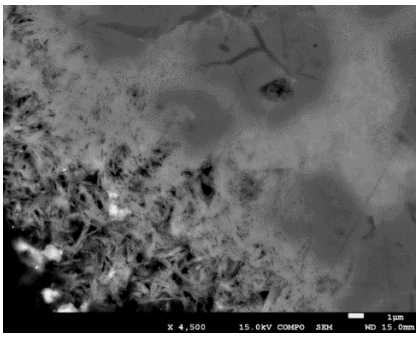

(G)

Figure 4.8: Spot magnification in A (A1), B (B1), C (C1), D (D1), E (E1) and F (F1) of Fig. 4.7; (G) fibrous-like structures appearing at the peripheries of spodumene grains during treatment.

Increasing temperature is observed to create more channels in spodumene grains, leading to increased reaction area and recovery. Thus, the recovery or extraction appears to depend on the degree of access of the molten $CaCl_2$ to the spodumene grains. It can then be supposed that the process is diffusion controlled rather than chemical reaction controlled. The different colorations due to the chlorination of spodumene were assigned "1", "2" and "3" and identified as spodumene, calcium aluminosilicate (CAS) and calcium silicate, respectively. A representative composition of the different portions is shown in Table 4.2. The internal portions of spodumene grain ("1"), which were unaffected by $CaCl_2$, still maintained their identity. It is an aluminosilicate with the atomic ratio Si/Al = 2.0 which

confirms its identity. The total wt% of this portion is approximately 94 and the difference may be attributed to lithium which could not be identified by EDS. Iron, the usual impurity associated with it, is also identified at relatively low concentrations.

Table 4.2: Elemental composition (EDS data) of sections of spodumene grain during chlorination.

Elements	Spot "1"		Spot "2"		Spot "3"		Spot "4"		Spot "5"	
	[1]wt%	[1]at%	wt%	at%	wt%	at%	wt%	at%	[1]wt%	at%
Al	14.38	11.53	16.68	13.39					6.33	5.60
Si	30.50	23.48	22.02	16.97	24.29	19.83	48.27	33.33	13.52	11.50
Cl			0.39	0.24					14.57	9.82
Ca			13.22	7.14	35.41	20.25			29.65	17.68
Fe	0.77	0.30	0.74	0.29					1.76	0.75
Na			0.26	0.25						
Mg									2.25	2.21
O	47.87	64.70	45.61	61.72	41.81	59.92	54.99	66.67	35.10	52.43
Total	93.52		98.92		101.5		103.3		103.2	

[1] wt% and at% represent mass and atomic percentage, respectively.

The next portion from the unaffected spodumene ("2") is dark grey area and identified as CAS. There is varying concentration of the constituent elements of this portion which suggests that different minerals of CAS may be present. The portion "3", which is light grey coloured (the external part of the spodumene), was revealed as calcium silicate ($CaSiO_3$) with approximate Ca/Si and O/Si of 1.0 and 3.0, respectively. Quartz, which forms a significant portion of the concentrate, is identified at several portions of the SEM photo as "4" with O/Si = 2.0. EDS again identified a type of CAS containing a significant amount of chlorine. Magnesium and iron are found in close association with these portions which makes it light coloured or whitish compared to all the other portions identified. We indicate this portion as "5" and call it "calcium aluminosilicate chloride" (CASCl) for the sake of this study. In Figure 4.7F and 4.8F1 where melting and agglomeration was observed, quartz, CAS and CASCl were found fused in the agglomerated mater which confirms melting that occurred. EDS could, however, not identify the specific type of mineral giving rise to these observations. The standard deviations of atomic percent of the different portions identified and the raw data including the spectra generated by SEM-EDS is given in Table B.1–B.10 and Fig. B.1–B.5 of the Appendix. A closer look at the edges of spodumene grains in Figure 4.8G reveals the formation of fibrous-like structures, which gradually eats into the internal parts suggesting again, an initial attack of $CaCl_2$ at the peripheries of the mineral before the interior portions.

XRD investigation

In addition to the SEM approach, different leached residues obtained after chlorination at 60 minutes residence time and MR of 2.0 were studied by XRD (Figure 4.9). The α-spodumene is observed up to 950 °C but at 1000 °C and beyond, it disappeared. Treatment at 800 °C shows chemical composition of plagioclases which became dominant towards the calcium pole with increasing temperature. Plagioclases corresponds to the CAS identified by SEM-EDS. From 900 °C only anorthite is identified (Figure 4.9), moreover, its concentration increases with temperature, reaching about 70% in the end at 1050 °C (Figure 4.10). Diopside ($CaMgSi_2O_6$) appears at 800 °C and persists throughout the treatments. Wollastonite ($CaSiO_3$) appears from 900 °C and like diopside, can be identified until the end of the treatment. Wollastonite is linked to the calcium silicate identified by EDS. Wadalite [$Ca_6(Al,Fe,Mg)_5Si_2O_{16}Cl_3$] was also identified by XRD but due to its comparatively small concentration and for clarity of presentation, it was not considered in the XRD diagram. In Figure 4.10, its concentration (< 4%) is observed. It corresponds to CASCl which was identified by EDS. A thermal influence can therefore be observed on the mineralogical assemblages. Spodumene persists up to 1000 °C and its concentration shows a continuous decrease with increasing temperature. As the temperature rises, the spodumene breaks down to interact with the molten calcium chloride. The decrease in spodumene is also related to anorthite formation (Figure 4.10) and obviously to the lithium recovery (Figure 4.5a). It is worth noting that, only the α-form of spodumene was identified in the residue. Two pathways may therefore be possible for the extraction: (1) directly from the α-phase or (2) an initial α- to β-phase conversion followed by a quick in situ lithium chloride formation due to the presence of calcium chloride (2α-spodumene → 2β-$LiAlSi_2O_6$ + $CaCl_2$ → 2LiCl + $2SiO_2$ + $CaAl_2Si_2O_8$).

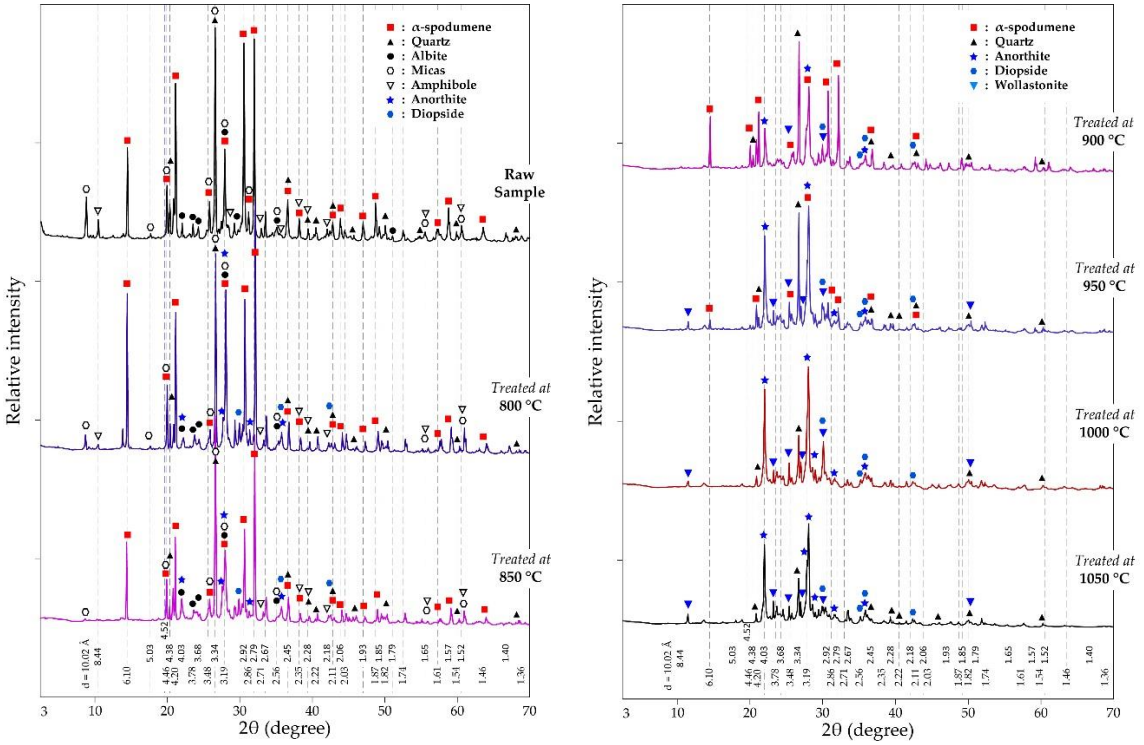

Figure 4.9: XRD pattern of evolving phases as a function of temperature at 60 minutes treatment and MR = 2.0.

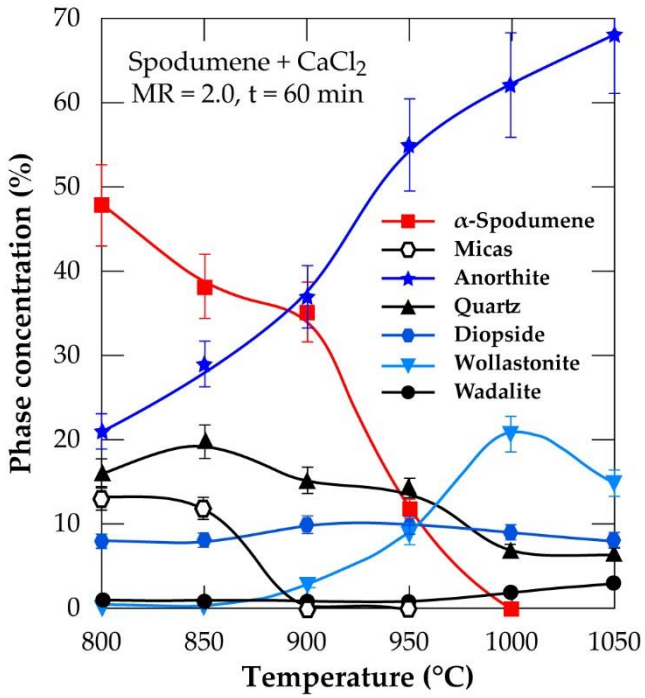

Figure 4.10: XRD semi-quantification of phases at varying temperatures for 60 minutes treatment and MR = 2.0.

Effect of residence time

To investigate the process further, chlorination was performed at MR of 2.0, 1000 °C temperature and residence time from 30 to 120 minutes. The result is presented in Figure 4.11. Recovery increases sharply from 30 minutes and peaks around 60 minutes, achieving about 85% recovery. A decline is observed afterwards such that, at 120 minutes, about 5% lithium chloride had volatilised and entrained within the off-gas leading to a decline in recovery. Both temperature and time thus, contributed to lithium extraction in this study though temperature effect is more profound.

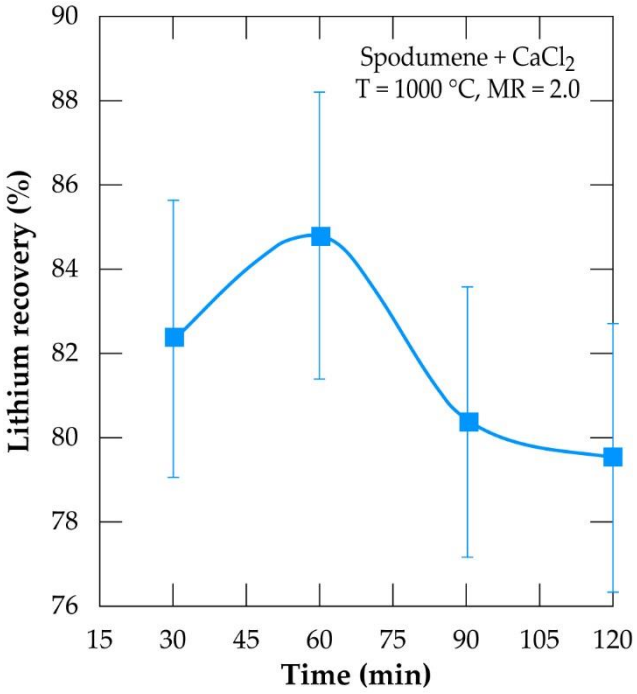

Figure 4.11: Evolution of the lithium recovery as a function of residence time for samples treated at 1000°C and MR = 2.0.

SEM-EDS investigation

Figure 4.12 shows the morphology of leached residues arising due to residence time as revealed by SEM-EDS. Figure 4.12A (treatment for 30 minutes) reveals clear portions of dark grey colour corresponding to spodumene. A zoom in at A1 (Figure 4.12E) confirms spodumene ("1") by EDS at the internal portions of the grain. Two major phases (dark and light grey) are observed and identified as CAS ("2") and calcium silicate or wollastonite ("3") after 30 minutes treatments (Figure 4.12B–D).

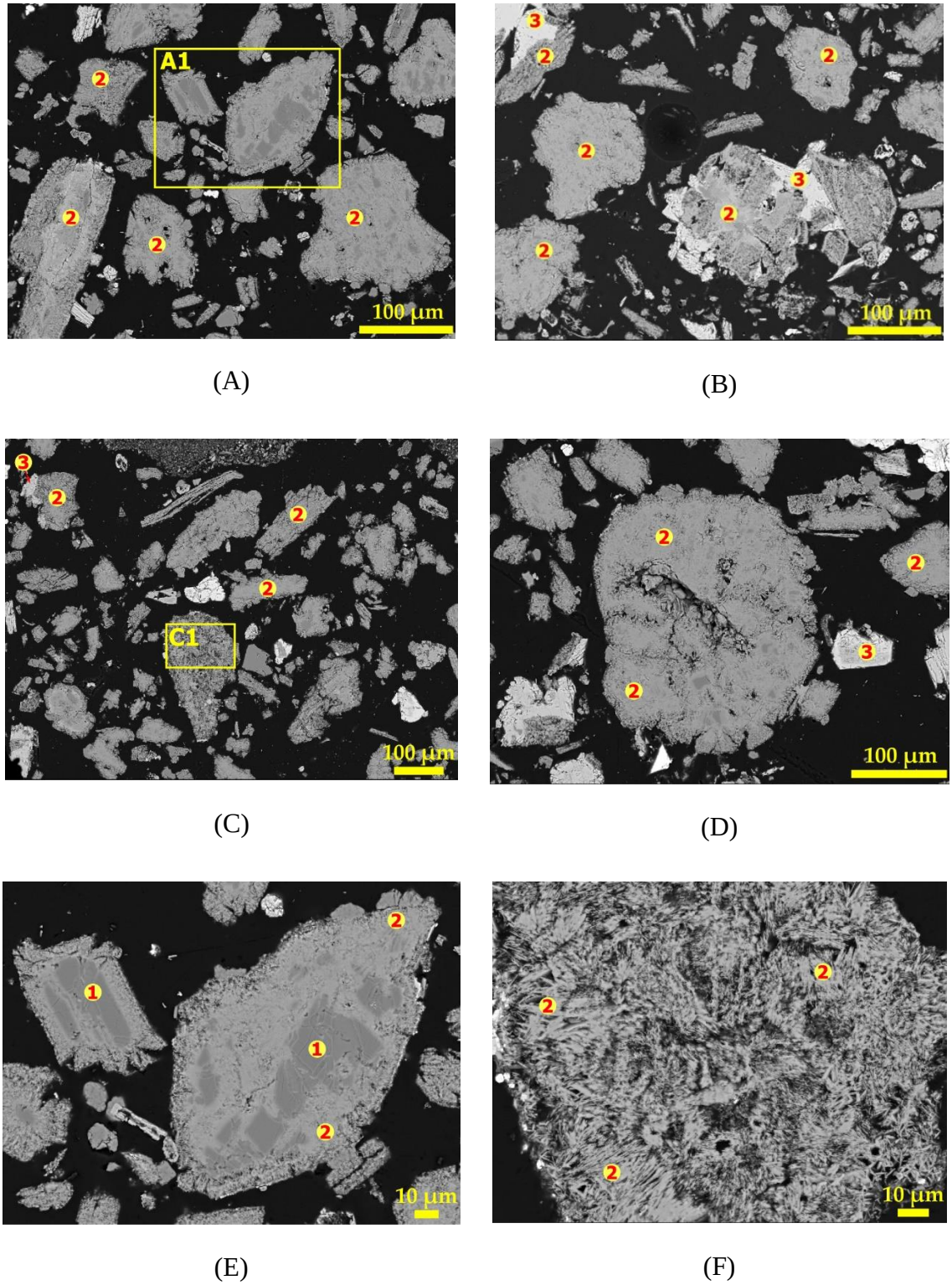

(A) (B)

(C) (D)

(E) (F)

Figure 4.12: SEM photomicrographs showing morphological changes of spodumene during 1000 °C treatment for (A) 30 min, (B) 60 min, (C) 90 min and (D) 120 min; (E) and (F) magnification at A1 and C1 respectively.

Wollastonite is often found attached to the CAS phase at the exterior parts. Observation also shows that, only few CAS grains had wollastonite phase associated with them which gives

an indication that, it may be present in small quantity. It may also imply that, both phases evolved concurrently from a mineral in the concentrate and a particular condition is responsible for their segregation into the different phases. There was no observed melting and agglomeration at the various residence time during the treatment at 1000 °C suggesting that temperature is the main factor responsible for this effect rather than time. A detailed look at a portion in Figure 4.12C is shown in Figure 4.12F. It reveals a uniform fibrous-like structure. This may be attributed to the movement of molten calcium chloride through grains, enabling reaction and subsequent lithium extraction which renders the grains fibrous and porous. EDS analysis reveals that, the entire grain is composed of CAS ("2"). CAS (anorthite) and calcium silicate (wollastonite) are the predominant phases observed from 60 minutes onward according to EDS investigation. It is therefore a confirmation that, they are the major phases at the end of the process as revealed by XRD earlier.

XRD analysis

XRD was used to investigate the mineralogical evolution in leached residues as a function of residence time. XRD diagrams and the semi-quantitative estimation are display in Figure 4.13A and B respectively. Spodumene is observed only in residue treated for 30 minutes which confirms SEM-EDS results in Figure 4.12E. Anorthite is the predominant new phase throughout with minor diopside and wollastonite. In Figure 4.13B, the anorthite concentration is significantly higher than wollastonite which confirms earlier observation and HSC software predictions. It increases slightly at the beginning to reach an approximate constant value around 90 minutes. There is no major and significant change in the concentration of the other minerals (quartz, wollastonite, diopside and wadalite).

Table 4.3 is a mass balance to compare the percent lithium recovered in solution and extraction efficiency at varying residence times. Almost all extracted lithium from the concentrate was recovered in solution at 30- and 60-minutes residence time. Afterwards, the extraction exceeded recovery. Since no melting and agglomeration was observed in residues after leaching, the difference may be attributed to the evaporation of lithium chloride after its formation and allowing it to stay in the furnace. A maximum of 89% extraction was achieved during 120 minutes of treatment. Spodumene was not identified in residues obtained beyond the optimal values of the two critical conditions identified. Tables 4.1 and 4.3, nonetheless reveal the presence of residual lithium beyond these conditions. This suggests a possibility that, the lithium might be in another phase rather than spodumene which has not been confirmed by this study.

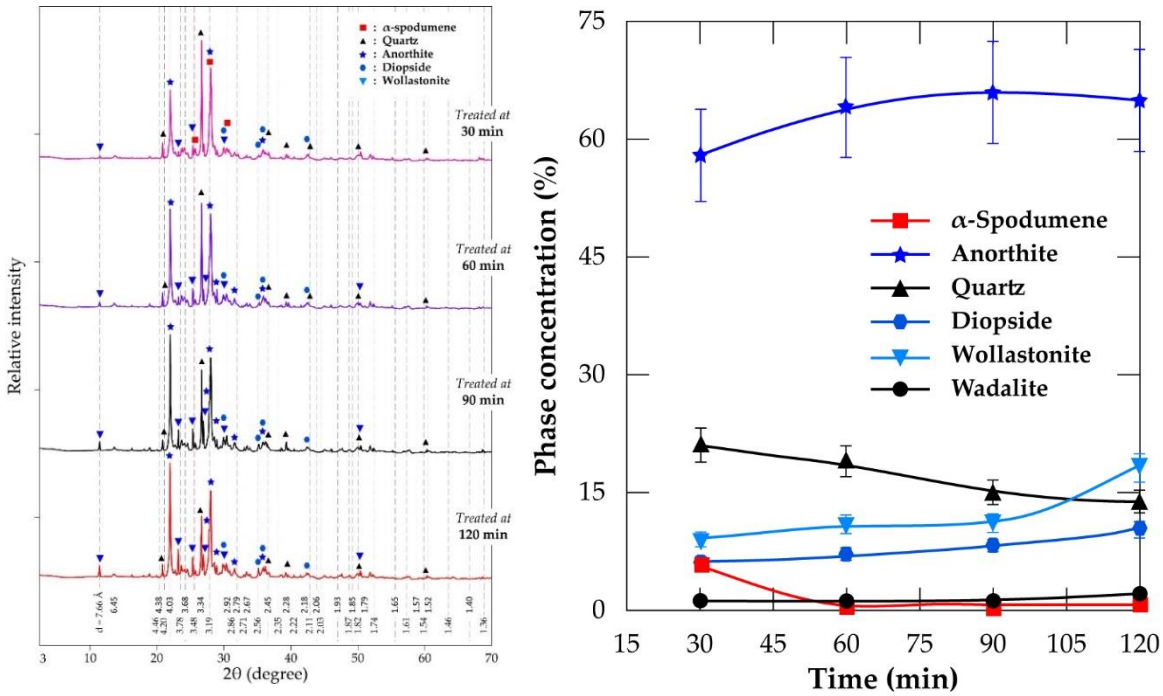

(A) (B)

Figure 4.13: (A) XRD pattern and (B) concentration of evolving phases as a function of residence time at 1000°C and $CaCl_2$/spodumene of 2.0.

Table 4.3: Mass balance comparing percent lithium recovery and extraction at 1000°C and different residence times.

Time (mins)	Residual lithium (wt%)	Recovery (%)	Extraction (%)
30	0.37	82.3	82.7
60	0.28	84.8	86.9
90	0.25	80.4	88.3
120	0.24	79.5	88.8

4.3.2 Mechanisms for phase evolution

Major gangue minerals in the concentrate are mica, amphibole, alkali feldspars, albeit and quartz. These minerals can interact with each other or respond differently with temperature and the chlorinating agent (calcium chloride).

Mica

Muscovite and biotite were the mica minerals identified in the concentrate. Decrepitation behaviour of mica species have been studied extensively by Hutchison [12]. He discovered two consecutive kinds of decomposition which begins and ends around 300 ℃ and 1000 ℃ respectively. They attributed the decomposition to the loss of two types of

chemically bound water within the ranges of 305 to 340 ℃ and 550 to 1000 ℃. It can be inferred therefore that the decomposition of mica begins around 300 ℃ and increases with increasing temperature. The model reactions for muscovite ($KAl_3Si_3O_{10}(OH)_2$ and biotite (specifically, annite ($KFe_3AlSi_3O_{10}(OH)_2$), which is an end member of the biotite solid solution) during thermal treatment can be illustrated by Equation (4.22) to (4.25). It is observed that, K-feldspar ($KAlSi_3O_8$) is a common product irrespective of the reaction path of mica decomposition.

$$KAl_3Si_3O_{10}(OH)_2 + SiO_2 \rightarrow [KAlSi_3O_8]_{melt} + Al_2SiO_5 + H_2O_{(g)}. \quad (4.22)$$

$$KFe_3AlSi_3O_{10}(OH)_2 + 3SiO_2 \rightarrow [KAlSi_3O_8]_{melt} + 3FeSiO_3 + H_2O_{(g)} \quad (4.23)$$

$$KAl_3Si_3O_{10}(OH)_2 \rightarrow [KAlSi_3O_8]_{melt} + Al_2O_3 + H_2O_{(g)} \quad (4.24)$$

$$KFe_3AlSi_3O_{10}(OH)_2 \rightarrow [KAlSi_3O_8]_{melt} + 3FeO + H_2O_{(g)} \quad (4.25)$$

This is a confirmation of earlier study on the pressurised decomposition of muscovite [13, 14] and biotite [15, 16]. One profound observation was that plagioclase grains act as a seed for epitaxial nucleation of peritectic K-feldspar [14]. Thus, a stable nucleus can be formed from plagioclase for the nucleation and growth of K-feldspar owing to their common silicate framework with similar crystal structure. K-feldspar can also evolve from plagioclase by percolation and diffusion of the melt, leading to cationic replacement of K^+ (from muscovite) with Na^+ (from plagioclase) [14]. The ionic diffusion mentioned falls in line with observation in our previous study [17].

Alkali feldspars (Albite and K-feldspar)

Alkali feldspars in the concentrate including K-feldspar synthesized from mica transform to anorthite by replacing alkali metals in their monoclinic crystal structure with calcium atoms [18]. The increased bond vibration during thermal treatment destroys the tetrahedral aluminosilicate structure of the feldspars, releasing their alkali metal ions to interact with chloride ions of calcium chloride to form either sodium or potassium chloride. This changes the crystal structure of the feldspars to anorthic system when replaced with calcium from calcium chloride [19]. Anorthite, wollastonite and quartz are therefore, possible products expected in residue after leaching whereas the alkali metal chlorides formed are washed into the leach liquor during leaching (Equation (4.26) and (4.27)).

Anorthite formed may decompose further to form kyanite and wollastonite (Equation (4.28)).

$$CaCl_2 + 2NaAlSi_3O_8 \rightarrow CaAl_2Si_2O_8 + 4SiO_2 + 2NaCl \quad (4.26)$$

$$CaCl_2 + 2KAlSi_3O_8 \rightarrow CaAl_2Si_2O_8 + 4SiO_2 + 2KCl \quad (4.27)$$

$$CaAl_2Si_2O_8 \rightarrow CaSiO_3 + Al_2SiO_5 \quad (4.28)$$

Amphiboles

Amphiboles transform to their respective pyroxenes and quartz through topotactical dehydration decomposition at temperatures above 600 ℃ [20–22]. The transformation is pseudopolymorphic because it occurs at a fixed temperature for a given pressure. There is also a close resemblance of the resultant products to the reactant which is typical of polymorphic transitions [22]. Using tremolite (the amphibole considered in this study), the decomposition gives rise to diopside and enstatite) (Equation (4.29)) at about 740 ℃ according to Xu et al. [21].

$$Ca_2Mg_5Si8O_{22}(OH)_2 \rightarrow 2CaMgSi_2O_6 + 3MgSiO_3 + SiO_2 + H_2O_{(g)} \quad (4.29)$$

4.3.3 Thermochemical investigation of phase evolution

Possible reactions identified during the process may occur in oxygen deficient (non-oxidizing) or oxygen rich (oxidizing) atmosphere. HSC Chemistry software was used to determine the feasibility of these reactions and predict the influence of temperature on phases evolving.

Non-oxidizing atmosphere

Gibbs free energy changes for the formation of products in a non-oxidizing environment in Equations (4.22)–(4.29) is plotted as a function of temperature in Figure 4.14. All the reactions are found feasible either throughout or at a point within the operating temperatures except for the decomposition of anorthite (Equation (4.28)). The micas are observed to have similar feasibility which starts after 300 ℃ (confirming earlier study [12] that, the low dehydroxylation temperature begins at 305 or 340 ℃) and increase with temperature to form K-feldspar which also confirms earlier study [12]. All alkali feldspars also have similar chemical reactivity to produce the same products (anorthite and quartz,

Equation (4.26) and (4.27)) in addition to their respective alkali metal chlorides, but their thermodynamic behaviour is somewhat different. Specifically, K-feldspar (Equation (4.27)) is feasible throughout, but the feasibility of albeit (Equation (4.26)) is only up to 927 ℃. K-feldspars (synthesized or originally present in the concentrate) end up forming anorthite as the prominent new phase at the end of the process. Furthermore, anorthite is favourably synthesised from the interaction of spodumene and calcium chloride (Equation (4.19) and (4.20)). That is, the software predictions agree with XRD findings, revealing that, anorthite is a major mineral in leached residues. This is because it is a product from a feasible reaction for the decomposition of spodumene (the major component of the concentrate) as well as other minerals which are present in a fairly high amount.

The decomposition of anorthite to other components was investigated as modelled by Equation (4.28) but its decomposition is, nonetheless, not possible in Figure 4.14. It is suspected that, sodium and potassium which may be found in the leached liquor is obtained principally from Equation (4.26) and (4.27). The Gibbs free energy change for the decomposition of tremolite (amphibole) in Equation (4.29) is negative after 527 ℃ which relates very well with the assertion that, amphiboles decomposition begins around 600 ℃ [20–22]. However, the software gives an extrapolated data after 527 ℃ which may be due to either lack of data for tremolite in the software or its breaks down beyond this temperature. Drawing inference from earlier work [22] we attribute this to its pseudo-polymorphic decomposition to diopside and enstatite (Equation (4.29)). Extrapolation of data is also observed for albit and spodumene at 927 ℃ as well as biotite (annite) at 727 ℃.

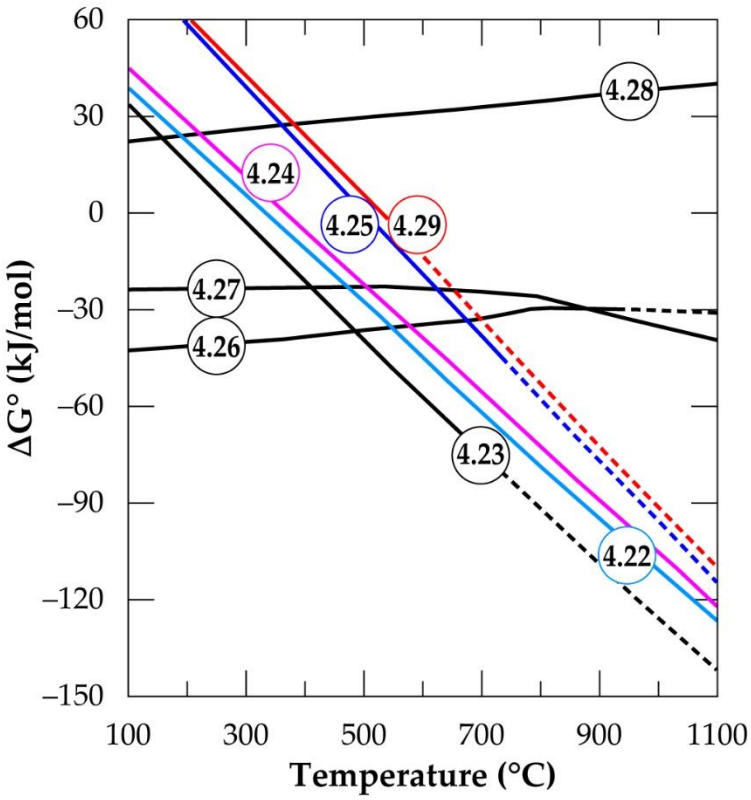

Figure 4.14: The standard Gibbs energy changes for phase transformation of gangue minerals in concentrate in oxygen deficient environment (Eqs (4.22)–(4.29)) versus temperature (data from the HSC Chemistry® 5.1).

Oxidizing atmosphere

The Gibbs free energy changes for product formation in oxidizing environment is presented in Figure 4.15. Except for annite decomposition (Equation (4.30)), chlorination reactions with $CaCl_2$ in oxidizing environment (Equations (4.31)-(4.35)), can be said to be primarily impossible but by manipulating the oxygen concentration, feasibility can be achieved to some extent in the alkali feldspars.

$$2KFe_3AlSi_3O_{10}(OH)_2+O_{2(g)} \rightarrow 2[KAlSi_3O_8]_{melt}+2Fe_3O_4+2H_2O_{(g)} \quad (4.30)$$

$$2NaAlSi_3O_8(A)+2CaCl_2+0.5O_{2(g)} \rightarrow 2NaCl+CaAl_2Si_2O_8+3SiO_2+CaSiO_3+Cl_{2(g)} \quad (4.31)$$

$$2KAlSi_3O_8(M)+2CaCl_2+0.5O_{2(g)} \rightarrow 2KCl+CaAl_2Si_2O_8+3SiO_2+CaSiO_3+Cl_{2(g)} \quad (4.32)$$

$$2NaAlSi_3O_8(A)+3CaCl_2+O_{2(g)} \rightarrow 2NaCl+CaAl_2Si_2O_8+2SiO_2+2CaSiO_3+2Cl_{2(g)} \quad (4.33)$$

$$2KAlSi_3O_8(M)+3CaCl_2+O_{2(g)} \rightarrow 2KCl+CaAl_2Si_2O_8+2SiO_2+2CaSiO_3+2Cl_{2(g)} \quad (4.34)$$

$$2\alpha LiAlSi_2O_6 + 3CaCl_2 + O_{2(g)} \rightarrow 2LiCl + CaAl_2Si_2O_8 + 2CaSiO_3 + 2Cl_{2(g)} \quad (4.35)$$

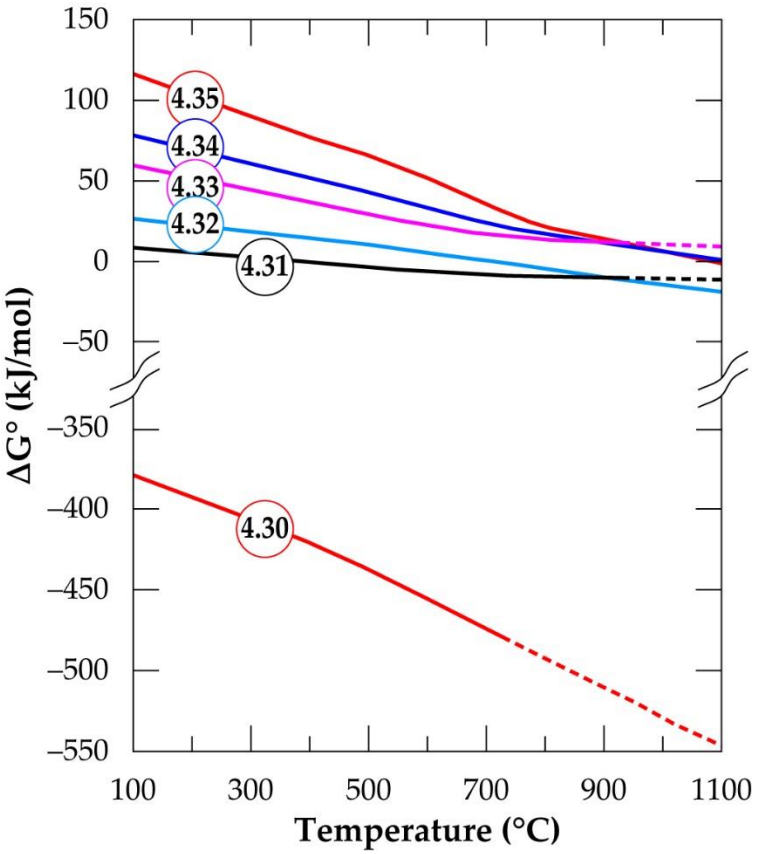

Figure 4.15: The standard Gibbs energy changes for phase transformation of gangue minerals in concentrate in oxidizing environment (Eqs (4.30)–(4.35)) versus temperature (data from the HSC Chemistry® 5.1).

Oxidizing reactions for alkali feldspars occurring in one mole oxygen (Equation (4.33) and (4.34)) are not feasible but by halving it (Equation (4.31) and (4.32)), the Gibbs free energy achieves some level of negativity (though not high), producing anorthite and wollastonite as new phases with the release of chlorine gas. Thus, anorthite formation is highly suspected by the software which was confirmed XRD results. Wollastonite can also be a possible product in the residue depending on the oxygen concentration during treatment only if HSC Software predictions are valid. Spodumene feasibility in the chlorination process is also observed to be affected by oxygen concentration such that, it is non-spontaneous in oxidizing atmosphere (Equation 4.35) but spontaneous in oxygen deficient atmosphere (Equation (4.19) and Figure 4.2) depending on the temperature. In general, the process feasibility is high in oxygen deficient (non-oxidizing) environment than oxidizing.

4.3.4 Correlating XRD results, HSC Chemistry software predictions and reaction mechanisms

HSC software predicts anorthite as the predominant new phase at the end of the process, arising primarily from spodumene, mica and alkali feldspar decomposition in the presence of calcium chloride. Amphibole and mica persist only up to 850 ℃ after which they disappear from XRD diagram of leached residue. This implies that, after 850 ℃, their transformation to other phases is complete which agrees with observation by reference [12] and [22]. As indicated earlier, the decomposition of mica and amphibole basically form K-feldspar melt and pyroxenes respectively. The appearance of diopside after 850 ℃ may be linked to the decomposition of tremolite, though enstatite (its corresponding pyroxene during decomposition) was not identified, probably it transformed further to another phase. K-feldspar may evolve from mica decomposition and its feasibility is confirmed by HSC software, but it was not identified in any of the residues. This suggests that it appears as a metastable phase and hence, quickly transforms to anorthite in the presence of calcium chloride. According to reference [23], the decomposition of K-feldspars in the presence of calcium chloride begins around 600 ℃. Potassium chloride and anorthite are the resulting products such that at 900 ℃, the optimum extraction is achieved. This identified temperature range falls within the operating temperatures of the study. Therefore, the absence of K-feldspar in the residue (XRD pattern) may be attributed to its fast conversion to anorthite as it is synthesised during the process. Equation (4.28) suggests that, wollastonite may evolve from the decomposition of anorthite or the chlorination of alkali feldspar in an oxidizing atmosphere (Equation (4.31)–(4.34)). Since HSC Software predicts Equation (4.28) to be nonspontaneous, the close association of wollastonite with CAS (as revealed in SEM image) may lead to the conclusion that, the decomposition of alkali feldspars is responsible for the synthesis of both phases and a limiting oxidizing atmosphere is a prerequisite for the synthesis.

4.4 Conclusion

Investigation into the pyrometallurgical synthesis of lithium chloride directly from α-spodumene by chlorination with $CaCl_2$ followed by water leaching was conducted. Though the $CaCl_2$ to spodumene ratio has influence on lithium recovery, temperature and time are the major factors which, if are not regulated lead to evaporation of lithium chloride. Lithium recovery to leach solution generally increases with all investigated parameters, which are MR, temperature and time until they peak at 2.0, 1000 °C and 60 minutes

respectively. These optimal conditions led to about 90 percent lithium extraction, but 85 percent was recovered to solution with the remainder exiting via the gas phase. In a process, this gas phase lithium could be also recovered by leaching the gas treatment dust. Though recovery plateaus after MR of 2.0, evaporation coupled with melting and agglomeration occurs after 1000 °C, which in addition, leads to a decrease in recovery.

Investigating the behaviour of gangue minerals (micas, alkali feldspars, and amphiboles) using XRD, HSC software and SEM-EDS during the process revealed that, micas first decomposes to form K-feldspar which subsequently transforms to anorthite by reacting with calcium chloride. Alkali feldspars (and spodumene) also form anorthite when they react with calcium chloride whilst amphiboles (tremolite) decomposes, forming diopside and enstatite. XRD results confirmed HSC software and SEM-EDS predictions which reveals anorthite as predominant phase (accounting for about 70 percent) alongside quartz, wollastonite and diopside as minor phases. Predictions by HSC software are in good agreement with experimental observation. The oxidising effect of the system on process feasibility was investigated where it was found favourable in non-oxidising environment than oxidising.

Spodumene identified in leached residue is in the α-form with no identification of the β-form. This suggests that the extraction of lithium as chloride is directly from the α-phase. A possible transformation of α-spodumene into β-spodumene followed by a fast synthesis of lithium chloride from β-spodumene (2α-spodumene → 2β-$LiAlSi_2O_6$ + $CaCl_2$ → 2LiCl + $2SiO_2$ + $CaAl_2Si_2O_8$) may also occur. However, we treat this as tentative at this stage. The relatively low apparent activation energy of 122±6 kJ mol^{-1} obtained could suggest diffusion of calcium chloride as the rate limiting step of the process.

REFERENCES

[1] G. G. Gabra, A. E. Torma, and C. A. Olivier, “Pressure leaching of beta-spodumene by sodium chloride,” *Canadian Metallurgical Quarterly*, vol. 14, no. 4, pp. 355–359, Oct. 1975, doi: 10.1179/000844375795050049.

[2] N. Kanari, D. Mishra, J. Mochón, L. F. Verdeja, F. Diot, and E. Allain, “Some kinetics aspects of chlorine-solids reactions,” *Revista de Metalurgia*, vol. 46, no. 1, pp. 22–36, Feb. 2010, doi: 10.3989/revmetalm.0852.

[3] N. Kanari, D. Mishra, L. Filippov, F. Diot, J. Mochón, and E. Allain, “Kinetics of hematite chlorination with Cl2 and Cl2 + O2: Part I. Chlorination with Cl2,” *Thermochim Acta*, vol. 497, no. 1–2, pp. 52–59, 2010, doi: 10.1016/j.tca.2009.08.007.

[4] P. K. Jena and E. A. Brocchi, “Metal extraction through chlorine metallurgy,” *Mineral Processing and Extractive Metallurgy Review*, vol. 16, no. 4, pp. 211–237, 1997, doi: 10.1080/08827509708914136.

[5] N. Kanari, B. R. Reddy, and I. Gaballah, “Kinetics of Carbochlorination of Chromium (III) Oxide,” *Metallurgical and Materials Transactions B: Process Metallurgy and Materials Processing Science*, vol. 29, no. 4, pp. 729–737, 1998, doi: 10.1007/s11663-998-0131-x.

[6] N. Kanari and I. Gaballah, “Chlorination and carbochlorination of magnesium oxide,” *Metall Mater Trans A Phys Metall Mater Sci*, vol. 30, no. 3, pp. 383–391, 1999, doi: 10.1007/s11663-999-0070-1.

[7] L. I. Barbosa, J. A. González, and M. del C. Ruiz, “Extraction of lithium from β-spodumene using chlorination roasting with calcium chloride,” *Thermochim Acta*, vol. 605, pp. 63–67, Apr. 2015, doi: 10.1016/j.tca.2015.02.009.

[8] H. Dang *et al.*, “Recycled Lithium from Simulated Pyrometallurgical Slag by Chlorination Roasting,” 2018, doi: 10.1021/acssuschemeng.8b02713.

[9] H. Guo, G. Kuang, H. Wang, H. Yu, and X. Zhao, “Investigation of Enhanced Leaching of Lithium from α-Spodumene Using Hydrofluoric and Sulfuric Acid,” *Minerals*, vol. 7, no. 11, p. 205, Oct. 2017, doi: 10.3390/min7110205.

[10] A. C. Bidaye, S. Venkatachalam, and C. K. Gupta, “Studies on the Chlorination of Zircon : Part I . Static Bed Investigations,” vol. 30, no. April, 1999.

[11] L. I. Barbosa, N. G. Valente, and J. A. González, “Kinetic study on the chlorination of β-spodumene for lithium extraction with Cl2 gas,” *Thermochim Acta*, vol. 557, pp. 61–67, 2013, doi: 10.1016/j.tca.2013.01.033.

[12] W. W. Hutchison, “Two Stages of Decrepitation of Micas,” 1963.

[13] S. Israel, M. Anenburg, and Y. Katzir, “Muscovite dehydration melting in Si-rich metapelites : Microstructural Muscovite dehydration melting in Si-rich metapelites : microstructural evidence from trondhjemitic migmatites , Roded , Southern Israel,” no. May, 2014, doi: 10.1007/s00710-013-0289-z.

[14] B. Dyck, D. J. Waters, and M. P. Searle, “Muscovite dehydration melting : Reaction mechanisms , microstructures , and implications for anatexis,” no. April 2019, pp. 29–52, 2020, doi: 10.1111/jmg.12511.

[15] A., E., Douce Patino and J., S., BEARD, "Dehydration-melting of biotite gneiss and quartz amphibolite from 3 to 15 kbar," *Journal of Petrology*, vol. 36, no. 3, pp. 707--738, 1995.

[16] A. A. Graphchikov, A. N. Konilov, and J. D. Clemens, "Biotite dehydration, partial melting, and fluid composition: Experiments in the system $KAlO_2$-FeO-MgO-SiO_2-H_2O-CO_2," 1999.

[17] A. Y. Fosu, N. Kanari, H. Hodge, J. Vaughan, and A. Chagnes, "Physico-Chemical Characteristics of Spodumene Concentrate and Its Thermal Transformations," pp. 1–19, 2021.

[18] L. Li, S. Lei, Y. Liu, and H. Luo, "Extraction and reaction mechanism of potassium from associated phosphorus and potassium ore," *Journal Wuhan University of Technology, Materials Science Edition*, vol. 31, no. 6, pp. 1255–1260, Dec. 2016, doi: 10.1007/s11595-016-1522-5.

[19] L. Liang, L; Shaomin, L; uanyuan, L; Huihua, "Extraction and Reaction Mechanism of Potassium from Associated Phosphorus and Potassium Ore," pp. 1255–1260, 2016, doi: 10.1007/s11595-016-1522-5.

[20] N. M. Johnson and B. Fegley, "Tremolite decomposition on Venus II . Products , kinetics , and mechanism," vol. 164, pp. 317–333, 2003, doi: 10.1016/S0019-1035(03)00102-7.

[21] H. Xu, D. R. Veblen, G. Luo, and A. Xue, "Transmission electron microscopy study of the thermal decomposition of tremolite into clinopyroxene," vol. 81, pp. 1126–1132, 1996.

[22] F. Freeman, AG and Frazer, "Pseudo polymorphic transition: the amphibole→ pyroxene reaction," *Nature*, vol. 220, no. 5162, pp. 67--68, 1968.

[23] B. Yuan *et al.*, "Extraction of potassium from K-feldspar via the CaCl2 calcination route," *Chin J Chem Eng*, vol. 23, no. 9, pp. 1557–1564, Sep. 2015, doi: 10.1016/j.cjche.2015.06.012.

CHAPTER 5: Purification and Recovery of Lithium from Leach Liquor

5.1 Introduction

The battery industry requires high purity lithium salts (above 99.9%) for the manufacture of lithium-ion batteries used in vehicles [1]. Alkali and alkaline earth metal ions (Na^+, K^+, Mg^{2+}, Ca^{2+}) with concomitant chloride or sulphate ions are usually the predominant impurities encountered during processing brine to extract lithium. The divalent metal ions, particularly Mg^{2+} are impurities of major concern due to difficulty in separating from lithium because of similarity in their chemistry. The Mg/Li ratio is therefore, used as an indicator for the ease of processing a particular type of brine. The lower the value, the more suitable it is for lithium recovery and vice-versa. The recovery of the metal is now focused on brine whose Mg/Li is less than 8 because above it, serious processing challenges are encountered [2]. Even those with low Mg/Li ratio are found to consume high quantity of water and reagent alongside discharging voluminous waste into the environment during the chemical precipitation and removal of magnesium. It is preferred that the concentration of Mg^{2+} and Ca^{2+} in the resulting Li_2CO_3 from the process fall within 0 to 10 ppm and 3 to 10 ppm respectively [3]. The purity of Li_2CO_3 obtained from brine is about 99% (technical grade) which does not meet the requirement of the battery industry. It is refined further to improve the purity, sometimes by converting it to other compounds (LiCl or LiOH) [4, 5] before the battery grade (99.5%) or high purity form (99.99%) is achieved. The purification process calls for additional unit operations and cost. To curb this challenge, several studies to produce purer products directly from brine have been conducted by first, producing very pure solutions before lithium recovery [1, 6].

Like brine, the recovery of lithium from ores requires purification of the leach liquor before its precipitation into the desired lithium salt. Spodumene has the advantage of having a simple composition and hence, results in a liquor of lower impurity during processing compared to other minerals like lepidolite. However, the harsh treatment conditions needed to break the silicate structure and/or enable ion exchange for lithium salt formation leads to coextraction and leaching of significant portion of other components of the mineral (aluminium, silicon, iron, or magnesium) into the leach liquor as impurities. This affects downstream purification and lithium recovery from the leach liquor. This is a major challenge of the current commercialised process for extracting the metal from spodumene. Altura Mining Limited announced a lithium carbonate purity of 99.97% from sulphuric acid

processing of Pilgangoora spodumene sample from the flow diagram indicated in Figure 5.1. Chemical precipitation is normally used for softening the liquor which generate large volume of precipitate and carries along some lithium which decreases recovery [7]. The liquor goes through several purification steps before achieving the primary lithium carbonate (primary LC) of 99.59% purity. The produced lithium carbonate (technical grade) goes through refining (Figure 5.1) to meet the requirement for lithium-ion battery; adding to cost of production as indicated earlier.

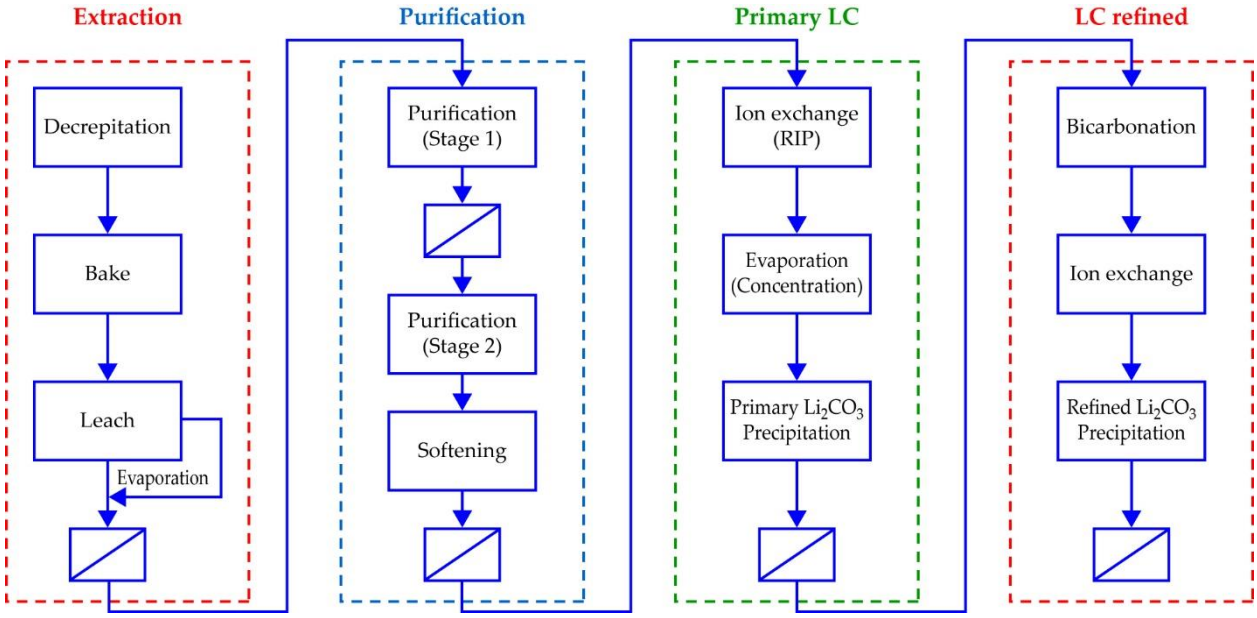

Figure 5.1: Process flowsheet for the conventional processing and purification to recover Li_2CO_3 [8].

Thus, the recovery of purer lithium salts depends on the extent of purification of the leach liquor before the recovery of the salts. An improved technology to obtain salts of higher purity from ores has also been reported [9].

Analysis of the liquor obtained in Chapter 4 indicated calcium as the predominant impurity arising from the use of calcium chloride in the chlorination unit. Investigation into technologies to purify the liquor by separating calcium and subsequently, recovering lithium salt of high purity; leading to the development of an overall flow chart for the process is conducted. Technologies to be investigated include selective crystallisation of calcium chloride to reduce the calcium concentration of the liquor, the softening efficiency of Lewatit® MDS TP 208 and the traditional carbonation precipitation.

Lewatit® MDS TP 208 is a new resin composed of cross linking polymeric material which has been made into macroporous beads. The monomers have iminodiacetic acid chemically active sites which act as high affinity ligands toward divalent metal ions

particularly, alkaline earth metals. It is said to offer superior advantages over its contemporaries regarding kinetics, total and operating capacity, stability (mechanical and osmotic), and degree of regeneration which makes it suitable and economical for softening the liquor obtained in this study [10].

The purification process is expected to be followed by investigating the efficiency of Cyanex® 936P (an organic extractant which is believed to have high affinity for lithium) to recover the lithium from the liquor.

5.2 Materials

Lewatit® MDS TP 208 manufactured by LANXESS was used as ion exchange resin. Na_2CO_3, NaOH and HCl were obtained from Sigma-Aldrich, France. The resin characteristics as indicated by manufacturers is shown in Table 5.1. The chemical composition (ppm) of leach liquor obtained at optimal chlorination and leaching conditions (1000 °C roasting for 60 minutes; calcium chloride to spodumene ratio of 2.0; water leaching at solid/liquid ratio of 50g/L) is Li, 895; Si, 0.963; Mn, 0.01; Fe, 0.021, Mg, 1.18; Ca, 11285; Na, 393, K, 537. Calcium is the predominant impurity; hence, a synthetic calcium chloride-lithium chloride solution with similar concentration as leach liquor was used for the study. Metal solution assays were determined by Inductively Coupled Plasma - Optical Emission Spectrometry (ICP-OES) in a sample matrix of 10% HNO_3.

Table 5.1: Characteristics of Lewatit MDS TP 208

Functional group	Iminodiacetic acid
Ionic form as shipped	Na^+
Matrix	Crosslinked polystyrene
Appearance	Beige
Mean bead size (mm)	0.39 (+/- 0.03)
Density (g/ml)	1.16
Water retention (wt. %)	59 – 65
Stability pH-range	0 – 14
Operating pH-range	2 – 12
Maximum Operating temperature (°C)	80

5.3 Method

Crystallisation study was done by heating to evaporate portion of the homogenous mixture of aqueous calcium chloride-lithium chloride mixture to visually obtain some level

of supersaturation. With the thermometer immersed in the solution, the hot saturated solution was slowly cooled until crystals started to form and the temperature recorded. The experiment was then repeated several times.

Ion exchange and carbonation experiments were performed with the same experimental set-up in a batch reactor (Figure 5.2). The resin received in the sodium form was protonated by contacting it with 1 molL^{-1} HCl for 120 min at 25±0.5 °C. The protonated resin was washed several times with deionised water to make sure it was free from residual acid and then filtered using the suction pump. During the calcium loading experiment, 50 mL of resin was contacted with 200 mL of the liquor in a 500 mL reactor. Sodium hydroxide was used to deprotonate the resin and enhance calcium loading and the mixture was agitated with an overhead stirrer operating at 300 rpm. The pH was monitored with a pH metre calibrated at pH = 4 and 7 and the temperature was controlled with a VTF digital thermoregulator manufactured by VELP Scientifica. Samples were then taken at a stabilised pH for metal assay. The quantity of metals (calcium and lithium) separated from the liquor either by the precipitation or ion exchange (%*K*) was computed by Equation (5.1) as:

$$\%K = \frac{[M]_i - [M]_f}{[M]_i} * 100 \qquad (5.1)$$

Where $[M]_i$ and $[M]_f$ are the metal concentration in aqueous phase before and after the softening processes respectively.

Stripping of the loaded resin was done with 8% HCl with the aim of regenerating resin as well as recovering eluted calcium chloride for reuse.

In the carbonation study, sodium carbonate was added to the liquor and the mixture continuously stirred. The addition was observed to increase the pH of the liquor, hence, some time was allowed to elapse until an equilibrium pH was achieved before sampling for elemental analysis.

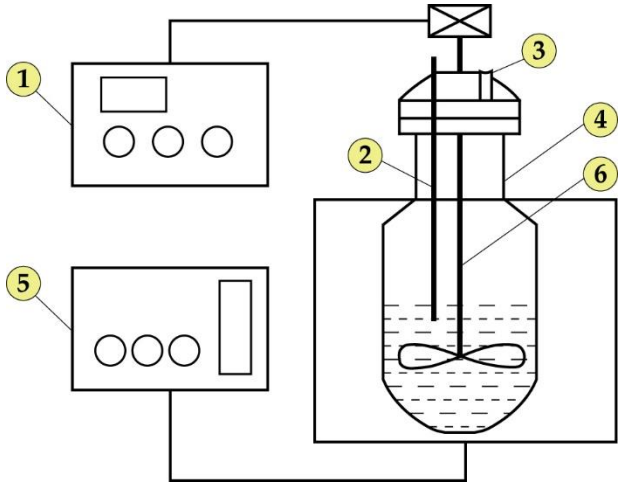

Figure 5.2: Experimental set-up for carbonation and ion exchange experiment. Abducted from Yi et al. [11]**. 1. Stirring controller. 2. Thermometer. 3. Discharge port. 4. Reaction vessel. 5. Thermostat.**

5.4 Results and discussion

Evaporation of the liquor to selectively crystallise and recover calcium chloride was challenging as it resulted in a supersaturated solution of high viscosity. The separation of the crystals that formed was thus, difficult, making the use of this approach as part of the purification techniques of this study challenging. This probably, may be due to the similarity in the chemistry of the two metals (calcium and lithium), particularly, the closeness of their solubility.

5.4.1 Carbonation precipitation of calcium

Figure 5.3a shows the variation of calcium and lithium concentration with Na_2CO_3 addition as well as the changes in pH of the liquor. The calcium concentration is greatly influenced by the addition of the salt, decreasing steadily until around 20.0 g where the solution becomes barren of calcium. The process, however, has minimal effect on lithium. Its concentration remains almost constant as can be observed in the figure. Percent metal separated (*%K*) through precipitation upon addition of Na_2CO_3 is presented in Figure 5.3b. Almost 100% calcium was precipitated on addition of 20.0 g of the salt. At this point almost 20% of lithium was coprecipitated and entrained in the $CaCO_3$ matrix which will leads to decreased recovery. It is therefore obvious that the method can effectively be used to separate calcium from the liquor to the barest minimum but it has a disadvantage of decreasing the recovery of lithium. It is essential that the developed process be designed in a way which enables the reuse of the resulting $CaCO_3$ precipitate. This will help to mitigate the challenge linked to its disposal whilst recovering lithium which otherwise may be lost.

One way is to integrate this process with brine processing of lithium in which case, the $CaCO_3$ can be used to precipitate magnesium and recover the lithium content alongside.

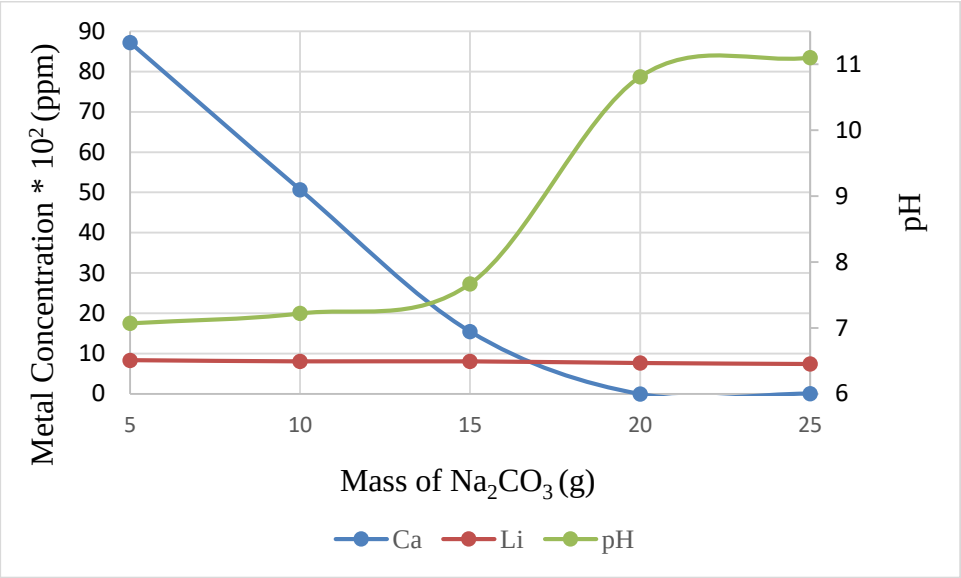

(a)

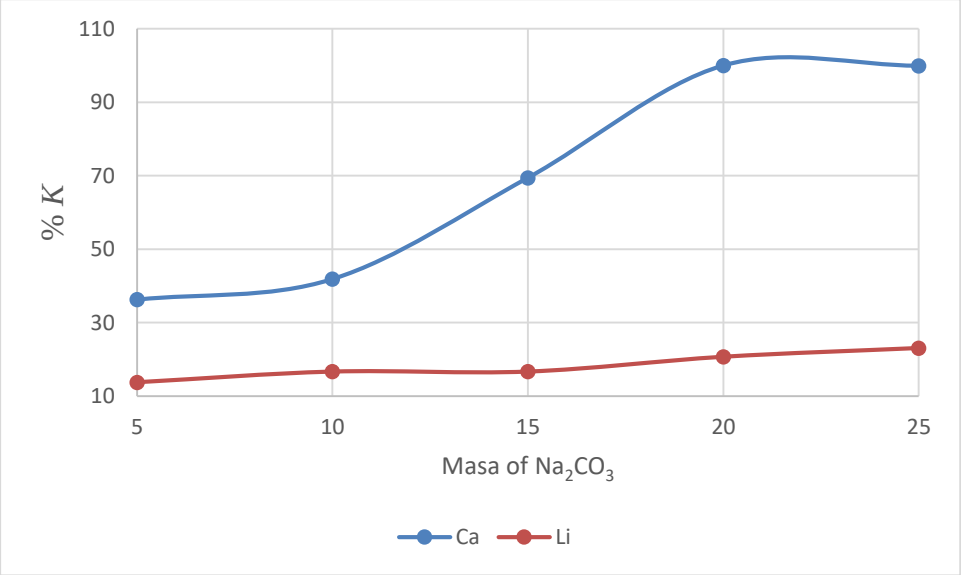

(b)

Figure 5.3: (a) Effect of metal concentration and pH (b) Percent metal preceiptated as a function of Na_2CO_3 addition.

The general carbonation study can be described by Equation 5.2 as:

$$Na^+ + CO_3^{2-} + Ca^{2+} + Li^+ + Cl^- \rightarrow CaCO_3 \downarrow + Li^+ + Na^+ + Cl^- \quad (5.2)$$

Detailed study can be viewed as occurring from Equation 5.3 to 5.5. Both lithium and calcium precipitate out in their carbonate form (Equation 5.3-5.4). From the solubility product constants (K_{sp}) of the two salts, $CaCO_3$ has the lowest making it stable compared to Li_2CO_3. It therefore remains in solution as precipitate whilst Li_2CO_3 on the other hand, is soluble (higher K_{sp}) and therefore dissolves, releasing its carbonate ions to form more stable $CaCO_3$ with the lithium remaining in solution (equation 5.5).

$$CO_3^{2-} + Ca^{2+} \rightarrow CaCO_3 \downarrow \qquad K_{sp}\,(CaCO_3) = 2.8 \times 10^{-9}\ [12] \qquad (5.3)$$

$$CO_3^{2-} + 2Li^{+} \rightarrow Li_2CO_3 \downarrow \qquad K_{sp}\,(Li_2CO_3) = 2.5 \times 10^{-2}\ [12] \qquad (5.4)$$

$$Li_2CO_3 + Ca^{2+} \rightarrow 2Li^{+} + CaCO_3 \downarrow \qquad (5.5)$$

Monitoring the pH of the liquor during the process was observed to increase with Na_2CO_3 addition as shown in the Figure 5.3a. This is expected since the salt is obtained from a neutralisation reaction of a strong base and a weak acid, hence, it can hydrolyse in the aqueous liquor to produce hydroxyl ions which makes the solution alkaline as observed with increased solution pH. The suspected equilibria for the phenomena and equilibrium constants, K at the temperature used for the study (25 °C) during hydrolysis is shown in Equation 5.6 to 5.9 [12-13].

$$H_2O_{(aq)} \rightleftharpoons H^{+}_{(aq)} + OH^{-}_{(aq)} \qquad 1.00 \times 10^{-14} \qquad (5.6)$$

$$CO_3^{2-}{}_{(aq)} + H_2O_{(l)} \rightleftharpoons HCO_3^{-}{}_{(aq)} + OH^{-}_{(aq)} \qquad 2.14 \times 10^{-4} \qquad (5.7)$$

$$HCO_3^{-}{}_{(aq)} + H_2O_{(l)} \rightleftharpoons H_2CO_{3(aq)} + OH^{-}_{(aq)} \qquad 2.24 \times 10^{-8} \qquad (5.8)$$

$$CaCO_{3(s)} \rightleftharpoons Ca^{2+}{}_{(aq)} + CO_3^{2-}{}_{(aq)} \qquad 2.80 \times 10^{-9} \qquad (5.9)$$

Equation 5.7 has the highest equilibrium constant (2.14×10^{-4}) which suggest that its products are predominant in the system. Thus, the OH^- generated from this equilibrium makes the solution alkaline as observed. The redissolution of the precipitate in Equation 5.9 is characterised by a relatively lower equilibrium constant suggesting stability of $CaCO_3$ as indicated earlier.

It can be observed from the figure (Figure 5.3a) that, the initial addition of the salt (Na_2CO_3) up to 15 g has a marginal increase in the pH but a sharp decline in the calcium concentration. This may be attributed to a higher supersaturation of the mixture at the initial stages of the reaction upon the addition which leads to high degree of nucleation and

consequently, higher $CaCO_3$ formation. At this point, hydrolysis of Na_2CO_3 is minimal as CO_3^{2-} directly reacts with Ca^{2+} to form the precipitate rather than hydrolysing. After addition of 15 g of the salt when significant quantity of calcium has precipitated, the forward reaction of Equation 5.7 is favoured which is characterised by sharp rise in pH until it levels.

5.4.2 Ion exchange (IX)

The calcium sorption capacity of the resin at varying pH was studied at 25 °C and 60 °C and results are presented in Figure 5.4. Adsorption of calcium is observed to increase with increasing pH in both cases such that, about 91% and 97% of calcium was separated from the liquor at pH of 12 and 10.7 at 25 °C and 60 °C respectively. Protonation and calcium loading of the resin is described by Equation 5.10 and 5.11 respectively.

$$2R^{-}Na^{+} + HCl \rightarrow 2R^{-}H^{+} + NaCl \quad (5.10)$$

$$2R^{-}H^{+} + Ca^{2+} + Li^{+} \rightarrow R_2Ca + Li^{+} + 2H^{+} \quad (5.11)$$

where R is an alkyl group.

It is observed that calcium loading on the resin releases hydrogen ions which makes the liquor acidic. To drive the reaction to the right and enhance the sorption capacity of the resin, the solution must be deprotonated by the addition of a suitable base, in this case with NaOH. The progressive deprotonation leads to a resultant increased loading capacity of the resin which resulted in the increasing calcium absorption with pH as observed. The resin can thus, be used to significantly soften the liquor. About 10% of lithium was nonetheless, co-adsorbed alongside in both cases. Comparing the efficiencies and the pH needed to achieve them, 60 °C is better for the process since the higher pH requirement (~12) at lower temperatures (25 °C) goes with high consumption of NaOH. The kinetics of the process at the higher temperature (60 °C) was observed to be better, reaching equilibrium faster compared to treatment at the lower temperature.

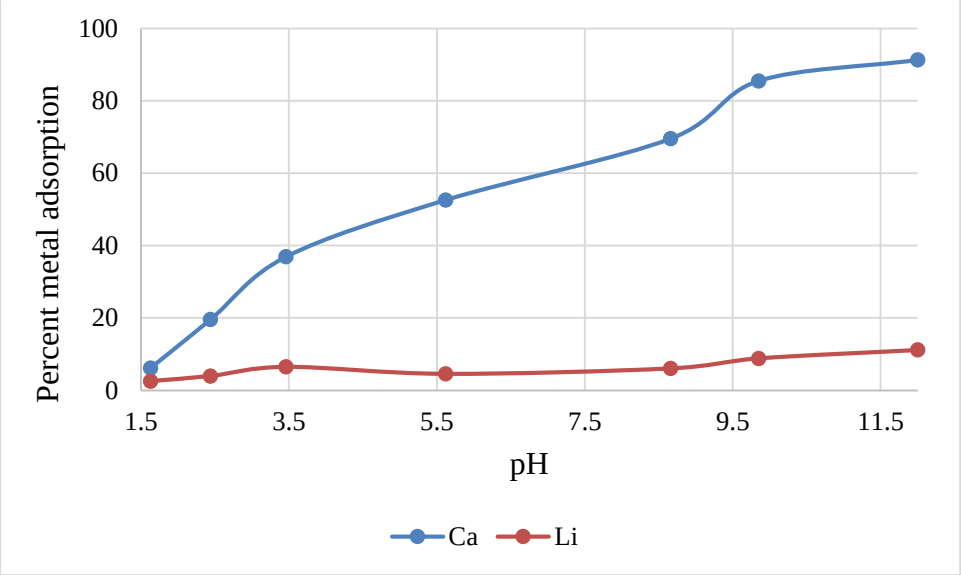

(a)

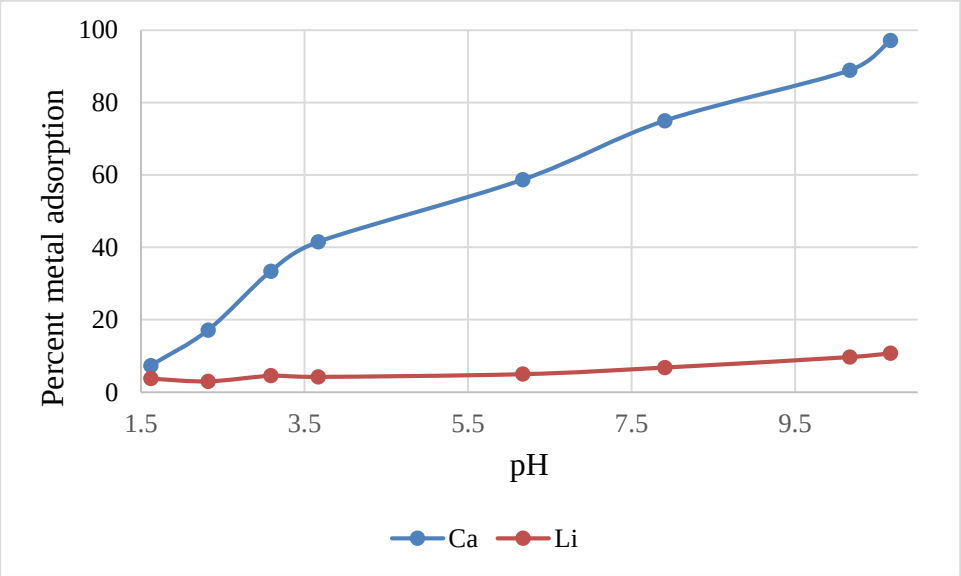

(b)

Figure 5.4: Percent metal adsorption at varying pH at (a) 25 °C and (b) 60 °C during IX; volume of resin and liquor = 50 mL and 250mL respectively.

5.5 Overview of the process

The two softening approaches may lead to two metallurgical flow diagrams for extracting lithium from the mineral in this study. Figure 5.5a describes the flow diagram resulting from softening of the liquor by carbonation which precipitates calcium as the carbonate which could be followed by solvent extraction (SX) using Cyanex® 936P; a high lithium affinity extractant (sometimes referred to as "the lithium magnet") to recover the lithium. It is a newly developed extractant aimed to selectively separate lithium from other alkali metals in any feed devoid of divalent metal ions. Thus, it will be suitable for the

recovery of lithium from the liquor after the softening. Not much is known about the extractant characteristics, but the little information obtained from manufacturers is given in Table 5.2.

Table 5.2: Characteristics of Cyanex 936P as indicated by manufacturers.

Appearance	Colourless to yellow
Dynamic viscosity	44.17 cp (25°C)
Flash point	>90°C (194°F) closed cap
Freezing point	< -32°C (-25.6°F)

The reagent has been used in the Tenova Advanced Technology Lithium Process for the recovery of lithium from brine where it is found to be fast and cheaper than the conventional process with the flexibility of yielding various lithium salts of high purity. No information in literature, to the best of our knowledge, is found about this material's behaviour for the recovery of lithium from leach liquor obtained from spodumene.

In Figure 5.5b (softening by IX), the liquor obtained after the IX which is almost barren of calcium may enters the SX unit after which the metal can be recovered. The loaded resin after regeneration with HCl produces calcium chloride solution which upon evaporation and dehydration may yield solid form of the salt which can be recycled to the chlorination unit. In this case the lithium that could have been lost through adsorption onto the resin is recycled alongside with calcium chloride.

Comparison of the two flow diagrams reveals that, activities suggested in Figure 5.5b if successful, leads to the recovery and reuse of the chlorination agent with little or no loss of lithium. Figure 5.5a on the other hand, may lead to loss of lithium through $CaCO_3$ precipitate formation except for its use for pH adjustment to precipitate magnesium in brine processing if the two processes are coupled. It must be noted that, solvent extraction experiments have been commenced but results are not currently available to be included in this thesis.

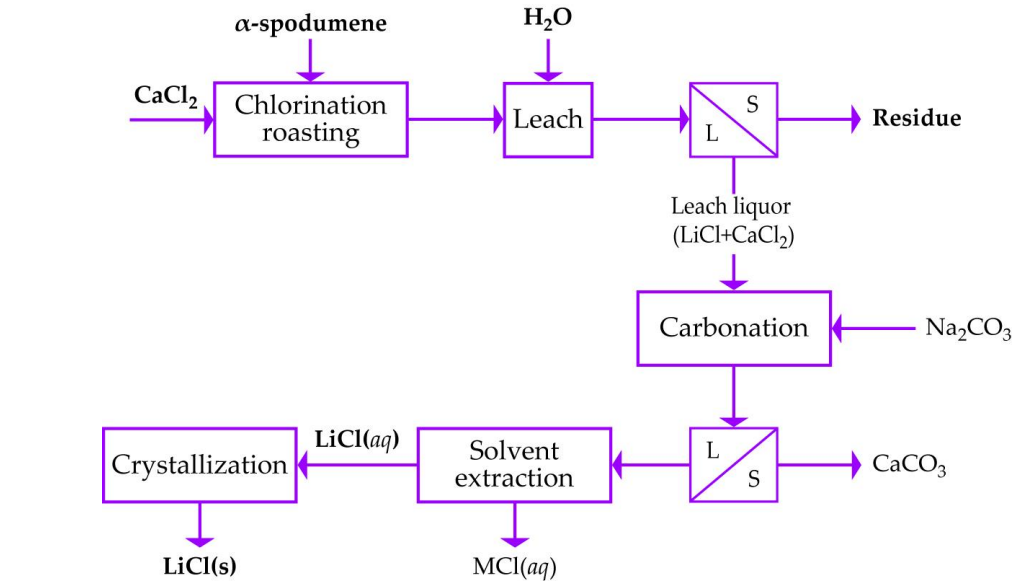

(a)

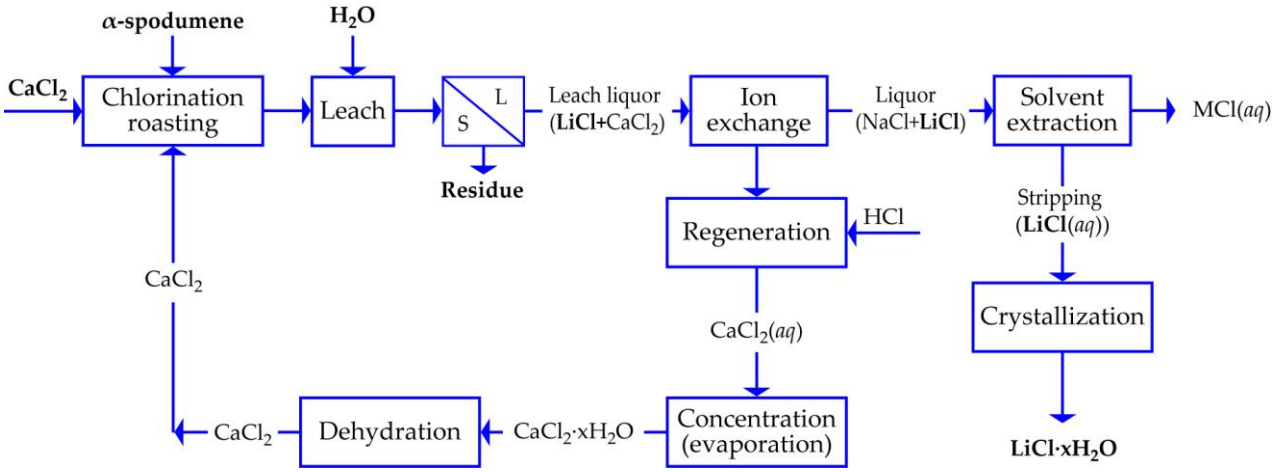

(b)

Figure 5.5: Process flow diagram for calcium separation by (a) carbonation precipitation and (b) ion exchange; M is an alkali metal.

5.6 Conclusion

Crystallisation to selectively recover calcium and reduce its concentration was a difficult task to execute because the viscous nature of the solution obtained after evaporation made separating crystals difficult. It was therefore considered not suitable to be incorporated into the process. Calcium separation from the liquor by the traditional carbonation approach can fully soften the liquor, apparently leaving no calcium in solution but the regeneration and recycle of calcium chloride is not possible with loss of about 20% of lithium alongside. An integrated approach that couples this process to the brine processing where there is a possibility of using the $CaCO_3$ is suggested. Ion exchange however, reveals the possibility

of recycling and reusing $CaCl_2$ which makes this option economically prudent compared to the conventional approach. Results from solvents extraction to enable a full description of the process is not available for the thesis due to time constraints.

REFERENCES

[1] S. Virolainen, M. Fallah Fini, V. Miettinen, A. Laitinen, M. Haapalainen, and T. Sainio, "Removal of calcium and magnesium from lithium brine concentrate via continuous counter-current solvent extraction," *Hydrometallurgy*, vol. 162, pp. 9–15, Jun. 2016, doi: 10.1016/j.hydromet.2016.02.010.

[2] Z. Li, J. Mercken, X. Li, S. Riaño, and K. Binnemans, "Efficient and Sustainable Removal of Magnesium from Brines for Lithium/Magnesium Separation Using Binary Extractants," *ACS Sustain Chem Eng*, vol. 7, no. 23, pp. 19225–19234, Dec. 2019, doi: 10.1021/acssuschemeng.9b05436.

[3] M. Grágeda, A. González, M. Grágeda, and S. Ushak, "Purification of brines by chemical precipitation and ion-exchange processes for obtaining battery-grade lithium compounds," *Int J Energy Res*, vol. 42, no. 7, pp. 2386–2399, Jun. 2018, doi: 10.1002/er.4008.

[4] P. M. Brown, "Process for the Production of High Purity Lithium Hydroxde." U.S. Patent No. 4,036,713, July 19, 1977.

[5] P. M. Brown, C., E., Falletta "Process for Producing High Purity Lithium Carbonate," U.S. Patent No. 4,207,297, Jun. 10, 1980.

[6] Z. Li and K. Binnemans, "Selective removal of magnesium from lithium-rich brine for lithium purification by synergic solvent extraction using β-diketones and Cyanex 923," *AIChE Journal*, vol. 66, no. 7, Jul. 2020, doi: 10.1002/aic.16246.

[7] T. E. Dwyer, "Recovery of lithium from spodumene ores," US Patent No. 2,801,153, July 30, 1957.

[8] Altura,"Lithium Carbonate Conversion Success", ASX Announcement, 16 January 2018. https://www.ansto.gov.au/media/1115/download (Accessed 30-01-2023).

[9] C., A. Olivier; J., J., Panneton and J., Perusse, "Continuous Production of Lithium Carbonate" US Patent No. 4,124,684, Nov. 7, 1978.

[10] S., Atkinson, "Ion exchangers make brine treatment using chlor-alkali electrolysis more efficient", *Membrane Technology*, No. 3, pp 8-8, 2019.

[11] W. T., Yi, Yi, C. Y., Yan, and P. H., Ma, “Removal of calcium and magnesium from LiHCO3 solutions for preparation of high-purity Li2CO3 by ion-exchange resin,” *Desalination*, vol. 249, no. 2, pp. 729–735, Dec. 2009, doi: 10.1016/j.desal.2009.01.034.

[12] X. Yu, X. Fan, Y. Guo, and T. Deng, “Recovery of lithium from underground brine by multistage centrifugal extraction using tri-isobutyl phosphate,” *Sep Purif Technol*, vol. 211, pp. 790–798, Mar. 2019, doi: 10.1016/j.seppur.2018.10.054.

[13] Y. Zeng, J. Cao, Z. Wang, J. Guo, and J. Lu, “Formation of Amorphous Calcium Carbonate and Its Transformation Mechanism to Crystalline CaCO3 in Laminar Microfluidics,” *Cryst Growth Des*, vol. 18, no. 3, pp. 1710–1721, Mar. 2018, doi: 10.1021/acs.cgd.7b01634.

CONCLUSION

This research work looks at developing a process to extract and recover high purity lithium salt from spodumene using the chlorination method with an overall decreased energy and reduced number of unit operations compared to the conventional and other contemporary processes. Literature on processing routes for minerals which was narrowed down to spodumene was conducted. HSC Chemistry® 5.1 was used to model and explain the processes reviewed and from a thermodynamic point of view, more insights and suggestions on promising reagents for the roasting process which are wealthy for future consideration were highlighted. After this, the sample which was obtained from the Pilgangoora (Australia) pegmatite deposit was characterised to envisage the mineralogical, physical, and chemical properties. The mineral characterisation was achieved by several analytical techniques including XRF, XRD, MLA, and SEM-EDS. This was followed by thermal treatment of the concentrate to understand the effect of temperature on the polymorphic and morphological changes. All three phases of the mineral (α, γ and β) were observed depending on the temperature and residence time. An application of a first order kinetic model enabled the determination of apparent activation energy for the transformation. Calcining the mineral altered the physical properties such as density, particle size and surface area with the degree of alteration being a function of temperature.

The thermochemical software was used as a guide to select calcium chloride as the most appropriate chlorination agent which was used in the study. Studies on the calcium chloride-spodumene roasting revealed 1000 °C treatment for 60 minutes and calcium chloride-spodumene molar ratio of 2.0 as optimal conditions for lithium extraction. Residence time ranging from 45 to 60 minutes was however, observed to be able to achieve the maximum extraction but above it, evaporation of lithium chloride occurs which leads to reduced recovery. The process was found to be characterised by an apparent activation energy of 122±6kJ mol^{-1} from 800 °C to 950 °C. Temperature was found essential for the extraction where the chlorinating agent attacks the mineral at its edges when the temperature is low but attacks the internal portions at high temperatures by creating channels through the mineral grains resulting in an increased extraction. Phases evolving due to the chlorination were predicted with HSC Chemistry® which were confirmed by XRD investigation. Anorthite was the major phase observed in the leached residue whose quantity increases with temperature. The increasing anorthite was found to correspond to the disappearing spodumene phase.

The last part of the study was focussed on purifying the leach liquor for subsequent lithium recovery. Calcium is the major impurity identified in the pregnant leach liquor arising from the chlorination agent used. Purification techniques were therefore primarily geared towards separating calcium from the liquor. Purification techniques investigated include selective crystallisation of calcium chloride, carbonation precipitation using sodium carbonate and ion exchange (IX). Calcium separation technologies were supposed to be followed by solvent extraction (SX) to separate lithium from alkali metals in the liquor and subsequently, recover the metal but this step was not touched on due to time limitation. Crystallisation of calcium chloride was to reduce the concentration of calcium before the application of subsequent purification techniques. Preliminary study revealed difficulty in achieving this goal due to the viscous nature of the liquor after evaporation and the difficulty in separating crystals. Carbonation precipitation of calcium as $CaCO_3$ achieves almost 100% efficiency but leads to loss of some lithium (about 20%). IX can also reduce the calcium concentration drastically with a possibility of recycling the chlorinating agent to the chlorination unit in the overall flow process. SX studies have been commenced but results are currently, not available for discussion.

Recommendation

It is recommended that, the SX studies be completed to enable the overall process assessment including the economics, purity of the recovered lithium salt and its suitability to produce Li-ion battery. At this point of the study, it is suggested that future work looks at the use of eutectic mixtures of chloride salts for the process. This is because the mixture is known to have a lower melting point than the individual salts, making it interesting to investigate the possibility of using it as a chlorination agent to reduce the energy requirements when processing the mineral.

Titre : Développement d'une voie chlorure pour la récupération du lithium contenu dans les minerais de spodumene

Contexte

Le lithium est un composant majeur des batteries Li-ion, utilisées dans la fabrication de nombreux appareils électroniques portables mais également pour les véhicules électriques. La récente vague de décarbonisation a en effet pour conséquent le passage des véhicules à combustibles fossiles à des véhicules électriques et hybrides dont la source d'énergie est stockée principalement dans des batteries Li-ion. Cela a conduit à une demande record en lithium sous forme de carbonate ou d'hydroxyde de lithium pour répondre à la production croissante de véhicules électriques mais aussi à la demande plus traditionnelle pour la production de lubrifiant, le domaine médical ou encore l'industrie chimique (base et agent nucléophile) [1].

Le lithium est extrait de de deux ressources principales : les saumures des salars et les minerais de pegmatite. Environ 50 % du lithium mondial est obtenu à partir de saumures, bien que sa teneur dans ces sources soit relativement plus faible (environ 200 à 700 ppm) que dans les minerais [2-3]. Les récentes études laissent penser que les saumures des Andes sont formées au cours du lavage des sels de lithium solubles contenus dans les cendres volcaniques dans les réservoirs endoréiques [4]. Si ce phénomène se produit dans un environnement aride ou à haute altitude, où il existe une corrélation inverse entre l'altitude et la pression atmosphérique, un taux élevé d'évaporation de l'eau de la saumure se produit, laissant derrière lui des lits secs communément appelés salars. Les conditions climatiques de l'Argentine, de la Bolivie et du Chili (généralement appelé le Triangle du lithium) favorisent la formation de salars, ce qui fait que ces pays abritent une part importante des réserves mondiales de lithium [5]. Les salars les plus connus de cette région sont le Salar de Uyuni, le Salar de Atacama et le Salar de Muerto Hombre, situés respectivement en Bolivie, au Chili et en Argentine. Des gisements de saumure sont également présents de manière significative aux États-Unis, en Chine, en Inde et au Canada.

Le traitement de la saumure pour le lithium se fait en pompant pendant 8 à 18 mois la saumure dans des bassins d'évaporation. L'évaporation conduit à l'élimination naturelle du calcium, du potassium et du magnésium sous forme de sels de chlorure. Le chlorure de lithium cristallise naturellement en dernier. Celui-ci est ensuite lavé puis converti en carbonate de lithium à l'aide de carbonate de sodium après des étapes de purification

consistant à éliminer les divalents ainsi que le bore. Cette étape de raffinage se fait généralement hors site. Ce procédé est moins coûteux, mais les principaux inconvenients sont la gestion des impuretés et le temps de traitement.

Les pegmatites sont des roches à gros grains qui contiennent plusieurs phases minéralurgiques de lithium ainsi que des éléments de terres rares qui sont exploités de manière sélective et économique à l'aide de techniques minières classiques. Ce gisement de lithium peut être classé en trois catégories : le type NYF, composé de niobium, d'yttrium et de fluor ; le type LCT, composé de lithium, de césium et de tantale, et enfin le type mixte NYF+LCT [6]. Les minéraux de lithium (spodumène, pétalite, lépidolite, etc.) et d'autres minéraux concomitants (colombo-tantalite, cassitérite, pollucite, comme la muscovite, l'albite, le quartz, le feldspath) sont généralement associés à la pegmatite LCT. L'association étroite du lithium avec les pegmatites est due à sa grande solubilité qui le concentre dans la dernière phase du refroidissement du magma et des liquides aqueux associés, là où les pegmatites se forment. Près de 145 minéraux contenant du lithium, y compris des argiles, ont été répertoriés, dont environ 25 contiennent plus de 2 % de Li_2O [4-5]. Parmi les minéraux contenant du lithium, le spodumène est le plus intéressant pour l'extraction industrielle du lithium.

Le processus conventionnel d'enrichissement du spodumène consiste à le transformer de la phase α naturelle à la phase β à des températures élevées (processus de décrépitation). La forme β du minéral est ensuite grillée pour former un sel de lithium approprié qui peut être lixivié en vue d'un traitement en aval pour récupérer le lithium. Le type de réactif utilisé pour le grillage détermine le nom du processus : traitement sulfatant, traitement alcalin, carbonatation, chloration et fluoration. La sulfatation utilise de l'acide sulfurique, des sulfates de métaux alcalins ou du SO_3 pour produire du sulfate de lithium soluble ; l'emploi de chaux alcaline ou de calcaire forme du Li_2O qui peut être lixivié pour produire une solution aqueuse de LiOH. Dans la carbonatation, le carbonate de lithium est produit par torréfaction du carbonate de sodium et du minéral, tandis que les procédés de chloration et de fluoration utilisent respectivement des agents de chloration ($CaCl_2$, Cl_2, NaCl) et des agents de fluoration (NaF, HF).

L'état de l'art révèle que l'un des principaux défis rencontrés dans toutes les voies de traitement ci-dessus est la décrépitation. Elle s'effectue en effet à des températures très élevées pendant une durée relativement longue, ce qui la rend le processus énergivore et augmente le coût de production. Parmi les différentes voies de traitement indiquées ci-dessus, le chloration est finalement assez peu décrite dans la littérature bien qu'elle présente

un avantage principal : des températures de traitement modérées conduisant à de bons rendements d'extraction. Ainsi, ce travail de thèse a consisté à évaluer la possibilité de mettre en œuvre une étape de chloration directe de l'α-spodumène en amont du traitement hydrométallurgique pour pouvoir extraire le lithium contenu dans la spodumène à une température réduite, et ainsi diminuer la consommation d'énergie liée à l'étape de décrépitation et à l'étape de grillage, ainsi que le temps de traitement. Ainsi, l'objectif principal de cette thèse est d'approfondir les connaissances pour mieux décrire les phénomènes prenant place pendant l'étape de chloruration, et de vérifier la faisabilité technique de l'extraction du lithium par chloration directe de l'α-spodumène.

Dans un premier temps, le logiciel HSC Chemistry® 5.1 a été utilisé pour réaliser une modélisation thermodynamique des processus de traitement du spodumène décrits dans la littérature. Cette modélisation thermodynamique nous a permis d'identifier des réactifs prometteurs et les conditions expérimentales pour réaliser une chloruration efficace.

Dans un second temps, nous avons caractérisé les propriétés minéralogiques, physiques et chimiques du concentré provenant du gisement de pegmatite de Pilgangoora (Australie) qui a été utilisé pour les essais de décrépitation et de chloruration dans ce travail de thèse. La caractérisation des minéraux a été réalisée à l'aide de plusieurs techniques analytiques, notamment XRF, XRD, MLA et SEM-EDS. Un traitement thermique du concentré a ensuite été effectué pour comprendre l'effet de la température sur les changements polymorphiques et morphologiques. A partir de la caractérisation du concentré, des calculs thermochimique réalisés par HSC Chemistry® 5.1 et de tests préliminaires, nous avons sélectionné le chlorure de calcium comme réactif de chloruration, puis nous avons optimisé les conditions opératoires afin de convertir efficacement le lithium contenu dans le spodumène en chlorure de lithium accessible pour l'étape suivante de lixiviation en vue de récupérer le lithium au cours d'étapes hydrométallurgiques ultérieures de purification et de concentration qui ont fait l'objet d'essais dans la dernière partie du manuscrit de thèse.

Résultats et discussion

Modélisation thermochimique du traitement thermique du spodumene.

Les calculs thermodynamiqes réalisés à l'aide du logiciel HSC Chemistry® 5.1 confirment que le traitement sulfatant, le traitement alcalin, la fluoration, la chloration ainsi que la carbonatation à l'aide de sels appropriés sont réalisables d'un point de vue thermodynamique. Il n'est donc pas surprenant que la sulfatation (à l'aide d'acide sulfurique)

et les traitmements alcalins soient industrialisables pour l'extraction du lithium contenu dans la spodumène. Si l'on considère la nature douce des réactifs utilisés dans les procédés alcalins, le procédé acide sera un véritable concurrent si l'on parvient à réduire d'une manière ou d'une autre la quantité d'énergie nécessaire à la décomposition du calcaire. Bien que le grillage à l'aide de la chaux soit possible même à des températures plus basses, la décomposition du calcaire est un précurseur de la production industrielle de chaux, ce qui rend le processus global très énergivore. Les travaux futurs doivent se concentrer sur la réduction de la quantité de chaleur élevée nécessaire à la décomposition du calcaire pour rendre le procédé alcalin économiquement viable. Dans le processus de grillage de l'acide, l'étude thermodynamique a révélé que le H_2SO_4 peut se décomposer au-dessus de 250 °C pour produire du $SO_{3(g)}$) et du $H_2O_{(g)}$. Bien que l'acide se décompose, l'espèce formée s'est avérée capable d'entraîner la réaction pour produire le sel de lithium, même à un rythme plus rapide en raison de la vitesse de diffusion plus élevée des gaz résultants que de l'acide (qui est en phase liquide). Malgré la vitesse de réaction plus rapide attendue de ces gaz (SO_3 et H_2O), nous ne savons que peu de choses sur leur utilisation pour extraire le lithium contenu dans les minerais porteur de lithium. La sulfatation est essentiellement réalisée avec de l'acide sulfurique bien qu'il soit intéressant d'identifier d'autres types de réactifs. Il existe une littérature considérable sur l'utilisation de certains sulfates de métaux alcalins et alcalino-terreux ainsi que de sulfates d'ammonium pour le traitement d'autres minéraux contenant du lithium, en particulier la lépidolite et le spodumène. Cependant, ces études se limitent à de simples essais expérimentaux alors qu'il serait judicieux de s'appuyer sur des outils de calculs thermodynamiques pour identifier les conditions conduisant à une extraction optimale du lithium. Selon la littérature, la chloration et la fluoration sont des étapes prometteuses pour l'extraction du lithium. Peu d'agents de chloration et de fluoration sont mentionnés dans la littérature. Il faudrait donc poursuivre les recherches pour trouver de nouveaux agents de fluoration et de chloration et optimiser les procédés. La thermodynamique du processus de carbonatation produisant du carbonate de lithium est très intéressante car cela permet potentiellement de produire du carbonate de lithium relativement pur à basse température. Des recherches complémentaires doivent être menées pour optimiser le processus. D'un point de vue thermodynamique, ces procédés ne doivent pas impliquer des températures supérieures à 300 °C pour éviter la décomposition de l'acide et du carbonate de lithium. Pour les autres procédés examinés, des températures inférieures à 600 °C sont conseillées, à l'exception de la fluoration, qui donne des résultats intéressants à des températures légèrement supérieures à 600 °C.

Effet du traitement thermique sur le concentré de spodumène

Les caractéristiques physicochimiques et les transformations thermiques du concentré de spodumène original ont révélé que les distributions en taille des particules d50 et d80 sont respectivement de 57 microns et de 113 microns. Le diamètre des particules varie de 10 à 200 microns, environ 68 % du volume total ayant un diamètre de 80 microns. Dans ces conditions, l'analyse de la libération des minéraux a révélé que le spodumène était bien libéré à environ 99 %, ce qui indique qu'une réduction suffisante de la taille des particules a été obtenue pour permettre un traitement ultérieur.

La transformation de phase de l'échantillon au cours du traitement thermique à une température variant de 900 à 1050 °C pendant un temps de séjour de 7,5 à 480 minutes a indiqué que le α-spodumène, le γ-spodumène et le β-spodumène sont les polymorphes présents au cours du processus. On sait généralement que le traitement thermique conduit aux transformation de phases suivantes :

$$\alpha \rightarrow \gamma + \beta \quad (1)$$

$$\gamma \rightarrow \beta \quad (2)$$

Ainsi, la phase α se transforme d'abord en formes γ et β, mais la forme γ est métastable et se transforme ensuite en forme β. On a observé que la transformation de la phase α s'achevait à 975 ou 1000 °C en fonction du temps de séjour. La transformation complète de la phase γ peut également se produire à 1025 °C et 1050 °C. La quantité maximale de γ-phase formée est d'environ 23 %. Nous indiquons que 1050 °C est la température seuil permettant de former le plus de phase β. Néanmoins, le procédé doit être optimisé car des études antérieures ont indiqué que la présence de moins de 10 % de phase γ dans le résidu n'a pas d'effet négatif majeur sur l'efficacité de l'extraction du lithium. Nous recommandons donc un traitement thermique à 1000 °C pendant 60 minutes pour réaliser une décrépitation efficace de ce concentré de spodumène compte tenu de l'économie et de la quantité de phase γ formée. Cependant, si seule la phase β est souhaitée pour une application industrielle, il est préférable de réaliser le traitement thermique entre 1025 ou 1050 °C en tenant compte du temps

nécessaire à la transformation, ainsi que de la fusion qui se produit à 1050 °C et de son effet sur le traitement en aval.

Un modèle cinétique du premier ordre a été appliqué aux deux processus de transformation (Eqs (1) et (2)). Ceci a permis de calculer l'énergie d'activation apparente de 655±20 pour la transformation de α en γ et β (Eq. 1). Les études MEB révèlent qu'avec l'augmentation de la température de traitement, les grains de spodumène subissent une fissuration, une destruction, suivie d'une fusion et d'une agglomération.

Extraction du lithium de l'α-spodumène par chloration à l'aide de chlorure de calcium.

Nous nous sommes également intéressé au cours de nos travaux à formation de chlorure de lithium directement à partir de l'α-spodumène par chloration au $CaCl_2$ puis à la lixiviation du chloure de lithium formé à l'eau afin de produire une solution pouvant être ensuite traitée pour produire un carbonate de lithium pur par voie hydrométallurgique. Les paramètres étudiés sont la température de grillage, le temps de séjour et le rapport chlorure de calcium/spodumène. Bien que le rapport $CaCl_2$/spodumène ait une influence sur la récupération du lithium, la température et le temps sont les principaux facteurs qui, s'ils ne sont pas régulés, entraînent l'évaporation du chlorure de lithium. La récupération du lithium dans la solution de lixiviation augmente généralement avec tous les paramètres étudiés. Dans des conditions optimales de température de 1000 °C, de temps de séjour de 60 minutes et un rapport chlorure de calcium/spodumène de 2, environ 90 % du lithium est éliminé du spodumène mais seulement 85 % de lithium est réellement récupéré en solution, le reste du lithium s’étant évaporé. Nous pouvons cependant envisager de récupérer le lithium évaporé en récupérant les poussières en sortie du procédé pyrométallurgiques et en les lixiviant. La fusion et l'agglomération se produisent à une température supérieure 1000 °C, ce qui entraîne une diminution de la récupération.

L'étude du comportement de la gangue (micas, feldspaths alcalins et amphiboles) en combinant des informations fournies par la diffraction des rayons X (XRD), des calculs thermodynamiques réalisés par HSC et des analyses par microscopie électronique à balayage couplée avec des analyses EDS (SEM-EDS) au cours du processus thermique a révélé que les micas se décomposent d'abord pour former du feldspath K qui se transforme ensuite en anorthite en réagissant avec le chlorure de calcium. Les feldspaths alcalins (et le spodumène) forment également de l'anorthite lorsqu'ils réagissent avec le chlorure de calcium, tandis que les amphiboles (trémolite) se décomposent pour former du diopside et de l'enstatite. Les résultats de la XRD ont confirmé les conclusions tirés des calculs

thermodynamique et les observations réalisées au SEM-EDS, qui révèlent que l'anorthite est la phase prédominante (représentant environ 70 %), tandis que le quartz, la wollastonite et le diopside sont des phases mineures. L'effet oxydant du système sur la faisabilité du processus a été étudié et s'est avéré plus favorable dans un environnement non oxydant qu'oxydant.

Le spodumène identifié dans les résidus lixiviés est sous forme α, sans identification de la forme β. Ceci suggère que l'extraction du lithium sous forme de chlorure se fait directement à partir de la phase α. Une transformation possible de l'α-spodumène en β-spodumène suivie de la formation rapide de chlorure de lithium à partir du β-spodumène (2α-spodumène $\rightarrow 2\beta$-$LiAlSi_2O_6 + CaCl_2 \rightarrow 2LiCl + 2SiO_2 + CaAl_2Si_2O_8$) peut également se produire. Cependant, nous n'avons pas pu vérifier totalement cette hypothèse à ce stade. L'énergie d'activation apparente relativement faible de 122±6 kJ mol^{-1} obtenue pourrait suggérer que la diffusion du chlorure de calcium est l'étape limitant la vitesse du processus.

Récupération du lithium contenu dans le jus de lixiviation du spodumene.

L'analyse de la liqueur obtenue après la lixiviation des résidus chlorés a révélé que le calcium provenant du chlorure de calcium utilisé pour la chloruration était l'impureté prédominante. Nous nous sommes donc intéressés à l'élimination du le calcium contenu dans le jus de lixiviation. Les technologies étudiées comprennent la cristallisation sélective du chlorure de calcium, l'extraction solide/liquide du calcium à l'aide de Lewatit® MDS TP 208 et la précipitation traditionnelle du calcium par carbonatation.

La cristallisation pour récupérer sélectivement le calcium et réduire sa concentration était une tâche difficile car la viscosité élevée de la solution obtenue après évaporation rendait la filtration difficile. Elle n'a donc pas été jugée appropriée pour la suite de l'étude. L'élimination du calcium du jus de lixiviation par carbonatation a été réalisée avec succès, mais la régénération et le recyclage du chlorure de calcium ne sont pas possibles. Cette méthode a également entraîné une perte d'environ 20 % du lithium. Une approche intégrée qui associe cette opération au traitement d'une saumure où il est possible d'utiliser le $CaCO_3$ est suggérée. L'élimination du calcium à l'aide d'une résine échange d'ions (IX) s'est également avérée très efficace puisque presque 100% du calcium a pu être éliminé. Il peut être envisagé de traité ensuite la solution de chlorure de lithium exempte de calcium par extraction par solvant (SX) en utilisant le Cyanex® 936P pour récupérer le lithium. Cet extractant récemment mis au point qui présente une grande affinité pour le lithium. Il a été utilisé dans le procédé Tenova pour récupérer le lithium contenu dans des saumures.

Schéma du procédé pyro-hydrométallurgique pour la récupération du lithium contenu dans la spodumène

L'objectif de la thèse était notamment de développer un schéma de procédé pyro-hydrométallurgique alternatif au procédé actuel reposant sur le grillage sulfatant de spodumène. Une choruration permettant d'extraire le lithium du spodumène sous forme de chlorure de lithium a l'avantage de produire une solution aqueuse de lithium en milieu chlorure dont la concentration en lithium et la chimie en milieu chlorure se rapproche de celle mise en œuvre dans l'extraction du lithium contenu dans les saumures. Il est alors possible d'imaginer un procédé de chloruration suivi d'un procédé d'extraction du lithium en milieu chlorure utilisant les technologies récemment développées pour extraire sélectivement le lithium d'un milieu chlorure (procédé Solvay-Tenova basé sur l'utilisation du Cyanex® 936P). La première étape de ce procédé doit pouvoir éliminer le calcium qui est l'impureté principale générée par la chloruration qui empêche une extraction efficace du lithium par le Cyanex® 936P. Les deux approches mises au point pour éliminer le calcium peuvent conduire à deux schémas de procédé permettant d'extraire le lithium contenu dans le spodumène. La Figure 1a décrit le schéma de procédé impliquant l'élimination du calcium par carbonatation, c'est-à-dire par précpitation du calcium sous forme de carbonate de calcium, puis l'extraction du lithum par extraction par solvant à l'aide de Cyanex® 936P. La Figure 1b présente un schéma de procédé reposant sur l'utilisation d'une résine échange d'ions (Lewatit® MDS TP 208) pour éliminer le calcium de la solution. La solution obtenue après traitement avec la résine échangeuse d'ions, qui est presque dépourvue de calcium, peut entrer dans l'atelier d'extraction par solvant pour extraire sélectivement et concentré le lithium. La résine chargée, après régénération avec de l'acide chlorhydrique, produit une solution de chlorure de calcium qui, après évaporation et déshydratation, conduite à la formation d'un sel de chlorure de calcium qui peut être recyclée dans l'unité de chloration. Dans ce cas, le lithium qui aurait pu être perdu par co-adsorption sur la résine pourrait être recyclé avec le chlorure de calcium.

Le schéma de procédé de la figure 1b permet de récupérer et de réutiliser l'agent de chloration avec peu ou pas de perte de lithium. La figure 1a, en revanche, peut entraîner une perte de lithium lors de la précipitation du carbonate de calcium, sauf si l'on associe ce processus au traitement de la saumure, auquel cas le précipité peut être utilisé pour l'ajustement du pH et pour la précipitation du magnésium. Dans ce cas, le lithium qui aurait pu être perdu pourrait être récupéré.

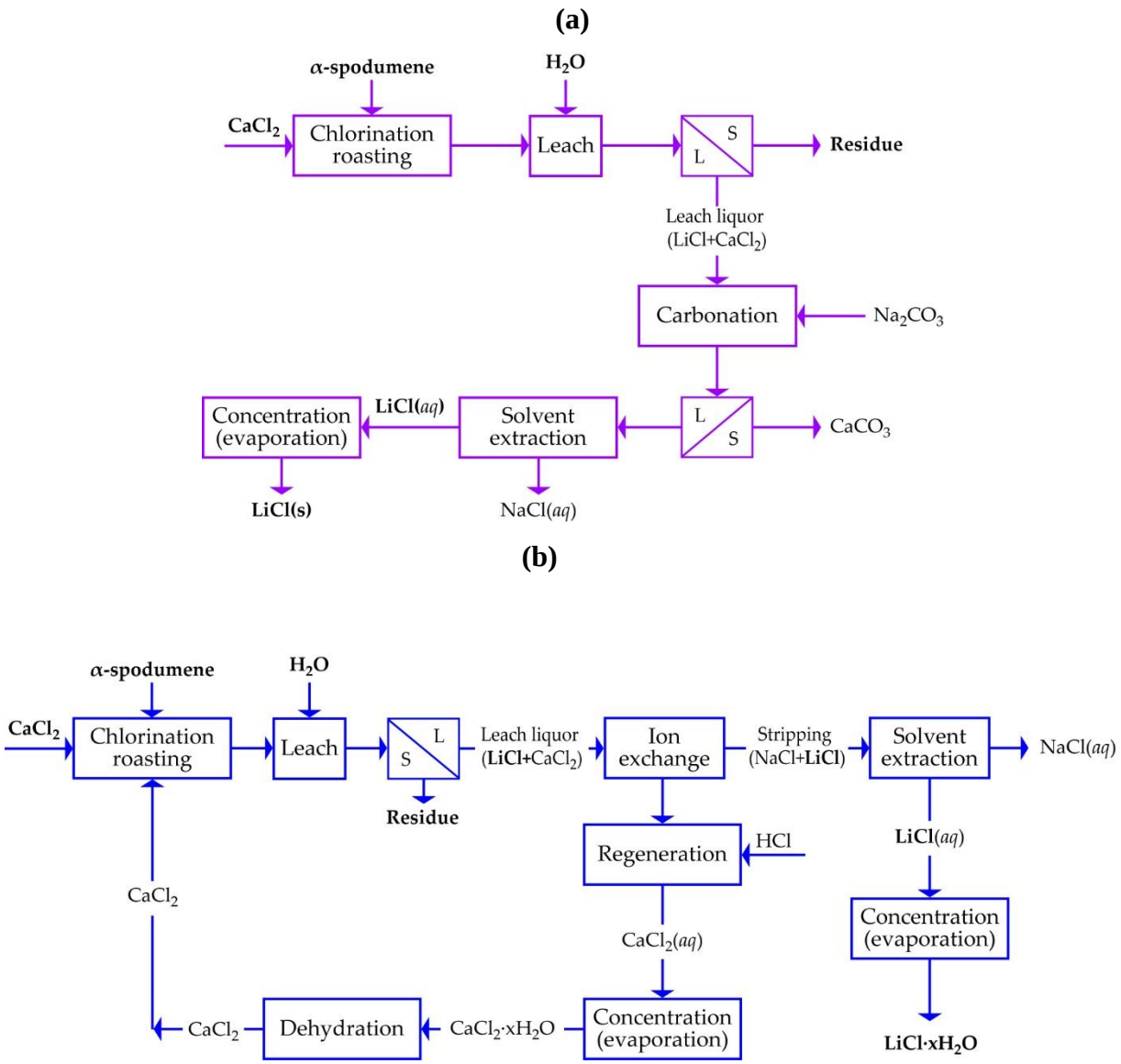

Figure 1 : Schémas de procédé (a) utilisant la précipitation par carbonatation et (b) une résine échange d'ions suivi d'une étape d'extraction liquide-liquide pour extraire et concentrer le lithium en cue de sa cristallisation sous forme de chlorure de lithium.

Conclusion

Des recherches ont été menées sur l'extraction directe et la récupération du lithium à partir de l'α-spodumène. Les investigations thermochimiques ont identifié le chlorure de calcium comme le sel de chlore le plus approprié pour le processus de chloration où, dans des conditions optimales de rapport chlorure de calcium/spodumène de 2,0, et de traitement à 1000 °C pendant 60 minutes, on a extrait environ 90 % de la teneur en lithium du minéral. Grâce à HSC Chemistry® 5.1 et à d'autres outils analytiques, le mécanisme du processus a

été expliqué pour rendre compte des nouvelles phases synthétisées pendant le grillage. À ce stade, il est suggéré que les travaux futurs portent sur l'utilisation de mélanges eutectiques de sels de chlorure pour le processus. En effet, on sait que le mélange a un point de fusion plus bas que les sels individuels, ce qui rend intéressante l'étude de la possibilité d'utiliser ces mélanges pour réduire les besoins en énergie lors du traitement du minéral.

REFERENCES

[1] J.-M. Tarascon, "'Is lithium the new gold?,'" *Nat Chem*, vol. 2, no. 6, pp. 510–510, 2010.

[2] P. K. Choubey, M. Kim, R. R. Srivastava, J. Lee, and J.-Y. Lee, "Advance review on the exploitation of the prominent energy-storage element: Lithium. Part I: From mineral and brine resources," *Miner Eng*, vol. 89, pp. 119–137, Apr. 2016, doi: 10.1016/j.mineng.2016.01.010.

[3] Z. Li, J. Mercken, X. Li, S. Riaño, and K. Binnemans, "Efficient and Sustainable Removal of Magnesium from Brines for Lithium/Magnesium Separation Using Binary Extractants," *ACS Sustain Chem Eng*, vol. 7, no. 23, pp. 19225–19234, Dec. 2019, doi: 10.1021/acssuschemeng.9b05436.

[4] D. E. Garrett, *Handbook of lithium and natural calcium chloride*. Elsevier, 2004.

[5] L. Kavanagh, J. Keohane, G. G. Cabellos, A. Lloyd, and J. Cleary, "Global lithium sources-industrial use and future in the electric vehicle industry: A review," *Resources*, vol. 7, no. 3. MDPI AG, 2018. doi: 10.3390/resources7030057.

[6] P. Černˊy and Č. Černˊy, "The Classification of Granitic Pegmatites Revisited," 2005. *The Canadian Mineralogist* 43, no. 6: 2005-2026.

APPENDICES

APPENDIX A: SUPPLEMENTARY MATERIAL FOR CHAPTER 3

Table A.1: Calculated elemental assay of major elements by MLA and their corresponding oxides.

Element	Wt%	Oxides	Wt%
Al	11.58	Al_2O_3	21.87
Ca	1.94	CaO	2.76
Fe	2.00	Fe_2O_3	2.86
K	1.34	K_2O	3.23
Li	1.96	Li_2O	4.22
Mg	0.50	MgO	0.83
Mn	0.22	MnO	0.41
Na	0.76	Na_2O	2.05
P	0.17	P_2O_5	0.22
S	0.07	SO_3	0.18
Si	29.47	SiO_2	63.15

Table A.2: MLA data for degree of mineral liberation in concentrate used to generate Figure 3.6.

Mineral	Liberation degree
Pyrite	98.3
Quartz	98.8
Orthoclase	93.7
Albite	98.2
Anorthite	97.2
Biotite	98.4
Muscovite	96.0
Chlorite	97.2
Amphibole	96.9
Spessartine	94.1
Spodumene	98.8
Tantalite_Mn	96.6
Calcite	95.8
Apatite	96.2

Table A.3: SD on atomic percent of elemental composition of spodumene in concentrate.

Element	**Atomic %**													**SD**
Al	11.3	11.3	11.6	11.5	11.5	11.5	11.4	11.3	11.3	11.4	11.4	11.2	11.3	0.1036
Si	23.9	23.9	23.7	23.7	23.8	23.6	23.7	23.8	23.9	23.6	23.6	23.8	23.7	0.1029
O	64.8	64.8	64.7	64.7	64.7	64.7	64.7	64.8	64.8	64.7	64.7	64.8	64.7	0.0231
Fe						0.2		0.2		0.2	0.3	0.2	0.5	0.0539
Mn							0.2							

Table A.4: SD on atomic percent of elemental composition of amphiboles in concentrate.

E*	**Atomic %**															**SD**
Mg	6.1	5.5	4.6	7.3	10.5	6.4	10.3	9.6	7.1	4.2	8.6	6.0	4.3		5.6	2.1346
Al	0.2	0.2	3.6	0.4	4.6	2.8	3.2	1.7	3.3	4.8	9.1		5.2	9.5		2.9863
Si	19.7	19.7	21.8	19.9	18.3	19.2	3.8	19.6	18.0	17.1	12.8	19.7	16.8	14.8	19.6	4.3916
Ca	9.6	9.6	3.2	9.5	0.4	5.0	0.3	4.7	5.0	3.9		9.6	4.8	0.2	9.7	3.6591
Fe	3.6	3.9	3.0	2.2	2.9	4.5	20.3	2.8	4.8	6.9	7.4	3.7	6.2	6.3	4.2	4.3969
O	60.8	60.9	62.1	60.6	60.4	61.2	58.4	60.8	60.7	61.0	60.1	60.8	60.8	61.3	60.9	0.7813
Na			0.8		1.3	0.5		0.4	0.8	0.9	1.0		1.1			0.2947
K			1.0		1.4	0.4		0.3	0.4	1.0	1.0		0.5			0.4113
Cr					0.3		2.5	0.2			0.2					1.1491
Mn						0.2	1.2			0.2		0.2	0.2	8.0		3.1233

***Element**

Table A.5: SD on atomic percent of elemental composition of quartz in concentrate

Element	Atomic %										SD
Si	33.3	33.3	33.3	33.3	33.3	33.3	33.3	33.3	33.3	33.3	0.0
O	66.7	66.7	66.7	66.7	66.7	66.7	66.7	66.7	66.7	66.7	0.0

Table A.6: SD on atomic percent of elemental composition of albite in concentrate.

Element	Atomic %								SD
Na	5.5	7.3	7.0	6.7	7.0	7.0	6.7	5.5	0.6861
Al	5.4	7.8	7.7	7.8	7.7	7.6	7.7	5.4	1.0706
Si	26.0	23.1	23.4	23.2	23.5	23.5	23.3	26.0	1.2354
O	63.0	61.7	61.9	61.8	61.9	61.9	61.9	63.0	0.5219
Ca	0.1	0.2	0.1	0.3			0.2	0.1	0.0579

Table A.7: SD on atomic percent of elemental composition of mica in concentrate.

Element	Atomic %			SD
Al	15.0	15.0	15.1	0.0557
Si	17.7	17.5	17.5	0.1300
K	4.9	5.1	5.3	0.1823
Fe	0.9	0.9	0.8	0.0702
O	61.6	61.4	61.4	0.0985

Table A.8: SD on atomic percent of elemental composition of hematite in concentrate.

Element	Atomic %					SD
Fe	37.9	40.0	38.1	38.7	38.9	0.8418
O	60.1	60.0	60.2	60.2	60.1	0.0728
Si	1.3		1.0	1.0	0.6	0.2971
Ca	0.4					
Mn	0.4					
Al			0.8	0.4	0.4	0.2136

Table A.9: SD on atomic percent of elemental composition of apatite in concentrate.

Element	Atomic %				SD
F	7.9	8.1	7.9	8.6	0.3320
P	14.5	14.6	14.5	14.6	0.0455
Ca	20.4	19.8	20.1	20.2	0.2443
Mn	0.3	0.6	0.5		0.15875
O	56.9	56.9	57.0	56.6	0.1656

SD* represents the standard deviation on measured atomic percent of elements in mineral phases of the concentrate.

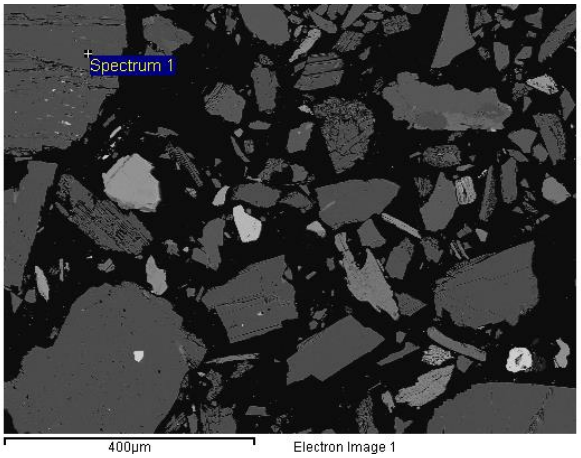

(a)

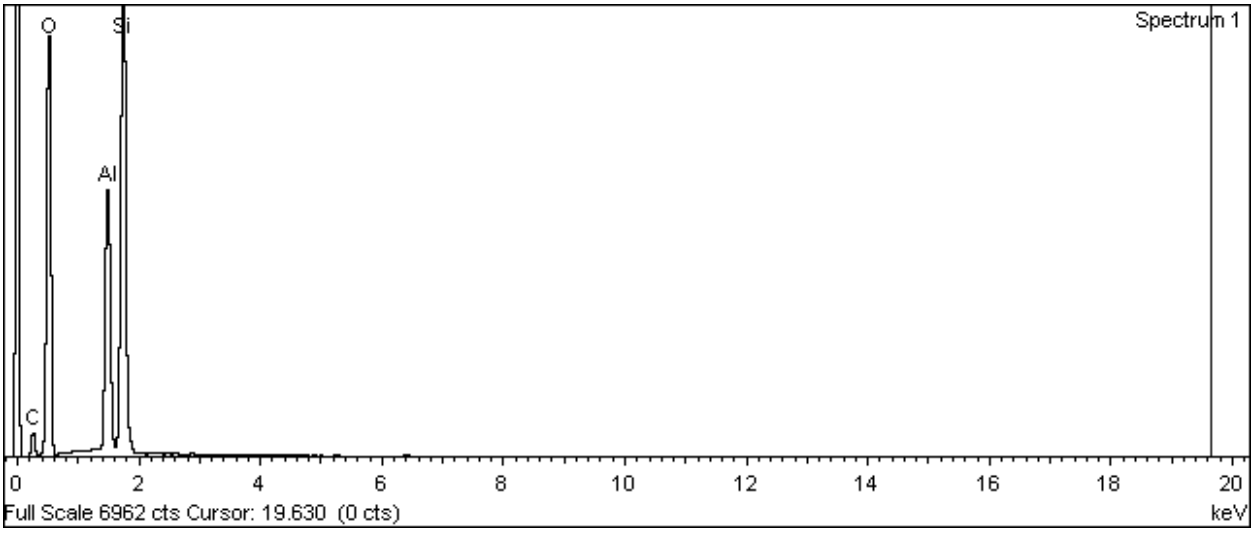

(b)

Figure A.1: Spot analysis (a) and spectrum (b) of elemental composition of spodumene grain in concentrate.

Table A.10: Raw data of spodumene grain generated by SEM-EDS for spectrum 1.

Element	App Conc.	Intensity Corrn.	Weight%	Weight% Sigma	Atomic%	Compd%	Formula	Number of ions
Al K	15.23	1.0706	14.23	0.14	11.32	26.88	Al_2O_3	1.40
Si K	29.53	0.9441	31.28	0.22	23.90	66.92	SiO_2	2.95
O			48.29	0.27	64.78			8.00
Total			93.79					
							Cation sum	4.35

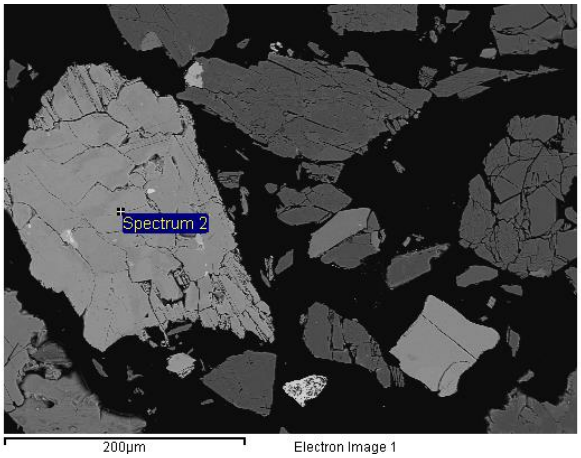

(a)

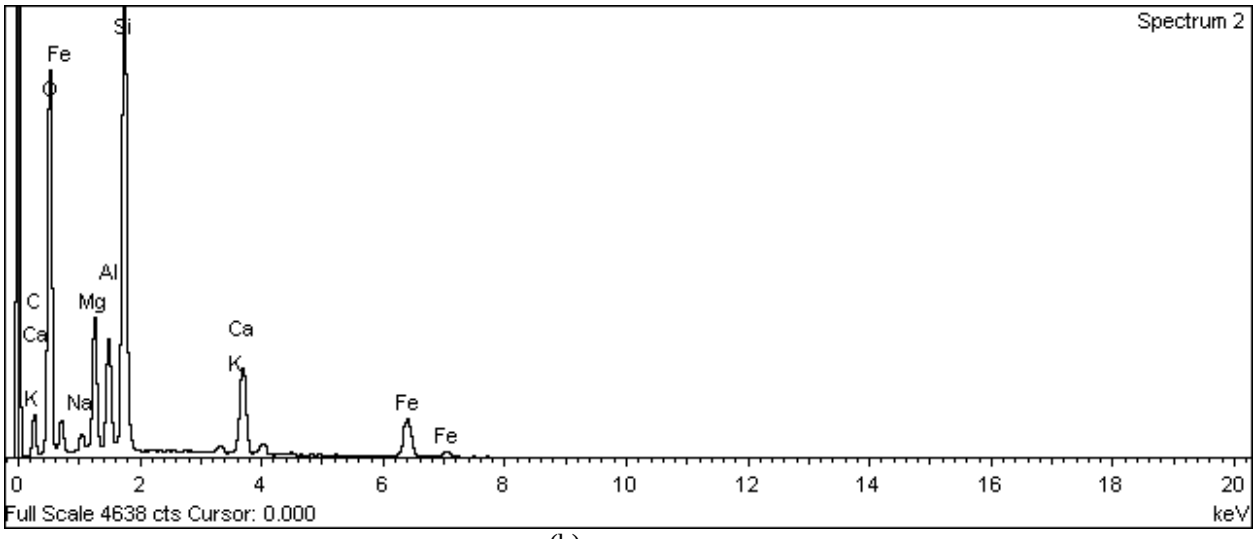

(b)

Figure A.2: Spot analysis (a) and spectrum (b) of elemental composition of amphibole grain in concentrate.

Table A.11: Raw data of amphibole grain generated by SEM-EDS for spectrum 2.

Element	App Conc.	Intensity Corrn.	Weight%	Weight% Sigma	Atomic%	Compd%	Formula	Number of ions
Na K	0.76	0.7734	0.98	0.09	0.99	1.32	Na_2O	0.13
Mg K	5.09	0.8572	5.94	0.11	5.65	9.84	MgO	0.74
Al K	4.14	0.8850	4.68	0.10	4.01	8.84	Al_2O_3	0.53
Si K	19.24	0.9257	20.78	0.19	17.11	44.45	SiO_2	2.26
K K	0.75	1.0364	0.73	0.07	0.43	0.88	K_2O	0.06
Ca K	8.83	0.9932	8.89	0.16	5.13	12.44	CaO	0.68
Fe K	12.98	0.8989	14.44	0.35	5.98	20.64	Fe_2O_3	0.79
O			41.99	0.35	60.70			8.00
Total			98.42					
							Cation sum	5.18

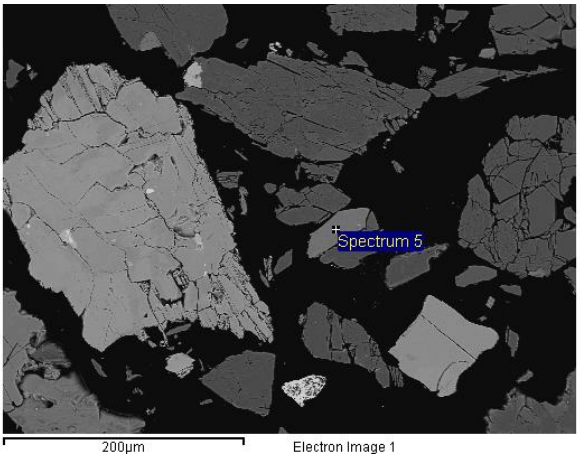

(a)

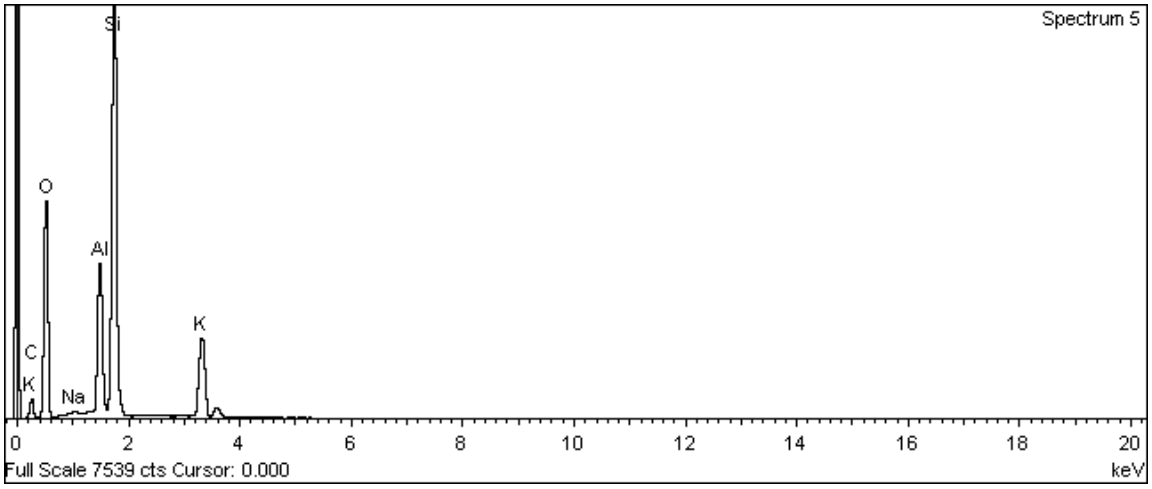

(b)

Figure A.3: Spot analysis (a) and spectrum (b) of elemental composition of mica grain in concentrate.

Table A.12: Raw data of mica grain generated by SEM-EDS for spectrum 5.

Element	App Conc.	Intensity Corrn.	Weight%	Weight% Sigma	Atomic%	Compd%	Formula	Number of ions
Na K	0.25	0.9318	0.27	0.07	0.24	0.37	Na_2O	0.03
Al K	10.22	1.0583	9.66	0.12	7.41	18.24	Al_2O_3	0.96
Si K	31.64	0.9966	31.75	0.22	23.42	67.92	SiO_2	3.04
K K	13.62	0.9978	13.65	0.19	7.23	16.45	K_2O	0.94
O			47.65	0.28	61.69			8.00
Total			102.98					
							Cation sum	4.97

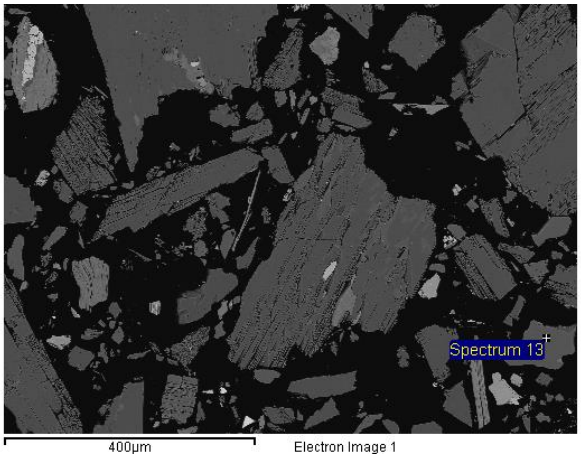

(a)

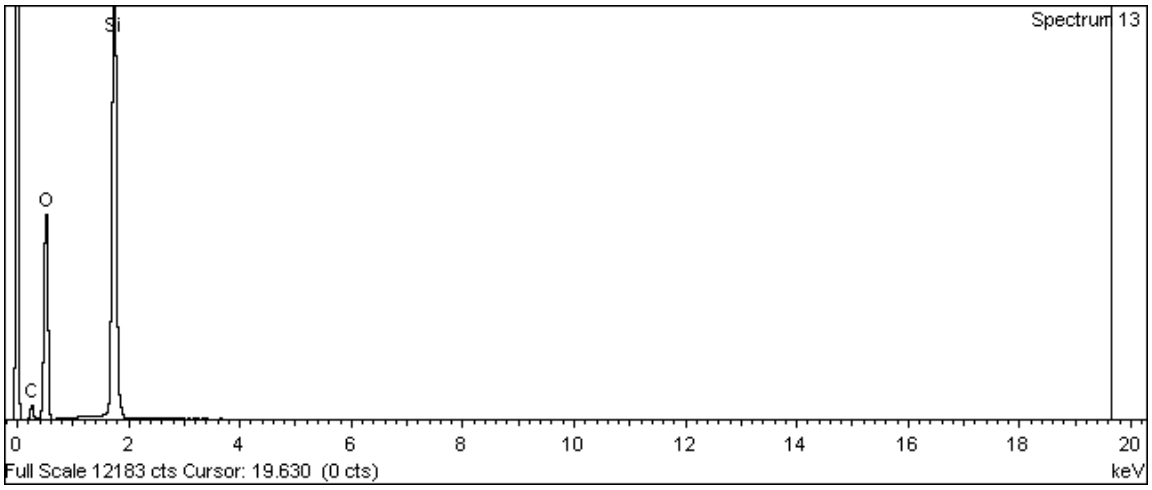

(b)

Figure A.4: Spot analysis (a) and spectrum (b) of elemental composition of quartz grain in concentrate.

Table A.13: Raw data of quartz grain generated by SEM-EDS for spectrum 13.

Element	App Conc.	Intensity Corrn.	Weight%	Weight% Sigma	Atomic%	Compd%	Formula	Number of ions
Si K	51.87	*1.0841*	47.84	0.25	33.33	102.34	SiO_2	4.00
O			54.50	0.27	66.67			8.00
Total			102.34					
							Cation sum	4.00

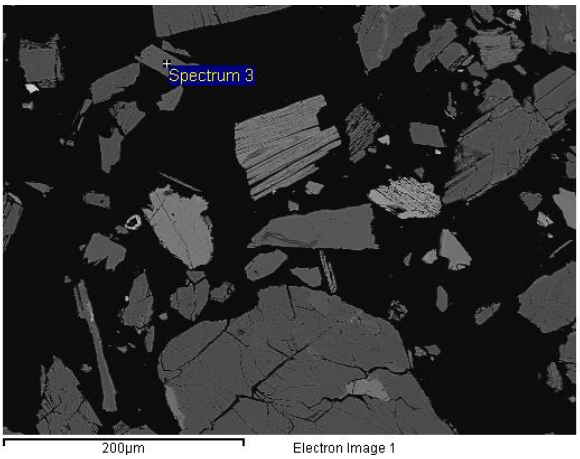

(a)

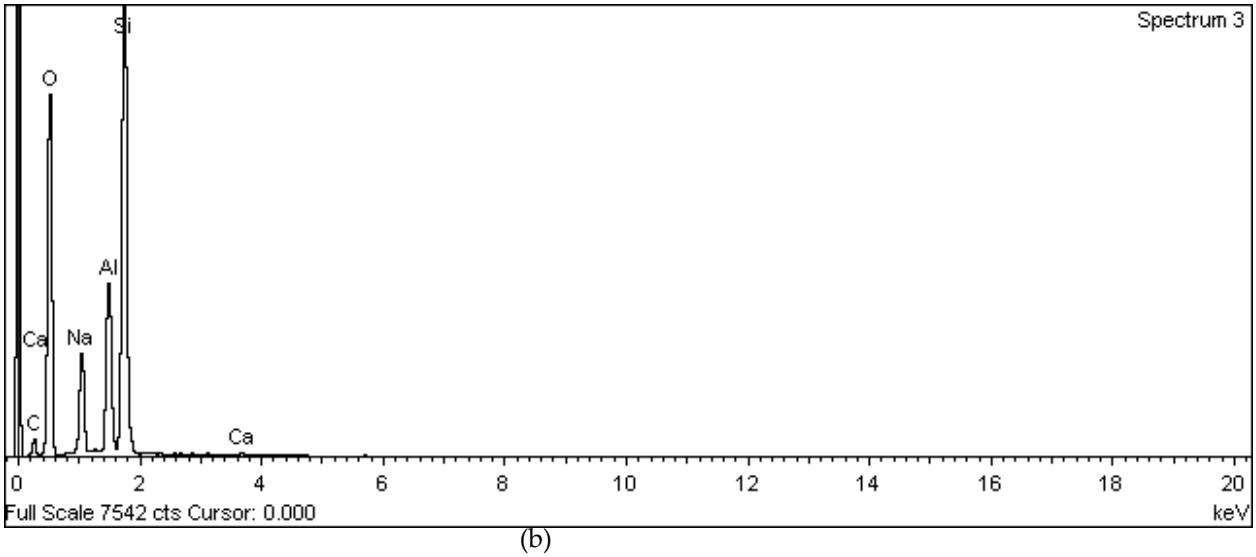

(b)

Figure A.5: Spot analysis (a) and spectrum (b) of elemental composition of albite grain in concentrate.

Table A.14: Raw data of albite grain generated by SEM-EDS for spectrum 3.

Element	App Conc.	Intensity Corrn.	Weight%	Weight% Sigma	Atomic%	Compd%	Formula	Number of ions
Na K	8.03	0.9852	8.16	0.14	6.97	10.99	Na_2O	0.90
Al K	10.59	1.0027	10.56	0.13	7.69	19.95	Al_2O_3	0.99
Si K	31.65	0.9473	33.41	0.23	23.37	71.48	SiO_2	3.02
Ca K	0.22	0.9489	0.23	0.06	0.11	0.33	CaO	0.01
O			50.39	0.29	61.86			8.00
Total			102.74					
							Cation sum	4.93

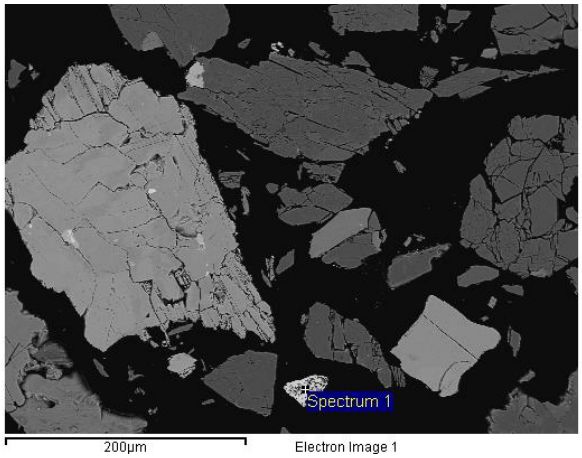

(a)

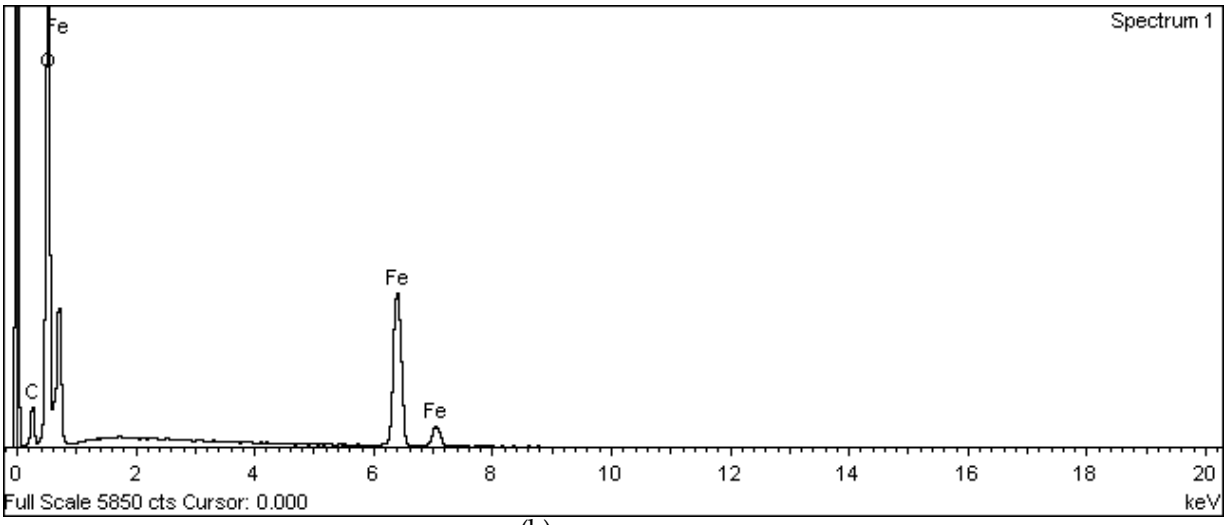

(b)

Figure A.6: Spot analysis (a) and spectrum (b) of elemental composition of hematite grain in concentrate.

Table A.15: Raw data of hematite grain generated by SEM-EDS for spectrum 1.

Element	App Conc.	Intensity Corrn.	Weight%	Weight% Sigma	Atomic%	Compd%	Formula	Number of ions
Fe K	70.80	0.9998	70.81	0.66	40.00	101.24	Fe_2O_3	5.33
O			30.43	0.43	60.00			8.00
Total			101.24					
							Cation sum	5.33

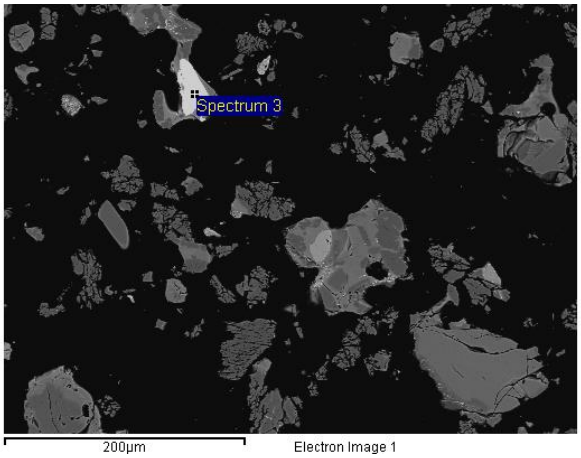

(a)

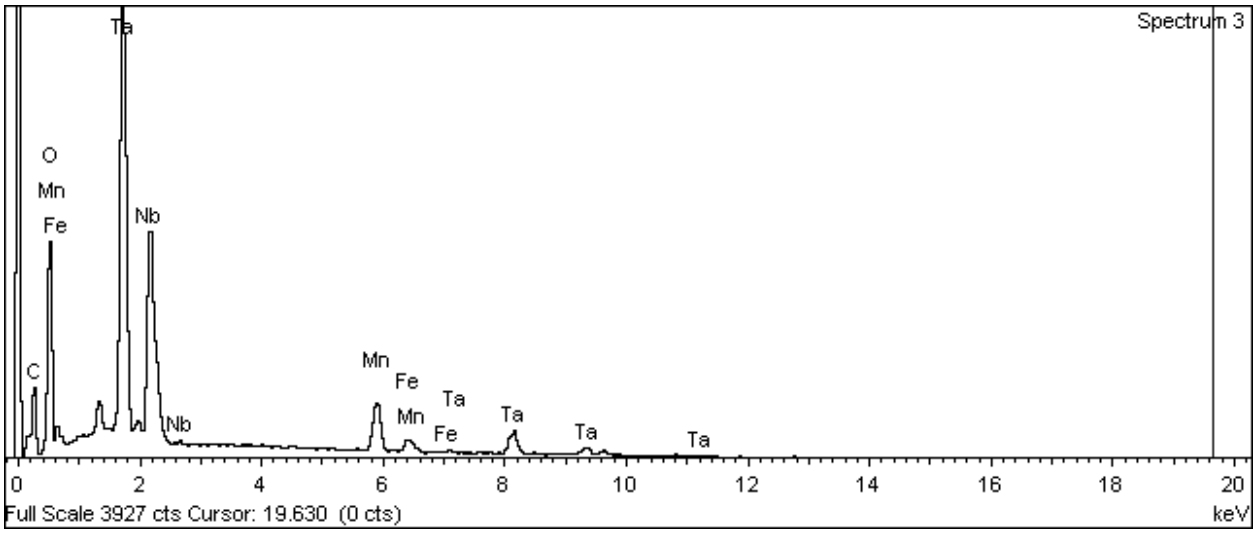

(b)

Figure A.7: Spot analysis (a) and spectrum (b) of elemental composition of tantalite grain in concentrate.

Table A.16: Raw data of tantalite grain generated by SEM-EDS for spectrum 3.

Element	App Conc.	Intensity Corrn.	Weight%	Weight% Sigma	Atomic%	Compd%	Formula	Number of ions
Mn K	12.43	1.1398	10.90	0.28	8.49	14.08	MnO	1.01
Fe K	2.77	1.1131	2.49	0.24	1.90	3.56	Fe_2O_3	0.23
Nb L	19.04	0.7267	26.21	0.54	12.06	37.49	Nb_2O_5	1.44
Ta M	35.55	0.8159	43.57	0.53	10.30	53.20	Ta_2O_5	1.23
O			25.16	0.49	67.25			8.00
Total			108.32					
							Cation sum	3.90

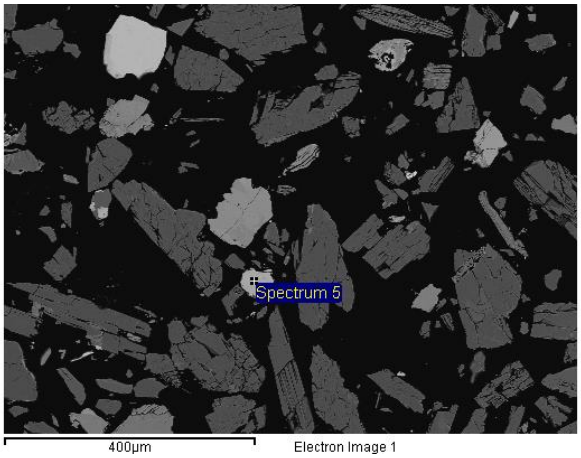

(a)

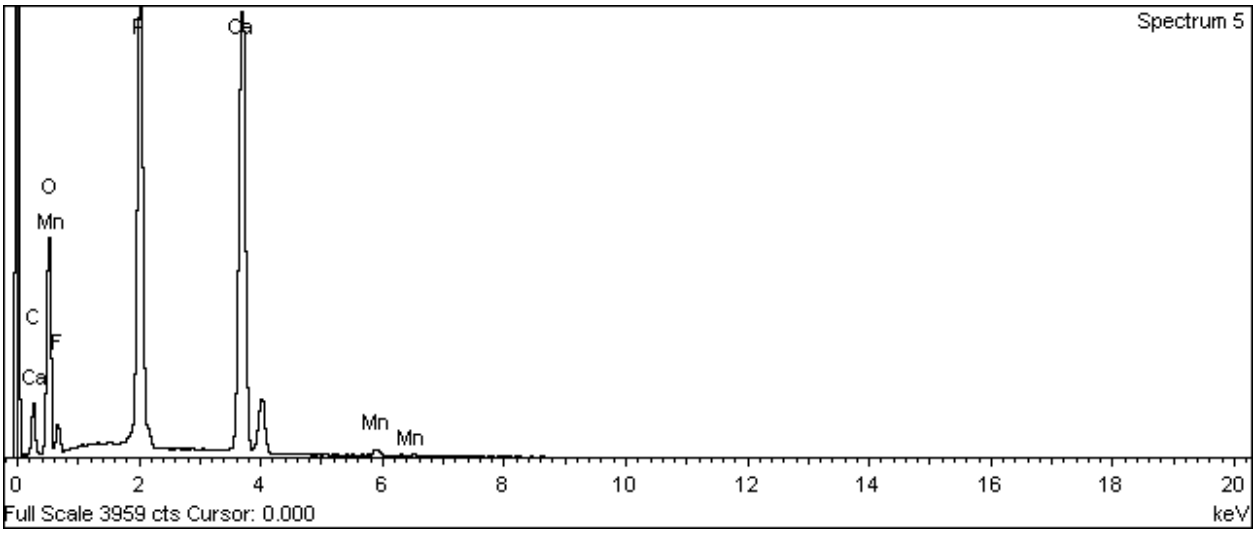

(b)

Figure A.8: Spot analysis (a) and spectrum (b) of elemental composition of apatite grain in concentrate.

Table A.17: Raw data of apatite grain generated by SEM-EDS for spectrum 5.

Element	App Conc.	Intensity Corrn.	Weight%	Weight% Sigma	Atomic%	Compd%	Formula	Number of ions
F K	1.52	0.2085	7.28	0.51	7.92	0.00		0.98
P K	30.90	1.4168	21.81	0.22	14.54	49.97	P_2O_5	1.79
Ca K	39.28	1.0094	38.91	0.29	20.05	54.44	CaO	2.47
Mn K	1.30	0.9151	1.43	0.16	0.54	1.84	MnO	0.07
O			44.11	0.32	56.95			7.02
Total			113.53					
							Cation sum	4.33

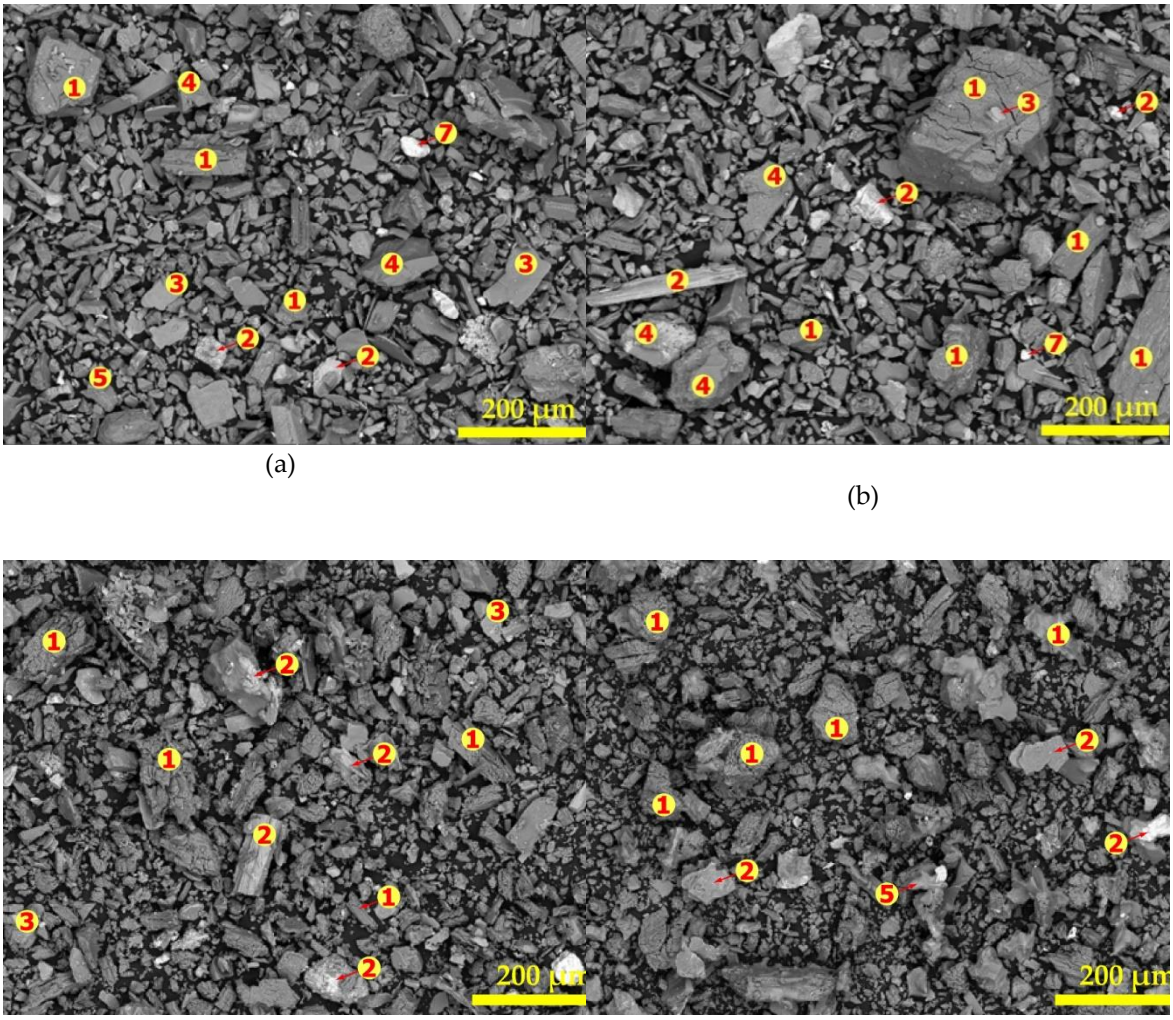

(a) (b)

(c) (d)

Figure A.9: SEM and spot elemental composition determination for powdered unpolished sample treated in air at (a) 900 °C, (b) 950 °C (c) 1000 °C and (d) 1050 °C. The numbers (1-5, 7) indicate the locations of the elemental determination.

Table A.18: Atomic percentage of some elemental composition identified by SEM-EDS at 900 °C.

Elements	Spot "1"	Spot "2"	Spot "3"	Spot "4"	Spot "5"	Spot "7"	Spot "9"
O	64.8	60.6	61.8	66.7	61.9	60.0	56.9
Al	11.2	0.4	7.4		7.7		
Si	23.8	19.6	23.5	33.3	23.4		
Fe	0.3	2.8				40.0	
Mg		6.8					
Ca		9.6			0.1		20.2
Mn		0.3					
Na			0.1		7.0		
K			6.5				
F							8.6
P							14.6
Sn							

Table A.19: Atomic percentage of some elemental composition identified by SEM-EDS at 950 °C.

Elements	Spot "1"	Spot "2"	Spot "3"	Spot "4"	Spot "6"	Spot "7"	Spot "9"
O	64.8	60.9	61.5	66.7	2.1	60.1	56.9
Al	11.5	9.5	14.9		15.9	0.4	
Si	23.7	14.8	17.8	33.3	17.7	0.6	
Fe		4.5	0.7		0.2	38.9	
Mg						0.05	
Ca		0.3			0.2		19.8
Mn		9.9					0.6
Na			0.9		---		
K			4.3		2.3		
F							8.1
P							14.6

Table A.20: Atomic percentage of some elemental composition identified by SEM-EDS at 1000 °C.

Elements	Spot "1"	Spot "2"	Spot "3,5&6	Spot "4"
O	64.6	60.7	61.8	66.7
Al	11.1	3.3	15.9	
Si	23.6	18.0	17.7	33.3
Fe	0.4	4.8	0.2	
Mg		7.1		
Ca		5.0	0.2	
Mn				
Na	0.3	0.8	2.1	
K		0.4	2.3	
Sn				

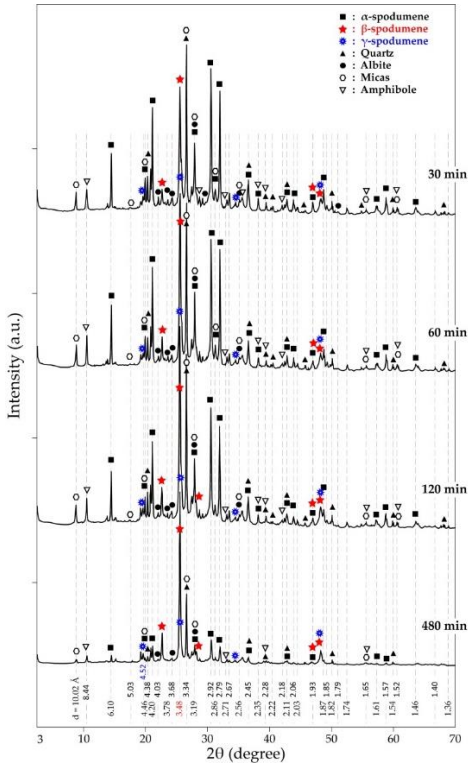
■ : α-spodumene
★ : β-spodumene
● : γ-spodumene
▲ : Quartz
● : Albite
○ : Micas
▽ : Amphibole
30 min
60 min
120 min
480 min
Intensity (a.u.)
2θ (degree)

(**a**)

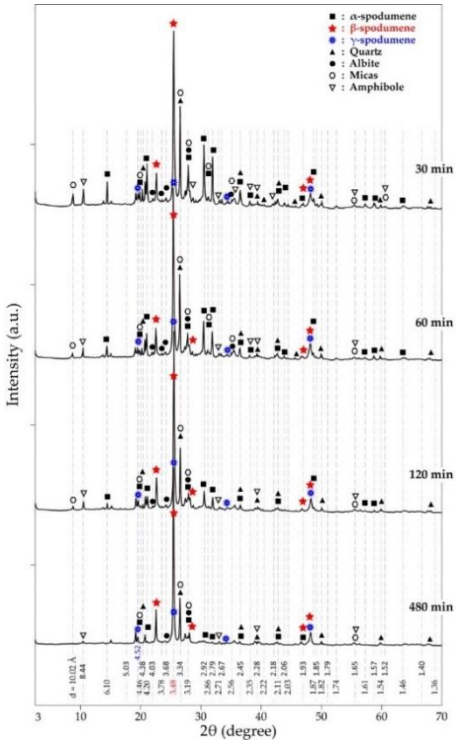
■ : α-spodumene
★ : β-spodumene
● : γ-spodumene
▲ : Quartz
● : Albite
○ : Micas
▽ : Amphibole
30 min
60 min
120 min
480 min
Intensity (a.u.)
2θ (degree)

(**b**)

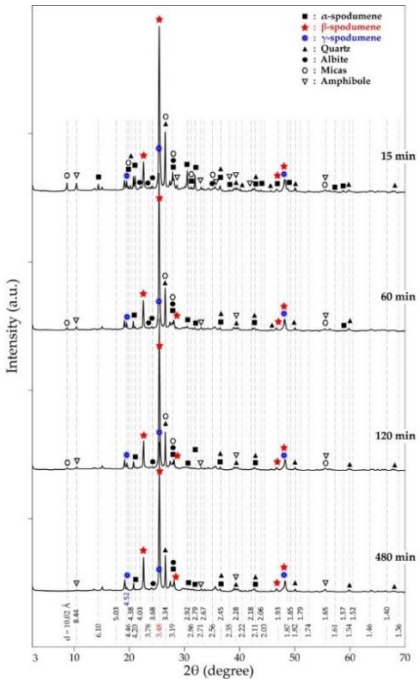
■ : α-spodumene
★ : β-spodumene
● : γ-spodumene
▲ : Quartz
● : Albite
○ : Micas
▽ : Amphibole
15 min
60 min
120 min
480 min
Intensity (a.u.)
2θ (degree)

(c)

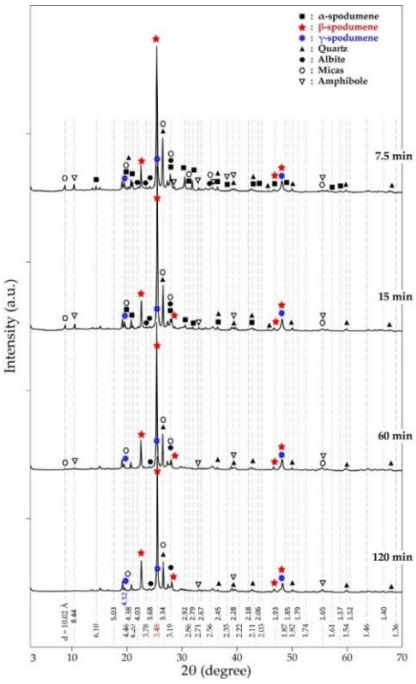
■ : α-spodumene
★ : β-spodumene
● : γ-spodumene
▲ : Quartz
● : Albite
○ : Micas
▽ : Amphibole
7.5 min
15 min
60 min
120 min
Intensity (a.u.)
2θ (degree)

(d)

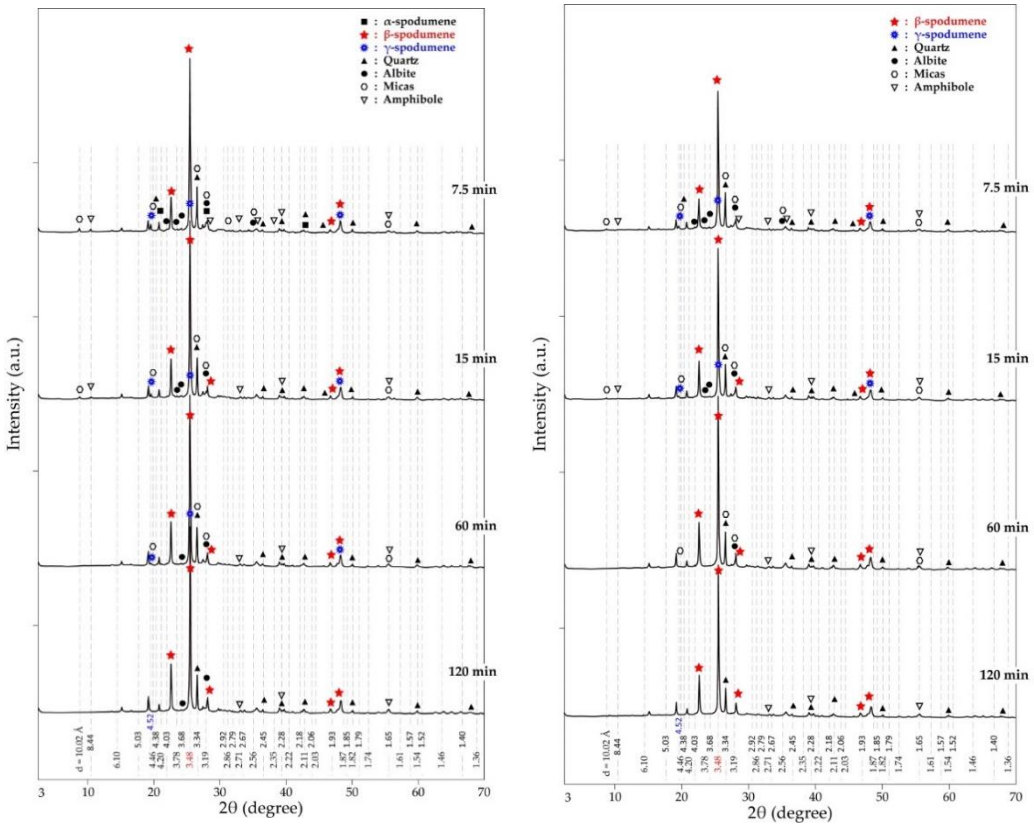

Figure A.10: XRD patterns of residues obtained during treatment of concentrate in air as a function of residence time at 925 °C (a), 950 °C (b), 975 °C (c), 1000 (d), 1025 °C (e) and 1050 °C (f).

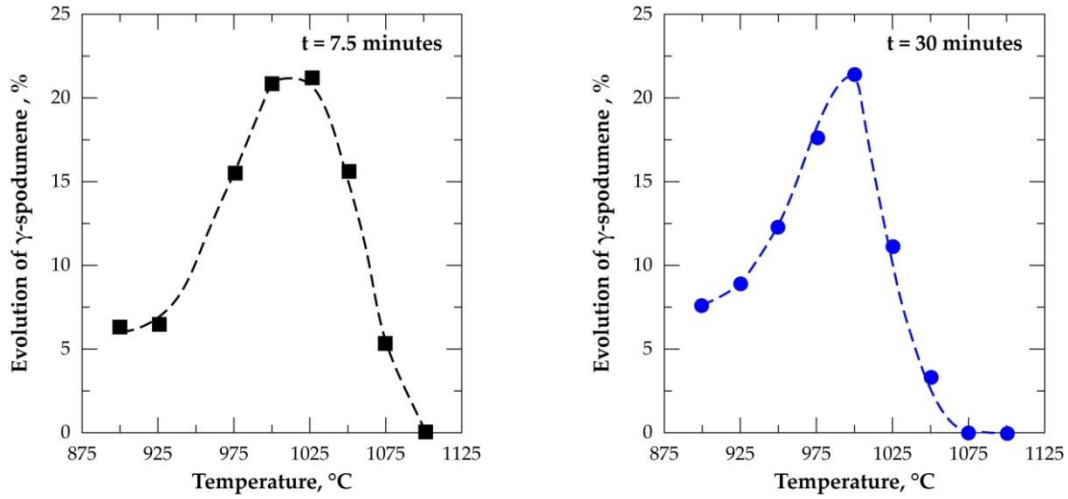

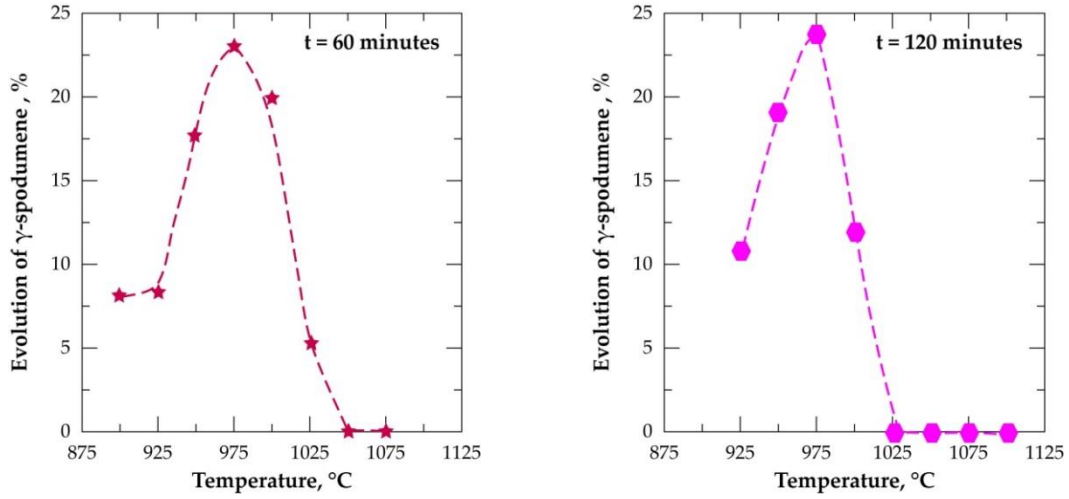

(**c**) (**d**)

Figure A.11: Evolution of the relative γ-spodumene content [$(\gamma/(\alpha+\beta+\gamma)*100]$ during treatment as a function of temperature for residence times: (a) 7.5 minutes, (b) 30 minutes, (c) 60 minutes and (d) 120 minutes.

Table A.21: Data for determination of apparent rate constants, k_1 for α-decay from Equation (3.3).

Time/min	**%α**					**ln %α**				
	900 °C	***925 °C***	***950 °C***	***975 °C***	***1000 °C***	***900 °C***	***925 °C***	***950 °C***	***975 °C***	***1000 °C***
7.5		88.07		46.73	24.44		4.48		3.84	3.2
15		75.33		32.8	9.76		4.32		3.49	2.28
30		79.42	55.66	18.2	3.42		4.37	4.02	2.9	1.23
60	88.64	75.2	43.04	5.89	0	4.48	4.32	3.76	1.77	
120	84.77	67.06	24.47	3.71	0	4.44	4.21	3.2	1.31	
240	77.78	51.2	15.01	0	0	4.35	3.94	2.71		
480	75.09	33.92	4.51	0	0	4.32	3.52	1.51		

Table A.22: %γ-values for determination of apparent rate constants, k_2 for γ-decay.

Time/min	900 °C	925 °C	950 °C	975 °C	1000 °C	1025 °C	1050 °C
7.5		6.44		15.45	21.01	21.17	15.63
15		6.78		10.75	20.63	7.18	7.14
30		9.05	12.45	17.82	21.58	11.31	3.42
60	6.33	8.4	17.77	23.02	19.88	5.3	0
120	6.79	10.85	19.23	24.03	12.02	0	0
240	7.72	13.65	19.53	9.36	7.47	0	0
480	8.12	16.67	20.14	13.47	0	0	0

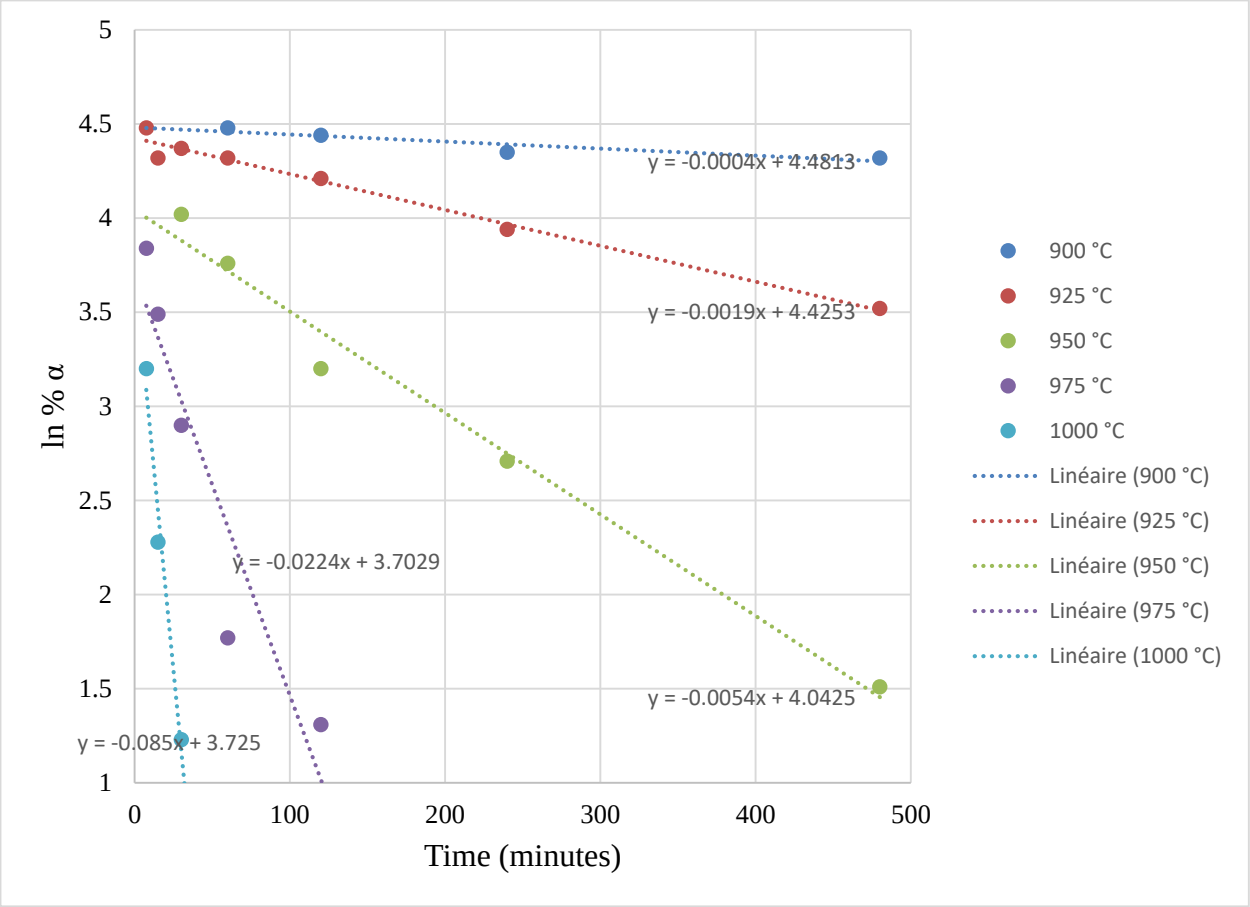

Figure A.12: Fitting plot of ln %α versus time used for the estimation of k_1.

Table A.23: Regression at the varying temperatures for the determination of k_1.

Temperature / °C	**R^2**
900	0.8509
925	0.9821
950	0.9839
975	0.8823
1000	0.9771

Table A.24: Data for calculating apparent activation energy for α-decay from Equation (3.5).

Temp/°C	**E_a for α conversion to γ and β = 652 kJ mol^{-1}**		
	10000/Temp (K)	k_1	ln k_1
900	**8.53**	0.0004	**-7.824**
925	**8.35**	0.0019	**-6.266**
950	**8.18**	0.0054	**-5.221**
975	**8.01**	0.0224	**-3.799**
1000	**7.86**	0.0850	**-2.465**

APPENDIX B: SUPPLEMENTARY MATERIAL FOR CHAPTER 4

Table B.1: Standard deviation on measured atomic percent of elemental composition of spodumene (Spot "1") in leached residue.

Element	**Atomic %**													**SD**
Al	11.3	11.3	11.6	11.5	11.5	11.5	11.4	11.3	11.3	11.4	11.4	11.2	11.3	0.11
Si	23.9	23.9	23.7	23.7	23.8	23.6	23.7	23.8	23.9	23.6	23.6	23.8	23.7	0.11
O	64.8	64.8	64.7	64.7	64.7	64.7	64.7	64.8	64.8	64.7	64.7	64.8	64.7	0.05
Fe						0.2		0.2		0.2	0.3	0.2	0.5	0.12
Mn							0.2							

Table B.2: Standard deviation on measured atomic percent of elemental composition of calcium aluminisilicate (Spot "2") in leached residue.

Element	**Atomic %**										**SD**
Al	12.24	7.59	7.00	13.39	11.76	11.21	10.10	10.42	9.10	10.68	2.00
Si	17.57	23.18	19.34	16.97	17.21	19.22	21.33	20.71	18.94	20.46	1.97
Ca	7.33	4.64	11.21	7.14	8.60	5.98	5.03	5.18	8.24	5.28	2.07
O	61.81	62.54	60.91	61.72	61.27	62.42	63.12	62.33	60.78	62.87	0.81
Mg	0.28				0.16				0.28		0.07
Fe	0.45		0.34	0.29	0.30	0.79	0.14		0.50	0.36	0.19
Cl	0.32	1.75	1.20	0.24	0.70	0.38	0.13	1.15	2.16	0.14	0.72
Na		0.30		0.25			0.15	0.22		0.22	0.05

Table B.3: Standard deviation on measured atomic percent of elemental composition of calcium silicate in leached residue.

Element	**Atomic %**										**SD**
Si	19.80	19.07	20.02	20.02	19.84	19.83	20.00	20.33	20.28	20.23	0.36
Ca	19.93	21.12	19.89	19.97	48.15	20.25	19.61	19.12	19.08	19.13	8.99
Cl	0.73	0.57	0.15								0.30
Mg							0.39	0.39	0.50	0.53	0.07
O	59.53	59.25	59.93	60.01	59.92	59.92	60.00	60.16	60.14	60.11	0.29

Table B.4: Standard deviation on measured atomic percent of elemental composition of quartz in leached residue.

Element	**Atomic %**										**SD**
Si	33.3	33.3	33.3	33.3	33.3	33.3	33.3	33.3	33.3	33.3	0.0
O	66.7	66.7	66.7	66.7	66.7	66.7	66.7	66.7	66.7	66.7	0.0

Table B.5: Standard deviation on measured atomic percent of elemental composition of calcium aluminisilicate (Spot "2") in leached residue.

Element	**Atomic %**					**SD**
Al	6.99	5.60	4.46	4.39	5.91	1.08
Si	10.09	11.50	20.10	19.95	20.03	5.08
Ca	17.66	17.68	10.93	11.18	9.91	3.86
O	52.46	52.43	59.04	58.83	59.80	3.73
Mg	1.34	2.21	0.64	0.72	0.52	0.70
Fe	1.86	0.75	0.38	0.29	0.29	0.67
Cl	9.59	9.82	4.44	4.64	3.53	3.04

SD represents the standard deviation on measured atomic percent of elements in mineral phases of chlorinated residue.

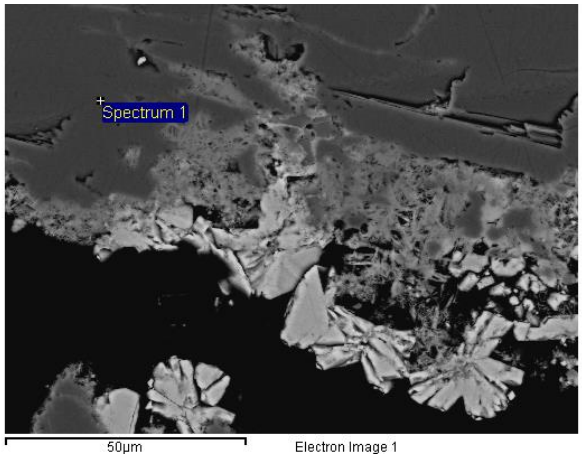

(a)

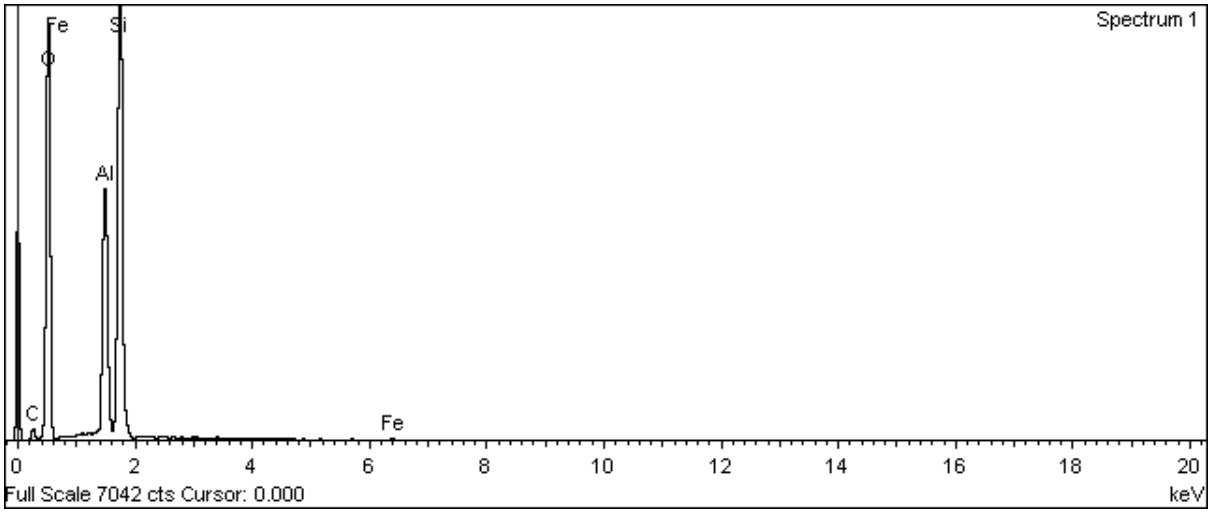

(b)

Figure B.1: Spot analysis (a) and spectrum (b) of elemental composition of unaffected spodumene grain in chlorinated residue.

Table B.6: Raw data of unaffected spodumene grain in chlorinated residue.generated by SEM-EDS for spectrum 1.

Element	App Conc.	Intensity Corrn.	Weight%	Weight% Sigma	Atomic%	Compd%	Formula	Number of ions
Al K	15.57	1.0666	14.60	0.15	11.33	27.58	Al_2O_3	1.40
Si K	29.99	0.9424	31.82	0.23	23.73	68.08	SiO_2	2.93
Fe K	0.44	0.8737	0.50	0.13	0.19	0.72	Fe_2O_3	0.02
O			49.46	0.29	64.75			8.00
Totals			96.38					
							Cation sum	4.36

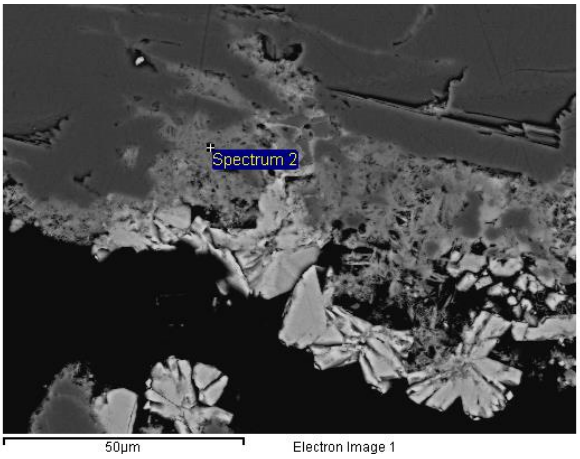

(a)

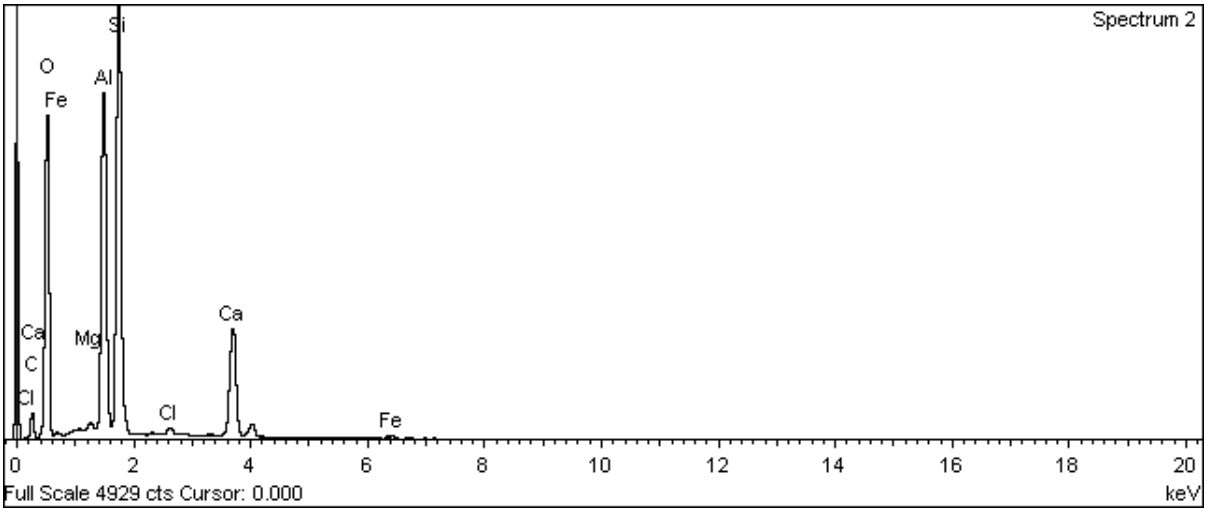

(b)

Figure B.2: Spot analysis (a) and spectrum (b) of elemental composition of calcium aluminosilicate in chlorinated residue.

Table B.7: Raw data of calcium aluminosilicate in chlorinated residue.generated by SEM-EDS for spectrum 2.

Element	App Conc.	Intensity Corrn.	Weight%	Weight% Sigma	Atomic%	Compd%	Formula	Number of ions
Mg K	0.30	0.9735	0.31	0.05	0.28	0.51	MgO	0.04
Al K	15.20	1.0317	14.74	0.15	12.24	27.85	Al_2O_3	1.58
Si K	20.44	0.9283	22.02	0.19	17.57	47.10	SiO_2	2.26
Cl K	0.38	0.7624	0.50	0.07	0.32	0.00		0.04
Ca K	12.75	0.9721	13.11	0.19	7.33	18.35	CaO	0.94
Fe K	0.99	0.8785	1.13	0.16	0.45	1.61	Fe_2O_3	0.06
O			44.11	0.30	61.80			7.96
Totals			95.91					
							Cation sum	4.88

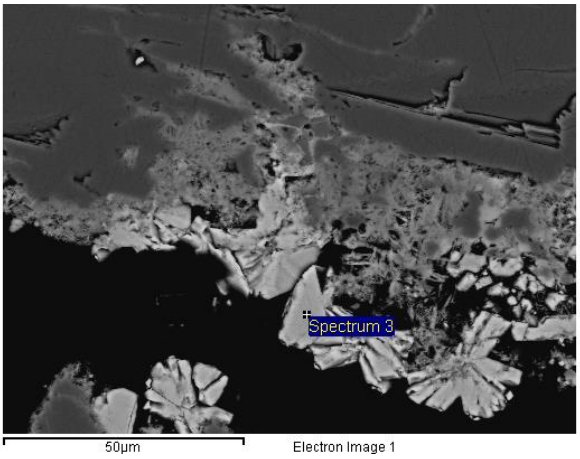

(a)

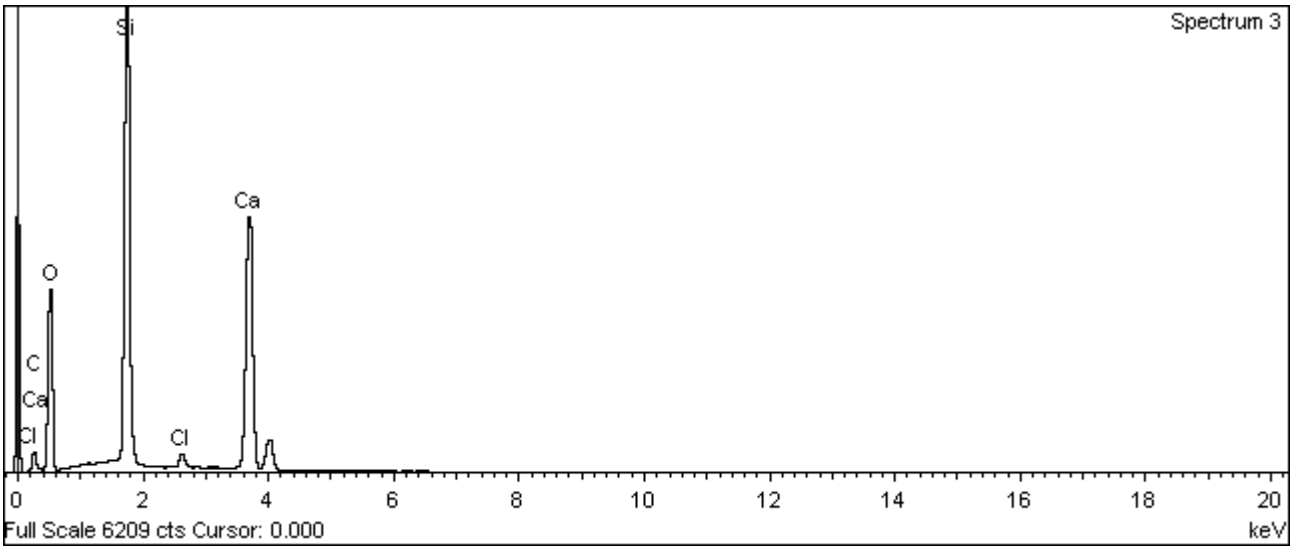

(b)

Figure B.3: Spot analysis (a) and spectrum (b) of elemental composition of calcium silicate in chlorinated residue.

Table B.8: Raw data of calcium silicate in chlorinated residue generated by SEM-EDS for spectrum 3.

Element	App Conc.	Intensity Corrn.	Weight%	Weight% Sigma	Atomic%	Compd%	Formula	Number of ions
Si K	26.05	1.0545	24.70	0.19	19.80	52.84	SiO_2	2.63
Cl K	0.94	0.8109	1.15	0.08	0.73	0.00		0.10
Ca K	35.40	0.9977	35.48	0.29	19.93	49.64	CaO	2.65
O			42.30	0.27	59.53			7.90
Totals			103.63					
							Cation sum	5.27

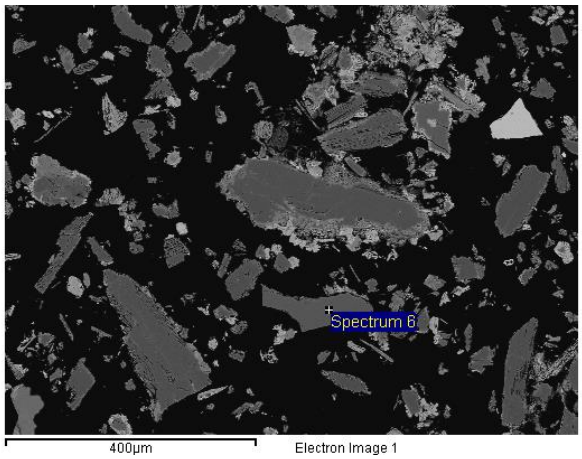

(a)

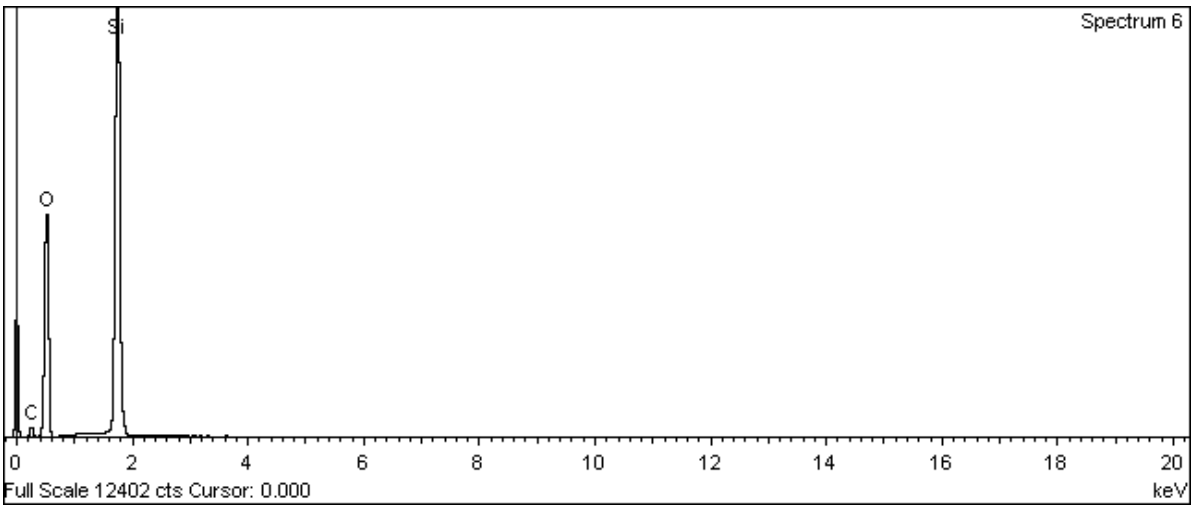

(b)

Figure B.4: Spot analysis (a) and spectrum (b) of elemental composition of quartz grain in chlorinated residue.

Table B.9: Raw data of quartz grain in chlorinated residue generated by SEM-EDS for spectrum 6.

Element	App Conc.	Intensity Corrn.	Weight%	Weight% Sigma	Atomic%	Compd%	Formula	Number of ions
Si K	52.70	1.0841	48.61	0.26	33.33	103.99	SiO_2	4.00
O			55.38	0.27	66.67			8.00
Totals			103.99					
							Cation sum	4.00

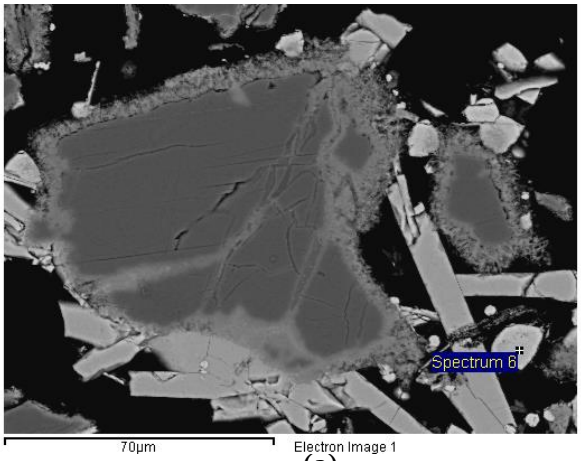

(a)

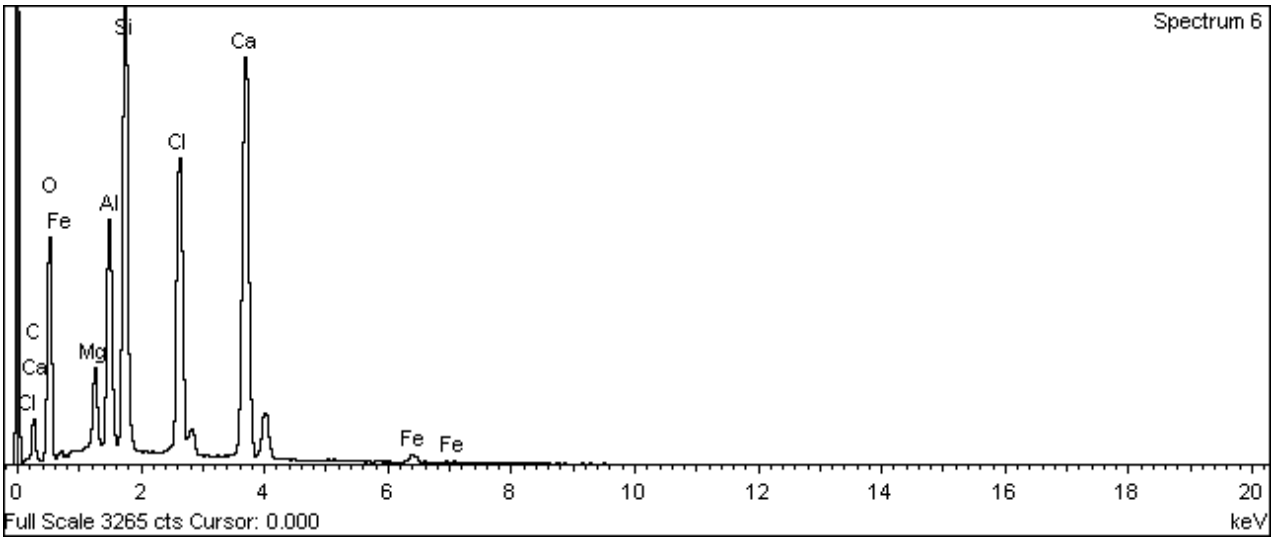

(b)

Figure B.5: Spot analysis (a) and spectrum (b) of elemental composition of calcium aluminosilicate chloride in chlorinated residue.

Table B.10: Raw data of calcium aluminosilicate chloride in chlorinated residue generated by SEM-EDS for spectrum 6.

Element	App Conc.	Intensity Corrn.	Weight %	Weight % Sigma	Atomic %	Compd %	Formula	Number of ions
Na K	2.26	0.9627	2.35	0.10	2.11	3.17	Na_2O	0.26
Al K	11.45	1.0478	10.92	0.13	8.36	20.64	Al_2O_3	1.04
Si K	33.27	0.9663	34.43	0.23	25.31	73.66	SiO_2	3.15
O			49.76	0.28	64.22			8.00
Totals			97.47					
							Cation sum	4.46

metals

MDPI

Review

Literature Review and Thermodynamic Modelling of Roasting Processes for Lithium Extraction from Spodumene

Allen Yushark Fosu [1], Ndue Kanari [1], James Vaughan [2] and Alexandre Chagnes [1,*]

[1] CNRS, GeoRessources, Université de Lorraine, 54000 Nancy, France; allen.fosu@univ-lorraine.fr (A.Y.F.); ndue.kanari@univ-lorraine.fr (N.K.)

[2] School of Chemical Engineering, The University of Queensland, Brisbane, QLD 4072, Australia; james.vaughan@uq.edu.au

* Correspondence: alexandre.chagnes@univ-lorraine.fr; Tel.: +33(0)-372-744-544

Received: 24 August 2020; Accepted: 28 September 2020; Published: 30 September 2020

Abstract: This review adds to the public domain literature on the extraction of lithium from mineral ores. The focus is on the pyrometallurgical pre-treatment of spodumene. Information on the phase transformation from α to β, the heat treatment methods as well as the behavior of various compounds in the roasting processes are evaluated. Insight into the chemical thermodynamics of the baking process is evaluated using HSC Chemistry software up to 1200 °C. It was observed that the alkaline, sulfation, chlorination (using Cl_2 and $CaCl_2$), carbonizing (to form Li_2CO_3) and fluorination processes were feasible either throughout or at a point within the temperature range considered. Chlorination using KCl and carbonizing to form Li_2O are the processes found to be nonspontaneous throughout the temperatures considered.

Keywords: spodumene; thermodynamics; lithium; roasting

1. Introduction

Lithium is used in several industries as a component of products such as glass–ceramics, greases and casting-alloys. Over the last two decades, lithium's use in batteries, particularly for making vehicles, has resulted in an increased need for lithium compounds. Global lithium demand has risen to about 60% in this time and a 20% yearly increase is expected over the next few decades [1,2]. Such a boom in lithium production is accompanied by a drastic increase of its price, which has tripled in a little more than three years (from 5000 US dollars per ton in 2014 to more than 15,000 US dollars per ton by the end of 2017) [3]. The astronomical demand for the metal has caught the attention of metallurgists around the globe and has prompted the development of novel beneficiation approaches to meet this demand by focusing on extraction from mineral ores. Extracting lithium from ores has higher operating costs than conventional extraction from brine, however, the theory of supply and demand makes the processing economically prudent because of the increasing price of lithium.

Spodumene is the main ore of interest due to its high lithium content (~8 wt.% as Li_2O in a pure mineral specimen) [4,5]. Table 1 shows the mineralogical composition of a typical spodumene ore sample with 2.14 wt.% Li_2O. The concentration of Li_2O in this ore indicates that it is low grade. Spodumene is a lithium aluminum silicate ($Li_2O{\cdot}Al_2O_3{\cdot}4SiO_2$ or $LiAlSi_2O_6$) of the pyroxene group; it is found in close association with quartz, feldspar and micas [6]. Its color may vary from purple, green, yellow, gray or white, depending on the presence and concentrations of sodium, manganese, iron, magnesium or titanium [7–9].

Spodumene is naturally present in the stable α-monoclinic (highly packed crystal structure) form with high grindability and hence the mineral is difficult to leach without pretreatment. It is made

amenable to lixiviation by calcination at 1000 °C to the β-tetragonal form [5]. During the thermal process, there is a dislocation of Al^{3+} in the α-spodumene leading to aβ-spodumene crystal structure with a comparably larger crystal volume. This increases the mobility of lithium atoms which then become easily accessible to aqueous lixiviant solutions [4,10,11]. The phase transformation has also been shown to improve comminution, as β-spodumene is relatively soft and flaky [9,10,12]. Recently, an intermediary hexagonal metastable γ-phase was discovered during calcination. This phase is predicted to influence the extraction of lithium. Therefore the sequence of the phase transformation is now understood to be α→γ→β [4,10,13]. Though interlocking gangue in spodumene can adversely affect downstream beneficiation processes, Salakjani et al. [9] as well as White and McVay [14] indicated that these impurities facilitate heat conduction and efficient transformation since spodumene itself exhibits low thermal conductivity.

Table 1. The mineralogical composition of a typical spodumene ore sample.

Mineral	Cr_2O_3	MgO	MnO	Li_2O	SO_3	Fe_2O_3	K_2O	Na_2O	TiO_2	P_2O_5	SiO_2	Al_2O_3	CaO
%	0.03	1.30	0.32	2.14	0.15	4.29	1.26	1.14	0.10	0.33	61.31	20.79	1.72

Prior to the hydrometallurgical treatment of the ore after calcination, the β-spodumene phase is baked or roasted with additional compounds which define the next processing route as acidic, alkaline or chlorination.

This review focuses on the various methods of processing spodumene ore, providing theoretical insight from the thermodynamic point of view using the reaction equation and the equilibrium module of HSC Chemistry software version 5.1 (Outokumpu Research Oy, Pori, Finland).

2. Decrepitation of Spodumene Ore

The amenability of spodumene to lixiviation is greatly enhanced by its transformation from the α-form to β-form at elevated temperature, however, a process for direct extraction of lithium from α-spodumene using the HF/H_2SO_4 system was introduced by Guo et al. [15]. The thermal behavior of spodumene has been studied extensively by a number of researchers [4,5,10,11,16] and it is worthy to note that the process is carried out below 1040 °C which is the fusion temperature of spodumene [17].

It has been established that the phase change of α-phase spodumene starts at 800 °C and is completed by 1100 °C, though there is a report of the phase transformation commencing above 634 °C using microwave heating [5,10]. Peltosaari et al. [10] considered the effect of particle size to be insignificant with respect to the conversion rate of spodumene. Salakjani et al. [4] revealed that heating leads to volumetric expansion and makes the ore porous. The final β-spodumene consequently has a larger surface area which enhances subsequent chemical processing. They found that a greater extent of the β-spodumene formed corresponded to a higher surface area produced but a relatively low density. It is anticipated that the inversion of α-spodumene to γ-spodumene is exothermic and that the heat released helps to offset the heat requirement of the process, however, the phase change from α directly to β is endothermic [9,18]. Investigations by Moore et al. [16] indicate that the temperature and the heating method have negligible effect on the mass fraction of the phases transformed during the decrepitation process and that the quantities of inversion products are almost equal at the initial stage before the final conversion to the β-phase. Conversely, Salakjani et al. [5] explained that temperature and residence time are the major factors that determine the inversion of the phases in spodumene; the temperature requirement is subsequently influenced by the chemical composition and the feed particle size of the spodumene sample.

The phase transformation process at the elevated temperature is known to be influenced by many factors including the heating method employed, the morphology of the sample after comminution and the quantity of gangue minerals present [4,10,11,16].

Recently, microwave heat treatment of spodumene has been studied extensively by several authors and compared with conventional methods [4,5,10,16,19]. Spodumene is passive to microwave

irradiation so the heat treatment with this method is made possible by hybrid microwave heating with the aid of SiC [9,10]. It was found that β-phase spodumene absorbs significantly higher microwave energy than the α-phase spodumene, resulting in local sintering when the β-phase is reached [9]. Treatment of spodumene using microwave irradiation is still under development and much additional research is required to overcome challenges such as local sintering that results in unequal heating, transparency of spodumene to microwave irradiation and other factors that generally affect the treatment of ores using microwave irradiation. Salakjani et al. [9] suggested that mechanical stirring and the addition of additives (which do not affect downstream processes) could be a remedy for the sintering and passive behavior of spodumene to microwave irradiation, respectively. The microwave heat treatment was found to have a fast transformation rate compared with conventional heating. The transformation of α-spodumene commenced and was almost complete at 110 and 170 s of microwave irradiation respectively [10], but it appears that an hour of heating in a muffle furnace is needed to achieve a 100% conversion to the β-phase [9]. The operating temperature was, however, found to be invariant with regards to the heating methods. There appears to be an inconsistency in the inversion temperatures of these two investigations during the conventional approach. According to Salakjani et al. [9], no phase change was observed for temperatures below 950 °C irrespective of the heating time. They observed the first γ and β-phases at 950 °C for at least 30 min of residence time but Peltosaari et al. [10] observed the first γ-phase at 800 °C. This inconsistency might be due to some factors such as the concentration of impurities, the amorphous nature created due to the mechanical treatment and even particle size to a lesser degree. A minimum of 5 min of conventional heating at 1100 °C was observed by Salakjani et al. [4] to almost complete the conversion of α to β-spodumene while Peltosaari et al. [10] indicated that 100% conversion was achieved within 15 min. However, Salakjani et al. [4] observed some γ-phase present even after 1-h of residence time at 1100 °C.

Comparing the energy requirement for the microwave and the muffle furnace heating for the phase conversion process shows that the microwave approach requires a relatively low energy input for the transformation compared to the conventional method [5]. The conversion to the β-phase requires 5 times less energy by using microwave heating than conventional furnace. The reason for the high energy requirement in the conventional process can be due to the fact that heating begins from the outside and moves to the inside of the sample by conduction (the furnace needs to heat up evenly before the sample undergoes heating) therefore, most of the energy is wasted while in the microwave process, heating starts from the inside of the sample and extends radially outside (the sample absorbs the microwave radiation directly for heating), leading to little or no loss of energy. In another paper [19], the comparison of the microwave and conventional heat treatment for acid roasting of β-spodumene showed that microwave heating resulted in higher lithium extraction than the muffle furnace with regards to key parameters like processing time, excess acid and energy requirement. Indeed, 10.4 MJ of energy was needed for the conventional process whereas only 15.4 kJ was required for the microwave for the same quantity of lithium extracted. Microwave irradiation again required shorter time (20 s) to achieve this goal while an hour was needed in the muffle furnace for the extraction. Particle size was found to have an important effect on the amount of lithium extracted by microwave heat. Finer particles have been confirmed to enhance maximum (93%) lithium extraction with as low as 15% excess acid requirement as compared to 80% excess acid, which is normally used in roasting.

3. Roasting of Spodumene Ore

Roasting β-spodumene with appropriate reagents results in a chemoselective ion exchange reaction where lithium is exchanged for atoms of similar characteristics in the reagent used. This may be done after decrepitation where β-spodumene is roasted with chemicals, or may be performed in-situ during decrepitation. This leads to the formation of soluble lithium salt (such as LiCl, Li_2SO_4 or LiOH). Various reagents have been employed for forming the lithium salt during roasting and rigorous investigations are ongoing for optimization. Unlike roasting, the decrepitation process appears to be nearly optimized and little can be done to further adjust parameters like the operation temperature

and granulometry of the comminuted ore [13]. The reagent used for the roasting determines the name of the process. Generally, at a given pH, reagents are selected based on their selectivity for the metal of interest, stability in the aqueous phase, environmental friendliness, cost and ease of regeneration after dissolution. These reasons have resulted in a series of investigations in search of suitable chemicals that satisfy a majority of these criteria during lithium ore beneficiation.

There are three well-known methods for roasting spodumene. The first is acid roasting, which involves baking the calcined spodumene product with an excess of concentrated sulphuric acid at a temperature of about 250 °C (for conventional heat treatment) or 320 °C (for microwave irradiation for 20 s) [19]. The second is the alkaline process which utilizes limestone ($CaCO_3$) or lime ($Ca(OH)_2$ or CaO) and lastly, the chloride route which uses various chlorinating reagents. There are other new approaches such as the carbonizing (using Na_2CO_3 in the presence of CO_2 and other additives) and fluorination (using NaF). Figure 1 shows the main high-temperature routes for spodumene treatments which are described below (sulfation, alkaline and chlorination processes for processing spodumene).

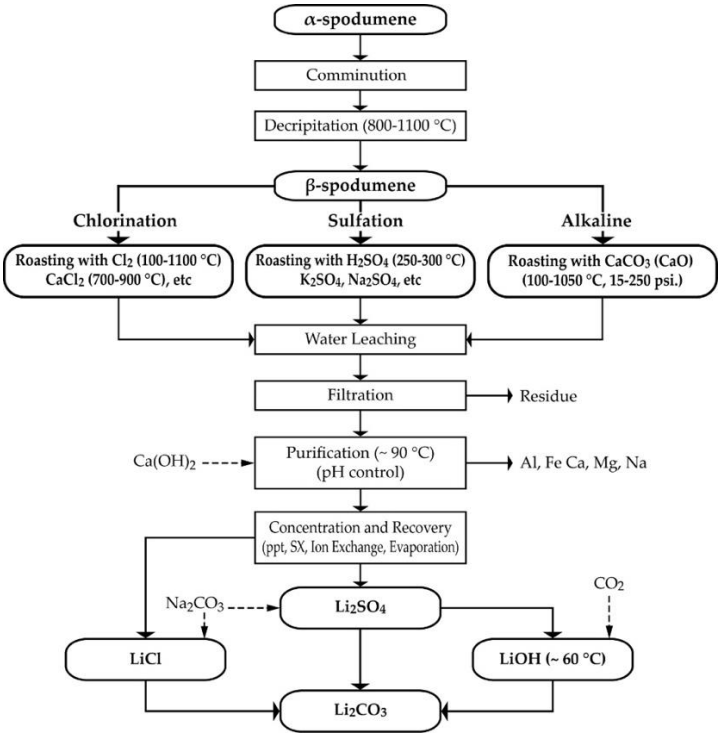

Figure 1. The flow diagram of the major treatment processes for spodumene (chlorination, sulfation and alkaline processes).

3.1. Sulfation Processing of Spodumene

In this process, alkali metal sulfates, sulfuric acid or SO_3 gas in the presence of water and oxygen are employed as reagent (s) to produce soluble lithium sulfate which can be water leached. This process benefits from the high stability and solubility of lithium sulfate in the aqueous phase during leaching. The drawbacks are the difficulty in producing high purity lithium carbonate resulting from the unselectivity of sulfate reagents towards other metals such as Al, Na, Mg, Fe and K. Aluminum and iron impurities may be significant such that precipitating them from the leachate carries along some lithium, decreasing overall lithium recovery [17]. The presence of some alkali metals also affects the purity of the final product since they are leached alongside lithium and separating them becomes complicated due to their similar chemistry to lithium in aqueous solution.

The sulfation process consumes a large amount of reagent which affects the economic viability of the process [20,21]. Sulfates of potassium, ammonium and sodium have been successfully used for the

extraction of lithium from several lithium bearing minerals. Sulfate roasting of lepidolite followed by water leaching has been studied widely using $Na_2SO_4/K_2SO_4/CaO$, Na_2SO_4 and $FeSO_4$ at roasting temperatures of 880, 1000, 850 °C respectively. The corresponding approximate extraction extents were 95, 99.5 and 90% extraction, respectively [21–24]. The sulfating behavior of zinnwaldite, petalite and montmorillonite have also been discussed elsewhere [21,25–27] using Na_2SO_4 and H_2SO_4 and yielding 90, 97.3 and 90% lithium extraction, respectively.

In the case of spodumene, the transformation from the α to the β-phase is crucial before the application of sulphates as indicated above. Several authors have conducted systematic experimental studies to understand and optimize the amenability of sulfates to spodumene beneficiation [17,19,28–31]. The use of sulfuric acid is renowned and currently, the commercialized process for lithium extraction while the others are still undergoing research. In the acid process, the ore is roasted with sulfuric acid at a temperature of about 250 °C. Investigations by Salakjani et al., [19] indicate that one hour is optimal for conventional heating while only 20 s is needed with microwave roasting. It is essential that this process is operated below 337 °C to prevent the evaporation of the acid [19]. During this process, the H^+ of the acid is chemoselectively exchanged with Li^+ of spodumene as indicated in Equation (1) to form water soluble $Li_2SO_{4(s)}$. The water-soluble part of the roasting process is water leached according to Equation (2), lime precipitation is conducted at 90 °C for pH adjustment and removal of impurities from solution. Lithium carbonate is recovered by the addition of sodium carbonate solution to the extract as indicated by Equation (3):

$$2LiAlSi_2O_{6(s)} + H_2SO_{4(l)} \rightarrow Li_2SO_{4(s)} + 4SiO_{2(s)} + Al_2O_{3(s)} + H_2O_{(g)} \quad (1)$$

$$Li_2SO_{4(s)} \rightarrow Li_2SO_{4(aq)} \quad (2)$$

$$Li_2SO_{4(aq)} + Na_2CO_{3(aq)} \rightarrow Li_2CO_{3(s)} + Na_2SO_{4(aq)} \quad (3)$$

It must be noted that the diffusion of the acid through the ore for the ion exchange is the rate determining step for the reaction. Unlike gaseous reagents, the viscous nature of the liquids (acid and lithium bisulphate produced around 170 °C) slows their penetration through tiny pores and cracks, thereby slowing down the reaction [32].

3.2. Alkaline Process

This process benefits from the economics and the nonaggressive nature of the salt used as a reagent compared to the acid process which requires the use of concentrated acid [33]. It involves roasting the lithium bearing ore with lime or limestone within the temperature range of 100–205 °C or 825–1050 °C respectively. Roasting with limestone is specified by Equation (4) where water soluble $Li_2O_{(s)}$ is formed with calcium aluminosilicate and carbon dioxide. $Li_2O_{(s)}$ is water leached to produce aqueous LiOH [21,34], which is separated from residual solids by filtration. Instead of direct baking of spodumene with limestone to produce $Li_2O_{(s)}$, limestone can initially be decomposed thermally to produce CaO (Equation (5)).The CaO that was produced is then roasted with spodumene in the presence of water to produce LiOH (Equation (6)).

$$Li_2O{\cdot}Al_2O_3{\cdot}4SiO_{2(s)} + CaCO_{3(s)} \rightarrow Li_2O_{(s)} + CaO{\cdot}Al_2O_3{\cdot}4SiO_{2(s)} + CO_{2(g)} \quad (4)$$

$$CaCO_{3(s)} \rightarrow CaO_{(s)} + CO_{2(g)} \quad (5)$$

$$LiAlSi_2O_{6(s)} + CaO_{(s)} + H_2O_{(l)} \rightarrow LiOH_{(aq)} + CaAl_2Si_2O_{8(s)} \quad (6)$$

The lithium hydroxide that is produced can be converted to LiCl or $LiCO_3$ by reaction with hydrochloric acid or carbon dioxide, respectively, if they are the final products desired. This process has been used by Jandova et al. [35] to recover 90% lithium from zinnwaldite waste. Some additives such as gypsum, lithium carbonate and sodium sulphate may be employed in the baking process to enhance lithium recovery; recording 96%, 96% and 90%, respectively [33,36,37]. The downside of this approach is the high energy requirement for the decomposition of limestone and dicalcium silicate. This may result in the evolution of unbearable heat which makes temperature control in the system difficult [14].

3.3. Chlorination Process

The use of chlorine gas and chloride bearing salts in mineral beneficiation is the least considered process due to the toxicity of chlorine gas that may be generated alongside the products, and the high cost of corrosion resistant equipment needed for the process. However, there are several benefits of chlorine metallurgy in minerals processing. The main benefit is the high selectivity of chlorine and the comparatively lower operating temperature. The generated chlorides have low melting and boiling points and are easily separated from the wastes due to the vapor pressure difference [38–40]. In addition, the use of chlorine results in high recovery of metals, which makes it easy for treating low grade ores. Lastly, the process results in the generation of environmentally green waste. These advantages call for a closer look at chlorine for beneficiating lithium ores, however, it has attracted little attention and few literature articles have been written about it [41–46].

Peterson et al. [41] patented a blend of muriate of potash and sylvinite ore (sodium and potassium chloride) to recover lithium from its ores at 980–1100 °C. The reaction of this invention is an exchange reaction between the alkali metals of the chlorides and the lithium of the ore, thereby forming soluble LiCl, which was further converted to lithium carbonate by reaction with sodium carbonate. About 97.5% of the lithium carbonate was recovered by this approach. Chlorination of lepidolite using sodium and calcium chloride at 880 °C yielded 93% lithium recovery [42]. Recently, the same approach was applied to recover the lithium value in spodumene using chlorine gas and calcium chloride, respectively; 900 °C and 120 min were suggested as the optimal chlorination conditions, which resulted in 90% lithium extraction when calcium chloride was used [43,44].

3.4. Other Processes to Spodumene Treatment

Other less known processes for beneficiating lithium ores worthy of discussion are the carbonizing and fluorination processing. Lithium carbonate can be produced by carbonizing lithium bearing ore with sodium carbonate between 525 and 675 °C in a solid–solid intimate reaction followed directly by leaching or hydrothermal decomposition treatment (between 90 and 225 °C) prior to leaching [47]. The reactions of the process (Equations (7) and (8)) must be carried out above the minimum temperatures suitable for the individual lithium bearing ore (1080, 850, 980 and 870 °C respectively for petalite, lepidolite, eucryptite and spodumene). They indicated the need to carry out this roasting in the presence of alkali metal chlorides, alkali metal sulfate or carbon dioxide which act as a catalyst for the process. However, a specific preference for sodium and potassium chloride or sulfate was indicated. By this process, 75–97% of lithium contained in the ore could be leached for recovery. The inventors of this process [47] highlighted some advantages of this process which include the possibility of using Na_2CO_3 as the only reactant to produce Li_2CO_3 of high purity. They indicated that the reagent is ideally employed to decompose refractory ores into fragments to enhance leaching. The process is therefore expected to require serious purification steps since the decomposition may give rise to several impurities. Using it as a plant production of Li_2CO_3 with good recovery and high purity without major purification is therefore a breakthrough. This approach is also said to have a short processing time and to be economically viable. This is because, the reagent is added to the cooling calcined spodumene midway during the process, for it reacts with the mineral, thereby reducing the time for processing and also utilizing the energy which would have gone wasted.

$$2LiAlSi_2O_{6(s)} + Na_2CO_{3(s)} + 4H_2O_{(l)} \rightarrow Li_2CO_{3(s)} + Na_2O.Al_2O_3.4SiO_2.H_2O_{(s)} \quad (7)$$

$$Li_2CO_{3(s)} + CO_{2(g)} + H_2O_{(l)} \rightarrow 2LiHCO_{3(s)} \quad (8)$$

Owing to this invention several other investigations have revolved around it for its optimization [48,49]. Chen et al. [48] employed pressurized roasting of spodumene concentrate with sodium carbonate in an autoclave, yielding 94% lithium carbonate production with 99.6% purity. Research by dos Santos et al. [49] using spodumene and sodium carbonate, promoted by sodium chloride, resulted in 70% lithium yield. The involvement of NaCl by dos Santos et al. [49] was to aid the extraction of the residual lithium bound at the interstitial positions of the ore. This reaction was conducted within 550–650 °C for 120 min.

The only fluorination roasting report available in literature was performed by Rosales et al. [50], though there are some hydrometallurgical processes of spodumene beneficiation using some fluorination agents [15,51]. In this approach, roasting of NaF with β-spodumene at 600 °C spodumene: NaF from 1:1 to 1:2.5 and 4 h was investigated. 90 % maximum lithium recovery was achieved and it occurred at spodumene: NaF of 1:2 and 2 h of roasting. Equation (9) illustrates the reaction process:

$$2LiAlSi_2O_{6(s)} + 2NaF_{(s)} \rightarrow 2LiF_{(s)} + NaAlSi_3O_{8(s)} + NaAlSiO_{4(s)} \quad (9)$$

The processes discussed with some relevant information are summarized in Table 2.

Table 2. Summary of literature for the recovery of lithium from spodumene using the major beneficiation processes.

Process	Experimental Conditions						Product	Recovery/%	Reference
	Roasting			Leaching					
	Reagent	Temp./ °C	Time/min.	Time/hr	Temp./ °C	Lixiviant			
Sulfating	Conc.·H_2SO_4	200–300	30–60	-	-	H_2O	Li_2SO_4	85	[52]
	Na_2SO_4 + CaO	-	-	3	230	Na_2SO_4 + CaO	Li_2SO_4	93.30	[28]
	Na_2SO_4 + NaOH	200–300	-	3	230	Na_2SO_4 + NaOH	Li_2SO_4	90.70	[28]
	$(NH_4)_2SO_4$	150–370	-	-	-	NH_3 (aq)	Li_2SO_4	-	[17]
	$CaSO_4$ + $CaCO_3$	1000–1150	120–180	-	-	H_2O	Li_2SO_4	85–90	[53] *
	Conc. H_2SO_4	250–300	-	1	-	H_2O	Li_2SO_4	86	[31]
	H_2O+O_2 + SO_3	350–425	10-40	-	-	H_2O	Li_2SO_4	97	[32]
Alkaline	CaO + H_2O	100–205	60			H_2O	LiOH	~97	[34]
	CaO + H_2O	1000–1230			100	H_2O	LiOH	80	[34] *
Chlorination	KCl, NaCl	1000–1050	15–60	-	85	H_2O/HCl	LiCl	85–97.50	[41]
	Cl_2	1100	150	-	-	-	LiCl	-	[43]
	$CaCl_2$	900	120	-	60	H_2O	LiCl	90.2	[44]
	$CaCl_2$	800–1200	-	-	-	Alcohol	LiCl	9.5–98.5	[46]
Carbonizing	Na_2CO_3	525–675	10–120	-	-	H_2O, NH_4^+ (aq)	Li_2CO_3	75–97	[47]
	Na_2CO_3	150–250	10–120	–	-	H_2O	Li_2CO_3	~94	[48]
	Na_2CO_3 + NaCl	~923	120	-	-	H_2O	Li_2CO_3	70	[49]
Fluorination	NaF	600	120	0.5	25	HF	LiF	90	[50]

* roasting of spodumene done in the alpha phase.

4. Chemical Thermodynamics of Spodumene Processing

Insight into thermodynamics of the beneficiation approaches of spodumene are scarce in literature. This section looks at the thermodynamic modelling of the various approaches of lithium processing encountered in literature using the HSC Chemistry software version 5.1 reaction equation and equilibrium module. The standard Gibbs free energy changes as a function of temperature for the following reactions involved during spodumene roasting with various reagents (sulfating, alkaline, fluorinating, carbonizing and chlorinating agents, Equations (10)–(22) are found in Figure 2:

$$2LiAlSi_2O_6(B)_{(s)} + CaCl_{2(s)} \rightarrow 2LiCl_{(s)} + 2SiO_{2(s)} + CaAl_2Si_2O_{8(s)} \quad (10)$$

$$2LiAlSi_2O_6(B)_{(s)} + Cl_{2(g)} \rightarrow 2LiCl_{(s)} + 4SiO_{2(s)} + Al_2O_{3(s)} + 0.5O_{2(g)} \quad (11)$$

$$2LiAlSi_2O_6(B)_{(s)} + Na_2CO_{3(s)} \rightarrow Li_2O_{(s)} + 2NaAlSi_2O_{6(s)} + CO_{2(g)} \quad (12)$$

$$2LiAlSi_2O_6(B)_{(s)} + Na_2CO_{3(s)} \rightarrow Li_2CO_{3(s)} + 2NaAlSi_2O_{6(s)} \quad (13)$$

$$LiAlSi_2O_6(B)_{(s)} + NaF_{(s)} \rightarrow LiF_{(s)} + 0.5NaAlSi_3O_{8(s)} + 0.5NaAlSiO_{4(s)} \quad (14)$$

$$2LiAlSi_2O_6(B)_{(s)} + K_2SO_{4(s)} \rightarrow Li_2SO_{4(s)} + 2KAlSi_2O_{6(s)} \quad (15)$$

$$2LiAlSi_2O_6(B)_{(s)} + Na_2SO_{4(s)} \rightarrow Li_2SO_{4(s)} + 2NaAlSi_2O_{6(s)} \quad (16)$$

$$0.5LiAlSi_2O_6(B)_{(s)} + CaO_{(s)} \rightarrow 0.5LiAlO_{2(s)} + CaSiO_{3(s)} \quad (17)$$

$$2LiAlSi_2O_6(B)_{(s)} + H_2SO_{4(aq)} \rightarrow Li_2SO_{4(s)} + 4SiO_{2(s)} + Al_2O_{3(s)} + H_2O_{(g)} \quad (18)$$

$$2LiAlSi_2O_6(B)_{(s)} + SO_{3(g)} + 3H_2O_{(g)} \rightarrow Li_2SO_{4(s)} + 4SiO_{2(s)} + 2Al(OH)_{3(s)} \quad (19)$$

$$LiAlSi_2O_6(B)_{(s)} + KCl_{(s)} \rightarrow LiCl_{(s)} + 2SiO_{2(s)} + KAlO_{2(s)} \quad (20)$$

$$6LiAlSi_2O_6(B)_{(s)} + Fe_2(SO_4)_{3(s)} \rightarrow 3Li_2SO_{4(s)} + 3Al_2O_{3(s)} + Fe_2O_{3(s)} + 12SiO_{2(s)} \quad (21)$$

$$6LiAlSi_2O_6(B)_{(s)} + Al_2(SO_4)_{3(s)} \rightarrow 3Li_2SO_{4(s)} + 4Al_2O_{3(s)} + 12SiO_{2(s)} \quad (22)$$

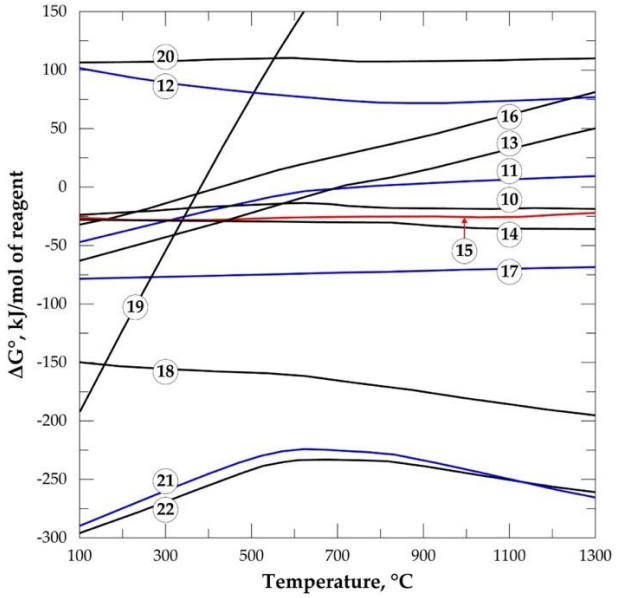

Figure 2. The standard Gibbs energies for roasting of spodumene for processes encountered in the literature (reactions (10)–(22)) versus temperature (data from the HSC Chemistry 5.1 software).

It is worth noting from Figure 2 that all the reagents used in literature for alkaline, sulfating, fluorination, chlorination (with the exception of KCl) and carbonizing to yield Li_2CO_3 were spontaneous at a point or throughout the operating temperature for roasting spodumene. Chlorination with KCl and carbonization to produce Li_2O were the only processes which are not thermodynamically favorable throughout the temperature range. All reagents for sulfating roasting except K_2SO_4 and the feasible carbonizing process showed a major variation of spontaneity with temperature while reagents for other processes did not. Sulfation and chlorination using Na_2SO_4, SO_3 and Cl_2 as well as the spontaneous carbonizing process benefit from feasibility only at low temperatures; they are not feasible at high temperatures. The observed spontaneity of $CaCl_2$ chlorination parallels observations by Barbosa et al. [44]. However, those observations are contrary to observations made by the same authors earlier, which indicated feasibility with Cl_2 even at higher temperatures [43]. The reason for this difference is not yet apparent.

To gain a deeper understanding of the approaches outlined in literature, the HSC Chemistry 5.1 software equilibrium module was further employed to investigate the equilibrium amount of each process as a function of temperature. Figure 3 displays the equilibrium moles for the sulfating process using Na_2SO_4, K_2SO_4, H_2SO_4, $SO_{3(g)}/H_2O_{(g)}$, $Fe_2(SO_4)_3$ and $Al_2(SO_4)_3$ as reagents. As indicated earlier (Figure 2), Na_2SO_4 is feasible only below 400 °C. It is only below this temperature that the equilibrium moles of the products (lithium sulfate and sodium aluminosilicate, $NaAlSiO_6$) are higher than spodumene (Figure 3a), confirming feasibility. It can be inferred that the highest amount of lithium sulfate can be obtained below 200 °C above which it starts decreasing until 400 °C, where the reaction ceases feasibilityAround 400 °C and above, solid lithium sulfate begins to change into a liquid state due to the increasing temperature but the amount is relatively smaller in the system; resulting from the decreased feasibility of the reaction. Temperatures less than 400 °C appear to be the best for Na_2SO_4/spodumene roasting, however, 1000 °C was required to achieve 90.4% lithium extraction according to Luong et al. [23] for Na_2SO_4/lepidolite roasting for 30 min. Unlike Na_2SO_4, K_2SO_4 drives the reaction to the right within the whole temperature range considered, forming lithium sulfate in the solid phase (Figure 3b), moles of lithium sulfate then are at levels higher than spodumene within the entire temperature range considered. There is a steady decrease in moles of solid lithium sulfate and a simultaneous increase of the liquid phase with increasing temperature. This is a result of the conversion of the solid into liquid as liquid is formed until around the melting point (859 °C); where all the solid phase changes to liquid and remains constant. Thermodynamics of the sulfuric acid process predicts feasibility throughout the entire temperature range considered (Figure 2) with ΔG^o becoming more negative with increasing temperature. The highest amount of soluble Li_2SO_4 produced by modelling of this process occurs around 200 °C. When the temperature is close to 300 °C and beyond, there is a steady decrease in quantity. These observations are in line with observations by Salakjani et al. [19] whose maximum recovery occurred at 250 °C, but a decrease in lithium recovery was observed at 300 °C and beyond. This occurrence is as a result of the decomposition of sulfuric acid between 300 and 400 °C (Figure 3c). However, the process remains spontaneous even after the decomposition of the acid because the products of the decomposition (SO_3 and H_2O) from Equation (23) are capable of driving the reaction to the product in Equation (25) but with a limited amount of lithium sulfate production. SO_3 breaks down further into SO_2 and O_2 (Equation (24)), which remain as spectator species. Precautionary measures are advised at this point due to the toxicity of SO_2 produced. Thus above 400 °C the sulfuric acid process has thermodynamic behavior similar to the sulfation process using $SO_{3(g)}/H_2O_{(g)}$ invented by Archambault et al. [32].

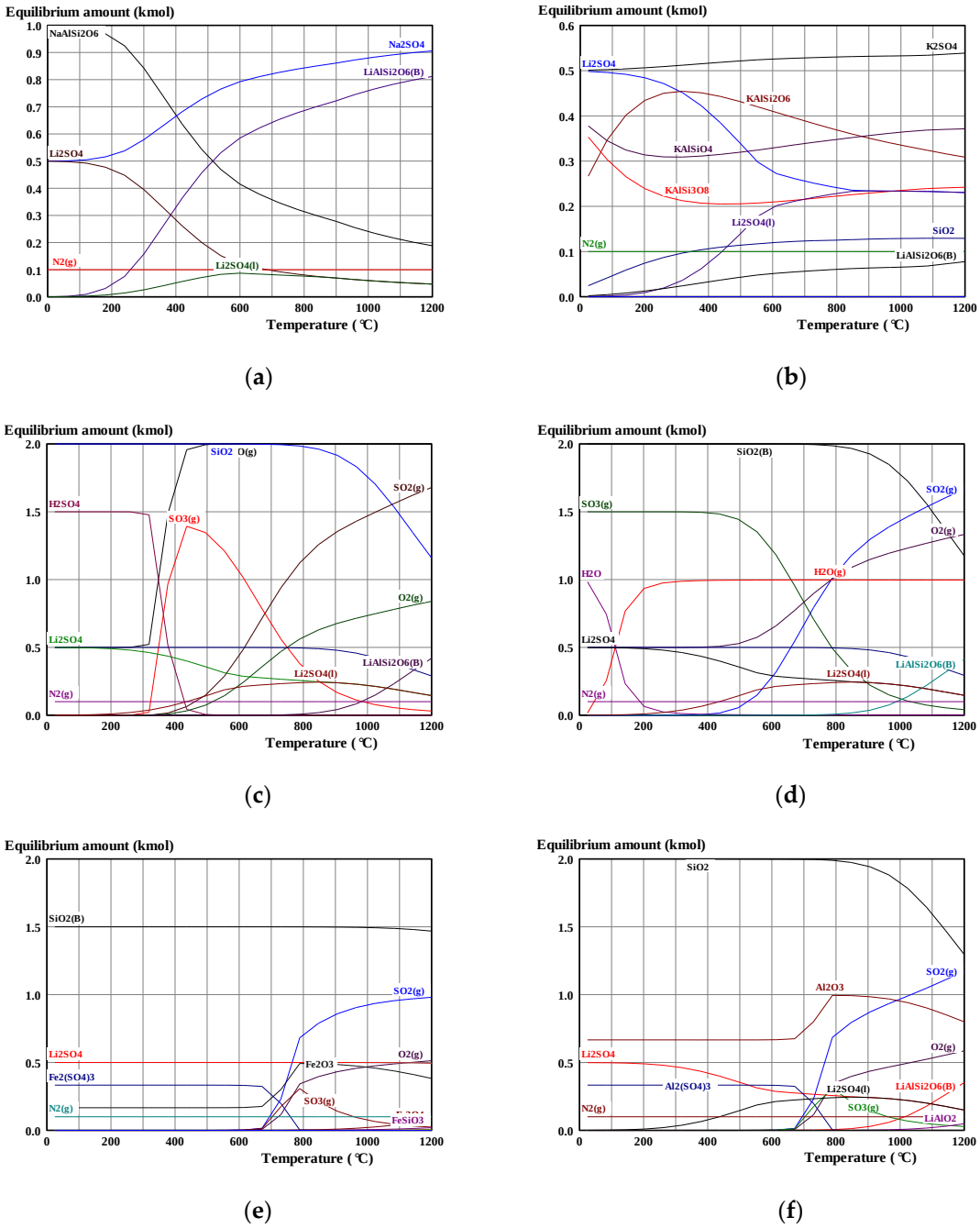

Figure 3. Equilibrium amounts versus temperature for sulfate roasting of spodumene using (**a**) Na_2SO_4, (**b**) K_2SO_4, (**c**) H_2SO_4, (**d**) $SO_{3(g)}$, (**e**) $Fe_2(SO_4)_3$ and (**f**) $Al_2(SO_4)_3$ (data from HSC Chemistry 5.1 software).

Solid lithium sulfate in the reaction medium melts above 800 °C. The equilibrium amount of lithium sulfate decreases after the decomposition of the acid but the kinetics of the process is expected to be favored due to the production of the gaseous reactants which easily access reaction sites by diffusion compared to the percolation of sulfuric acid as a result of its viscosity. Around 900 °C and above the sulfation process with sulfuric acid and $SO_{3(g)}/H_2O_{(g)}$ ceases spontaneity, signified by a sharp increase in the amount of spodumene in Figure 3c,d. This observation is attributed to the sintering effect and the formation of lithium silicate, which has close resemblance to β-sopodumene [54,55].

$$H_2SO_{4(aq)} \rightarrow SO_{3(g)} + H_2O_{(g)} \quad (23)$$

$$2SO_{3(g)} \rightarrow 2SO_{2(g)} + O_{2(g)} \quad (24)$$

$$Li_2O.Al_2O_3.4SiO_{2(s)} + SO_{3(g)} + 4H_2O_{(g)} \rightarrow Li_2SO_{4(s)} + Al_2O_3.4SiO_2.H_2O_{(s)} \quad (25)$$

Spodumene roasting using $Fe_2(SO_4)_3$ and $Al_2(SO_4)_3$ have similar behavior (Figure 3e,f), except for a constant production of Li_2SO_4 in the case of $Fe_2(SO_4)_3$, but its amount is higher only at temperatures below 500 °C for $Al_2(SO_4)_3$. Metal sulfates also break down, producing SO_3/SO_2 at higher temperatures, which may influence the roasting process. According to Luong et al. [24], Na_2SO_4 like K_2SO_4 has high thermal stability, ergo they break down at higher temperatures, producing a small amount of SO_3/SO_2, which apparently has no effect on the process. This is confirmed by the absence of these gases in their modelled process (Figure 3a,b). For iron and aluminum sulfates, the amount of the gases generated during the decomposition is large enough to influence the process. From Figure 3e,f, the sulfate of these metals is observed to decompose around 700 °C, producing the gases but their effect is minimal in spodumene as compared to observation in lepidolite by Luong et al. [24], which may be due to the sintering of spodumene above 800 °C [54,55].

Calcium oxide was considered the reagent for alkaline roasting of spodumene. $LiAlO_2$ is predicted by HSC as a product of the reaction (Equation (17)). $Ca(OH)_2$ produced from the reaction of Equation (26) reacts with $LiAlO_2$ (Equation (27)), producing LiOH in the solid or liquid phase depending on the temperature.

$$CaO_{(s)} + H_2O_{(g)} \rightarrow Ca(OH)_{2(s)} \quad (26)$$

$$2LiAlO_{2(s)} + Ca(OH)_{2(s)} \rightarrow 2LiOH_{(s)} + CaAl_2O_{4(s)} \quad (27)$$

It can be found from Figure 2 that the process is feasible throughout the temperature range considered. This is confirmed by Figure 4 where soluble lithium hydroxide is formed as the useful product. Other products formed include silica, silicates and other aluminosilicate with traces of calcium hydroxide. The moles of lithium hydroxide in the solid phase decreases sharply with increasing temperature. This occurrence is attributed to the conversion of the solid into the liquid phase, confirmed by the sharp rise of the liquid phase with increasing temperature until around its melting point (462 °C), where there is a total transformation into the liquid phase (Figure 4).

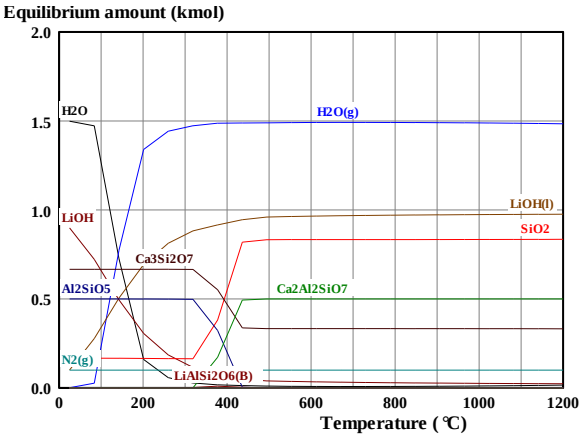

Figure 4. Equilibrium amounts versus temperature for alkaline roasting of spodumene using CaO (data from HSC Chemistry 5.1 software).

Figure 5a–c shows the modelling of chlorination roasting using $CaCl_2$, Cl_2 and KCl, performed experimentally by several authors [41,43,44,46]. From Figure 2, it is observed that the reactions with $CaCl_2$ and Cl_2 are favored at a point or in the entire temperature range, however, it is not feasible with KCl. This infeasibility is confirmed in Figure 5a where an appreciable mole of spodumene is observed

in the equilibrium mixture. There is an onset production of solid LiCl which is converted into the liquid phase as soon as it is produced (Figure 5b,c). At ~610 °C (the melting point of lithium chloride) lithium chloride in the medium is predominantly in the liquid phase. A high volatilization temperature is expected due to the high vapor pressure of LiCl. Barbosa et al. [43] observed the gaseous phase at ~1000 °C, however, it was not the case in the chlorination processes that were modelled.

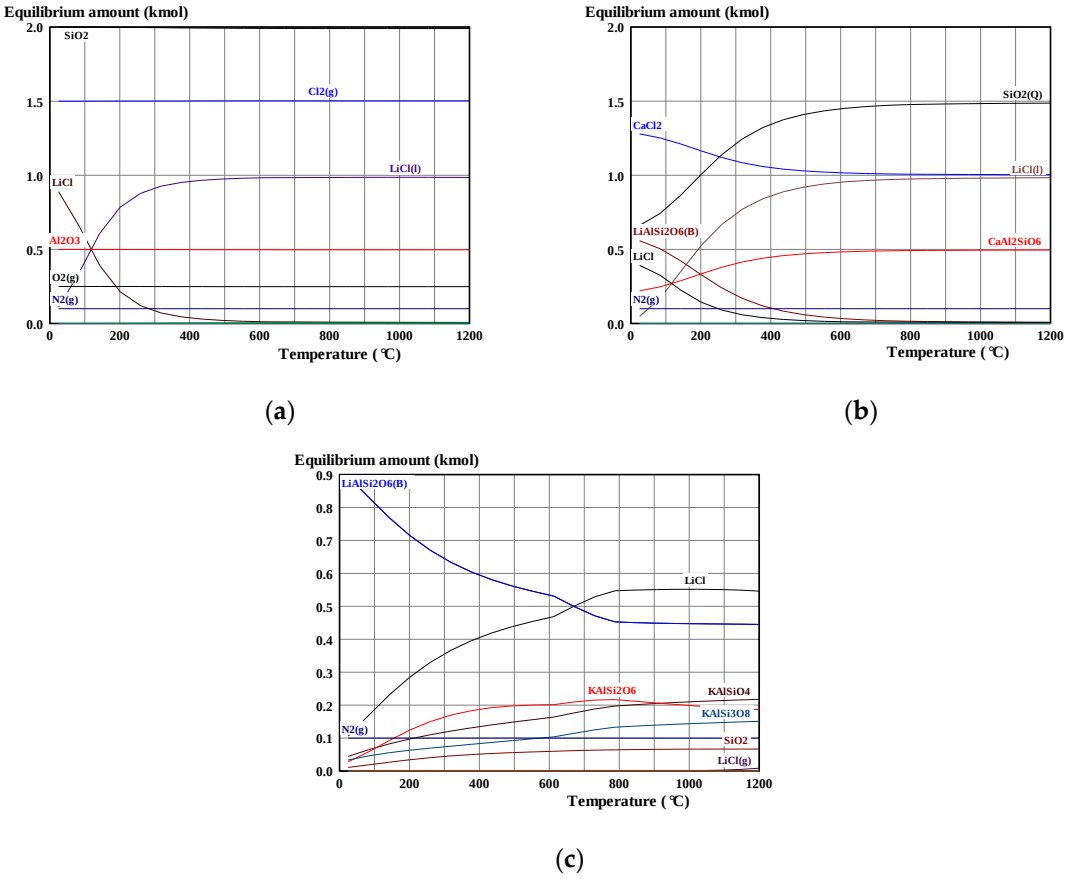

Figure 5. Equilibrium amounts versus temperature for chlorination of spodumene using (**a**) $CaCl_2$, (**b**) Cl_2 and (**c**) KCl (data from HSC Chemistry 5.1 software).

Carbonizing roasting of spodumene using Na_2CO_3 as seen earlier in in Equations (12) and (13) may yield either Li_2O or Li_2CO_3.The Li_2O that is produced can be made to go into leaching to produce LiOH but the prediction from the HSC software indicates that the reaction is not spontaneous except for the production of Li_2CO_3 (Figure 2). The infeasibility of Equation (12) is confirmed in Figure 6a, where there is apparently, no leachable lithium product formed. The production of Li_2CO_3 from this process is feasible below 700 °C (Figure 2) which is confirmed in Figure 6b where Li_2CO_3 is observed below this temperature. Around 300 °C, the Li_2CO_3 that was produced decomposes, forming carbon dioxide, silicates, aluminates and aluminosilicates (Figure 6b). Thus, though there is feasibility until 700 °C, it is not recommended to operate up to this temperature due to the decomposition which occurs alongside the process. This confirms investigations by [47] that the ideal hydrothermal decomposition temperature for the process as 90–225 °C. It is mentioned that, the mixture of products from the decomposition process may be converted to sodic zeolite which when tapped increases the recovery and the purity of lithium carbonate produced. 94% and 70% lithium recovery were reached by working under high pressure and by adding sodium chloride, respectively, with this process [48,49].

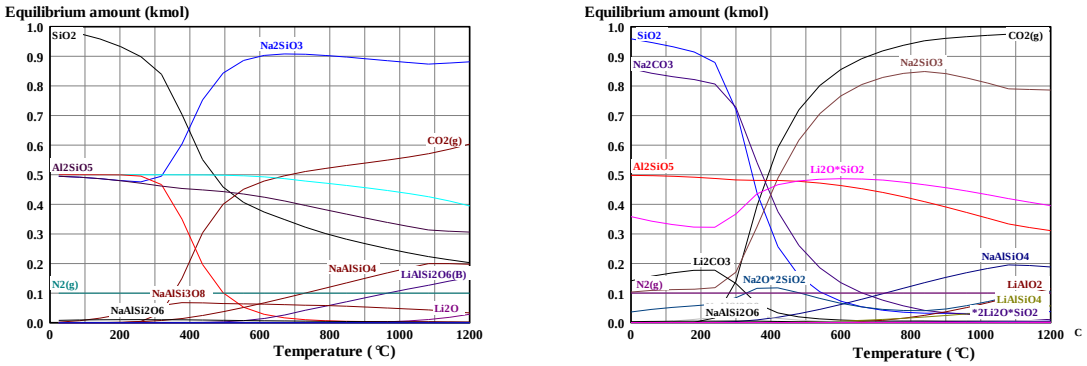

Figure 6. Equilibrium amounts versus temperature for carbonizing roasting of spodumene using Na_2CO_3 by considering reactions reported in (**a**) Equation (12) and in (**b**) Equation (13), leading to the formation of Li_2O and Li_2CO_3, respectively (data from HSC Chemistry 5.1 software).

Fluorination roasting of calcined spodumene using NaF is found favored throughout the temperatures (Figure 2), which is confirmed by the formation of lithium fluoride in the solid or liquid phase (Figure 7) [50]. On the other hand, the predicted reversal of the process at higher temperatures, signified by the rise of spodumene in their model with increasing temperature, was not observed in this study. The disparity may be attributed to the absence of liquid lithium fluoride in their model. Solid lithium fluoride begins to form but it melts and its amount decreases due to the simultaneous formation of the liquid phase with increasing temperature. The liquid phase becomes the stable one at higher temperatures and its absence from the HSC equilibrium calculation leads to some errors in the result. There is a leveling of the liquid lithium Fluoride production at around 845 °C (the melting point of LiF) due to the transformation of all of the solid phase into liquid. Their maximum extraction (~90%) occurred at 600 °C, which is just around what is predicted in this study. Gaseous lithium fluoride was not observed within this temperature range, but it is expected to appear around its boiling point (1676 °C) and beyond.

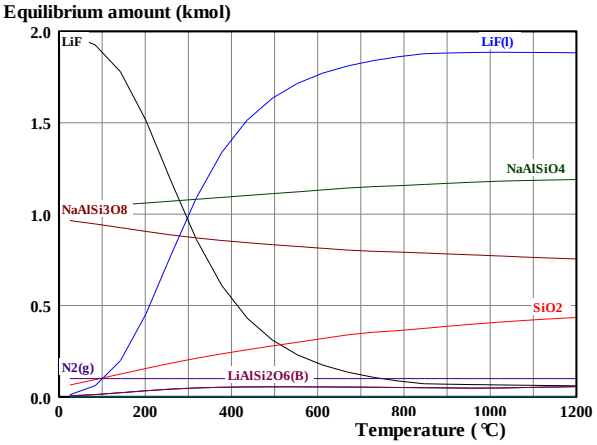

Figure 7. Equilibrium amounts versus temperature for fluorination roasting of spodumene using NaF (data from HSC Chemistry 5.1 software).

5. Conclusions

Besides the general review of the processes for spodumene treatment, an evaluation of the chemical thermodynamics reveals that, sulfation, alkaline, fluorination, chlorination as well as carbonizing to produce lithium carbonate were processes which had the required thermodynamic driving force

to move the reaction to the products for the reagents encountered in the literature. It is therefore not surprising sulfation (using sulfuric acid) and alkaline processes are considered as an industrial approach for lithium extraction. Looking at the mild nature of the reagents in the alkaline processes, it will be a real contender to the acidic process if the high energy requirement in the decomposition of limestone can be decreased by some means. Though roasting with lime is feasible even at lower temperatures, the decomposition of limestone is a precursor for the industrial production of lime which makes the overall process energy intensive. Future work must be focused on reducing the high heat needed for decomposing limestone to make the alkaline process economically viable. In the acid roasting process, SO_3 and H_2O from the acid decomposition may drive the reaction to produce at a faster rate due to the higher diffusion rate of gases compared to liquids. In spite of the expected faster rate of reaction of these gases (SO_3 and H_2O), little is known concerning their use for beneficiating lithium bearing minerals. It will be interesting if the behavior of these species as well as other gases are considered for processing lithium from ores. Sulfation as a method of spodumene beneficiation is mostly limited to sulfuric acid, with little focus on other sulfating reagents, but from the thermodynamics of this group of compounds it will also be interesting to pay attention to other members of this compound. There is considerable literature on the use of some alkali and alkaline earth metal sulfates as well as sulfates of ammonium for processing other lithium bearing minerals than spodumene. Even in those cases, there is minimal explanation of the chemical thermodynamics of the processes. Future work must therefore look at the use of other sulfating reagents for spodumene processing as well as their thermodynamics, both on spodumene and other lithium bearing minerals. Chlorination and fluorination have been found to be promising for lithium extraction. Few chlorination and fluorination agents are encountered in the literature for the process, despite their thermodynamic feasibility. More research should be pursued in search for new fluorination and chlorination agents and the processes should be optimized. The thermodynamics of the carbonizing process yielding lithium carbonate is very interesting; in particular its low operating temperature and the direct production of a considerably pure product. It is surprising that it has not attracted much attention. Further research must be pursued to optimize the process. From a thermodynamic point of view, temperatures below 300 °C are predicted for the acid process and the feasible carbonizing process due to the acid and lithium carbonate decomposition. For the other processes discussed, temperatures less than 600 °C are advised, except for fluorination, which works well a little above 600 °C.

Author Contributions: Conceptualization, A.C. and N.K. and software, A.Y.F. and N.K.; A.Y.F. writing—original draft preparation and writing—review and editing, A.C., N.K. and J.V.; Supervision, A.C. and N.K.; Funding acquisition, A.C. All authors have read and agreed to the published version of the manuscript.

Funding: This work was supported by the French National Research Agency through the national program "Investissements d'avenir" with the reference ANR-10-LABX-21-RESSOURCES21.

Conflicts of Interest: The authors declare no conflict of interest.

References

1. Christmann, P.; Gloaguen, E.; Labbé, J.-F.; Melleton, J.; Piantone, P. Global Lithium Resources and Sustainability Issues. In *Lithium Process Chemistry*; Elsevier: Amsterdam, The Netherlands, 2015; pp. 1–40. ISBN 9780128014172.
2. Meng, F.; McNeice, J.; Zadeh, S.S.; Ghahreman, A. Review of Lithium Production and Recovery from Minerals, Brines, and Lithium-Ion Batteries. *Miner. Process. Extr. Metall. Rev.* **2019**, 1–19. [CrossRef]
3. Pillot, C. The Rechargeable Battery Market and Main Trends 2015–2025. In *Avicenne Energy, Proceedings of the 18th International Meeting on Lithium Batteries*; Chicago, IL, USA, 19–24 June 2016, ENSAM: Paris, France, 2016.
4. Salakjani, N.K.; Singh, P.; Nikoloski, A.N. Mineralogical transformations of spodumene concentrate from Greenbushes, Western Australia. Part 1: Conventional heating. *Miner. Eng.* **2016**, *98*, 71–79. [CrossRef]
5. Salakjani, N.K.; Nikoloski, A.N.; Singh, P. Mineralogical transformations of spodumene concentrate from Greenbushes, Western Australia. Part 2: Microwave heating. *Miner. Eng.* **2017**, *100*, 191–199. [CrossRef]

6. Zelikman, A.N.; Belyaevskaya, L.V.; Samsonov, G.V.; Krein, O.E. *Metallurgy of Rare Metals*; Program for Scientific Translations: Jerusalem, Israel, 1966.
7. Claffy, E.W. Composition, tenebrescence and luminescence of spodumene minerals. *Am. Mineral.* **1953**, *38*, 919–931.
8. Gabriel, A.; Slavin, M.; Carl, H.F. Minor constituents in spodumene. *Econ. Geol.* **1942**, *37*, 116–125. [CrossRef]
9. Salakjani, N.K.; Singh, P.; Nikoloski, A.N. Production of Lithium–A Literature Review Part 1: Pretreatment of Spodumene. *Miner. Process. Extr. Metall. Rev.* **2020**, *41*, 335–348. [CrossRef]
10. Peltosaari, O.; Tanskanen, P.; Heikkinen, E.-P.; Fabritius, T. α→ γ→ β -phase transformation of spodumene with hybrid microwave and conventional furnaces. *Miner. Eng.* **2015**, *82*, 54–60. [CrossRef]
11. Abdullah, A.A.; Oskierski, H.C.; Altarawneh, M.; Senanayake, G.; Lumpkin, G.; Dlugogorski, B.Z. Phase transformation mechanism of spodumene during its calcination. *Miner. Eng.* **2019**, *140*, 105883. [CrossRef]
12. Fraas, F.; Ralston, O.C.; States., U.; Mines., B. *Beneficiation of Spodumene by Decrepitation*; U.S. Deptartment of the Interior; Bureau of Mines: Washington, WA, USA, 1937.
13. Dessemond, C.; Lajoie-Leroux, F.; Soucy, G.; Laroche, N.; Magnan, J.-F. Spodumene: The Lithium Market, Resources and Processes. *Minerals* **2019**, *9*, 334. [CrossRef]
14. White, G.D.; McVay, T.N. *Some Aspects of the Recovery of Lithium from Spodumene*; Oak Ridge National Laboratory: Oak Ridge, TN, USA, 1958.
15. Guo, H.; Kuang, G.; Wang, H.; Yu, H.; Zhao, X. Investigation of Enhanced Leaching of Lithium from α-Spodumene Using Hydrofluoric and Sulfuric Acid. *Minerals* **2017**, *7*, 205. [CrossRef]
16. Moore, R.L.; Mann, J.P.; Montoya, A.; Haynes, B.S. In situ synchrotron XRD analysis of the kinetics of spodumene phase transitions. *Phys. Chem. Chem. Phys.* **2018**, *20*, 10753–10761. [CrossRef] [PubMed]
17. Dwyer, T.E. Recovery of Lithium from Spodumene Ores. U.S. Patent No. 2801153A, 30 July 1957.
18. Gasalla, H.; Pereira, E. Activation-deactivation mechanisms in spodumene samples. *Solid State Ion.* **1990**, *42*, 1–6. [CrossRef]
19. Salakjani, N.K.; Singh, P.; Nikoloski, A.N. Acid roasting of spodumene: Microwave vs. conventional heating. *Miner. Eng.* **2019**, *138*, 161–167. [CrossRef]
20. Choubey, P.K.; Kim, M.; Srivastava, R.R.; Lee, J.; Lee, J.-Y. Advance review on the exploitation of the prominent energy-storage element: Lithium. Part I: From mineral and brine resources. *Miner. Eng.* **2016**, *89*, 119–137. [CrossRef]
21. Meshram, P.; Pandey, B.D.; Mankhand, T.R. Extraction of lithium from primary and secondary sources by pre-treatment, leaching and separation: A comprehensive review. *Hydrometallurgy* **2014**, *150*, 192–208. [CrossRef]
22. Yan, Q.; Li, X.; Wang, Z.; Wu, X.; Guo, H.; Hu, Q.; Peng, W.; Wang, J. Extraction of valuable metals from lepidolite. *Hydrometallurgy* **2012**, *117–118*, 116–118. [CrossRef]
23. Luong, V.T.; Kang, D.J.; An, J.W.; Kim, M.J.; Tran, T. Factors affecting the extraction of lithium from lepidolite. *Hydrometallurgy* **2013**, *134–135*, 54–61. [CrossRef]
24. Luong, V.T.; Kang, D.J.; An, J.W.; Dao, D.A.; Kim, M.J.; Tran, T. Iron sulphate roasting for extraction of lithium from lepidolite. *Hydrometallurgy* **2014**, *141*, 8–16. [CrossRef]
25. Siame, E.; Pascoe, R.D. Extraction of lithium from micaceous waste from china clay production. *Miner. Eng.* **2011**, *24*, 1595–1602. [CrossRef]
26. Sitando, O.; Crouse, P.L. Processing of a Zimbabwean petalite to obtain lithium carbonate. *Int. J. Miner. Process.* **2012**, *102*, 45–50. [CrossRef]
27. Amer, A.M. The hydrometallurgical extraction of lithium from egyptian montmorillonite-type clay. *JOM* **2008**, *60*, 55–57. [CrossRef]
28. Kuang, G.; Liu, Y.; Li, H.; Xing, S.; Li, F.; Guo, H. Extraction of lithium from β-spodumene using sodium sulfate solution. *Hydrometallurgy* **2018**, *177*, 49–56. [CrossRef]
29. Lajoie-Leroux, F.; Dessemond, C.; Soucy, G.; Laroche, N.; Magnan, J.-F. Impact of the impurities on lithium extraction from β-spodumene in the sulfuric acid process. *Miner. Eng.* **2018**, *129*, 1–8. [CrossRef]
30. Tian, Q.; Chen, B.; Chen, Y.; Ma, L.; Shi, X. Roasting and leaching behavior of spodumene in sulphuric acid process. *Chin. J. Rare Met.* **2011**, *35*, 118–123. [CrossRef]
31. Ellestad, R.B.; Milne, L. Method of Extracting Lithium Values From Spodumene Ores. U.S. Patent No. 2,516,109, 25 July 1950.
32. Maurice, A.; Macewan, J.U.; Olivier, C.A. Method of Producing Lithium Carbonate from Spodumene. U.S. Patent No. 3,017,243, 16 January 1962.

33. Jandová, J.; Dvořák, P.; Vu, H.N. Processing of zinnwaldite waste to obtain Li2CO3. *Hydrometallurgy* **2010**, *103*, 12–18. [CrossRef]
34. Mcintosh, N. Production of Lithium Compounds. U.S. Patent No. 2,413,644, 31 December 1946.
35. Jandová, J.; Vu, H.N.; Kondas, J.; Dvořák, P. Lithium recovery from wastes after mining of Sn-W ore. In Proceedings of the European Metallurgical Conference, EMC 2007, Düsseldorf, Germany, 11–14 June 2007; pp. 667–677.
36. Jandova, J.; Vu, H.N. Processing of zinnwaldite wastes to obtain lithium and rubidium compounds. In Proceedings of the 2008 Global Symposium on Recycling, Waste Treatment and Clean Technology, REWAS 2008, Cancun, Mexico, 12–15 October, 2008.
37. Jandová, J.; Vu, H.N.; Beloková, T.; DvořÁk, P.; Kondás, J. Obtaining Li2CO3 from Zinnwaldite wastes. *Ceram. Silik.* **2009**, *53*, 108–112.
38. Kanari, N.; Allain, E.; Joussemet, R.; Mochón, J.; Ruiz-Bustinza, I.; Gaballah, I. An overview study of chlorination reactions applied to the primary extraction and recycling of metals and to the synthesis of new reagents. *Thermochim. Acta* **2009**, *495*, 42–50. [CrossRef]
39. Kanari, N.; Mishra, D.; Mochón, J.; Verdeja, L.F.; Diot, F.; Allain, E. Some kinetics aspects of chlorine-solids reactions. *Rev. Metal.* **2010**, *46*, 22–36. [CrossRef]
40. Gaballah, J.; Kanari, N.; Djona, M. Use of chlorine for mineral processing, metal extraction and recycling via synthesis of new reagent. *Chloride Metall.* **2002**, *1*, 203–225.
41. Peterson, J.A.; Glioss, G.H. Lithium Values Recovery Process. U.S. Patent No. 2,893,828, 7 July 1959.
42. Yan, Q.; Li, X.; Wang, Z.; Wang, J.; Guo, H.; Hu, Q.; Peng, W.; Wu, X. Extraction of lithium from lepidolite using chlorination roasting–water leaching process. *Trans. Nonferrous Met. Soc. China* **2012**, *22*, 1753–1759. [CrossRef]
43. Barbosa, L.I.; Valente, G.; Orosco, R.P.; González, J.A. Lithium extraction from β-spodumene through chlorination with chlorine gas. *Miner. Eng.* **2014**, *56*, 29–34. [CrossRef]
44. Barbosa, L.I.; González, J.A.; del Carmen Ruiz, M. Extraction of lithium from β-spodumene using chlorination roasting with calcium chloride. *Thermochim. Acta* **2015**, *605*, 63–67. [CrossRef]
45. Dang, H.; Li, N.; Chang, Z.; Wang, B.; Zhan, Y.; Wu, X.; Liu, W.; Ali, S.; Li, H.; Guo, J.; et al. Lithium leaching via calcium chloride roasting from simulated pyrometallurgical slag of spent lithium ion battery. *Sep. Purif. Technol.* **2020**, *233*, 116025. [CrossRef]
46. Erasmus, H.D. Method of Treating Lithiferous Ores to Recover Lithium as Lithium Chloride. U.S. Patent No. 2,561,439, 24 July 1951.
47. Maurice, A.; Olivier, C.A. Carbonatizing Roast of Lithium Bearing Ores. U.S. Patent No. 3,380,802, 30 April 1968.
48. Chen, Y.; Tian, Q.; Chen, B.; Shi, X.; Liao, T. Preparation of lithium carbonate from spodumene by a sodium carbonate autoclave process. *Hydrometallurgy* **2011**, *109*, 43–46. [CrossRef]
49. Dos Santos, L.L.; do Nascimento, R.M.; Pergher, S.B.C. Beta-spodumene: Na_2CO_3: NaCl system calcination: A kinetic study of the conversion to lithium salt. *Chem. Eng. Res. Des.* **2019**, *147*, 338–345. [CrossRef]
50. Rosales, G.D.; Resentera, A.C.J.; Gonzalez, J.A.; Wuilloud, R.G.; Rodriguez, M.H. Efficient extraction of lithium from β-spodumene by direct roasting with NaF and leaching. *Chem. Eng. Res. Des.* **2019**, *150*, 320–326. [CrossRef]
51. Rosales, G.D.; Ruiz, M.D.C.; Rodriguez, M.H. Novel process for the extraction of lithium from β-spodumene by leaching with HF. *Hydrometallurgy* **2014**, *147–148*, 1–6. [CrossRef]
52. Robinson, G.P. Recovery of Lithium from Ore. U.S. Patent No. 2,983,576, 9 May 1961.
53. Hayes, E.T.; Williams, F.P.; Sternberg, W. Production of Lithium Chloride from Spodumene. U.S. Patent No. 2,533,246, 12 December 1950.
54. Sharratt, H.J. The Extraction of Lithium from Spodumene. Master's Thesis, McGill University, Montreal, QC, Canada, 1955.
55. Salakjani, N.K.; Singh, P.; Nikoloski, A.N. Production of Lithium–A Literature Review. Part 2. Extraction from Spodumene. *Miner. Process. Extr. Metall. Rev.* **2019**, 1–16. [CrossRef]

materials

MDPI

Article

Physico-Chemical Characteristics of Spodumene Concentrate and Its Thermal Transformations

Allen Yushark Fosu [1], Ndue Kanari [1], Danièle Bartier [1], Harrison Hodge [2], James Vaughan [2] and Alexandre Chagnes [1,*]

[1] Université de Lorraine, CNRS, GeoRessources, F-54000 Nancy, France; allen.fosu@univ-lorraine.fr (A.Y.F.); ndue.kanari@univ-lorraine.fr (N.K.); daniele.bartier@univ-lorraine.fr (D.B.)
[2] School of Chemical Engineering, The University of Queensland, Brisbane, QLD 4072, Australia; h.hodge@uq.edu.au (H.H.); james.vaughan@uq.edu.au (J.V.)
* Correspondence: alexandre.chagnes@univ-lorraine.fr; Tel.: +33-372-744-544

Abstract: Spodumene concentrate from the Pilbara region in Western Australia was characterized by X-ray diffraction (XRD), Scanning Electron Microscope Energy Dispersive Spectroscopy (SEM-EDS) and Mineral Liberation Analysis (MLA) to identify and quantify major minerals in the concentrate. Particle diameters ranged from 10 to 200 microns and the degree of liberation of major minerals was found to be more than 90%. The thermal behavior of spodumene and the concentration of its polymorphs were studied by heat treatments in the range of 900 to 1050 °C. All three polymorphs of the mineral (α, γ and β) were identified. Full transformation of the α-phase was achieved at 975 °C and 1000 °C after 240 and 60 min treatments, respectively. SEM images of thermally treated concentrate revealed fracturing of spodumene grains, producing minor cracks initially which became more prominent with increasing temperature. Material disintegration, melting and agglomeration with gangue minerals were also observed at higher temperatures. The metastable γ-phase achieved a peak concentration of 23% after 120 min at 975 °C. We suggest 1050 °C to be the threshold temperature for the process where even a short residence time causes appreciable transformation, however, 1000 °C may be the ideal temperature for processing the concentrate due to the degree of material disintegration and α-phase transformation observed. The application of a first-order kinetic model yields kinetic parameters which fit the experimental data well. The resultant apparent activation energies of 655 and 731 kJ mol^{-1} obtained for α- and γ-decay, respectively, confirm the strong temperature dependence for the spodumene polymorph transformations.

Keywords: spodumene concentrate; thermal transformation; activation energy; first-order kinetics; morphological changes; physicochemical properties

Citation: Fosu, A.Y.; Kanari, N.; Bartier, D.; Hodge, H.; Vaughan, J.; Chagnes, A. Physico-Chemical Characteristics of Spodumene Concentrate and Its Thermal Transformations. *Materials* **2021**, *14*, 7423. https://doi.org/10.3390/ma14237423

Academic Editor: Giuseppe Cruciani

Received: 4 October 2021
Accepted: 1 December 2021
Published: 3 December 2021

1. Introduction

Lithium is undergoing important investigations in order to meet its worldwide stable supply as this element is now considered a critical metal by many countries. It is produced from salar brines or ores. The production from salar brines involves three major steps; evaporation, purification and precipitation. The recovery of the metal by this approach faces many challenges, including the delay in production due to solar evaporation and the presence of many impurities which demand the implementation of refining stages. The main interest of lithium production from salar brine comes from the low cost of the operations. However, the recent increase in the price of lithium has resulted in huge investments into lithium production from ores.

Lithium–Cesium–Tantalum (LCT) pegmatites are the main source of lithium as well as a rich source of tantalum and cesium as they contain spodumene, columbite–tantalite and pollucite, respectively [1]. They may also contain lepidolite, petalite, eucryptite and amblygonite as lithium sources. Muscovite, albite, quartz and feldspar are common minerals that are in close association with LCT; often considered as gangue but may be

a by-product of lithium processing. In spite of the high processing cost from ores, the increasing demand and its price make it economically viable. About half of the lithium produced is now obtained from ores [2] and spodumene ($LiAlSi_2O_6$) stands out as the most significant ore-type due to the high lithium content (about 4%) in its pure state as well as its ease of processing.

Spodumene belongs to the clinopyroxene group, occurring naturally as α monoclinic polymorph which is immune to chemical attack due to its compact nature. In this form, lithium and aluminum sit at the *M2* and *M1* octahedral sites respectively, whilst silicon is hosted at the middle of the tetrahedron. The octahedral parts through the sharing of common oxygen atoms, bridge to form chains. The octahedral chains are parallelly arranged to Si in the tetrahedron through O–Si–O ionic bond with the Li and Al atoms. Its original space group is C2/c and in this form, lithium bonds with six atoms of oxygen; with a pair of oxygen atoms having a definite Li–O bond length of 2.120, 2.267 and 2.281 Å [3]. At pressures of around 3.2 GPa, the original stable space group (C2/c) may change to P21/c upon reversible transition [4–6] and assumes cell parameters of a = 9.471 Å, b = 8.400 Å, c = 5.223 Å, $\alpha = \gamma$ = 90.0 degrees and β = 110.2 degrees.

β-spodumene, another polymorph of the mineral consists of two separate tetrahedron structures which are joined in a three-dimensional form with their central parts hosting aluminum or silicon [7]. Lithium in this phase is located between the cavity of five-member rings, formed by the individual tetrahedron. Zeolite-like channels created from the five-member rings run parallel to the (100) or (010) planes [8]. The zeolite-like channels which are parallel to the a and b axis are comparatively larger and account for the tremendous ion-exchange capacity of β-spodumene during roasting [8]. It has the space group $P4_32_12$ with cell parameters $a = b$ = 7.534 Å and c = 9.158 Å [7]. An intermediary metastable γ-phase which transforms to the β-phase upon continuous heating has also been identified. It has a hexagonal symmetry where Si and Al sit at the middle of the tetrahedrons. This polymorph of the mineral starts appearing between 700 °C and 900 °C during the thermal process.

Lithium is sequentially extracted from spodumene via three processes namely decrepitation, roasting to form soluble salt by sulfation, carbonation, chlorination or fluorination [9]; followed by water leaching of the products of roasting to form an aqueous lithium solution. During decrepitation, the mineral is roasted at high temperatures (above 800 °C) to convert the monoclinic α form to the tetragonal β form. The conversion of α to the β-phase leads to volumetric enlargement of the lattice; making the β-spodumene structure comparatively open for the chemical attack. A series of investigations were conducted to enhance the decrepitation process [3,10,11] using different heating techniques [12] as well as optimizing the extraction efficiency at different leaching conditions [12–16].

The Pilbara region in Western Australia has a rich deposit of LCT-spodumene-type pegmatite ore where lithium concentrate is produced and exported. Numerous companies are also on the move to mine this type of ore. The need to understand the physicochemical characteristics of the concentrate prior to beneficiation is crucial for efficient lithium recovery. This study aims to characterize that concentrate as well as understand its thermal transformation behaviors.

2. Materials and Methods

2.1. Spodumene Concentrate Preparation

The concentrate was achieved by several unit operations including crushing, grinding, gravity separation (Dense Media Separation (DMS)) and froth flotation. The ore was crushed with primary and secondary crushers to particle size of 32 mm onto a stockpile. It was then fed into High-Pressure Grinding Rolls to reduce the size further to 3.35 mm. This was followed by a two-stage DMS which led to the recovery of course spodumene concentrate. The lower grade unrecovered material was fed into a ball mill which reduced the size to 115 microns prior to tantalite recovery as a by-product via gravity separation. The spodumene-containing fraction was conditioned at a little above 50% pulp density in a neutral pH using sodium oleate as collector. Spodumene in the conditioned material

was floated at 30% pulp density and gangue minerals rejected to tailings. This led to 85% recovery and an upgraded concentrate of about 4.6% Li_2O. The floated material then entered the cleaning stage yielding the concentrate. The concentrate produced as described above was provided by Pilbara Minerals for the study. It consisted of damp, fine-grained material with a significant portion composed of large agglomerated particles that were several centimeters in diameter. The bulk of the material was greenish-brown in color. Breaking apart the agglomerate particles revealed a light grey material. An image of the bulk and grey material is shown in Figure 1. The different coloration observed may be due to the presence of varying concentrations of Fe and Mn which substitute for Al at the various locations. Spodumene is usually associated with Fe which gives it a greenish color. At lower Fe concentration resulting from substitution by Mn, a grey/white color is observed as in this case [17].

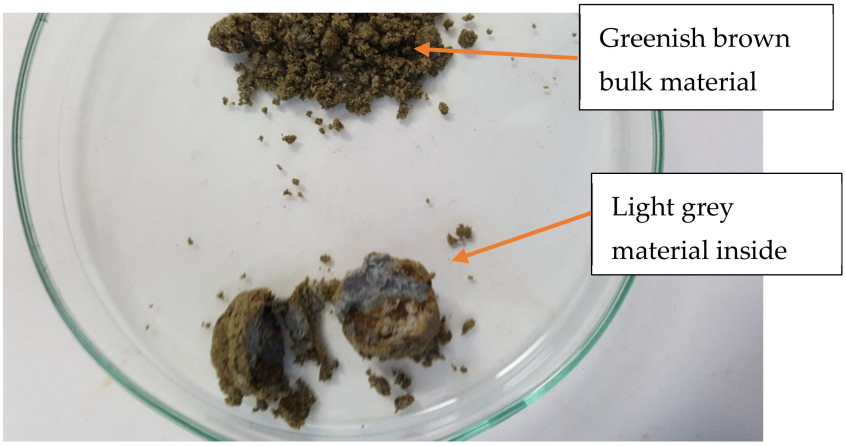

Figure 1. Optical image showing both the bulk and grey material contained in agglomerate particles.

The as-received sample was formed into a cone and tarp and then cut into approximately two portions. A portion was dried at 60 °C for 48 h after which it was passed through a 3.25 mm screen to break agglomerate particles. The dried material was split into eight subsamples using a rotary splitter. These subsamples were further split using a riffle splitter to generate representative samples of about 1 kg in mass. A representative subsample of the other moist portion was sectioned off by pie splitting which was used to determine the elemental and mineral composition.

2.2. Particle Size Distribution

A representative subsample of the dried material was used to determine the particle size distribution. Approximately, 15 g of the sample was slurred in a 1 L stirred baffled reactor containing water. A small amount of detergent was added to enhance breaking the agglomerates and reduce hydrophobicity. This slurry was then sampled using a pipette across the entire depth of the reactor. Sample was transferred to a Malvern Mastersizer for particle size analysis. A total of 5 repeats with two additional rejected runs were completed.

2.3. Thermal Treatment

Samples were roasted at varying temperatures from 900 to 1050 °C at 25 °C intervals and residence times of 7.5, 15, 30, 60, 240 and 480 min. A cylindrical quartz crucible was used to hold the sample for heating using a Carbolite Gero electric furnace which heats up to 1500 °C. The furnace provides a constant homogeneous heating 20 cm at its center, therefore, samples placed in the middle have constant temperature throughout the experiment. It was calibrated such that the extent of deviation from the set temperature was ±5 °C throughout the study. The reactor was made of quartz tube placed inside the furnace and the whole setup was operated in air with a flow rate of 25 L/h. The furnace was preheated for 60 min to achieve a steady temperature for samples to attain the

reaction temperature within the shortest possible time. This was important for accurate time measurements. Residence time was measured immediately after the sample was introduced into the furnace until the specified time elapsed. Samples were weighed and some portions pulverized with an agate mortar prior to XRD analysis and the other portions kept for SEM analyses.

2.4. XRD Analyses

X-ray diffraction (XRD) patterns of samples were collected at ambient temperature, using a CuKα radiation D2 Phaser Bruker diffractometer which is equipped with LYNXEYE detector under 30 kV and 10 mA. The analyses were performed on the powdered samples which have non-oriented flat plates. XRD patterns were recorded between $2\theta = 2.5^\circ$ and $2\theta = 70^\circ$ at a scan step of $2\theta = 0.02^\circ$ and step exposure time of 1 s. Semi-quantitative relative abundances of the phases were estimated using the EVA© software coupled with the PDF2 database of the International Centre for Diffraction Data. The semi-quantitative analyses were performed based on the pattern's relative heights and I/I_{cor} values by assuming that all crystalline phases were detected and their sum was 100%.

2.5. SEM-EDS Analyses

Two preparation procedures were employed on samples before analysis. First, powdered samples were glued on a graphite support and the surfaces covered with a thin layer of carbon. The second was performed by placing the powdered sample in an epoxy resin and allowed to stand until they hardened. Surfaces of the hardened materials were polished and ultrasonically cleaned with deionized water to achieve a highly polished surface. The surfaces of the samples prepared by the two approaches were coated with a thin film of carbon. The coating is to enhance good electrical conductivity during analysis.

2.6. Mineral Liberation Analysis

Mineral Liberation Analysis (MLA) used in this study makes use of BSE images and point-generated X-ray signals coupled with modern image and pattern identification for its measurements [18,19]. The samples were prepared by allowing the untreated concentrate to stand in resin to harden, followed by surface polishing as in Section 2.5 above. The prepared samples were then subjected to the MLA. Grain particles touching each other due to their settling mode in the resin were detected by DataView with its online program software package and then separated from each other using the shadow/boundary identification procedure. This was to ensure that, all grain particles in the sample were well separated from each other to avoid possible interference which may lead to errors in liberation results and mineral phase identification. Mineral phase identification was achieved by comparing elemental composition X-ray analysis with a standard database. Here, particles of the concentrate (which are in the resin) were divided into their individual mineral grains and their boundaries demarcated using their average BSE grey level. The device performs a systematic point X-ray elemental map which is associated with specific grains based on the differences in the grey level from the BSE map of the composite particles. The X-ray elemental map generated is matched to the corresponding average atomic number (AAN) of each mineral for their identification. In situations where mineral identification uncertainties arise due to overlap of grey level or minerals of similar AAN, the area X-ray analysis detects these anomalies and with the help of X-ray mapping, these minerals are discriminated and identified. Data obtained on the minerals are then stored for presentation in MLA DataView software.

2.7. X-ray Fluorescence (XRF) Microscopy and Inductively Coupled Plasma—Optical Emission Spectrometry (ICP-OES)

The bulk assay for the sample was carried out by a commercial laboratory (ALS Environmental Testing, Stafford, QLD) by combining XRF and digestion/ICP-OES for major components and minor components, respectively.

3. Results and Discussion

3.1. Bulk Chemical Analysis

The result of the elemental composition of the concentrate as oxides obtained from XRF and ICP-OES is presented in Table 1. The lithium concentration was determined as 2.14 wt.%; consequently, the calculated lithium oxide and spodumene concentrations were 4.61 wt.% and 57.39 wt.% respectively. This is in close agreement with the 60.21 wt.% spodumenes indicated by the MLA result (Table 2) and 3 wt.% Li content in spodumene from the Pilbara region reported in the literature [17]. All elements identified are also in agreement with the previous investigation by Aylmore et al. [17] with the exception of Ba and Co which were not identified in this study.

Table 1. Elemental composition of concentrate determined by XRF and ICP-OES.

Major	Al_2O_3	CaO	Cr_2O_3	Fe_2O_3	K_2O	MgO	MnO	Na_2O	P_2O_5	SO_3	SiO_2	TiO_2	Li	Cs	Rb	Ta	Nb	Sn
(wt.%)	20.79	1.72	0.03	4.29	1.26	1.30	0.32	1.14	0.33	0.15	61.31	0.10	2.14					
(ppm)														116	1033	202	180	140

Table 2. MLA modal mineralogy.

Mineral	Formula	wt.%
Spodumene	$LiAl(Si_2O_6)$	60.21
Pyrite	FeS_2	0.13
Quartz	SiO_2	7.58
Orthoclase	$KAlSi_3O_8$	4
Albite	$NaAlSi_3O_8$	9.1
Anorthite	$CaAl_2Si_2O_8$	1
Biotite	$KMg_{2.5}Fe^{2+}0.5AlSi_3O_{10}(OH)_{1.75}F_{0.25}$	3.32
Muscovite	$KAl_3Si_3O_{10}(OH)_{1.9}F_{0.1}$	4.9
Chlorite	$(Mg,Fe)_3(Si,Al)_4O_{10}(OH)_2{\cdot}(Mg,Fe)_3(OH)_6$	0.33
Amphibole	$CaFeSi_2O_6$	7.3
Spessartine	$Mn_2{}^{+3}Al_2(SiO_4)_3$	0.61
Tantalite-(Mn)	$MnTa_2O_6$	0.12
Calcite	$Ca(CO_3)$	0.47
Apatite	$Ca_5(PO_4)(F,Cl,OH)$	0.93

3.2. Mineralogy

XRD spectra of the concentrate are shown in Figure 2. Spodumene, mica (muscovite and biotite), quartz, feldspars (orthoclase, albite, anorthite) and the amphiboles are the predominant minerals identified which are typical minerals of spodumene ore of Pilbara. XRD has become the common analytical tool for determining the mineral composition of samples, it has, therefore, been used with the support of other analytical techniques (MLA and EDS) for the finest detection of mineral assemblage in the concentrate.

The modal mineralogy identified by MLA with their concentrations are shown in Table 2. This result is consistent with the XRD analyses, however, spessartine, tantalite, calcite and apatite which appeared as trace minerals were not identified by XRD. An operator decision was made to take into account only minerals that present at least two diffraction peaks (the main and secondary peaks). Thus, minerals with a very low concentration and showing only their main peak, which was difficult to dissociate from the background noise, could have been neglected. This could result in some trace minerals unidentified by XRD contrary to MLA and EDS point analysis.

The results are in close agreement with the mineralogy of LCT-spodumene ore except with the presence of amphibole which is identified in this work. Elemental assay of the concentrate was also calculated by MLA and the results are presented in Table 3. Computing the oxides of these elements shows a close agreement with chemical analyses in Table 1. The results of this computation are shown in Table S1 of the Supplementary Material.

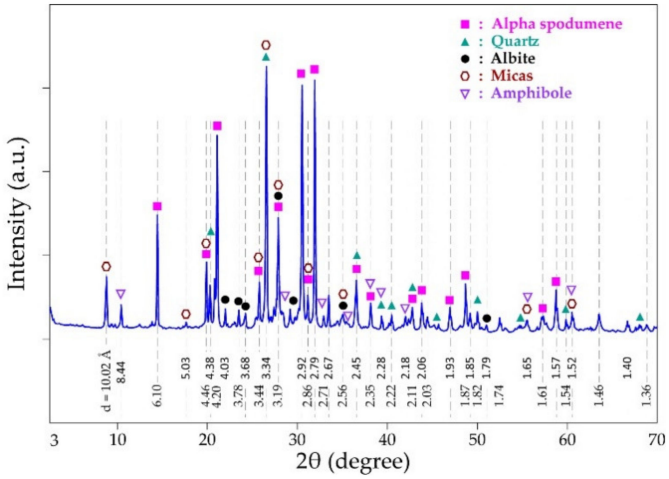

Figure 2. XRD patterns of spodumene concentrate.

Table 3. Calculated elemental assay from MLA.

Li	Al	Si	C	S	Fe	K	Na	Ta	P	Mn	Mg	Ca	Cl	F	H	O
1.96	11.58	29.47	0.06	0.07	2.0	1.34	0.76	0.09	0.17	0.22	0.5	1.97	0.02	0.09	0.04	49.39

The particle size of the major minerals was also determined by MLA and the corresponding results are displayed in Figure 3. There are no significant differences between the particle sizes of the minerals in the concentrate. The grain sizes are small with the majority below 100 microns (d80 around 100 microns). At this particle size, the minerals are well liberated as the degree of liberation of all of them is above 90% (Figure 4). Spodumene is the most liberated mineral as its degree of liberation reaches nearly 99%. It follows that the comminution conditions employed for processing this ore are good since they yield concentrate which can be easily processed for maximum lithium extraction, provided the spodumene itself does not passivate. A raw MLA data generated for obtaining Figure 4 is provided in Table S2 of the Supplementary Material.

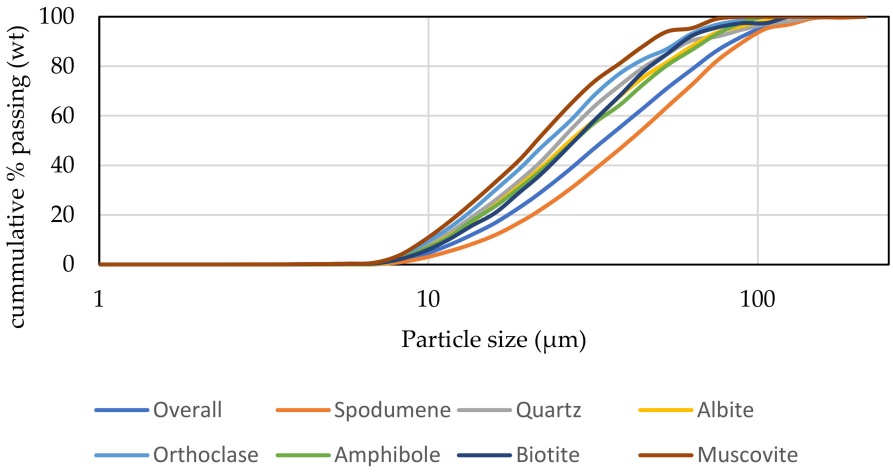

Figure 3. Mineral particle size determined by MLA.

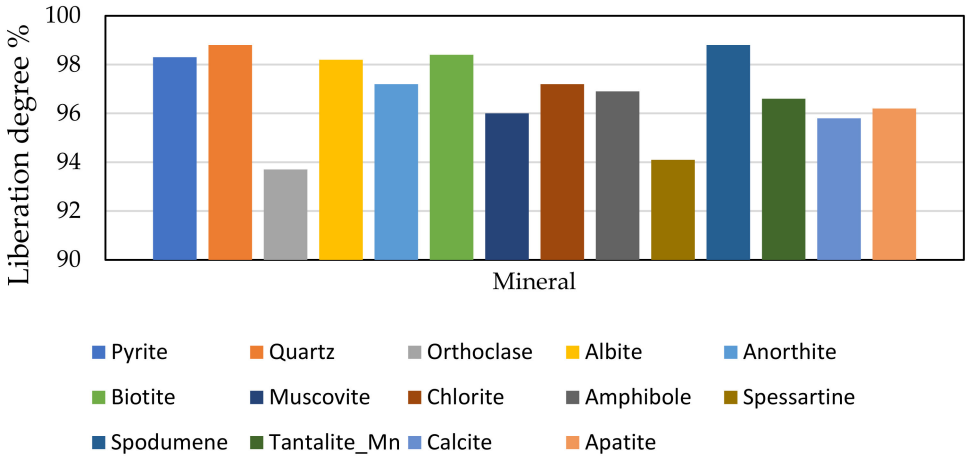

Figure 4. Degree of liberation of the main mineral phases.

3.3. Morphology, Texture of Particles and Mineralogy

Figure 5 shows the volume distribution and cumulative passing of the concentrate particles. Particle diameter ranges from 10 to 200 microns with about 68% of the total volume being 80 microns in diameter. The d50 and d80 are indicated as 57 and 113 microns respectively. The d80 found is in close agreement with the 100 microns suggested earlier. Considering the higher liberation of spodumene grains, it may be indicated that, d80 of 113 microns and particle diameter of 80 microns are good comminution parameters for processing spodumene ore, particularly pegmatites ores of Pilbara origin.

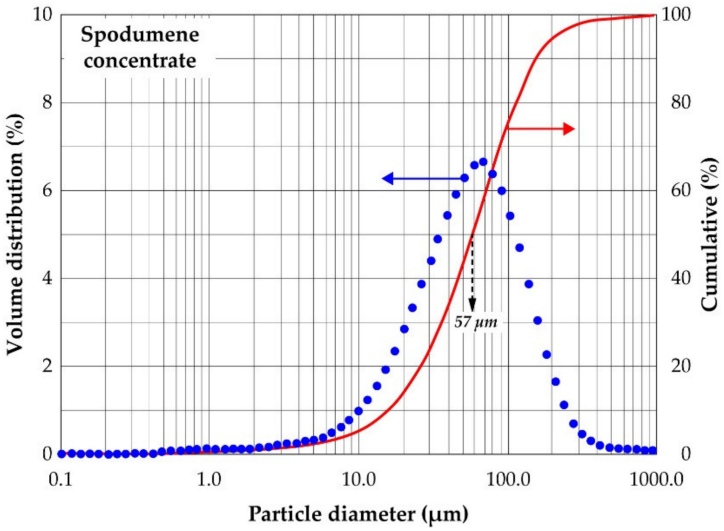

Figure 5. Volume distribution and cumulative passing of spodumene concentrate.

The BSE of the SEM was further used to investigate the morphology and texture of particles in the concentrate. It was coupled with EDS to determine the elemental composition at some points and hence the mineral composition. Figure 6 and Table 4 are the SEM photomicrograph and spot elemental composition of the concentrate respectively. It is observed (from Figure 6a,b) that, it is a well liberated coarse and loose material with varying particles of several microns in diameter; confirming earlier observation.

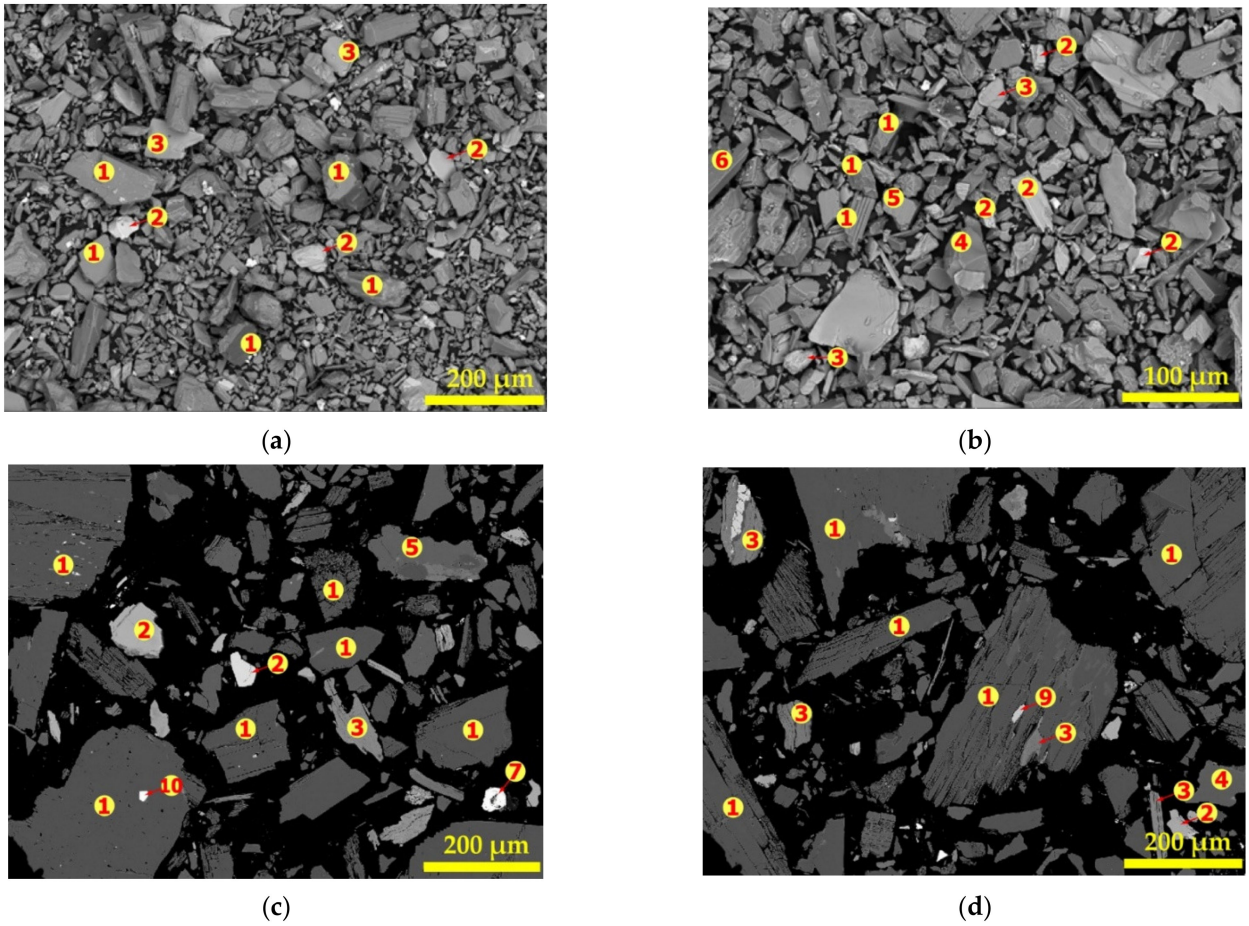

(**a**) (**b**)

(**c**) (**d**)

Figure 6. SEM of powdered (**a**,**b**) and polished samples (**c**,**d**) of concentrate. The numbers (1 to 7, 9, 10) indicate the locations of the elemental determination.

Table 4. Atomic percentage of mineral phases identified by SEM-EDS.

Elements	Spot "1"	Spot "2"	Spot "3"	Spot "4"	Spot "5"	Spot "6"	Spot "7"	Spot "8"	Spot "9"	Spot "10"
O	64.7	60.9	54.4	66.7	61.9	61.6	60.1	67.3	56.6	67.8
Al	11.5	5.2	4.1		7.7	7.5	0.4			
Si	23.6	16.8	16.1	33.3	23.3	23.2	0.6			
Fe	0.2	6.2	2.2				38.9	1.9		
Mg		4.3	10.6				0.1			
Ca		4.8			0.2				20.2	
Mn		0.2						8.5		
Na		1.1			6.9	2.4				
K		0.5	3.9			5.2				
F			8.6						8.6	
P									14.6	
Nb								12.1		
Ta								10.3		0.4
N										6.2
Sn										25.6

Spodumene grains were identified using the Si/Al ratio since EDS cannot detect the presence of lithium. The atomic ratio of Si to Al in spodumene is 2.0 hence all grains with spot elemental composition mainly of Al, Si, O and Si/Al ratio of approximately 2.0 corresponds to spodumene. All spots indicated "1" are identified as spodumene. Figure 6c,d confirm that spodumene is a coarse, dense, crystalline solid with a smooth surface, however, scratches were observed on some grains, which may be due to abrasion

during comminution. It suggests that spodumene is a hard mineral that resists wear and tear except when in contact with a harder material. This is confirmed by its relatively high 6.5 to 7.0 value on the Mohs scale of mineral hardness. Spodumene is the major mineral found in the concentrate. It is well liberated but with few mineral associations. Spot "2" has a complex composition with Fe, Mg, Ca, Al, Si, O as the major elements but with varying concentrations at different spots. We attribute these grains to the amphibole group of minerals as indicated in XRD spectra due to the higher concentration of Fe, Mg and Ca at some spots. We could not attribute them to the mica group since the mica group identified by MLA in the concentrate are muscovite and biotite which all contain K in their chemistry but K is absent at these spots. Spots identified as amphibole do not have specific color but ranges from light gray to white depending on the concentration of heavy metals that may be present. The micas (muscovite and biotite) are identified by spot 3 where there is an appreciable higher concentration of K. Spots "4" are composed mainly of Si and O with an O/Si ratio of approximately 2 and therefore identified as quartz. Spots "5" and "6" have a complex composition of Ca, K and Na and are linked to the feldspars, specifically, alkali feldspars and anorthite. We specifically identify spot "5" as albite due to the high concentration of Na at these areas and spots "6" as other feldspars. Hematite was not identified by XRD nor MLA but Spot "7" is identified as such based on the composition. It is composed mainly of Fe and O with an O/Fe ratio of approximately 1.5, confirming its identity. Tantalite and apatite which are typical of LCT-spodumene ore of the Pilbara region are also identified at spot "8" and "9", respectively. The standard deviations calculated for atomic percent obtained on some mineral grains in the concentrate are shown in Tables S3–S9. Spot "10" is composed of Sn, Ta, N and O. Though the identification of Sn by EDS is a confirmation of elemental composition in Table 1, we could not link the identity of this spot to any mineral since its composition did not match with any. We treat it as an impurity that is locked up in the spodumene grain. All major minerals in the concentrate were identified using spot elemental identification by EDS, confirming XRD and MLA analytical results. Raw data (elemental spectrum with their corresponding intensities, weight percent, etc.) generated by SEM-EDS instrument for mineral phases identified can be found in Figures S1–S8 and Tables S10–S17. Other elements such as Cr, Ti, F, Th, Sn, Zn, Cu, Ni, V, and S were also identified which are associated with the fine inclusion of some minerals. Though Ta, Nb, Sn and other valuable metals were observed, their concentrations are too low to be extracted in an economical manner.

3.4. Morphological Changes in Spodumene during Thermal Treatment

The morphological changes in the spodumene grain during decrepitation are of great importance since it gives an indication of the extent of structural changes and openness of the mineral for chemicals to interact with lithium atoms. Changes in the morphology of spodumene grains were studied on the residues treated at 900, 950, 1000 and 1050 °C using the BSE of SEM coupled with EDS. Figure 7 gives the SEM images with spots analyzed by EDS for both polished and unpolished samples. There are cracks and disintegration followed by melting and agglomeration with increasing temperature (Figure 7e–h). At 900 °C, micro-cracks are observed (Figure 7e) which becomes prominent at 950 °C (Figure 7f) such that at 1000 °C (Figure 7g), the spodumene grains had disintegrated and was well open for subsequent processes. From this observation, one may advise that 1000 °C is the ideal decrepitation temperature for processing the concentrate though 1050 °C has normally been used by several researchers for processing spodumene ores. At 1050 °C, melting and agglomeration of spodumene with impurities are observed (Figure 7h). A closer look at a portion in Figure 7h (square "A") confirms the melting and agglomeration (Figure 7i). We observe several regions of dark and light grey as well as dotted white regions with each coloration corresponding to a mineral phase which are fused together in Figure 7i due to melting. Specifically, spots "1"2"4" and "6" were identified in Figure 7i which corresponds to spodumene, amphibole, quartz and feldspars which were fused together. Tantalite and other minerals were also seen fused with some spodumene at other portions.

Most investigations of lithium extraction from spodumene are performed at a decrepitation temperature of 1050 °C, however, we advise 1000 °C as the ideal decrepitation temperature for this concentrate owing to the agglomeration at this temperature which can affect downstream processes and the extraction efficiency of lithium.

Most minerals were identified in the residues and thermal treatment did not have any major influence on their composition except melting and agglomeration of the particles at higher temperatures. A representative elemental composition as determined by EDS for samples treated at 900, 950 and 1000 °C are indicated in Tables S18–S20. Though there was no major effect of thermal treatment on the mineral phases, ionic diffusion was observed in some of the residues at increased temperatures which becomes prominent at 1050 °C. Due to this diffusion, the segregation of the feldspars into their individual minerals as well as differentiating them from the micas by EDS becomes a challenge since they appear to have similar elemental compositions. Table 5 shows some elemental associations with spodumene (spot "1"), amphiboles (spot "2") and representative composition of micas and feldspars (spot "3", "5", "6") as a result of ionic diffusion between minerals at 1050 °C. The composition of quartz, hematite, tantalite and apatite were not greatly affected regarding the ionic diffusion and are indicated at spots 4, 7, 8 and 9, respectively.

Table 5. Atomic percentage of some mineral phases identified by SEM-EDS at 1050 °C.

Elements	Spot "1"	Spot "2"	Spot "3, 5 and 6"	Spot "4"	Spot "7"	Spot "8"	Spot "9"
O	64.3		62.8	66.7	60.1	67.3	56.9
Al	11.4	3.4	6.6		0.4		
Si	23.1	19.5	24.3	33.3	0.6		
Fe	0.2	14.4	0.8		38.9	1.9	
Mg	0.2	3.9	0.3		0.1		
Ca	0.1	1.7	0.5				2.4
Mn	0.1	0.2				8.5	0.3
Na	0.6	0.9	2.0				
K	0.2	0.8	2.7				
Ti		0.3					
F							7.9
P							14.5
Nb						12.1	
Ta						10.3	

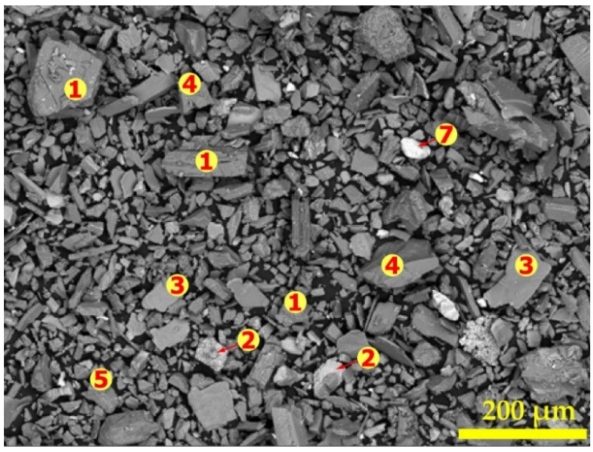

(**a**)

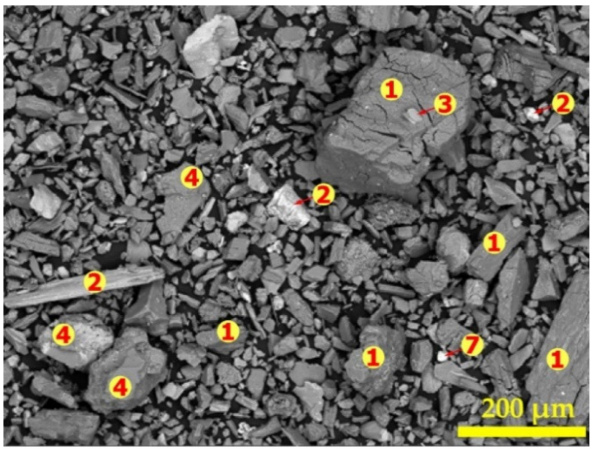

(**b**)

Figure 7. *Cont.*

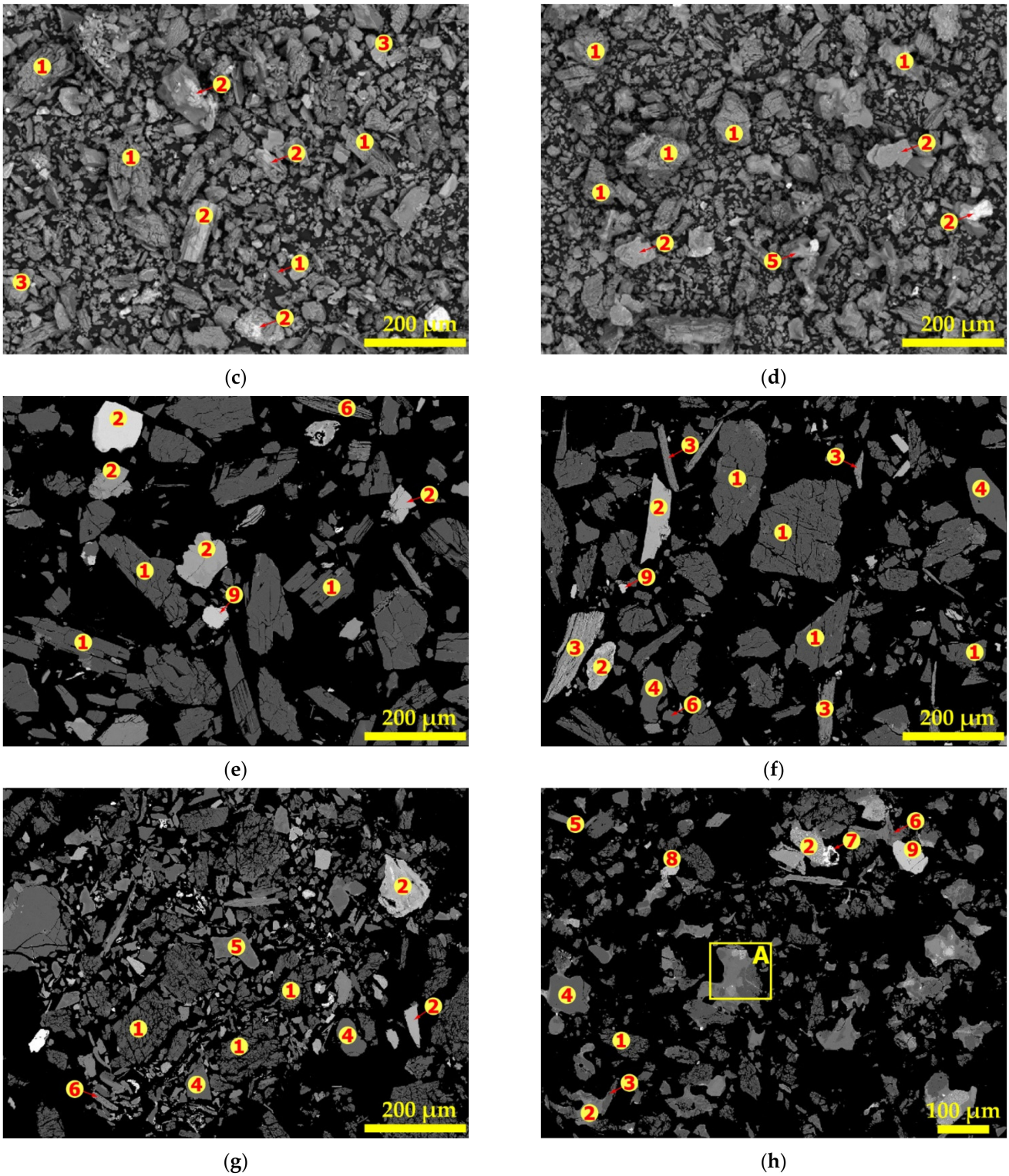

(**c**) (**d**)

(**e**) (**f**)

(**g**) (**h**)

Figure 7. *Cont.*

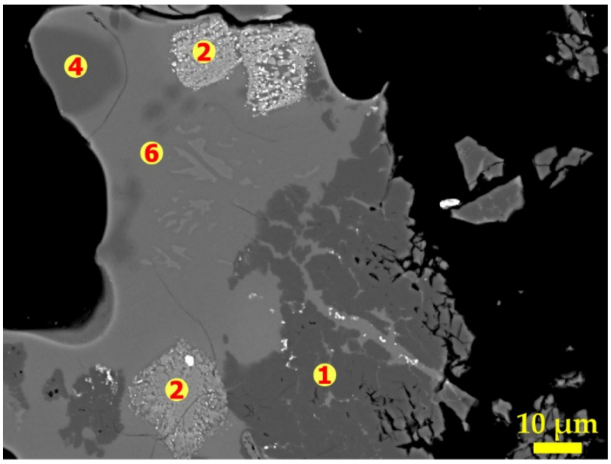

(**i**)

Figure 7. SEM and spot elemental determination of powdered (**a**–**d**) and polished sample (**e**–**h**) residues obtained after concentrate treatment in air at 900 °C (**a**,**e**), 950 °C (**b**,**f**), 1000 °C (**c**,**g**), 1050 °C (**d**,**h**) and melting and agglomeration occurring in square "A" (**i**). The numbers (1 to 9) indicate the locations of the elemental determination.

3.5. Conversion Extent of α-Spodumene

The extent of conversion of α-spodumene to both γ and β was studied at temperatures ranging from 900 to 1000 °C as a function of residence time (7.5 to 480 min). The result is presented in Figure 8. It is evident that the transformation increases with temperature and residence time. At 900 °C, conversion of the α-phase was observed after 60 min treatment which is characterized by peaks of γ and β in XRD diffractogram in Figure 9a. An almost full conversion was achieved at 975 and 1000 °C as XRD patterns do not show the presence of α-phase after 240 and 60 min, respectively (Figure S9c,d). At 900 °C, transformation increased slightly over time. Only 25% conversion was achieved even after 480 min, 17% of the transformed phase being the β-phase (Figure 8). After 480 min the α-phase was still dominant indicating that the phase transformation is more sensitive to temperature than dwelling time. A sharp increase in conversion is observed by increasing the temperature a little above 900 °C (925 °C). More than 60% transformation was attained after 480 min. Few of the transformed phase (17%) is due to the γ-phase and the majority (50%) are the β-phase. Peaks of the initially dominant α-phase gradually decreased whilst the β-phase increased with residence time (Figure S9a), confirming also increasing transformation with time. The higher experimental temperature required a shorter residence time for the transformation and vice versa. Further investigations at 1025 and 1050 °C also did not show any α-phase in the XRD spectrum (Figure S9b,e).

3.6. Evolution Extent of β-Spodumene

The formation of β-spodumene is favored by increasing the temperature and residence time (Figure 10). The maximum formed at 900 °C is about 17% while almost 100% was achieved at 1050 °C after 60 min. Temperature is observed to be the most sensitive parameter for the process and once the threshold temperature is attained, a few minutes of heating result in appreciable formation. The temperature of 1050 °C is found as the threshold temperature in this study for treating the concentrate; resulting in almost 100% α-conversion and 85% β-formation in just 7.5 min respectively. This is seen in Figure 9b where only γ and β-phases are present in the diffractogram after 7.5 min of treatment. The threshold temperature for the process was also documented elsewhere [20,21]. Investigations by Peltosari et al. [10] and Salakjani et al. [22] revealed a comparatively higher temperature (1100 °C) as the threshold for the β-phase formation. We suspect that the difference in temperatures reported in the literature and that presented in this study are due to different gangue concentrations in ores, the heat treatment process as well the nature of calibration applied to the furnace. Peltosari et al. [10] nor Salakjani et al. [22], however, gave detailed

information on these parameters in order to confirm this speculation. Additionally, there is an influence due to particle size; a higher reaction rate at a lower particle size was observed by Peltosari et al. [10]. The particle size identified in this concentrate is, however, good enough to achieve considerable mineral liberation as well as a β-phase formation at a comparatively lower temperature.

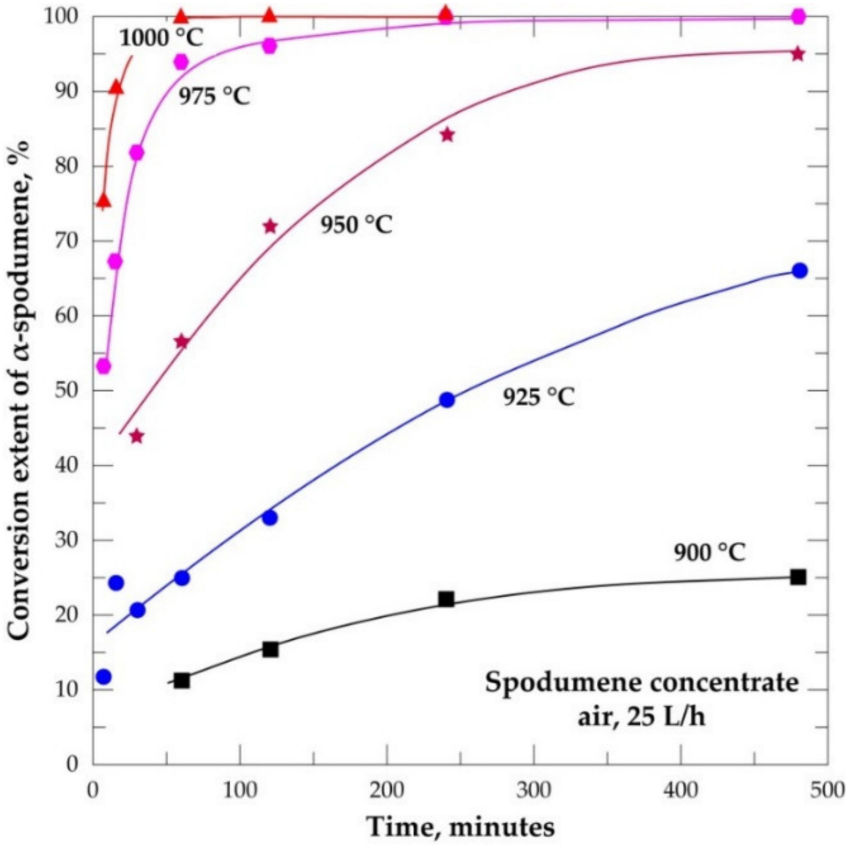

Figure 8. Conversion extent of α-spodumene into (β + γ) form during treatment of the concentrate between 900 and 1000 °C as a function of residence time.

3.7. Evolution of the Relative γ-Spodumene

Peaks of metastable γ-phase are seen in XRD diffractogram from the start of the experiment and persist throughout until after 60 min treatment at 1050 °C where it disappears. This phase might be formed at lower temperatures below the minimum temperature of this study as mentioned by Moore et al. [3] and Peltosaari et al. [10] who identified this phase at 800 and 896 °C respectively. The present observation is in agreement with what was reported at 915 °C by Abdullah et al. [11]. The peaks are not very intense compared to the other phases due to the continuous conversion into β-form as it is formed. Percent evolution of the γ-phase throughout the operating temperatures as a function of the residence time in this study is shown in Figure S10. About 23% was the maximum quantity formed in this study at 975 °C after 120 min (Figure S2d), which is comparable to the maximum quantity identified by Abdullah et al. [11] at 1125 °C. Likewise, Moore et al. [3] and Peltosaari et al. [10] recorded 35% and 40% as the highest in their studies, respectively. According to Abdullah et al. [11] and Gasalla et al. [23], the quantity of this phase formed is influenced by the particle size of the feed as well as the heat treatment technique employed; finer particles impact amorphicity which easily recrystallizes into the γ-phase on heating compared to larger-sized particles. The heating rate employed also influences the quantity formed; slow heating rates form higher amounts due to the slow rate of conversion to the β-form. There was no major change in the quantity of this phase formed as a function of the residence time in the present work. This may be as a result of the constant heating

rate which was maintained throughout the study, hence converting it to the β-form at the same rate. Though Moore et al. [3] indicated the importance of residence time on the transformation, they observed only a marginal 20% increase in this phase after increasing time from 45 min to 240 min at 981 °C.

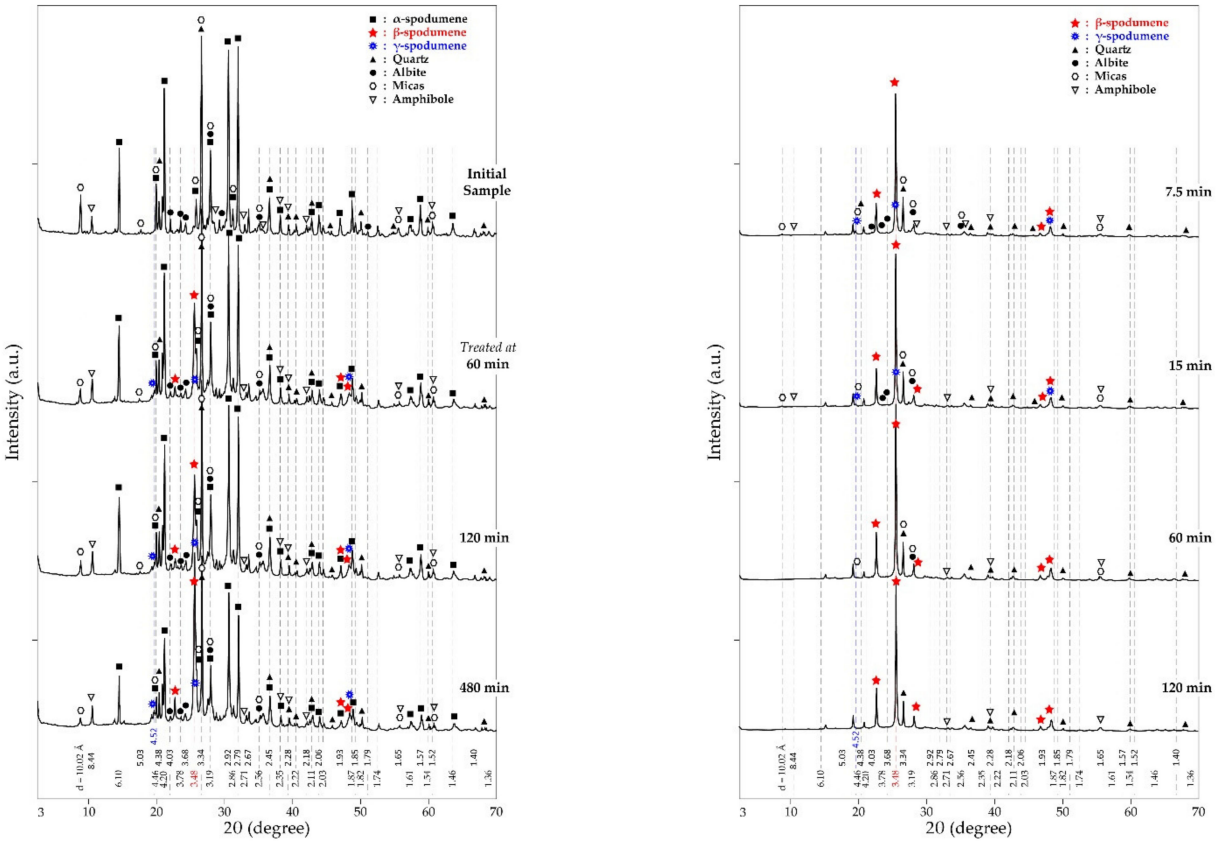

Figure 9. XRD patterns of residues obtained after concentrate treatment in air as a function of residence time at 900 °C (**a**) and 1050 °C (**b**).

It is interesting to note that, the shape of the curves in Figure S10 may predict the rate of its formation and conversion into the β-phase. There is a gentle rise and fall of the curve at lower residence time which becomes steeper with increasing residence time. This indicated a lower rate of formation and conversion at lower residence time and vice versa. From Figure 11, both γ- and β-phases evolve from the onset of the experiment but their concentration varies considerably; the quantity of γ-phase being lower than the β-phase at all times. This observation is contrary to research by Moore et al. [3] who indicated that both phases occur in equal amounts with no preference of formation of one phase over the other. We also find that the quantity of each phase formed is temperature dependent with increasing temperature favoring the quantities evolved; which is also in opposition to their findings. At 975 °C, almost all the α-phase had decayed and subsequent β-phase formation was solely dependent on the available γ-phase. Dessemond et al. [24] investigated the effect of this phase concomitant with the β-phase and its effect on lithium extraction. They indicated that its presence adversely affects the lithium extraction if its content is above 10%, however, below it, its effect is minimal, and a typical industrial lithium recovery of 95% is attainable. This therefore calls for a closer look at the ideal temperature and residence time required for the porcess, paying attention to the economics, possible melting and agglomeration and its effects on downstream processes.

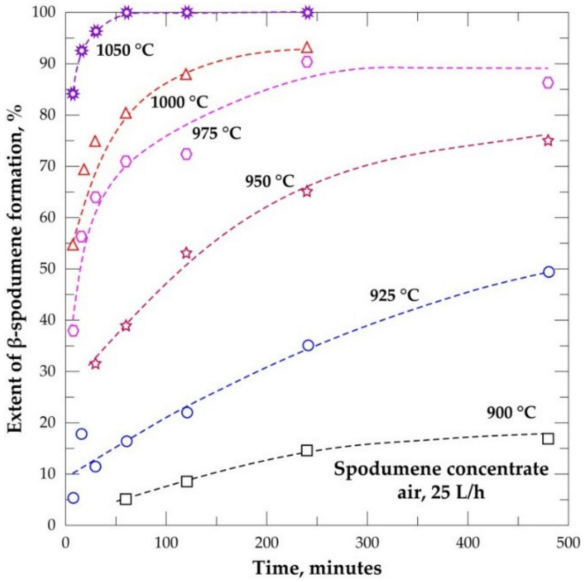

Figure 10. Spodumene formation during treatment of concentrate between 900 and 1050 °C as a function of residence time.

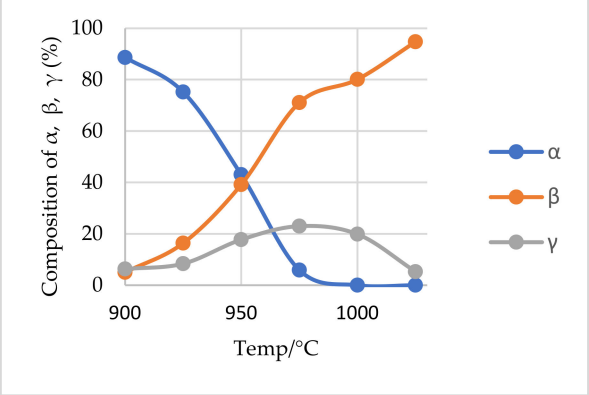

Figure 11. Percentage phase composition of α, β and γ as a function of temperature after 60 min treatment.

3.8. Phase Transformation and Kinetic Parameters

The phase transformation of spodumene during thermal treatment was extensively studied by many researchers [3,10,11] revealing α, β and γ as the phases which are present during the process. The transition is generally known to follow the following pathways:

$$\alpha \xrightarrow{k_1} \gamma + \beta \quad (1)$$

$$\gamma \xrightarrow{k_2} \beta \quad (2)$$

where k_1 and k_2 are the rate constants for α and γ decay, respectively.

Thus, from Equation (1), α-spodumene decays to form γ and β phases. The γ-phase which is formed finally transforms to the β-phase (Equation (2)). Previous studies have suggested a first-order kinetic model for the two transitions. We therefore apply this kinetic theory to both transitions to estimate the fitting kinetic parameters. From an integrated rate Equations of (1) and (2), it follows that:

$$\ln\ \alpha_t = \ln\ \alpha_o - k_1 t \quad (3)$$

$$\ln\ \gamma_t = \ln\ \gamma_o - k_2 t \quad (4)$$

where α_o and γ_o are the initial concentration of α- and γ-phase; α_t and γ_t are concentrations of α- and γ-phase at time t, respectively.

We estimate the rate constants for the decay processes (k_1 and k_2) by plotting data in Tables S21 and S22 using Equations (3) and (4). The resulting k_1 and k_2 are indicated in Table 6. These values are found to increase with increasing temperature and they confirm the sensitivity of the processes to temperature. The activation energy can be obtained from a linearized Arrhenius Equation (5):

$$\ln k = \ln A - \frac{E_a}{RT} \quad (5)$$

where k is the rate constant; A, the pre-exponential factor; Ea, the activation energy; R, the gas constant; T, the absolute temperature. The apparent activation energies obtained from the Arrhenius plots (Figure 12) for both decay processes using our data in Tables S23 and S24 are 655 and 731 kJ mol^{-1}, respectively. Thus, a comparatively larger amount of energy is required for the decay of γ-spodumene in the second phase of the process than the decay of the α-phase. This is expected due to the higher temperature required for the decay of α-phase prior to the γ-decay. However, α-decay occurs at a faster rate compared to γ-decay (Table 6). Estimated standard errors) for the regression for obtaining the activation energies are very minimal (0.1297 and 0.0489 respectively for α and γ decay); suggesting a good fit and reliable activation energy values for a first-order kinetic model. We record lower apparent activation energy for α-decay than reported in the literature [3]. Abdullah et al. [11] suggested that γ-phase may evolve either from amorphous or crystalline spodumene and suggested the following reaction pathways for the process;

$$\text{Amorphous spodumene} \rightarrow \gamma\text{-spodumene} \rightarrow \beta\text{-spodumene} \quad (6)$$

$$\text{Crystalline } \alpha\text{-spodumene} \rightarrow \gamma\text{-spodumene} \rightarrow \beta\text{-spodumene} \quad (7)$$

Table 6. Reaction rate constants k_1 and k_2 estimated for α- and γ-decay, respectively.

T °C	900	925	975	1000	1025	1050
k_1 (min^{-1})	0.0004	0.0019	0.0224	0.0054	0.0224	0.085
k_2 (min^{-1})				0.0048	0.0192	0.065

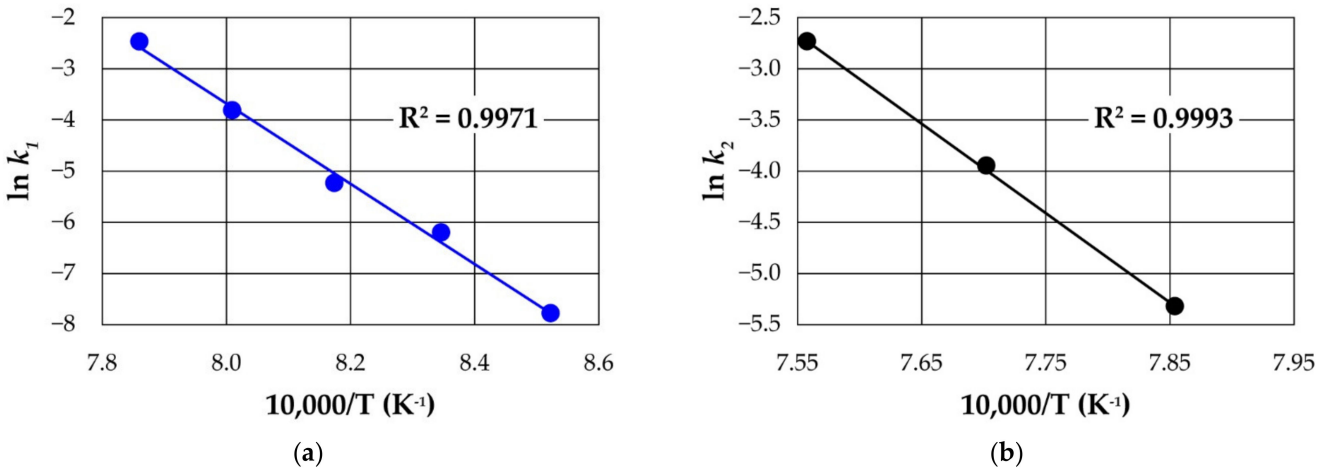

Figure 12. (**a**) ln k_1 against temperature (**b**) ln k_2 against temperature employing first-order kinetic model rate constants of decay plotted in Arrhenius form.

The path of the mechanism may influence the overall activation energy. They predicted low and high activation energies for (5) and (6), respectively. They indicated that finer particles introduce amorphicity, which easily crystalizes out with reduced activation energy. Comparing their particle size to what was used in the current study reveals that our sample is finer and more amorphous than theirs. This suggests that the evolution of the γ-phase from α-spodumene in this study is from the amorphous phase rather than crystalline. Reaction path (5) is therefore suggested for this study and as a result, contributes to the lower activation energy recorded for α-decay in this work than in previous studies.

4. Conclusions

The physicochemical characteristics of spodumene concentrate from the Pilbara region were studied. The d50 and d80 of the sample were obtained to be 57 microns and 113 microns, respectively. Particle diameter ranges from 10 to 200 microns with about 68% of the total volume being 80 microns in diameter. At these conditions, spodumene is well liberated at approximately 99%, indicating that sufficient particle size reduction was achieved to enable further processing. Mineral phase identification by the analytical techniques employed in this study is consistent with each other for major minerals. The phase transformation of spodumene from 900 to 1050 °C and 7.5 to 480 min dwelling time was studied using XRD. α transformation was complete at 975 and 1000 °C whilst that of γ occured at 1025 °C and 1050 °C all at different treatment times. About 23% was the maximum quantity of γ-phase formed. We indicate 1050 °C as the threshold temperature for maximum β-phase formation. That notwithstanding, the process must be optimized since previous studies have indicated that the presence of less than 10% γ-phase in the residue does not have a major adverse effect on lithium extraction efficiency. Should this study be valid, then we recommend 1000 °C thermal treatment for 60 min as an ideal decrepitation temperature for this concentrate considering the economics and quantity of γ-phase formed. However, if only a β-phase is required for industrial application, then a choice must be made at 1025 or 1050 °C, paying attention to the time required for the transformation, as well as the melting, which occurs at 1050 °C and its effect on downstream processing. In view of these uncertainties, we recommend further investigation between these temperatures which leads to good lithium extraction efficiency on this material.

Applying first-order kinetic models to the two processes provides a satisfactory fit to the experimental data and yields kinetic parameters and apparent activation energies of 655 and 731 kJmol^{-1}, respectively for α- and γ-decay. SEM investigations reveal that, with increasing intensity of thermal treatments, spodumene grains undergo cracking, disintegration, followed by melting and agglomeration.

Supplementary Materials: The following are available online at https://www.mdpi.com/article/10.3390/ma14237423/s1, Figure S1: Spot analysis (a) and spectrum (b) of elemental composition of spodumene grain in concentrate, Figure S2: Spot analysis (a) and spectrum (b) of elemental composition of amphibole grain in concentrate, Figure S3: Spot analysis (a) and spectrum (b) of elemental composition of mica grain in concentrate, Figure S4: Spot analysis (a) and spectrum (b) of elemental composition of quartz grain in concentrate, Figure S5: Spot analysis (a) and spectrum (b) of elemental composition of albite grain in concentrate, Figure S6: Spot analysis (a) and spectrum (b) of elemental composition of hematite grain in concentrate, Figure S7: Spot analysis (a) and spectrum (b) of elemental composition of tantalite grain in concentrate, Figure S8: Spot analysis (a) and spectrum (b) of elemental composition of apatite grain in concentrate, Figure S9: XRD patterns of residues obtained during treatment of concentrate in air as a function of residence time at 925 °C (a), 950 °C (b), 975 °C (c), 1000 (d), 1025 °C (e), Figure S10: Evolution of the relative γ-spodumene content [(γ/(α + β + γ) * 100] during treatment as a function of temperature for residence times: (a) 7.5 min, (b) 30 min, (c) 60 min and (d) 120 min, Table S1: Calculated elemental assay of major elements by MLA and their corresponding oxides, Table S2: MLA data for degree of mineral liberation in concentrate used to generate Figure 4, Table S3: Standard deviation on atomic percent of elemental composition of spodumene in concentrate, Table S4: Standard deviation on atomic percent of elemental composition of amphiboles in concentrate, Table S5: Standard deviation

on atomic percent of elemental composition of quartz in concentrate, Table S6: Standard deviation on atomic percent of elemental composition of albite in concentrate, Table S7: Standard deviation on atomic percent of elemental composition of mica in concentrate, Table S8: Standard deviation on atomic percent of elemental composition of hematite in concentrate, Table S9: Standard deviation on atomic percent of elemental composition of apatite in concentrate, Table S10: Raw data of spodumene grain generated by SEM-EDS for spectrum 1, Table S11: Raw data of amphibole grain generated by SEM-EDS for spectrum 2, Table S12: Raw data of mica grain generated by SEM-EDS for spectrum 5, Table S13: Raw data of quartz grain generated by SEM-EDS for spectrum 13, Table S14: Raw data of albite grain generated by SEM-EDS for spectrum 3, Table S15: Raw data of hematite grain generated by SEM-EDS for spectrum 1, Table S16: Raw data of tantalite grain generated by SEM-EDS for spectrum 3, Table S17: Raw data of apatite grain generated by SEM-EDS for spectrum 5, Table S18: Atomic percentage of some mineral phases identified by SEM-EDS at 900 °C, Table S19: Atomic percentage of some mineral phases identified by SEM-EDS at 950 °C, Table S20: Atomic percentage of some mineral phases identified by SEM-EDS at 1000 °C, Table S21: Data for determination of apparent rate constants, k1 for α-decay from Equation (3), Table S22: Data for determination of apparent rate constants, k2 for γ-decay from Equation (4), Table S23: Data for calculating apparent activation energy for α-decay from Equation (5), Table S24: Data for calculating apparent activation energy for γ-decay from Equation (6).

Author Contributions: Conceptualization, A.C., N.K. and A.Y.F.; writing—original draft preparation and writing—review and editing, A.C., N.K. and J.V.; supervision, A.C. and N.K.; Methodology and analysis for XRD, D.B.; Methodology analysis and data acquisition funding acquisition for MLA, H.H. All authors have read and agreed to the published version of the manuscript.

Funding: This work was supported by the French National Research Agency through the national program "Investissements d'avenir" with the reference ANR-10-LABX-21-RESSOURCES21.

Institutional Review Board Statement: Not applicable.

Informed Consent Statement: Not applicable.

Data Availability Statement: The data presented in this study are available upon request to the corresponding author.

Conflicts of Interest: The authors declare no conflict of interest.

References

1. Bradley, D.C.; McCauley, A.D.; Stillings, L.M. *Mineral-Deposit Model for Lithium-Cesium-Tantalum Pegmatites*; U.S. Geological Survey: Reston, VA, USA, 2017.
2. Pickles, C.A.; Marzoughi, O. Thermodynamic modelling of spodumene decrepitation. *Miner. Process. Extr. Metall. Trans. Inst. Min. Metall.* **2020**, 1–15. [CrossRef]
3. Moore, L.R.; Mann, J.P.; Montoya, A.; Haynes, B.S. In situ synchrotron XRD analysis of the kinetics of spodumene phase transitions. *Phys. Chem. Chem. Phys.* **2018**, *20*, 10753–10761. [CrossRef] [PubMed]
4. Salakjani, N.K.; Singh, P.; Nikoloski, A.N. Production of Lithium–A Literature Review Part 1: Pretreatment of Spodumene. *Miner. Process. Extr. Metall. Rev.* **2020**, *41*, 335–348. [CrossRef]
5. Yonghua, D.; Lishi, M.; Ping, L.; Yong, C. First-principles calculations of electronic structures and optical, phononic, and thermodynamic properties of monoclinic α-spodumene. *Ceram. Int.* **2017**, *43*, 6312–6321. [CrossRef]
6. Arlt, T.; Angel, R. Displacive phase transitions in C-centred clinopyroxenes: Spodumene, $LiScSi_2O_6$ and $ZnSiO_3$. *Phys. Chem. Miner.* **2000**, *27*, 719–731. [CrossRef]
7. Moore, R.L.; Haynes, B.S.; Montoya, A. Effect of the Local Atomic Ordering on the Stability of β-Spodumene. *Inorg. Chem.* **2016**, *55*, 6426–6434. [CrossRef]
8. Li, C.-T.; Peacor, D.R. The crystal structure of LiAlSi2O6-II ("β spodumene"). *Z. Krist. Mater.* **1968**, *126*, 46–65. [CrossRef]
9. Fosu, A.Y.; Kanari, N.; Vaughan, J.; Chagnes, A. Literature Review and Thermodynamic Modelling of Roasting Processes for Lithium Extraction from Spodumene. *Metals* **2020**, *10*, 1312. [CrossRef]
10. Peltosaari, O.; Tanskanen, P.; Heikkinen, E.-P.; Fabritius, T. α→γ→β-phase transformation of spodumene with hybrid microwave and conventional furnaces. *Miner. Eng.* **2015**, *82*, 54–60. [CrossRef]
11. Abdullah, A.A.; Oskierski, H.C.; Altarawneh, M.; Senanayake, G.; Lumpkin, G.; Dlugogorski, B.Z. Phase transformation mechanism of spodumene during its calcination. *Miner. Eng.* **2019**, *140*, 105883. [CrossRef]
12. Salakjani, N.K.; Singh, P.; Nikoloski, A.N. Acid roasting of spodumene: Microwave vs. conventional heating. *Miner. Eng.* **2019**, *138*, 161–167. [CrossRef]

13. Rosales, G.D.; Resentera, A.C.J.; Gonzalez, J.A.; Wuilloud, R.G.; Rodriguez, M.H. Efficient extraction of lithium from β-spodumene by direct roasting with NaF and leaching. *Chem. Eng. Res. Des.* **2019**, *150*, 320–326. [CrossRef]
14. Rosales, G.D.; Ruiz, M.D.C.; Rodriguez, M.H. Novel process for the extraction of lithium from β-spodumene by leaching with HF. *Hydrometallurgy* **2014**, *147*, 1–6. [CrossRef]
15. Barbosa, L.I.; Valente, G.; Orosco, R.P.; González, J.A. Lithium extraction from β-spodumene through chlorination with chlorine gas. *Miner. Eng.* **2014**, *56*, 29–34. [CrossRef]
16. Barbosa, L.I.; González, J.A.; del Carmen Ruiz, M. Extraction of lithium from β-spodumene using chlorination roasting with calcium chloride. *Thermochim. Acta* **2015**, *605*, 63–67. [CrossRef]
17. Aylmore, M.G.; Merigot, K.; Rickard, W.D.A.; Evans, N.J.; Mcdonald, B.J.; Spitalny, P. Assessment of a spodumene ore by advanced analytical and mass spectrometry techniques to determine its amenability to processing for the extraction of lithium. *Miner. Eng.* **2018**, *119*, 137–148. [CrossRef]
18. Fandrich, R.; Gu, Y.; Burrows, D.; Moeller, K. Modern SEM-based mineral liberation analysis. *Int. J. Miner. Process.* **2007**, *84*, 310–320. [CrossRef]
19. Gu, Y. Automated Scanning Electron Microscope Based Mineral Liberation Analysis. An Introduction to JKMRC/FEI Mineral Liberation Analyser. *J. Miner. Mater. Charact. Eng.* **2003**, *02*, 33–41. [CrossRef]
20. Tian, Q.; Chen, B.; Chen, Y.; Ma, L.; Shi, X. Roasting and leaching behavior of spodumene in sulphuric acid process. *Xiyou Jinshu Chin. J. Rare Met.* **2011**, *35*, 118–123. [CrossRef]
21. White, G.D.; McVay, T.N. *Some Aspects Of The Recovery Of Lithium From Spodumene*; Oak Ridge National Laboratory: Oak Ridge, TN, USA, 1958.
22. Salakjani, N.K.; Singh, P.; Nikoloski, A.N. Mineralogical transformations of spodumene concentrate from Greenbushes, Western Australia. Part 1: Conventional heating. *Miner. Eng.* **2016**, *98*, 71–79. [CrossRef]
23. Gasalla, H.J.; Aglietti, E.F.; Lopez, J.M.P.; Pereira, E. Changes in physicochemical properties of α-spodumene by mechanochemical treatment. *Mater. Chem. Phys.* **1987**, *17*, 379–389. [CrossRef]
24. Dessemond, C.; Soucy, G.; Harvey, J.P.; Ouzilleau, P. Phase transitions in the α-γ-β spodumene thermodynamic system and impact of γ-spodumene on the efficiency of lithium extraction by acid Leaching. *Minerals* **2020**, *10*, 519. [CrossRef]

RSC Advances

PAPER

View Article Online
View Journal | View Issue

Cite this: *RSC Adv.*, 2022, **12**, 21468

Novel extraction route of lithium from α-spodumene by dry chlorination†

Allen Yushark Fosu, [a] Ndue Kanari, [a] Danièle Bartier,[a] James Vaughan [b] and Alexandre Chagnes *[a]

Processing spodumene for lithium is challenging as it requires a high temperature transformation of the natural α-monoclinic form to β-tetragonal form, usually followed by acid baking and digestion. This three-step extraction process requires significant heat energy, acid, process complexity and residence time, leading to both operating and capital costs. An approach which helps to eliminate this challenge will therefore be a milestone in processing spodumene. This study, thus, investigates a direct chlorination of α-spodumene using calcium chloride followed by water leaching of the residue to recover lithium, which reduces the energy requirement and number of unit operations. HSC Chemistry software was used to simulate the process using both phases (α and β) of the mineral up to 1100 °C prior to experimental investigation. The α-form was the only polymorph identified in residues after leaching, suggesting that the extraction is directly from the α-phase. However, an initial formation of a metastable β-form followed by a fast synthesis of lithium chloride from it is also suspected. Under optimal conditions of calcium chloride/spodumene molar ratio of 2.0, and 1000 °C treatment for 60 minutes, almost 90 percent lithium chloride was extracted and 85 percent was recovered to the leach solution with the remainder exiting with the off-gas. An apparent activation energy of about 122 ± 6 kJ mol^{-1} was obtained at temperatures ranging from 800 to 950 °C during the process.

Received 23rd May 2022
Accepted 19th July 2022

DOI: 10.1039/d2ra03233c

rsc.li/rsc-advances

1. Introduction

Chlorination is gaining popularity in mineral processing due to the advantages it presents for processing ores, concentrates and end-of-life resources. The merits of this technique for metal extraction stem from the high reactivity and selectivity of chlorine and chlorinating agents to many metals at minimal temperatures. The resulting metal chlorides/oxychlorides from the process have considerable difference in boiling point which makes management of impurities and product choices easier. Chlorination agents are also readily available at reasonable prices. The waste generated can easily be treated and disposed off with little or no environmental impact compared to other approaches.[1–3] For instance, chlorinated waste unlike other metallurgical wastes, may be easily neutralized with alkaline reagents. These factors make chlorination attractive for treating lean minerals and secondary materials as well as providing new pathways for some refractory ores that do not respond well to conventional approaches. Metal chlorides, Cl_2 and HCl have been used to treat ore types (silicates, oxides and sulphides) for subsequent processing according to the reactions below:

$$M''_2SiO_3 + M'Cl_2 \rightarrow 2M''Cl + M'SiO_3 \quad (1)$$

$$M''_2S + M'Cl_2 \rightarrow 2M''Cl + M'S \quad (2)$$

$$M''_2O + M'Cl_2 \rightarrow 2M''Cl + M'O \quad (3)$$

$$M''_2O + Cl_2 \rightarrow 2M''Cl + \frac{1}{2}O_2 \quad (4)$$

$$M''_2S + Cl_2 \rightarrow 2M''Cl + S \quad (5)$$

$$M''_2O + 2HCl \rightarrow 2M''Cl + H_2O \quad (6)$$

$$M''_2S + 2HCl \rightarrow 2M''Cl + H_2S \quad (7)$$

where M′ is a chlorine bearing metal used as chlorinating agent and M″ is a monovalent metal of interest present in the ore.

Chlorination sometimes requires a reducing environment to enhance the process. Due to this, carbochlorination of metal oxides and silicates have been investigated by some researchers,[4,5] where the carbon or carbonaceous material acts as reducing agent to enable or enhance reactions.

With the increasing demand for lithium, primarily due to the evolution of electric and hybrid vehicles coupled with its undersupply from Salar and brine, attention has been drawn to

[a]Université de Lorraine, CNRS, GeoRessources, F-54000 Nancy, France. E-mail: alexandre.chagnes@univ-lorraine.fr
[b]School of Chemical Engineering, The University of Queensland, Brisbane, QLD 4072, Australia

† Electronic supplementary information (ESI) available. See https://doi.org/10.1039/d2ra03233c

extraction from pegmatite ores, secondary resources and to a lesser extent, water produced from shale gas[6,7] in order to meet the increasing demand. Investigations for processing petalite,[8] zinnwaldite,[9–13] lepidolite,[14–18] spodumene[19–25] and secondary sources[26–29] are well documented. Of all lithium bearing minerals, spodumene ($LiAlSi_2O_6$) stands out as the one with high economic value resulting from its relatively high lithium content. The mineral occurs naturally as the α-monoclinic form which is compact, making it refractory to chemical attack. Consequently, the conventional approach to processing the mineral requires phase transformation from the α to the β-form which is crucial for opening up the mineral's crystalline structure enabling subsequent lithium extraction. The transformation is a thermal process requiring temperatures above 1000 °C. Previous investigations[30,31] have revealed two consecutive routes for the transition wherein the first involves the decay of the natural α-monoclinic phase to both γ and β-phases. The second is the decay of the metastable γ-phase formed from the previous decay to the final β-phase. Fosu *et al.*[32] demonstrated the high temperature requirement for the two decay processes based on the apparent activation energies for the transformations. The acidic process which is currently the industrial process for extracting the metal and its contemporary studies require this inevitable phase transformation step which is energy intensive, therefore increasing processing cost and time. The obsolete alkaline process, which did not necessitate the phase transformation, had inherent challenges including high energy requirement for the decomposition of limestone before calcination with α-spodumene. It also results in the formation of dicalcium silicates which releases large amount of heat and makes temperature control in the calcination stage difficult.[33] Thus, the phase transformation step stands out as an expedient step in processing the mineral, the cost implication and the time requirements notwithstanding. In an attempt to eliminate this step, some hydrometallurgical treatments such as employed by SiLeach® and LieNA® have been considered from which promising results have been achieved. Song *et al.*,[25] also by hydrometallurgical treatment using NaOH and CaO in an autoclave, reported 93% leaching efficiency. However, their approach requires high concentration of NaOH and special equipment (autoclave) in addition to long processing time. Owing to the inherent advantages of chlorination, it promises an efficient approach for processing the mineral. After a thorough review of literature by Fosu *et al.*[34] on processes used so far to recover the metal from spodumene, their thermodynamic modelling highlighted chlorination as one of the promising processes which has had the least of attention. In 1959, Peterson *et al.*[35] patented the possible extraction of lithium from α-spodumene using an alkali metal halide or their mixture (specifically, KCl and/or NaCl) in the presence of a refractory material. The amount of refractory material required by this approach was indicated to vary between 60 to 80 wt% of the quantity of spodumene treated. This high quantity of refractory material used results in a reduced amount of spodumene used as feed reducing the efficiency of the process. During a study on simulated pyrometallurgical slag from end-of-life lithium ion battery by chlorination, Dang *et al.*[36,37] reported interesting results. Studies by Barbosa *et al.*[38,39] revealed the metal's extraction from spodumene using $CaCl_2$ and Cl_2. Though they reported a successful chlorination for high conversion, their study was based on the calcined mineral (β-spodumene) which does not eradicate the phase transformation problem. This study investigates the direct baking of α-spodumene using $CaCl_2$, followed by aqueous leaching of the residue to recover lithium. The success of this study will help to reduce the processing cost and time, since the decrepitation step will be avoided.

Most thermodynamic studies in literature on the roasting of spodumene with reagents are performed with the β-phase. In this study, α to β-phase transformation of the mineral, followed by a comparative study of thermodynamic behaviour of both phases with $CaCl_2$ using HSC Software is considered. The suggested phase transformation and chemical equations of the mineral in both phases with $CaCl_2$ are given as:

$$\alpha\text{-}LiAlSi_2O_6 \rightarrow \beta\text{-}LiAlSi_2O_6 \quad (8)$$

$$2\alpha\text{-}LiAlSi_2O_6 + CaCl_2 \rightarrow 2LiCl + 2SiO_2 + CaAl_2Si_2O_8 \quad (9)$$

$$2\beta\text{-}LiAlSi_2O_6 + CaCl_2 \rightarrow 2LiCl + 2SiO_2 + CaAl_2Si_2O_8 \quad (10)$$

In Fig. 1, the Gibbs free energy change of the transformation and the reaction of both polymorphs with $CaCl_2$ (eqn (8)–(10)) as a function of temperature up to 1100 °C are plotted. It can be observed that, the phase transformation is feasible after 750 °C but after 927 °C (indicated by short dashes), the software relies on extrapolated data for the α-phase. This may be due to unavailability of data for the α-phase above this temperature. From our previous investigation,[32] it was found that, treating the α-phase at 925 °C did not complete the transformation. Rather, a maximum of about 65% α-phase conversion was

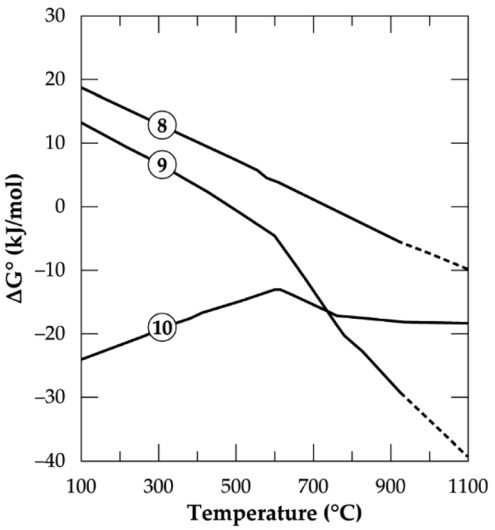

Fig. 1 Standard Gibbs energy changes as a function of temperature for α to β transformation (eqn 8), reaction of spodumene with $CaCl_2$ in α-phase (eqn (9)) and β-phase (eqn (10)) (data from HSC Chemistry 5.1 software).

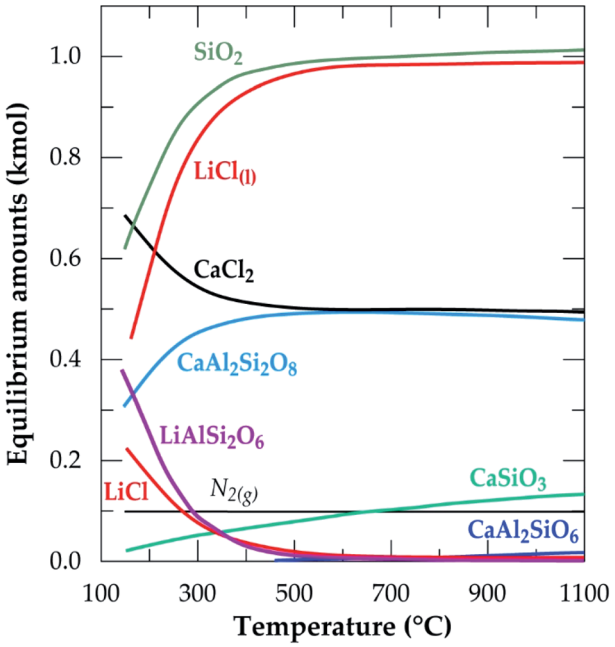

Fig. 2 Equilibrium amounts as a function of temperature for chlorination of α-spodumene using $CaCl_2$ (data from HSC Chemistry 5.1 software).

achieved even after 480 minutes treatment (the longest residence time of the study). Drawing insight from our studies on the kinetics of phase transformation, it is likely that, the extrapolation of data of the α-phase by HSC Software is due to the unavailability of data rather than completion of the transformation. Roasting the mineral in the β-phase with $CaCl_2$ is spontaneous throughout the temperatures studied whilst the direct roasting of α-phase is only feasible beyond 500 °C. This is expected since the refractory α-phase needs to open up prior to a feasible reaction with $CaCl_2$. If the feed spodumene has already been converted to the β-phase it is then feasible for a reaction with $CaCl_2$ throughout the wider range of operating temperatures. Combining the above scenarios, one can infer that, production of LiCl below 750 °C occurs strictly and directly from the α-phase (eqn (9)). Above this temperature, however, the phase transformation begins (according to HSC Software) and a mixture of both polymorphs may exist. LiCl can thus be obtained from both phases (eqn (9) and (10)) which should lead to higher lithium recovery. A transition point is observed between 600 and 800 °C for both α and β-phase chlorination (Fig. 1). We name this temperature range as the "reaction initiation zone" where melting of $CaCl_2$ and reaction with the mineral begin.

A differential thermal analysis by both Barbosa *et al.*[39] and Dang *et al.*[36] revealed interesting results in this temperature range during their study on spodumene and simulated slag respectively with $CaCl_2$. They both observed two endothermic peaks within this range where the low and high temperature peaks were linked to the commencement of reaction and the melting of $CaCl_2$ respectively. Chemical thermodynamic predictions have a downside of inability to give insight into the kinetics of processes. One may however, suspect that since the change in the Gibbs free energy remains almost constant for the β-phase after 800 °C (Fig. 1), it may be more kinetically dependant than thermodynamic. For the α-phase, chlorination may be both thermodynamic and kinetic controlled since the Gibb's free energy change decreases significantly with increasing temperature which confirms a strong dependence of α-phase chlorination on the thermodynamics.

The equilibrium composition module of the software was further used to simulate the process. Fig. 2 is the simulation showing the equilibrium composition at varying temperatures. Anorthite ($CaAl_2Si_2O_8$) and wollastonite ($CaSiO_3$) are new phases synthesized at the end of the process with the former being predominant (more than half of the composition of the later). All the new phases, including lithium chloride can be said to be obtained from the decomposition of spodumene since their synthesis have a corresponding decrease in the quantity of spodumene.

2. Materials and methods

2.1. Spodumene concentrate preparation

The sample used in this study is a spodumene concentrate received from the Pilbara region of Western Australia after flotation from a lithium–cesium–tantalum pegmatite ore. The method of production and characterization (X-ray diffraction (XRD), Scanning Electron Microscope Energy Dispersive Spectroscopy (SEM-EDS), X-ray fluorescence (XRF) microscopy and Inductively Coupled plasma-Optical Emission Spectrometry (ICP-OES)) is detailed in our previous work.[32] Analytical grade $CaCl_2$ supplied by Sigma-Aldrich, France was used as chlorination agent.

2.2. Chlorination and leaching experiments

Direct chlorination of α-spodumene was performed using a mixture of 5 g of the dry uncalcined spodumene concentrate and anhydrous $CaCl_2$. Alumina crucible was used as the reaction vessel while heating in a Carbolite Gero electric furnace which was conditioned as in earlier work.[32] Chlorinated samples were cooled to room temperature in a desiccator and weighed before leaching tests.

Leaching was carried out with deionized water at ambient temperature, solid/liquid ratio of 50 g L^{-1} and agitated using a Gerhardt laboratory thermoshake. The solid and liquid phases were separated with a 3–16 L Sigma Laboratory Centrifuge operating at 3000 rpm for 2 minutes. Leached residues were washed thoroughly with distilled water and dried at room temperature for further analysis. The leached liquor obtained was analyzed for lithium and other metals using the Microwave Plasma Atomic Emission Spectrophotometer (4210 MP-AES) manufactured by Agilent Technologies. Percent lithium recovery (%Li) was calculated as:

$$\%\ \mathrm{Li} = \frac{\text{Amount of lithium recovered in solution}}{\text{Amount of lithium in concentrate}} \times 100 \quad (11)$$

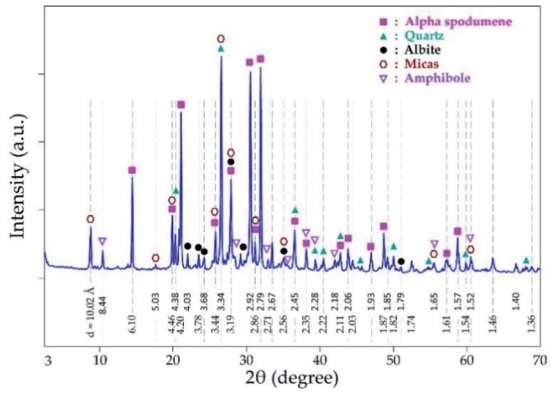

Fig. 3 XRD pattern of spodumene concentrate.

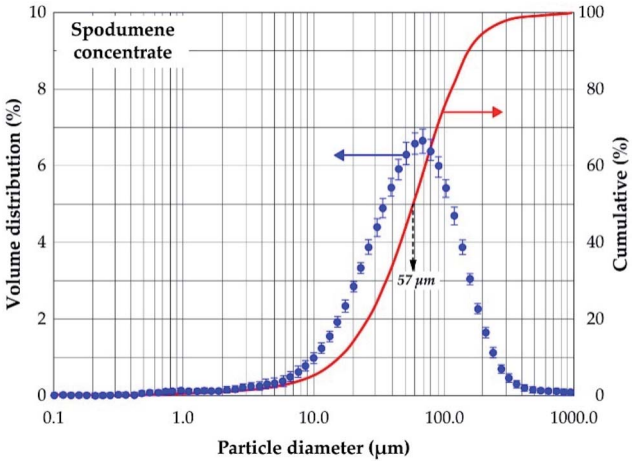

Fig. 4 Volume distribution and cumulative passing of spodumene concentrate.

Extraction efficiencies achieved was obtained by residual lithium determination, followed by mass balance calculation. Probing into the reaction mechanism, the leached residues were analyzed for their physicochemical alterations using SEM-EDS. Methods of sample preparation for XRD and SEM-EDS were previously detailed by Fosu *et al.*[32]

3. Results and discussion

3.1 Characterization of raw materials

Mineralogical identification and semi-quantitative analyses were carried out using the EVA© software coupled with the PDF2 database. The XRD diagram pattern of the raw spodumene concentrate (Fig. 3) shows the feed is predominantly α-spodumene (about 60%) with quartz, albite, mica and amphiboles as associated gangue minerals. Chemical composition is also provided in Table 1 with lithium accounting for 2.14 wt% whilst particle size analysis shows the d_{50} to be 57 μm (Fig. 4). Detailed characterization of the concentrate as well as its thermal transformations can be found in Fosu *et al.*[32]

3.2 Chlorination of α-spodumene concentrate

3.2.1 Effect of $CaCl_2$/spodumene molar ratio. The effect of $CaCl_2$/spodumene molar ratio (MR) on lithium recovery was studied in the range of 1.0 to 2.25, at 900 °C for 60 minutes residence time; the results are presented in Fig. 5. Lithium recovery increases with increasing molar ratio until it plateaus after MR = 2.0. Previous studies[21,36,40] have reported a decreased recovery for gaseous chlorination agents after the optimum flow rate is achieved with several explanations proposed by Bidaye *et al.*[41] for the observation. A MR of 2.0 was selected as the optimum for further investigation since there was no significant increase in the amount of lithium recovered after that.

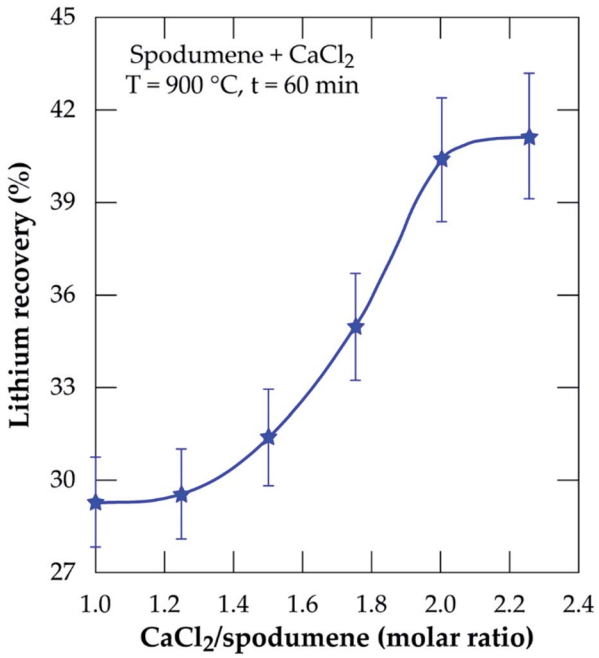

Fig. 5 Percent lithium recovery obtained as a function of $CaCl_2$/spodumene molar ratio for samples treated at 900 °C for 60 minutes.

3.2.2 Effect of temperature. Chlorination was performed at 60 minutes residence time and MR of 2.0 in order to optimize the temperature. During the simulation using the equilibrium composition module of HSC Software (Fig. 2), it was found that lithium chloride in the liquid phase attains a maximum

Table 1 Chemical composition of concentrate determined by XRF and ICP-OES

Major	Al_2O_3	CaO	Cr_2O_3	Fe_2O_3	K_2O	MgO	MnO	Na_2O	P_2O_5	SO_3	SiO_2	TiO_2	Li	Cs	Rb	Ta	Nb	Sn
(wt%)	20.79	1.72	0.03	4.29	1.26	1.30	0.32	1.14	0.33	0.15	61.31	0.10	2.14					
(ppm)														116	1033	202	180	140

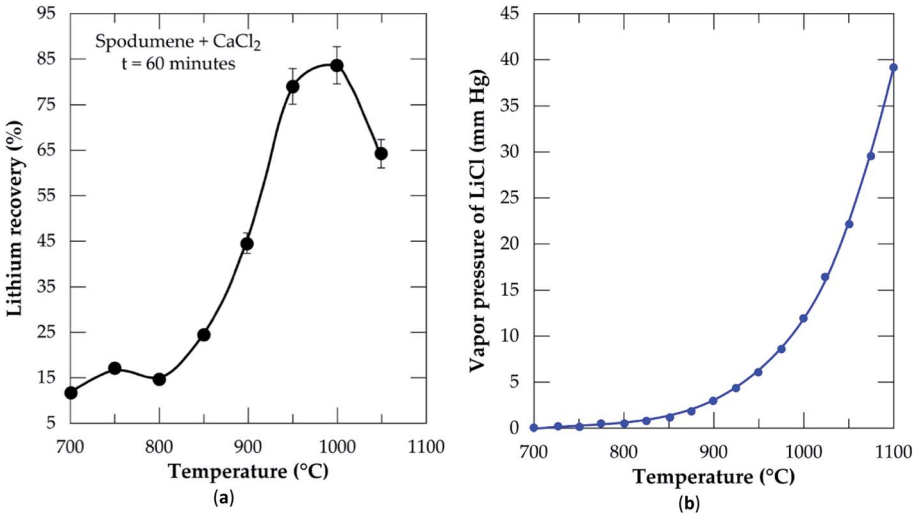

Fig. 6 (a) Percent lithium recovery *versus* temperature at $CaCl_2$/spodumene molar ratio of 2.0 and 60 min residence time; (b) vapor pressure of lithium chloride *versus* temperature.

Table 2 Mass balance comparison of percent lithium recovery and extraction at different temperature

Temperature, °C	Residual lithium in residues wt%	Recovery%	Extraction%
900	1.15	45.3	46.3
950	0.50	79.1	76.6
1000	0.23	83.5	89.3
1050	0.32	64.3	85.1

concentration after 600 °C. Based on this, temperatures ranging from 700 to 1050 °C at 50 °C intervals were selected for the chlorination and results are presented in Fig. 6a. Recovery increases with increasing temperature until it peaks at 1000 °C. From 700 to 800 °C which falls within the initiation zone of the process, the lowest quantity of LiCl (about 17%) is produced. This is expected since $CaCl_2$ (with melting point around 770 °C) starts melting to initiate reaction with spodumene to yield products. The range of this temperature however, may not be sufficient enough to provide appropriate conditions for appreciable recovery. After 800 °C, a sharp increase in recovery is observed until 1000 °C. In our previous studies,[32] it was established that, spodumene when heated gains minor cracks which become prominent with increasing temperature until it disintegrates. 1000 °C was indicated as the temperature where sufficient disintegration is attainable but above it, melting and agglomeration occurs. Thus, increasing temperature has a remarkable effect on the opening of the mineral for more lithium atoms to interact with molten $CaCl_2$. This leads to the production of more LiCl until it peaks at 1000 °C. After 1000 °C (1050 °C), a decline in recovery is observed. This may be attributed to two factors, either melting and agglomeration of spodumene with impurities or the evaporation of LiCl from the reaction medium as it is formed. It is possible also that, both mechanisms all contribute to the decline. A mass balance was performed on the leached residues in order to compare lithium recovery achieved and extraction efficiency and also to investigate the factor(s) responsible for the decline in recovery. These results are presented in Table 2. Residual lithium in residues is observed to decrease with increasing temperature with a corresponding increase in both recovery and extraction efficiency up to 1000 °C. Beyond 1000 °C, there is an increase in residual lithium. This may be attributed to melting and agglomeration which locks up some lithium atoms within the agglomerated matter, hence, preventing their access by $CaCl_2$ and subsequent extraction.

Recovery and extraction efficiency are comparable up to 1000 °C after which about 20% higher extraction was observed

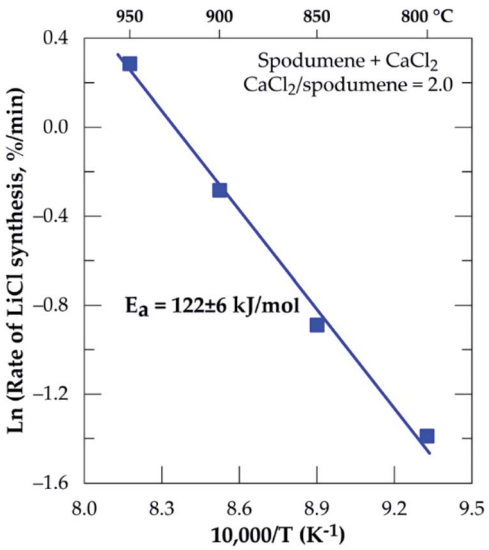

Fig. 7 Arrhenius diagram for lithium recovery during chlorination of spodumene concentrate between 800 and 950 °C, residence time = 60 minutes, $CaCl_2$/spodumene = 2.0.

than recovery (Table 2). The difference may be linked to the evaporation of LiCl as well as melting and agglomeration of materials suspected earlier. Previous studies[40] have confirmed formation and/or evaporation of lithium chloride at 1000 °C and above. They suggested the effect of vapor pressure evolution with temperature as a possible cause of the observation. A plot

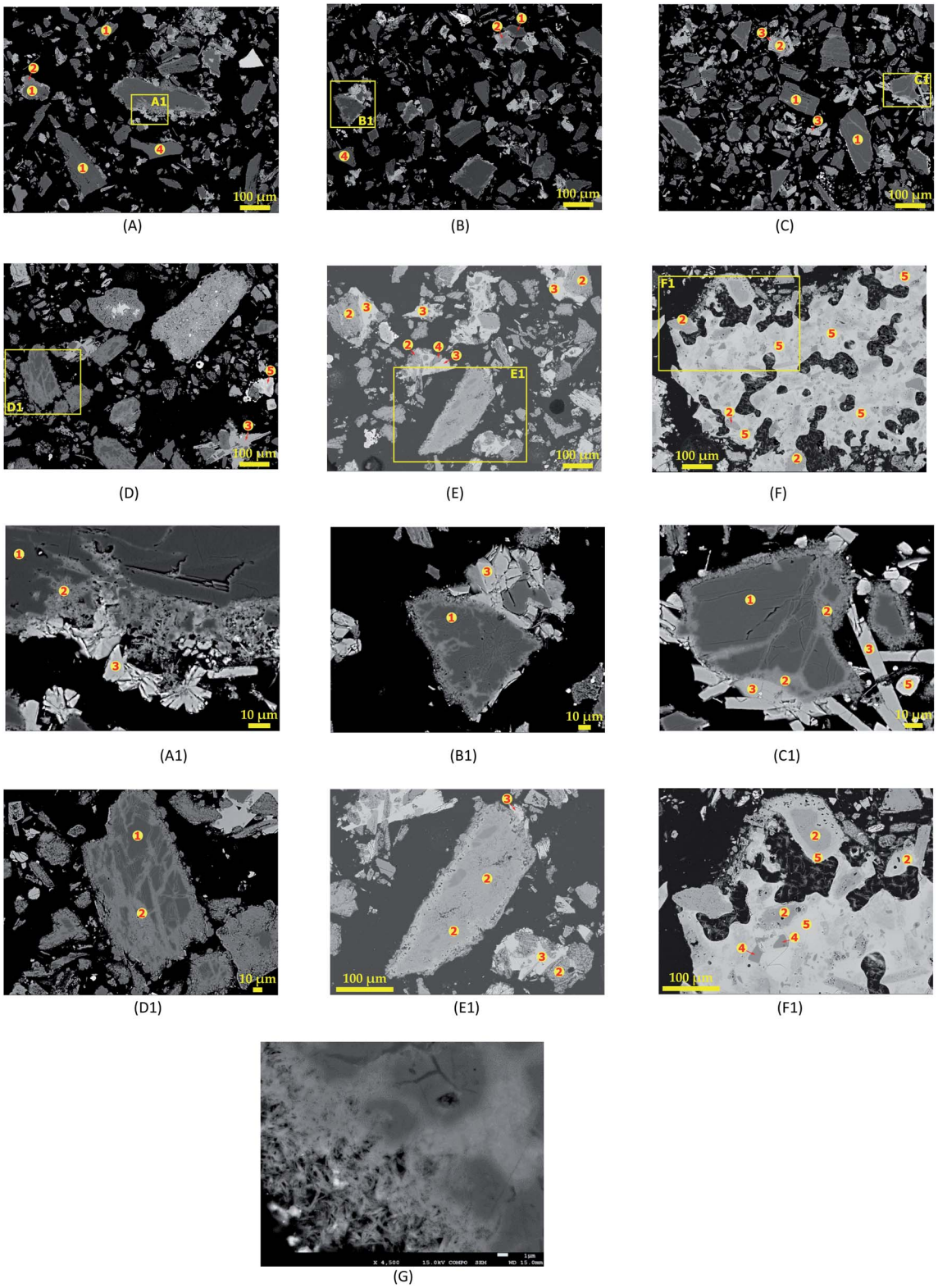

Fig. 8 SEM photomicrographs showing morphological changes of spodumene during 60 min and MR = 1.75 treatment at (A) 750 °C, (B) 800 °C, (C) 850 °C, (D) 950 °C, (E) 1000 °C, (F) 1050 °C and their corresponding spot magnification (A1), (B1), (C1), (D1), (E1) and (F1); (G) fibrous-like structures appearing at the peripheries of spodumene grains during treatment.

Table 3 Elemental composition (EDS data) of sections of spodumene grain during chlorination

	Spot "1"		Spot "2"		Spot "3"		Spot "4"		Spot "5"	
Elements	[a]wt%	[a]at%	wt%	at%	wt%	at%	wt%	at%	[a]wt%	at%
Al	14.38	11.53	16.68	13.39					6.33	5.60
Si	30.50	23.48	22.02	16.97	24.29	19.83	48.27	33.33	13.52	11.50
Cl			0.39	0.24					14.57	9.82
Ca			13.22	7.14	35.41	20.25			29.65	17.68
Fe	0.77	0.30	0.74	0.29					1.76	0.75
Na			0.26	0.25						
Mg									2.25	2.21
O	47.87	64.70	45.61	61.72	41.81	59.92	54.99	66.67	35.10	52.43
Total	93.52		98.92		101.5		103.3		103.2	

[a] wt% and at% represent mass and atomic percentage, respectively.

of changing vapor pressure of LiCl with temperature is shown in Fig. 6b. It increases sharply above 950 °C, where lithium chloride can volatilize and be lost to the gas phase. We suspect also, the possible formation of $CaCl_2$/LiCl, KCl/LiCl or $CaCl_2$/LiCl/KCl eutectic mixtures, which can result in the evaporation of LiCl at relatively low temperature. It can therefore be inferred that, both phenomena (melting and agglomeration and LiCl evaporation) play a role in the decline of lithium recovery.

The Arrhenius diagram for the chlorination process from 800 to 950 °C resulted in an apparent activation energy of 122 ± 6 kJ mol^{-1} (Fig. 7).

3.2.2.1 SEM-EDS investigation. To confirm the supposed phenomena, SEM-EDS analysis was performed on leached residues and results are presented in Fig. 8. Though the evaporation effect could not be established by this approach, a clear melting and agglomeration which could hinder lithium extraction is observed in Fig. 8F (treatment at 1050 °C) but it did not occur at lower temperatures. It is also clear that, $CaCl_2$ selectively attacks spodumene grains at the peripheries at lower temperatures, decolorizing its dark color to several shades of grey. Thus, after decolorizing the exterior portions of spodumene grains, it gradually attacks the internal parts by forming channels through them at increasing temperature. Details of spodumene grain remains in leached residue at 750, 800, 850, 950, 1000, and 1050 °C treatments are shown in Fig. 8A1–F1, respectively.

Increasing temperature is observed to create more channels in spodumene grains, leading to increased reaction area and recovery. Thus, the recovery or extraction appears to depend on the degree of access of the molten $CaCl_2$ to the spodumene grains. It can then be supposed that, the process is diffusion controlled rather than chemical reaction controlled. The

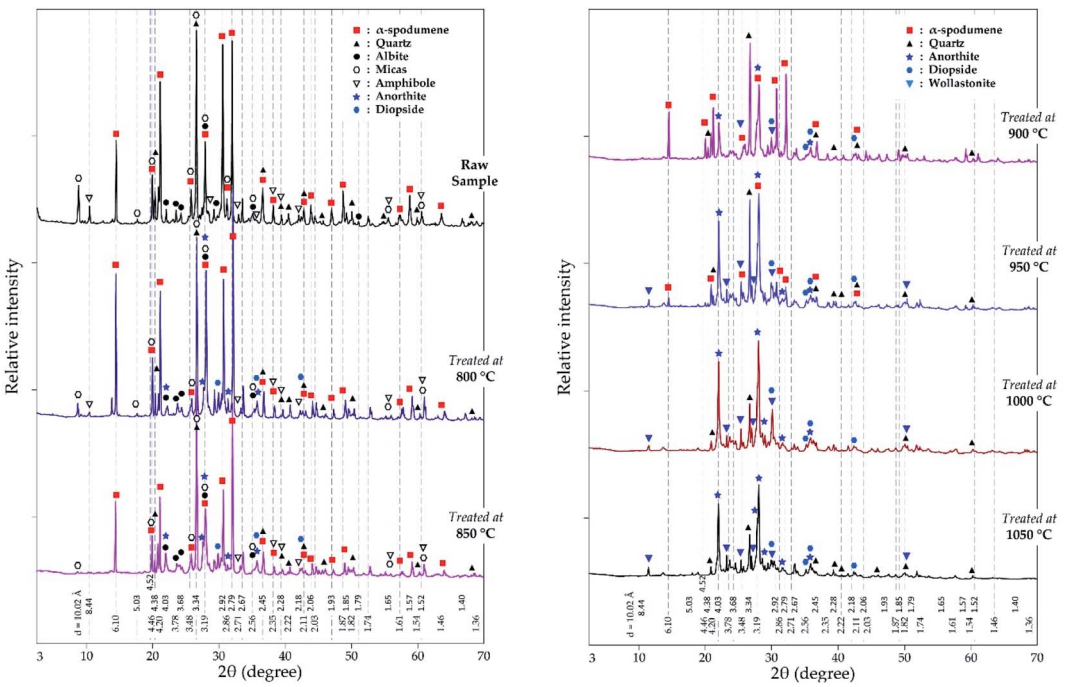

Fig. 9 XRD pattern of evolving phases as a function of temperature at 60 minutes treatment and MR = 2.0.

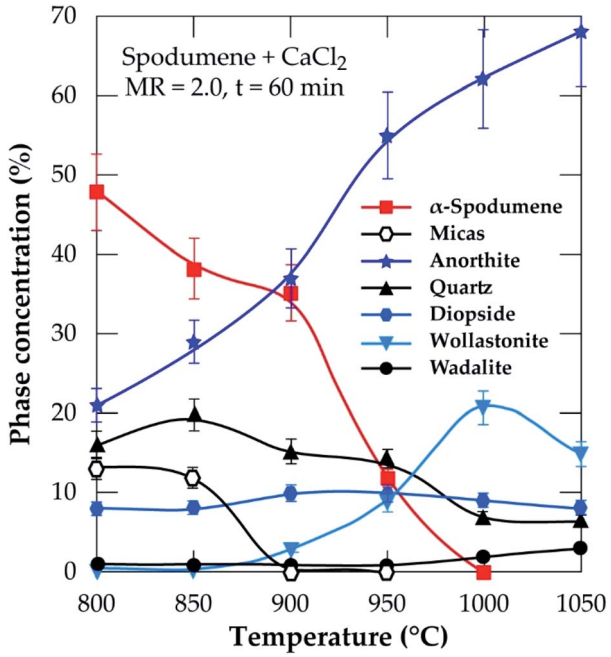

Fig. 10 XRD semi-quantitative analyses of temperature at 60 minutes residence and MR of $CaCl_2$/spodumene of 2.0.

different colorations due to the chlorination of spodumene were assigned "1", "2" and "3" and identified as spodumene, calcium aluminosilicate (CAS) and calcium silicate, respectively. A representative composition of the different portions are shown in Table 3. It is clear that, the internal portions of spodumene grain ("1"), which were unaffected by $CaCl_2$, still maintained their identity. It is an aluminosilicate with Si/Al = 2.0 which confirms its identity. The total wt% of this portion is approximately 94 and the difference may be attributed to lithium which could not be identified by EDS. Iron, the usual impurity associated with it, is also identified at relatively low concentrations. The next portion from the unaffected spodumene ("2") is dark grey area and identified as CAS. There is varying concentration of the constituent elements of this portion which suggests that, different minerals of CAS may be present. The portion "3", which is light grey coloured (the external part of the spodumene), was revealed as calcium silicate with approximate Ca/Si and O/Si of 1.0 and 3.0, respectively. Quartz, which forms a significant portion of the concentrate, is identified at several portions of the SEM photo as "4" with O/Si = 2.0. EDS again identified a type of CAS containing a significant amount of chlorine. Magnesium and iron are found in close association with these portions which makes it light coloured or whitish compared to all the other portions identified. We indicate this portion as "5" and call it "calcium aluminosilicate chloride" (CASCl) for the sake of this study. In Fig. 8F and F1 where melting and agglomeration was observed, quartz, CAS and CASCl were found fused in the agglomerated mater which confirms melting that occurred. EDS could however, not identify the specific type of mineral giving rise to these observations. The standard deviations of atomic percent of the different portions identified and the raw data including the spectra generated by SEM-EDS is given in Tables S1–S10† and Fig. S1–S5 of ESI.†

A closer look at the edges of spodumene grains in Fig. 8G reveals the formation of fibrous-like structures, which gradually eats into the internal parts suggesting again, an initial attack of $CaCl_2$ at the peripheries of the mineral before the interior portions.

3.2.2.2 XRD investigation. In addition to the SEM approach, different leached residues obtained after chlorination at 60 minutes residence time and MR of 2.0 were studied by XRD (Fig. 9). The α-spodumene is observed up to 950 °C but at 1000 °C and beyond, it disappeared. From the first treatment at 800 °C the chemical composition of the plagioclases shows a chemical evolution towards the calcium pole. Plagioclases corresponds to the CAS identified by SEM-EDS. From 900 °C only anorthite is identified (Fig. 9), moreover its content increases with temperature, reaching about 70% in the end at 1050 °C (Fig. 10). Diopside appears at 800 °C and persists throughout the treatments.

Wollastonite appears from 900 °C and like diopside, can be identified until the end of the treatment. Wollastonite is linked to the calcium silicate identified by EDS. Wadalite ($Ca_6(Al,Fe,Mg)_5Si_2O_{16}Cl_3$) was also identified by XRD but due to its comparatively small concentration and for clarity of presentation, it was not considered in XRD diagram. In Fig. 10, its concentration (< 4%) is observed. It corresponds to CASCl which was identified by EDS.

A thermal influence can therefore be observed on the mineralogical assemblages. Spodumene persists up to 1000 °C and its concentration shows a continuous decrease with increasing temperature. As the temperature rises, the spodumene breaks down to interact with the molten calcium chloride.

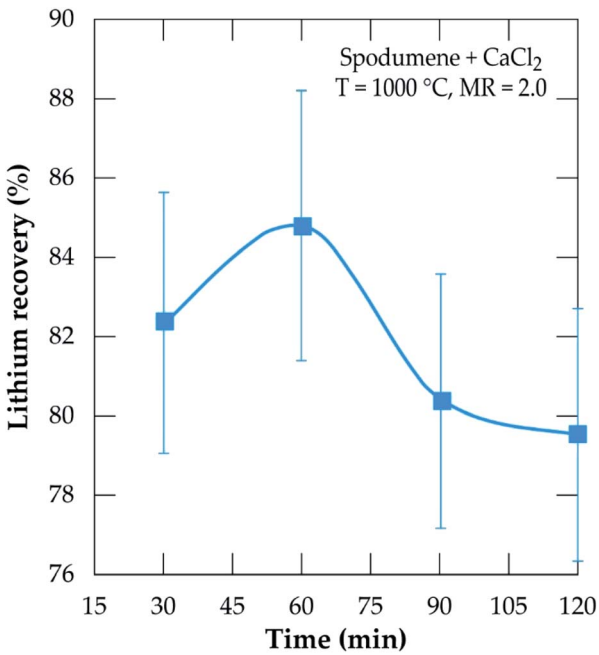

Fig. 11 Evolution of the lithium recovery as a function of residence time for samples treated at 1000 °C and MR = 2.0.

The decrease in spodumene is also related to anorthite formation (Fig. 10) and obviously to the lithium recovery (Fig. 6a).

It is worth noting that, only the α-form of spodumene was identified in the residue. Two pathways may therefore be possible for the extraction; (1) directly from the α-phase or (2) an initial α to β-phase conversion followed by a quick *in situ* lithium chloride formation due to the presence of calcium chloride (2α-spodumene → 2β-$LiAlSi_2O_6$ + $CaCl_2$ → $2LiCl$ + $2SiO_2$ + $CaAl_2Si_2O_8$).

3.3 Effect of residence time

To investigate the kinetics, chlorination was performed at MR of 2.0, 1000 °C temperature and residence time from 30 to 120 minutes. The result is presented in Fig. 11. Recovery increases sharply from 30 minutes and peaks at 60 minutes, achieving about 85% recovery. A decline is observed afterwards such that, at 120 minutes, about 5% lithium chloride was lost. The decline is primarily attributed to the evaporation of lithium chloride. Both temperature and time are thus, indicated as the most sensitive parameters contributing to lithium extraction by this process as suggested earlier.

3.3.1 SEM-EDS investigation. Fig. 12 shows the morphology of leached residues arising from section 3.3 as revealed by SEM-EDS. Fig. 12A (treatment for 30 minutes) reveals clear portions of dark grey colour corresponding to spodumene. A zoom in at A1 (Fig. 12A1) confirms spodumene ("1") by EDS at the internal portions of the grain. Two major phases (dark and light grey) are observed and identified as CAS

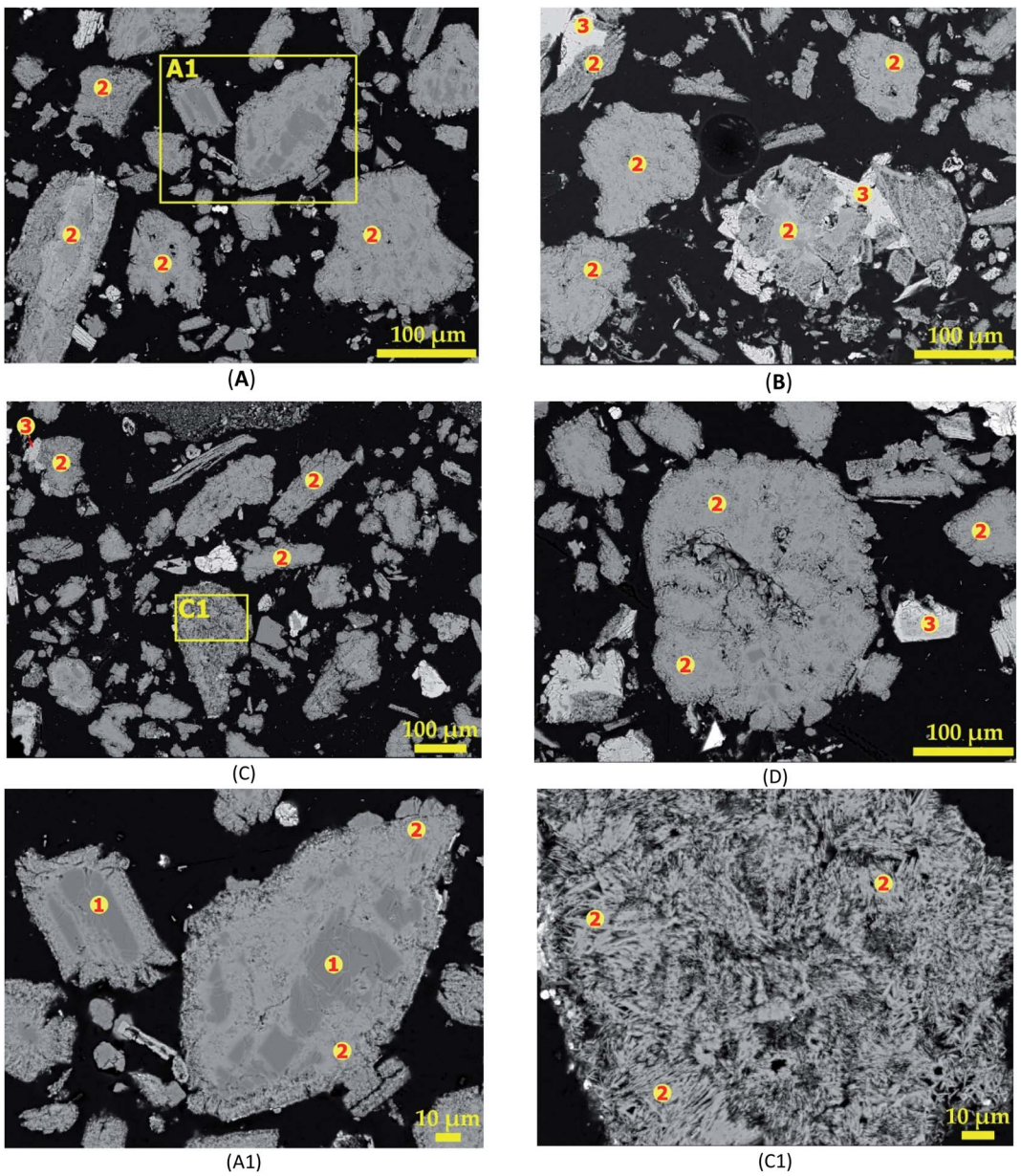

Fig. 12 SEM photomicrographs showing morphological changes of spodumene during 1000 °C treatment for (A) 30 min, (B) 60 min, (C) 90 min and (D) 120 min; (E) and (F) magnification at A1 and C1 respectively.

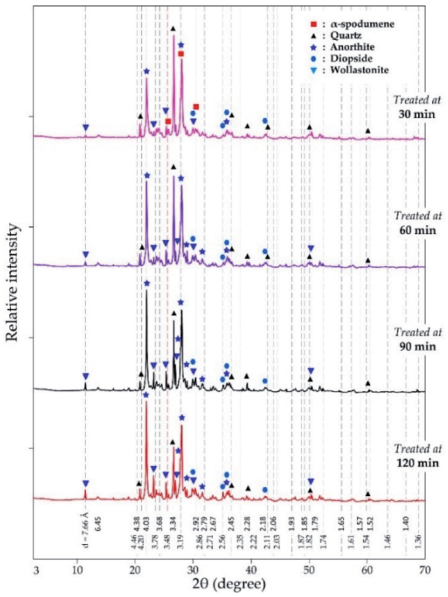

Fig. 13 XRD pattern of evolving phases as a function of residence time at 1000 °C and $CaCl_2$/spodumene of 2.0.

("2") and calcium silicate or wollastonite ("3") after 30 minutes treatments (Fig. 12B–D). Wollastonite is often found attached to the CAS phase at the exterior parts. Observation also shows that, only few CAS grains had wollastonite phase associated with them which gives an indication that, it may be present in small quantity. It may also imply that, both phases evolved concurrently from a mineral in the concentrate and a particular condition is responsible for their segregation into the different phases. There was no observed melting and agglomeration at the various residence time during the treatment at 1000 °C suggesting that, temperature is the main factor responsible for this effect rather than time. A detailed look at a portion in Fig. 12C is shown in Fig. 12C1. It reveals a uniform fibrous-like structure. This may be attributed to the percolation of molten calcium chloride through grains, enabling reaction and subsequent lithium extraction which renders the grains fibrous and porous. EDS analysis reveals that, the entire grain is composed of CAS ("2"). CAS (anorthite) and calcium silicate (wollastonite) are the predominant phases observed from 60 minutes onward according to EDS investigation. It is therefore a confirmation that, they are the major phases at the end of the process as revealed by XRD.

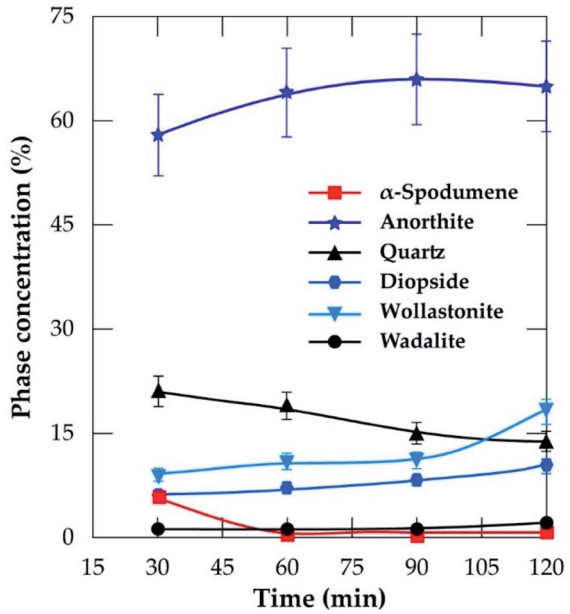

Fig. 14 Concentration of evolving phases as a function of residence time at 1000 °C and $CaCl_2$/spodumene of 2.0.

3.3.2 XRD analysis. XRD was used to access the mineralogical evolution in leached residues as a function of residence time. XRD diagrams and the semi-quantitative estimation are display in Fig. 13 and 14 respectively. Spodumene is observed only in residue treated for 30 minutes which confirms SEM-EDS results in Fig. 12A1. Anorthite is the predominant new phase throughout with minor diopside and wollastonite. In Fig. 14, the anorthite concentration is significantly higher than wollastonite which confirms earlier observation. It increases slightly at the beginning to reach a plateau at 90 minutes. There is no major and significant change in the concentration of the other minerals (quartz, wollastonite, diopside and wadalite).

Table 4 is a mass balance to compare the percent lithium recovered in solution and extraction efficiency at varying residence time. Almost all extracted lithium from the concentrate was recovered in solution at 30 and 60 minutes residence time. Afterwards, the extraction exceeded recovery. Since no melting and agglomeration was observed, the difference may be attributed to the evaporation of lithium chloride after its formation and allowing it to stay in the furnace. A maximum of 89% extraction was achieved during 120 minutes of treatment. Spodumene was not identified in residues obtained beyond the optimal values of the two critical conditions identified. Tables 2 and 4, nonetheless reveal the presence of residual lithium beyond these conditions. This suggests a possibility that, the lithium might be in another phase rather than spodumene which has not been confirmed by this study.

3.4 Mechanisms for phase evolution

Major gangue minerals in the concentrate are mica, alkali feldspar, amphibole, albite and quartz. These minerals interact with each other or respond differently with temperature and the chlorinating agent (calcium chloride). Decrepitation of mica species have been studied extensively by Hutchison.[42] He

Table 4 Mass balance comparison of percent lithium recoveries and extraction at 1000 °C and different residence time

Time (min)	Residual lithium wt%	Recovery%	Extraction%
30	0.37	82.3	82.7
60	0.28	84.8	86.9
90	0.25	80.4	88.3
120	0.24	79.5	88.8

discovered the decomposition to begin around 300 °C (305 to 340 °C). There is a foreknowledge that under pressure, the decomposition of muscovite[43,44] and biotite,[45,46] (the two mica species identified in the spodumene concentrate) form K-feldspar as shown from eqn (12)–(15). The formation is said to be an ionic exchange process[44] which is similar to observation in our previous study.[32]

$$KAl_3Si_3O_{10}(OH)_2 + SiO_2 \rightarrow [KAlSi_3O_8]_{melt} + Al_2SiO_5 + H_2O_{(g)}. \quad (12)$$

$$KFe_3AlSi_3O_{10}(OH)_2 + 3SiO_2 \rightarrow [KAlSi_3O_8]_{melt} + 3FeSiO_3 + H_2O_{(g)} \quad (13)$$

$$KAl_3Si_3O_{10}(OH)_2 \rightarrow [KAlSi_3O_8]_{melt} + Al_2O_3 + H_2O(g) \quad (14)$$

$$KFe_3AlSi_3O_{10}(OH)_2 \rightarrow [KAlSi_3O_8]_{melt} + 3FeO + H_2O(g) \quad (15)$$

Alkali feldspars including K-feldspar synthesized from mica transform to anorthite by replacing alkali metals with calcium atoms in their monoclinic crystal structure of the feldspar.[47] Wollastonite, quartz and alkali metal chlorides alongside the synthesized anorthite are products expected at the end of the process (eqn (16) and 17).

$$CaCl_2 + 2NaAlSi_3O_8 \rightarrow CaAl_2Si_2O_8 + 4SiO_2 + 2NaCl \quad (16)$$

$$CaCl_2 + 2KAlSi_3O_8\,(M) \rightarrow CaAl_2Si_2O_8 + 4SiO_2 + 2KCl \quad (17)$$

Amphiboles transform to their respective pyroxenes and quartz through topotactical dehydration decomposition at temperatures above 600 °C.[48–50] The transformation is pseudo-polymorphic because it occurs at a fixed temperature for a given pressure. There is also a close resemblance of the resultant products to the reactant which is typical of polymorphic transitions.[50] Using tremolite (the amphibole considered in this study), the decomposition gives rise to diopside and enstatite) (eqn (18)) at about 740 °C according to Xu *et al.*[49]

$$Ca_2Mg_5Si_8O_{22}(OH)_2 \rightarrow 2CaMgSi_2O_6 + 3MgSiO_3 + SiO_2 + H_2O_{(g)} \quad (18)$$

$$CaAl_2Si_2O_8 \rightarrow CaSiO_3 + Al_2SiO_5 \quad (19)$$

HSC Chemistry software was used to determine the feasibility of phases evolving and predict the influence of temperature on products formation. Gibbs free energy changes for the formation of products in eqn (12)–(19) is plotted as a function of temperature in Fig. 15. All the reactions are feasible either throughout or at a point within the operating temperatures with the exception of the decomposition of anorthite (eqn (19)).

The micas have similar feasibility which starts after 300 °C and increase with temperature to form K-feldspar which confirms earlier study.[42] Alkali feldspars also have similar chemical reactivity to produce the same products (anorthite and quartz) in addition to their respective alkali metal chlorides but their thermodynamic behaviour is somewhat different. Specifically, K-feldspar (eqn (17)) is feasible throughout but the feasibility of albite (eqn (16)) is only up to 927 °C. K-feldspars (synthesized or originally present in the concentrate) end up forming anorthite as the prominent new phase at the end of the process. Furthermore, anorthite is favorably synthesized from the interaction of spodumene and calcium chloride (eqn (9) and (10)). That is, HSC confirms that, anorthite is a major mineral in leached residues. This is because it is a product from a feasible reaction for the decomposition of spodumene (the major component of the concentrate) as well as other minerals which are present in a fairly high amount. The decomposition of anorthite to other components was investigated as modeled by

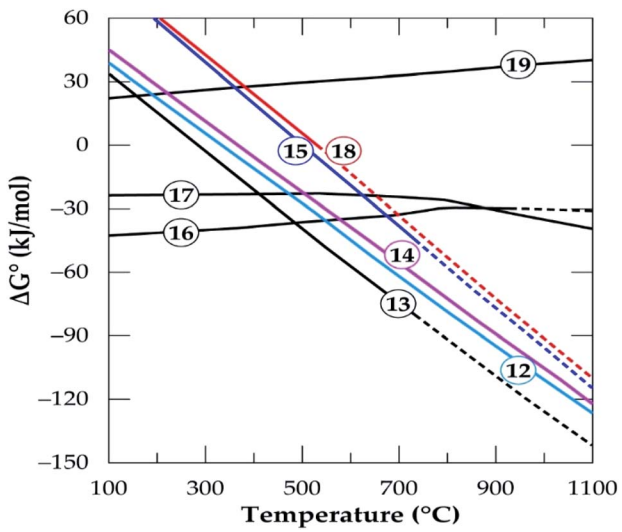

Fig. 15 The standard Gibbs energy changes for phase transformation of gangue minerals in concentrate in oxygen deficient environment (reactions (12)–(19)) *versus* temperature (data from the HSC Chemistry 5.1 Software).

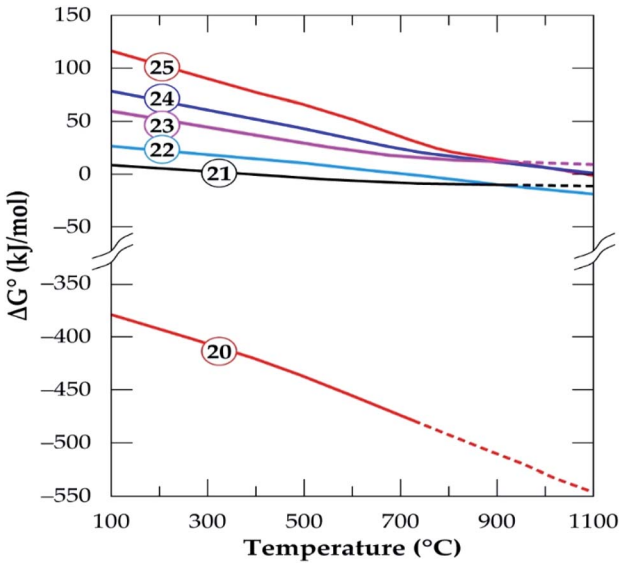

Fig. 16 The standard Gibbs energy changes for phase transformation of gangue minerals in concentrate in oxidizing environment (reactions (20)–(25)) *versus* temperature (data from the HSC Chemistry 5.1 Software).

eqn (19) but it was found not to be possible in Fig. 15. It is suspected that, sodium and potassium which may be found in the leached liquor is obtained principally from eqn (16) and (17). The Gibbs free energy change for the decomposition of tremolite (amphibole) in eqn (18) is negative after 527 °C. However, it is an extrapolated data after 527 °C which may be due to either lack of data for tremolite in the software or its breaks down beyond this temperature. Drawing inference from earlier work,[50] we attribute this to its pseudo-polymorphic decomposition to diopside and enstatite. Extrapolation of data is also observed for albite and spodumene at 927 °C as well as annite at 727 °C.

The effect of oxygen concentration in the process environment on products formation from individual minerals was investigated using the HSC software. Model equations for mica, alkali feldspars, amphibole and albite in the oxidizing atmosphere are presented in eqn (20)–(25). The Gibbs free energy changes for product formation is presented in Fig. 16. With the exception of annite decomposition (eqn (20)), the feasibility of all the reactions are primarily impossible but by manipulating the oxygen concentration, feasibility can be achieved to some extent in the alkali feldspars.

$$2KFe_3AlSi_3O_{10}(OH)_2 + O_{2(g)} \rightarrow 2[KAlSi_3O_8]_{melt} + 2Fe_3O_4 + 2H_2O_{(g)} \quad (20)$$

$$2NaAlSi_3O_8\ (A) + 2CaCl_2 + 0.5O_{2(g)} \rightarrow 2NaCl + CaAl_2Si_2O_8 + 3SiO_2 + CaSiO_3 + Cl_{2(g)} \quad (21)$$

$$2KAlSi_3O_8\ (M) + 2CaCl_2 + 0.5O_{2(g)} \rightarrow 2KCl + CaAl_2Si_2O_8 + 3SiO_2 + CaSiO_3 + Cl_{2(g)} \quad (22)$$

$$2NaAlSi_3O_8\ (A) + 3CaCl_2 + O_{2(g)} \rightarrow 2NaCl + CaAl_2Si_2O_8 + 2SiO_2 + 2CaSiO_3 + 2Cl_{2(g)} \quad (23)$$

$$2KAlSi_3O_8\ (M) + 3CaCl_2 + O_{2(g)} \rightarrow 2KCl + CaAl_2Si_2O_8 + 2SiO_2 + 2CaSiO_3 + 2Cl_{2(g)} \quad (24)$$

$$2\alpha LiAlSi_2O_6 + 3CaCl_2 + O_{2(g)} \rightarrow 2LiCl + CaAl_2Si_2O_8 + 2CaSiO_3 + 2Cl_{2(g)} \quad (25)$$

Oxidizing reactions for alkali feldspars occurring in half a mole of oxygen (eqn (21) and (22)) are not feasible but by doubling it (eqn (23) and (24)), the Gibbs free energy achieve some level of negativity (though not high). The resulting phases are anorthite and calcium silicate (wollastonite, which is identified by XRD) and the release of chlorine gas. Thus, anorthite formation is highly suspected by the software which confirms XRD results. From this observation, wollastonite can be a possible product in the residue depending on the oxygen concentration during treatment only if HSC Software predictions are valid. Spodumene feasibility is also observed to be affected by oxygen concentration such that, it is non-spontaneous in oxidizing atmosphere (eqn (25) and Fig. 16) but spontaneous in oxygen deficient atmosphere (eqn (9)) depending on the temperature. In general, the process feasibility is high in oxygen deficient environment than oxidizing.

3.5 Correlating XRD results, HSC software predictions and reaction mechanisms

HSC software predicts anorthite as the predominant new phase at the end of the process, arising primarily from spodumene, mica and alkali feldspar decomposition in the presence of calcium chloride. Amphibole and mica persist only up to 850 °C after which they disappear from XRD spectra of leached residue. This implies that, after 850 °C, their transformation to other phases is complete which is in agreement with observation by ref. 50 and 42. As indicated earlier, the decomposition of mica and amphibole basically form K-feldspar melt and pyroxenes respectively. The appearance of diopside after 850 °C may be linked to the decomposition of tremolite, though enstatite (its corresponding pyroxene during decomposition) was not identified, probably it transformed further to another phase. K-feldspar may evolve from mica decomposition and its feasibility is confirmed by HSC software but it was not identified in any of the residues. This suggests that, it appears as a metastable phase and hence, quickly transforms to anorthite in the presence of calcium chloride. According to ref. 51, the decomposition of K-feldspars in the presence of calcium chloride begins around 600 °C. Potassium chloride and anorthite are the resulting products such that at 900 °C, the optimum extraction is achieved. This identified temperature range falls within the operating temperatures of the study. Therefore, the absence of K-feldspar in the residue (XRD spectra) may be attributed to its fast conversion to anorthite in the course of the process. Eqn (19) suggests that, wollastonite may evolve from the decomposition of anorthite or the chlorination of alkali feldspar in an oxidizing atmosphere (eqn (21)–(25)). Since HSC Software predicts eqn (19) to be nonspontaneous, the close association of wollastonite with CAS (as revealed in Fig. 12) may lead to the conclusion that, the decomposition of alkali feldspars is responsible for the synthesis of both phases and a limiting oxidizing atmosphere is a prerequisite for the synthesis.

4. Conclusion

Investigation into the pyrometallurgical synthesis of lithium chloride directly from α-spodumene followed by water leaching was conducted. Though MR has influence on lithium recovery, temperature and time are the major factors which, if are not regulated leads to evaporation of lithium chloride. Lithium recovery to leach solution generally increases with all investigated parameters, which are MR, temperature and time until they peak at 2.0, 1000 °C and 60 minutes respectively. These optimal conditions led to about 90 percent lithium extraction but 85 percent was recovered to solution with the remainder exiting *via* the gas phase. In a process, this gas phase lithium could be also recovered by leaching the gas treatment dust. Though recovery plateaus after MR of 2.0, evaporation coupled with melting and agglomeration occurs after 1000 °C, which in addition, leads to a decrease in recovery. XRD results confirmed HSC software and SEM-EDS predictions which reveals anorthite as predominant phases (accounting for about 70 percent) alongside quartz, wollastonite and diopside as minor phases.

Predictions by HSC software are in good agreement with experimental observation. Spodumene identified in leached residue is in the α-form with no identification of the β-form. This suggests that, the extraction of lithium chloride is directly from the α-phase. A possible transformation of α-spodumene into β-spodumene followed by a fast synthesis of lithium chloride from β-spodumene (2α-spodumene → 2β-$LiAlSi_2O_6$ + $CaCl_2$ → $2LiCl + 2SiO_2 + CaAl_2Si_2O_8$) may also occur. However, we treat this as tentative at this stage. The relatively low apparent activation energy of 122 ± 6 kJ mol^{-1} obtained could suggest diffusion of calcium chloride as the rate limiting step of the process.

Author contributions

Conceptualization: AC, NK; formal analysis: AYF, AC, NK, DB; funding acquisition: AC; investigation: AYF; project administration: AC; supervision: AC, NK; visualization: AYF, NK; writing-original draft: AYF; writing-review and editing: AYF, NK, BD, JV, AC.

Conflicts of interest

There are no conflicts to declare.

Acknowledgements

This work was supported by the French National Research Agency through the national program "Investissements d'avenir" with the reference ANR-10-LABX-21-RESSOURCES21.

References

1 N. Kanari, D. Mishra, J. Mochón, L. F. Verdeja, F. Diot and E. Allain, Some kinetics aspects of chlorine-solids reactions, *Rev. Metal.*, 2010, **46**(1), 22–36, DOI: **10.3989/revmetalm.0852**.

2 N. Kanari, D. Mishra, L. Filippov, F. Diot, J. Mochón and E. Allain, Kinetics of hematite chlorination with Cl_2 and $Cl_2 + O_2$: part I. Chlorination with Cl_2, *Thermochim. Acta*, 2010, **497**(1–2), 52–59, DOI: **10.1016/j.tca.2009.08.007**.

3 P. K. Jena and E. A. Brocchi, Metal extraction through chlorine metallurgy, *Miner. Process. Extr. Metall. Rev.*, 1997, **16**(4), 211–237, DOI: **10.1080/08827509708914136**.

4 N. Kanari, B. R. Reddy and I. Gaballah, Kinetics of Carbochlorination of Chromium (III) Oxide, *Metall. Mater. Trans. B*, 1998, **29**(4), 729–737, DOI: **10.1007/s11663-998-0131-x**.

5 N. Kanari and I. Gaballah, Chlorination and carbochlorination of magnesium oxide, *Metall. Mater. Trans. A*, 1999, **30**(3), 383–391, DOI: **10.1007/s11663-999-0070-1**.

6 E. Jang, Y. Jang and E. Chung, Lithium recovery from shale gas produced water using solvent extraction, *Appl. Geochem.*, 2017, **78**, 343–350, DOI: **10.1016/j.apgeochem.2017.01.016**.

7 L. Tian, Y. Liu, P. Tang, Y. Yang, X. Wang, T. Chen, Y. Bai, A. Tiraferri and B. Liu, Lithium extraction from shale gas flowback and produced water using $H_{1.33}Mn_{1.67}O_4$ adsorbent, *Resour., Conserv. Recycl.*, 2022, **185**, 106476, DOI: **10.1016/j.resconrec.2022.106476**.

8 O. Sitando and P. L. Crouse, Processing of a Zimbabwean petalite to obtain lithium carbonate, *Int. J. Miner. Process.*, 2012, **102–103**, 45–50, DOI: **10.1016/j.minpro.2011.09.014**.

9 E. Siame and R. D. Pascoe, Extraction of lithium from micaceous waste from china clay production, *Miner. Eng.*, 2011, **24**(14), 1595–1602, DOI: **10.1016/j.mineng.2011.08.013**.

10 J. Jandova and H. N. Vu, Processing of zinnwaldite wastes to obtain lithium and rubidium compounds, in *Proceedings of the 2008 Global Symposium on Recycling, Waste Treatment and Clean Technology, REWAS 2008*, Cancun, Mexico, 2008.

11 J. Jandová, P. Dvořák and H. N. Vu, Processing of zinnwaldite waste to obtain Li_2CO_3, *Hydrometallurgy*, 2010, **103**(1–4), 12–18, DOI: **10.1016/j.hydromet.2010.02.010**.

12 J. Jandová, H. N. Vu, J. Kondas, and P. Dvořák, Lithium recovery from wastes after mining of Sn–W ore, in *Proceedings of the European Metallurgical Conference, EMC 2007*, Düsseldorf, Germany, 2007, pp. 667–677.

13 J. Jandová, H. N. Vu, T. Beloková, P. DvořÁk and J. Kondás, Obtaining Li_2CO_3 from Zinnwaldite wastes, *Ceram.–Silik.*, 2009, **53**, 108–112.

14 Q. Yan, et al., Extraction of valuable metals from lepidolite, *Hydrometallurgy*, 2012, **117–118**, 116–118, DOI: **10.1016/j.hydromet.2012.02.004**.

15 Q. Yan, et al., Extraction of lithium from lepidolite using chlorination roasting–water leaching process, *Trans. Nonferrous Met. Soc. China*, 2012, **22**(7), 1753–1759, DOI: **10.1016/S1003-6326(11)61383-6**.

16 Q. Yan, et al., Hydrometallurgy A novel process for extracting lithium from lepidolite, *Hydrometallurgy*, 2012, **121–124**, 54–59, DOI: **10.1016/j.hydromet.2012.04.006**.

17 V. T. Luong, D. J. Kang, J. W. An, D. A. Dao, M. J. Kim and T. Tran, Iron sulphate roasting for extraction of lithium from lepidolite, *Hydrometallurgy*, 2014, **141**, 8–16, DOI: **10.1016/j.hydromet.2013.09.016**.

18 V. T. Luong, D. J. Kang, J. W. An, M. J. Kim and T. Tran, Factors affecting the extraction of lithium from lepidolite, *Hydrometallurgy*, 2013, **134–135**, 54–61, DOI: **10.1016/j.hydromet.2013.01.015**.

19 G. D. Rosales, M. C. Ruiz and M. H. Rodriguez, Study of the Extraction Kinetics of Lithium by Leaching β-Spodumene with Hydrofluoric Acid, *Minerals*, 2016, **6**(4), 98, DOI: **10.3390/min6040098**.

20 G. D. Rosales, M. D. C. Ruiz and M. H. Rodriguez, Novel process for the extraction of lithium from β-spodumene by leaching with HF, *Hydrometallurgy*, 2014, **147–148**, 1–6, DOI: **10.1016/j.hydromet.2014.04.009**.

21 H. Guo, G. Kuang, H. Wang, H. Yu and X. Zhao, Investigation of Enhanced Leaching of Lithium from α-Spodumene Using Hydrofluoric and Sulfuric Acid, *Minerals*, 2017, **7**(11), 205, DOI: **10.3390/min7110205**.

22 G. D. Rosales, A. C. J. Resentera, J. A. Gonzalez, R. G. Wuilloud and M. H. Rodriguez, Efficient extraction of lithium from β-spodumene by direct roasting with NaF and leaching, *Chem. Eng. Res. Des.*, 2019, **150**, 320–326, DOI: 10.1016/j.cherd.2019.08.009.

23 Y. Chen, Q. Tian, B. Chen, X. Shi and T. Liao, Preparation of lithium carbonate from spodumene by a sodium carbonate autoclave process, *Hydrometallurgy*, 2011, **109**(1–2), 43–46, DOI: 10.1016/j.hydromet.2011.05.006.

24 G. Kuang, Y. Liu, H. Li, S. Xing, F. Li and H. Guo, Extraction of lithium from β-spodumene using sodium sulfate solution, *Hydrometallurgy*, 2018, **177**, 49–56, DOI: 10.1016/j.hydromet.2018.02.015.

25 Y. Song, T. Zhao, L. He, Z. Zhao and X. Liu, Hydrometallurgy a promising approach for directly extracting lithium from α-spodumene by alkaline digestion and precipitation as phosphate, *Hydrometallurgy*, 2019, **189**, 105141, DOI: 10.1016/j.hydromet.2019.105141.

26 P. Zhang, T. Yokoyama, O. Itabashi, T. M. Suzuki and K. Inoue, Hydrometallurgical process for recovery of metal values from spent lithium-ion secondary batteries, *Hydrometallurgy*, 1998, **47**(2–3), 259–271.

27 R. Gupta and A. Manthiram, Chemical Extraction of Lithium from Layered $LiCoO_2$, *J. Solid State Chem.*, 1996, **121**(2), 483–491.

28 T. Georgi-maschler, B. Friedrich, R. Weyhe, H. Heegn and M. Rutz, Development of a recycling process for Li-ion batteries, *J. Power Sources*, 2012, **207**, 173–182, DOI: 10.1016/j.jpowsour.2012.01.152.

29 V. T. Nguyen, J. C. Lee, J. Jeong, B. S. Kim and B. D. Pandey, The Separation and Recovery of Nickel and Lithium from the Sulfate Leach Liquor of Spent Lithium Ion Batteries using PC-88A, *Korean Chem. Eng. Res*, 2015, **53**(2), 137–144.

30 O. Peltosaari, P. Tanskanen, E.-P. Heikkinen and T. Fabritius, α → γ → β-phase transformation of spodumene with hybrid microwave and conventional furnaces, *Miner. Eng.*, 2015, **82**, 54–60, DOI: 10.1016/j.mineng.2015.04.012.

31 R. L. Moore, J. P. Mann, A. Montoya and B. S. Haynes, *In situ* synchrotron XRD analysis of the kinetics of spodumene phase transitions, *Phys. Chem. Chem. Phys.*, 2018, **20**(16), 10753–10761, DOI: 10.1039/C7CP07754H.

32 A. Y. Fosu, N. Kanari, D. Bartier, H. Hodge, J. Vaughan and A. Chagnes, Physico-Chemical Characteristics of Spodumene Concentrate and Its Thermal Transformations, *Materials*, 2021, **14**(23), 7423.

33 G. D. White and T. N. McVay, *Some Aspects of the Recovery of Lithium From Spodumene*, Oak Ridge, TN (United States), 1958, DOI: 10.2172/4352576.

34 A. Y. Fosu, N. Kanari, J. Vaughan and A. Chagnes, Literature review and thermodynamic modelling of roasting processes for lithium extraction from spodumene, *Metals*, 2020, **10**(10), 1312.

35 J. A. Peterson and G. H. Glioss, Lithium Values Recovery Process, *U.S. Patent*, No. 2893828, 1959.

36 H. Dang, B. Wang, Z. Chang, X. Wu, J. Feng, H. Zhou, W. Li and C. Sun, Recycled lithium from simulated pyrometallurgical slag by chlorination roasting, *ACS Sustain. Chem. Eng.*, 2018, **6**(10), 13160–13167.

37 H. Dang, et al., Lithium leaching *via* calcium chloride roasting from simulated pyrometallurgical slag of spent lithium ion battery, *Sep. Purif. Technol.*, 2020, **233**, 116025, DOI: 10.1016/j.seppur.2019.116025.

38 L. I. Barbosa, G. Valente, R. P. Orosco and J. A. González, Lithium extraction from β-spodumene through chlorination with chlorine gas, *Miner. Eng.*, 2014, **56**, 29–34, DOI: 10.1016/j.mineng.2013.10.026.

39 L. I. Barbosa, J. A. González and M. del C. Ruiz, Extraction of lithium from β-spodumene using chlorination roasting with calcium chloride, *Thermochim. Acta*, 2015, **605**, 63–67, DOI: 10.1016/j.tca.2015.02.009.

40 L. I. Barbosa, N. G. Valente and J. A. González, Kinetic study on the chlorination of β-spodumene for lithium extraction with Cl_2 gas, *Thermochim. Acta*, 2013, **557**, 61–67, DOI: 10.1016/j.tca.2013.01.033.

41 A. C. Bidaye, C. K. Gupta and S. Venkatachalam, Studies on the chlorination of zircon: Part I. Static bed investigations, *Metall. Mater. Trans. B*, 1999, **30**(2), 205–213.

42 W. W. Hutchison, Two stages of decrepitation of micas, *Can. Mineral.*, 1966, **8**(4), 437–460.

43 M. Anenburg and Y. Katzir, Muscovite dehydration melting in Si-rich metapelites: microstructural evidence from trondhjemitic migmatites, *Mineral. Petrol.*, 2014, **108**(1), 137–152.

44 B. Dyck, D. J. Waters, M. R. St-Onge and M. P. Searle, Muscovite dehydration melting: reaction mechanisms, microstructures, and implications for anatexis, *J. Metamorph. Geol.*, 2020, **38**(1), 29–52.

45 B. J. S. Douce Patino and E. Alberto, Dehydration-melting of biotite gneiss and quartz amphibolite from 3 to 15 kbar, *J. Petrol.*, 1995, **36**(3), 707–738.

46 A. A. Graphchikov, A. N. Konilov and J. D. Clemens, Biotite dehydration, partial melting, and fluid composition: experiments in the system $KAlO_2$–FeO–MgO–SiO_2–H_2O–CO_2, *Am. Mineral.*, 1999, **84**(1–2), 15–26, DOI: 10.2138/am-1999-1-202.

47 L. Li, S. Lei, Y. Liu and H. Luo, Extraction and Reaction Mechanism of Potassium from Associated Phosphorus and Potassium Ore, *J. Wuhan Univ. Technol.-Materials Sci. Ed.*, 2016, **31**(6), 1255–1260.

48 N. M. Johnson and B. Fegley, Tremolite decomposition on Venus II. Products, kinetics, and mechanism, *Icarus*, 2003, **164**(2), 317–333.

49 H. Xu, D. R. Veblen, L. Gufeng and X. Jiyue, Transmission electron microscopy study of the thermal decomposition of tremolite into clinopyroxene, *Am. Mineral.*, 1996, **81**(9–10), 1126–1132.

50 F. Freeman and A. G. Frazer, Pseudo polymorphic transition: the amphibole → pyroxene reaction, *Nature*, 1968, **220**(5162), 67–68, DOI: 10.1038/220067a0.

51 B. Yuan, et al., Extraction of potassium from K-feldspar *via* the $CaCl_2$ calcination route, *Chin. J. Chem. Eng.*, 2015, **23**(9), 1557–1564, DOI: 10.1016/j.cjche.2015.06.012.